A Journey across the Hertzsprung-Russell diagram with 3D hydrodynamical simulations of cool stars

A. Chiavassa

Laboratoire Lagrange, CNRS, UMR 2793
Université de Nice Sophia-Antipolis
Observatoire de la Côte d'Azur

A Journey across the Hertzsprung-Russell diagram with 3D hydrodynamical simulations of cool stars

Andrea Chiavassa

Thèse d'Habilitation à Diriger des Recherches
Ecole Doctorale Sciences Fondamentales et Appliquées
(ED-SFA)

Rapporteurs: **Tristan Guillot**, **Sophie Van Eck**, **Markus Wittkowski**
Membres du jury: **Tristan Guillot**, **Guy Perrin**, **Philippe Stee**, **Sophie Van Eck**, **Markus Wittkowski**

Observatoire de la Côte d'Azur
Date de soutenance 19 décembre 2018

Contents

List of Figures

Preface

In this manuscript (*mémoire*) I summarise the work I have carried out in the last ∼10 years. My research projects are articulated around various fields in astrophysics having, as unifying theme, the 3D modelling and the observation of stellar atmospheres. In particular, my field of research covers all late type stars, from the Main Sequence stars to the advanced stages (red giant and supergiant stars).

My work is based on the quantitative analysis of images, synthetic spectra, bolometric luminosity, planetary transits of different types of stars and on the modeling of their atmospheres. They include the use and development of 3D simunlations that are necessary for the interpretation of the data obtained with the new instruments equipping the space borne and ground telescopes. Interferometry and spectroscopy hold a privileged place in my research.

My research themes concern interdisciplinary aspects by addressing questions related to atmospheric physics in relation to 3D hydrodynamic models. The predictions thus obtained are used to drive a vast campaign of interferometric, astrometric, photometric, spectroscopic and imaging observations. Finally, 3D simulations are also directly used to drive the development of new generation instrument at the VLTI, as well as very large future observatories and are directly linked to the ESA Gaia and PLATO missions.

Nice, 7 November 2018. Andrea Chiavassa

1

Introduction

1.1 Context

THE INFORMATION we have to study the stars comes from the photons they emitted. The radiation that escapes from the atmosphere is the only source of information for the study of these objects. In this context, the description of stellar atmospheres is of paramount importance, because it is there that radiation is formed. Convection plays a central role in the structure, dynamics and appearance of evolved stars. In recent years, it has become possible to produce multidimensional (and in particular three-dimensional, 3D) hydrodynamic simulations of gas motion in the atmospheric layers of stars, coupled with radiation. A 3D approach is required for qualitative and quantitative surface analysis of most stars. The exchange of energy between the gas and the radiation field is essential because it determines the thermal gradient and drains convective movements. 3D models are ab initio, time-dependent, multidimensional and non-local. However, they require considerable computation time and do not yet allow the inclusion of a complex radiative transfer treatment as in the case of 1D. Understanding the stellar atmosphere is crucial for several reasons:

- The atmosphere is a window into the stars, and serves as a link between atmospheric models, stellar evolution models, and observations. Stellar evolution phenomena manifest themselves in stellar surfaces as a change in chemical composition and fundamental parameters (e.g. radius, surface gravity, effective temperature and brightness) due to dredge-up processes, internal waves, circulations, rotation. Atmospheric models are therefore necessary as a boundary condition for interior star models and are essential for comparison with observed stellar oscillations (Helio- and Astero-seismology).

- The atmosphere is also the interface with the interstellar medium. In this respect, the effects on the interstellar medium, through radiation and/or mass loss, reflect the physics of the atmosphere and affect the dynamic and chemical evolution of the Galaxy.

- Finally, modelling of the stellar atmosphere is also motivated by modernes observations of stellar surfaces, which show a very dynamic landscape and complex structures, especially in the presence of magnetic fields.

A realistic modelling taking into account all the richness of the processes at work in the atmosphere (convection, shocks, radiative transfer, ionization, formation of molecules/dust) is essential for the correct analysis of stellar observables. My research develops in this context: I study the atmosphere of late stars (from the Main Sequence to the red supergiant stage) with three-dimensional radiative hydrodynamic models. The key point of my research is the synergy between theory and observations. The 3D numerical simulations are compared to current and future observations (interferometric, photometric, spectroscopic, astrometric and images) using the OPTIM3D radiative transfer code, which I developed, to calculate the observables.

1.2 Open questions

As I will do in next chapter, I separate the discussions in two main topics: namely (1) stars from main sequence to Red Gian Branch (RGB) phase and (2) evolved stars such as Red SuperGiant (RSG) and Asymptotic Giant Branch (AGB) stars. This choice is arbitrary but supported by the fact that these objects share similar observational techniques, observational properties, and main astrophysical questions.

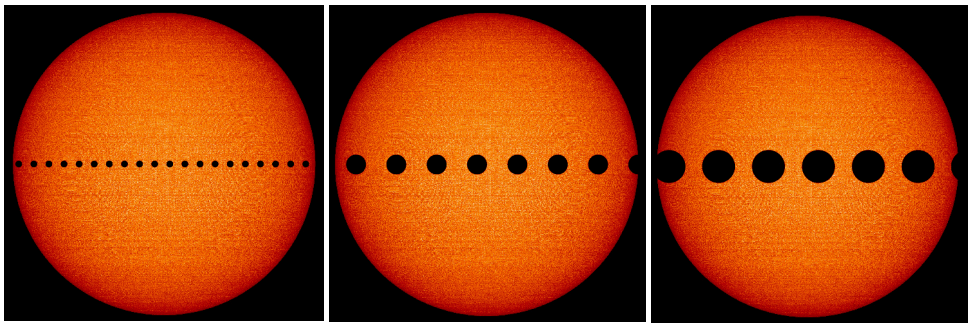

Figure 1.1: From main sequence stars to RGB phases. Example of a synthetic solar type star with terrestrial, neptunian, and hot Jupiter transiting planet.

From main sequence stars to RGB phases

Stars are not smooth. Their photosphere is covered by a granulation pattern associated with the heat transport by convection. The convection-related surface structures have different size, depth, and temporal variations with respect to the stellar type. The related activity (in addition to other phenomena such as magnetic spots, rotation, dust, etc.) potentially causes bias in stellar parameters determination, radial velocity, chemical abundances determinations, and exoplanet transit detections. Convection manifests in the surface layers as a particular pattern of downflowing cooler plasma and bright areas where hot plasma rises (Nordlund et al. 2009). The size of granules depends on the stellar parameters of the star and, as a consequence, to the extension of their atmosphere (Magic et al. 2013a). Eventually, the convection causes inhomogeneous stellar surface that changes with time. They affect the atmospheric stratification in the region where the flux forms and the emergent spectral energy distribution, with potential effects on precise determinations of stellar parameters (Bigot et al. 2011; Creevey et al. 2012; Chiavassa et al. 2012), radial velocity (Bigot & Thévenin 2008; Chiavassa et al. 2011a; Allende Prieto et al. 2013), chemical abundance (Asplund et al. 2005, 2009; Caffau et al. 2011), photometric colours

(Chiavassa et al. 2018a; Bonifacio et al. 2017) and on planet detection (Magic et al. 2015; Chiavassa et al. 2017a).

Convection is a difficult process to understand because it is nonlocal, and three-dimensional, and it involves nonlinear interactions over many disparate length scales. In this context, the use of numerical three-dimensional radiative hydrodynamical simulations of stellar convection is extremely important. In recent years, with increased computational power, it has been possible to compute grid of 3D simulations (see Stagger code in Section 1.3) that cover a substantial portion of the Hertzsprung-Russell diagram (Magic et al. 2013a; Trampedach et al. 2013; Beeck et al. 2013; Ludwig et al. 2009). With these tools, it is possible to predict reliable synthetic spectra and images for several stellar types. For a complete description of a star (and the planet hosted), a number of parameters are important, such as mass, luminosity, radius, age, pulsation period, chemical composition, angular momentum, magnetic field, mass-loss rate, and the circumstellar environment. The observational determination of several of these parameters requires a high spectral resolution. Furthermore, while some of these parameters are integrated quantities, several of them vary across the stellar disk and its environment, leading to the need for spatially resolved observations (Wittkowski 2004). In this context, the use of realistic 3D hydrodynamical stellar atmosphere simulations are essential for a large application range in addition to stellar convection studies and atmospheres themselves: stellar fundamental parameter determination, stellar spectroscopy and abundance analysis, asteroseismology, calibration of stellar evolutionary models, interferometry, and detection/characterisation of extrasolar planets.

Evolved objects, RSG and AGB stars

Evolved cool stars of various masses are major cosmic engines (Langer 2012), providing strong mechanical and radiative feedback on their host environment. Through strong stellar winds and supernova ejections, they enrich their environment with chemical elements, which are the building blocks of the planets and life. In particular, these objects are known to propel strong stellar winds that carry the mass and angular momentum of the star's surface at speeds that vary with stellar brightness, evolution phase and chemical composition. In addition, stellar evolution models are not able to reproduce these winds without "ad hoc" physics. A complete understanding of their evolution in the near and distant Universe cannot therefore be achieved without a detailed understanding of wind physics across the life cycle of these stars as well as in relation to their cosmic environment.
The evolved cool stars can be divided in two categories based on their mass:

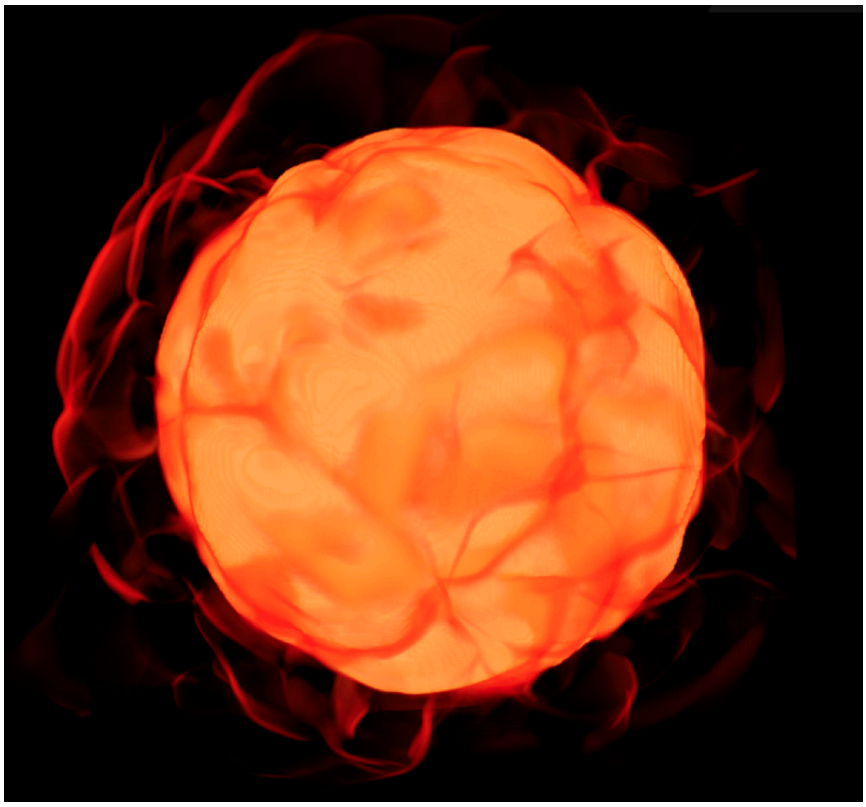

Figure 1.2: Evolved objects, synthetic RSG and AGB stars

- Stars of low to intermediate mass ($0.5 < M < 8M_{\odot}$, the exact value of the upper limit depends on the treatment of convection) evolve towards the red giant branch and the asymptotic branch of giants (AGB), increasing mass loss during this evolution. AGBs are characterized by very low effective temperatures (about 3000 K or less) and high luminosity (about 100 - 1000 $L_{\odot}$) which correspond to stellar radii of several hundred solar radii. Their high rate of mass loss ($\dot{M}$=10^{-6}-10^{-4} $M_{\odot}$/yr, De Beck et al. 2010) results from an interaction between pulsation, dust formation in the extended atmosphere and radiation pressure on dust (Höfner & Olofsson 2018). This loss of mass is accompanied by a structural modification of their circumstellar envelopes, particularly pronounced during the evolution AGB => post-AGB => Planetary Nebula. The magnetic field coupled with the atmospheric dynamics should play a key role in the process of initiating and maintaining a high mass loss (Lèbre et al. 2014),

or together with the evolution of the geometry of the stellar wind.

- More massive stars ($M > 8M_{\odot}$) evolve into red supergiant phase before they explode into type II supernovae. These stars are characterized by high luminosity ($L > 1000\ L_{\odot}$), effective temperatures between 3450 and 4100 K and stellar radii up to several hundreds of $R_{\odot}$, or even more than 1000 $R_{\odot}$ (Levesque et al. 2005). One of the properties of RSG stars is their rate of mass loss ($\dot{M}$=10^{-7}-10^{-4} $M_{\odot}$/yr, Wood et al. 1992), the origin of which being still poorly understood (radiation pressure, radiative and/or pressure shock waves, magnetism, dust, e.g., Josselin & Plez 2007). RSGs have a low intensity magnetic field (of the order of 1 gauss) that has been identified and monitored over several years (Aurière et al. 2010; Tessore et al. 2017; Mathias et al. 2018). In these circumstances, the photospheric convective motions would tend to generate a local dynamo responsible for such intermittent fields (Petit et al. 2013).

These stars are among the largest stars in the Universe and their luminosities place them among the brightest stars, visible to very long distances. This last point is very important for the quantitative analysis studies of metallicity in our Galaxy (e.g., with JWST Levesque 2018) and in nearby galaxies (Davies et al. 2017). However, their chemical composition is very difficult to be obtained due to their complex spectra with broad, asymmetric lines with variations suspected to stem from a convection pattern consisting of large granules and (super)-sonic velocities.

The use of state-of-the-art numerical simulation of stellar convection (see CO^{5}BOLD code in Section 1.3) is essential for the subsequent interpretation of the observations (spectroscopic, imaging, interferometry, astrometry...) and the solutions of the different open questions reported above. Interferometric observations, corroborated by the numerical simulations, show that the stellar surface of theses stars is covered by a few convective cells (Chiavassa et al. 2010b,c; Freytag et al. 2017; Montargès et al. 2017) evolving on timescales of several weeks to years (Chiavassa et al. 2018b, 2011c), and causing large temperature inhomogeneities. Their velocity can levitate the gas and contribute to the mass loss (Chiavassa et al. 2011b; Freytag et al. 2017; Kravchenko et al. 2018).

1.3 Hydrodynamic modelling of stellar atmospheres

Late type stellar atmosphere modelling is carried out using three-dimensional (3D) radiative hydrodynamical (RHD) simulations. The RHD codes solve the time-dependent, three-dimensional, compressible equations of radiative hydrodynamics in a cartesian grid. The horizontal dimensions are chosen to take into account several granules (typically 10 to 20) to extract a statistical behaviour. The depth of the simulation is adjusted so that at the base of the convective domain, the movements are homogeneous and adiabatic.

Two different geometries (Fig. 1.3) can be used with 3D simulations:

- The *box-in-a-star* configuration, where only a small portion of the upper layers is simulated. The computational time ranging from few days to few weeks depending on the stellar type) cover only a small section of the surface layers of the deep convection zone (typically ten pressure scale heights vertically), and the numerical box includes about $\sim$ 10 convective cells, which are large enough so that the cells are not constrained by the horizontal (cyclic) boundaries, while the bottom and upper boundaries are open. A constant gravitation is considered.

- The *star-in-a-box* configuration, where the entire convective envelope is taken into account. In fact, when the stellar surface gravity is lower than $\log g \sim 1$, the box-in-a-star simulations become inadequate because of the influence of sphericity becomes important. The computational domain is a cubic grid equidistant in all directions, and the same open boundary condition is employed for all sides of the computational box. A fixed external spherically symmetric gravitational field is used. The simulations computed with this setup are highly computer-time demanding and difficult to run, which is the reason why there are only few (less than $\approx$30) simulations available so far.

The *box-in-a-star* setup can be used as long as the granule size is small compared to the size of the star and the sphericity effects are negligible. It is mandatory to use a *star-in-a-box* approach for very low surface gravity stars, in particular RSG and AGB stars, where the granule size becomes extremely large. For all other stars in the main sequence up to RGB phase, it is fair to use the *box-in-a-star* configuration.

No fudge parameters in 3D RHD simulations

Unlike conventional 1D atmospheric models, which require the introduction of arbitrary quantities (e.g., micro and macro-turbulence) to straw their lack of physical realism, RHD simulations are ab-initio and without free parameters. The crucial

point of the RHD codes for stellar atmospheres lies in the coupling between hydrodynamic equations and radiative transfer with realistic opacities and adapted equations of state. A detailed and precise solution of the radiative transfer is essential for a realistic treatment of convection because it is the radiative losses in the surface layers of the star that drain the convective movements and thus influence the whole simulation domain.

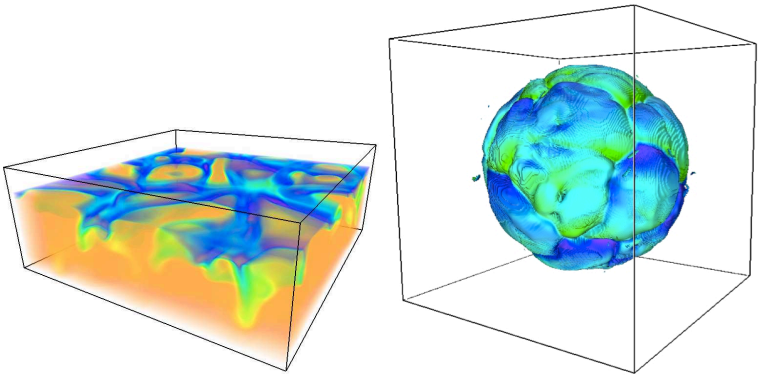

Figure 1.3: Setup of box-in-a-star (*left*) and star-in-a-box (*right*) configurations for 3D RHD simulations.

The RHD codes I use are:

- The CO^{5}BOLD code (Freytag et al. 2012) for the RHD simulations in the *star-in-a-box* configuration (i.e., global simulations).
- The STAGGER code (Nordlund et Galsgaard 1995[1], Nordlund et al. 2009; Collet et al. 2011) for the RHD simulations in the *box-in-a-star* configuration (i.e., local simulations).

CO^{5}BOLD code

The CO^{5}BOLD code solves the coupled non-linear equations of compressible hydrodynamics (with an approximate Roe solver,) and non-local radiative energy transfer (for global simulations with a short-characteristics scheme) in the presence of a fixed external gravitational field and in a 3D cartesian grid. The equation of state uses pre-tabulated values as functions of density and internal energy $(\rho, e_i \rightarrow P, \Gamma_1, T, s)$. It accounts for HI, HII, H_2, HeI, HeII, HeIII and a representative metal for any prescribed chemical composition. The equation of state does not account for the ionization states of metals, but it uses only one neutral element to achieve the appropriate

[1] http://www.astro.ku.dk/~kg/Papers/MHD_code.ps.gz

atomic weight (in the neutral case) for a given composition. The radiation transport step for global simulations uses a short-characteristics method and the frequency dependance of the radiation field is generally the gray approximation, which completely ignores the frequency dependence, for computational time reasons. However, for few global simulations the radiative transfer is calculated for up to five wavelengths groups according to the run of the monochromatic optical depth in a corresponding MARCS (Gustafsson et al. 2008) 1D model.

The code can be used for both local and global setups. Motions in the core are damped by a drag force to suppress dipolar oscillations. The hydrodynamics and the radiation transport scheme ignore the core completely and integrate right through it. The code is parallelized with hybrid Open Multi-Processing (OpenMP) and MPI directives.
For more details, see Chiavassa et al. (2011b) for the computation of RSG simulations and Freytag et al. (2017) for the AGB ones.

Stagger code

In the Stagger-code, the equations for the conservation of mass, momentum, and energy for compressible flows together with the induction equation are discretised using a high- order finite-difference scheme (sixth-order numerical derivatives, fifth-order interpolations) and solved on a rectangular Eulerian mesh, extending over a representative 3D, rectangular, volume located across the optical surface and including the photospheric layers as well as the upper part of the stellar convection zone. The simulation domains are chosen large enough to cover at least ten pressure scale heights vertically and to allow for about ten granules to develop at the surface. At the bottom of the simulation, the inflows have a constant entropy, and the whole bottom boundary is set to be a pressure node for p-mode oscillations. The code employs realistic input physics: the equation of state is an updated version of the one described by Mihalas et al. (1988), and the radiative transfer is calculated for a large number over wavelength points merged into 12 opacity bins (Nordlund 1982; Skartlien 2000; Magic et al. 2013b). They include continuous absorption opacities and scattering coefficients from Hayek et al. (2010) as well as line opacities described in Gustafsson et al. (2008), which in turn are based on the VALD-2 database (Stempels et al. 2001) of atomic lines. The code can be used for local setup only and is parallelized with MPI directives.

The paper, "Radiative hydrodynamics simulations of red supergiant stars. IV gray versus non-gray opacities" by Chiavassa et al. 2011, is attached at the end of the chapter..

1.4 Post-processing multidimensional radiation transport

During my Ph.D and afterwards, I developed a pure LTE radiative transfer code, Optim3D to generate synthetic spectra and intensity maps from snapshots of the 3D RHD simulations, taking account the Doppler shifts caused by the convective motions (Chiavassa et al. 2009). The radiation transfer is calculated in detail using pre-tabulated extinction coefficients based on MARCS opacities for molecules (Gustafsson et al. 2008) and VALD database (Piskunov et al. 1995) for atomic lines. These opacities are generated using TURBOSPECTRUM code (Alvarez & Plez 1998; Plez 2012). These tables are functions of temperature, density and wavelength, and are computed with the preferred solar (or not-solar) composition. For RHD simulations, no micro- and macro-turbulence is considered. The temperature and density distribution is optimised to cover the values encountered in the outer layers of the simulations. Eventually, the wavelength resolution is generally at least 3 times larger than the expected output and, at least, $R = \lambda/\Delta\lambda \geq 500\,000$.

In practice, what Optim3D *does*

In practice, 3D simulations provide a thermodynamic structure of the outer layers of the atmosphere (i.e., temperature, density and velocity field, as a function of optical depth). This structure is read by Optim3D. The latter then calculates the monochromatic intensity emerging with respect to the observer along a line-of-sight perpendicular to a face of the cube, and/or along several inclined rays. Optim3D interpolates the opacity tables in temperature and logarithmic density for all the simulation grid points using a bi-linear interpolation. The interpolation coefficients are computed only once, and stored. Bi-linear interpolation has been preferred to spline interpolation because: (i) spline is significantly more time consuming, (ii) and comparisons with other codes do not show noticeable improvements using splines. Then, the logarithmic extinction coefficient is linearly interpolated at each Doppler-shifted wavelength in each cell along the ray, and the optical depth scale along the ray is calculated. The numerical integration of the equation of radiative transfer gives the intensity emerging towards the observer at that wavelength and position. This calculation is performed for every line-of-sight perpendicular to the face of the computational box, and for all the required wavelengths.

Optim3D was initially conceived to be used with CO^{5}BOLD *star-in-a-box* simulations (Chiavassa et al. 2009). In Chiavassa et al. (2010a), I extended the code to *box-in-a-star* configuration computed with Stagger-code. I implemented a procedure to tilt the computational box (Fig. 1.3) by an angle θ with respect to the line of sight (vertical axis) and rotating it azimuthally by an angle ϕ. The final result is a spatially resolved intensity spectrum at different angles. More recently, Kateryna Kravchenko

implemented the computation of the contribution function to the line depression in OPTIM3D aiming at correctly identifying the depth of formation of spectral lines in order to construct numerical masks probing spectral lines forming at different optical depths (Kravchenko et al. 2018). OPTIM3D is optimised to be fast (slighter slower than a 1D calculation) also with high resolution simulations, and it can be easily parallelised on a cluster of computers.

The synergy between 3D RHD simulations and the detailed calculation of the radiative transfer with OPTIM3D makes it possible to approach a broad spectrum of astrophysical problems which are summarised in Fig. 1.4.

The paper, "Radiative hydrodynamics simulations of red supergiant stars: I. interpretation of interferometric observations" by Chiavassa et al. 2009, is attached at the end of the chapter..

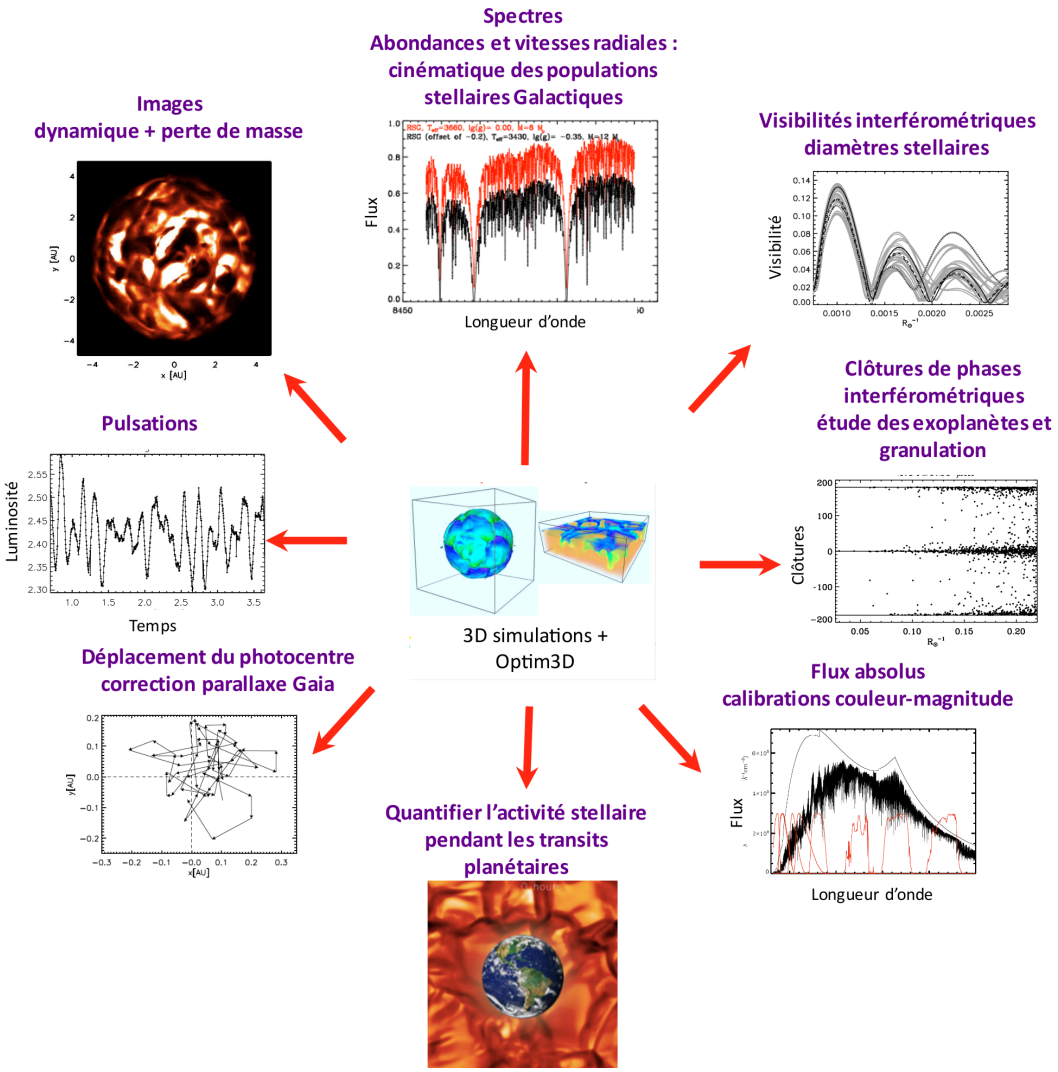

Figure 1.4: Scientific problems tackled thanks to the synergy between the 3D RHD simulations and the detailed calculations of the post-processing code Optim3D

A&A 535, A22 (2011)
DOI: 10.1051/0004-6361/201117463

Astronomy & Astrophysics

Radiative hydrodynamics simulations of red supergiant stars

IV. Gray versus non-gray opacities

A. Chiavassa[1], B. Freytag[2,3,4], T. Masseron[1], and B. Plez[5]

[1] Institut d'Astronomie et d'Astrophysique, Université Libre de Bruxelles, CP. 226, Boulevard du Triomphe, 1050 Bruxelles, Belgium
e-mail: achiavas@ulb.ac.be
[2] Centre de Recherche Astrophysique de Lyon, UMR 5574: CNRS, Université de Lyon, École Normale Supérieure de Lyon, 46 allée d'Italie, 69364 Lyon Cedex 07, France
[3] Department of Physics and Astronomy, Division of Astronomy and Space Physics, Uppsala University, Box 515, 751 20 Uppsala, Sweden
[4] Istituto Nazionale di Astrofisica, Osservatorio Astronomico di Capodimonte, via Moiariello 16, 80131 Naples, Italy
[5] LUPM, Laboratoire Univers et Particules, Université de Montpellier II, CNRS, Place Eugéne Bataillon 34095 Montpellier Cedex 05, France

Received 10 June 2011 / Accepted 15 September 2011

ABSTRACT

Context. Red supergiants are massive evolved stars that contribute extensively to the chemical enrichment of our Galaxy. It has been shown that convection in those stars produces large granules that cause surface inhomogeneities and shock waves in the photosphere. The understanding of their dynamics is crucial for unveiling the unknown mass-loss mechanism, their chemical composition, and their stellar parameters.

Aims. We present a new generation of red supergiant simulations with a more sophisticated opacity treatment performed with 3D radiative-hydrodynamics code CO5BOLD.

Methods. In the code the coupled equations of compressible hydrodynamics and non-local radiation transport are solved in the presence of a spherical potential. The stellar core is replaced by a special spherical inner boundary condition, where the gravitational potential is smoothed and the energy production by fusion is mimicked by a simply producing heat corresponding to the stellar luminosity. All outer boundaries are transmitting for matter and light. The post-processing radiative transfer code OPTIM3D is used to extract spectroscopic and interferometric observables.

Results. We show that if one relaxes the assumption of frequency-independent opacities, this leads to a steeper mean thermal gradient in the optical thin region that strongly affects the atomic strengths and the spectral energy distribution. Moreover, the weaker temperature fluctuations reduce the incertitude on the radius determination with interferometry. We show that 1D models of red supergiants must include a turbulent velocity that is calibrated on 3D simulations to obtain the effective surface gravity that mimics the effect of turbulent pressure on the stellar atmosphere. We provide an empirical calibration of the ad hoc micro- and macroturbulence parameters for 1D models using the 3D simulations: we find that there is no clear distinction between the different macroturbulent profiles needed in 1D models to fit 3D synthetic lines.

Key words. stars: atmospheres – supergiants – hydrodynamics – radiative transfer – methods: numerical

1. Introduction

The dynamical nature of the solar-surface layers, manifested for instance in granules and sunspots, has been known for a long time. With every improvement of ground-based or spaceborne instruments the complexity of the observed processes increased. Red supergiant (RSG) stars are among the largest stars in the universe and the brightest in the optical and near-infrared. They are massive stars with masses between roughly 10 and 25 $M_{\odot}$ with effective temperatures ranging from 3450 to 4100 K, luminosities of 20 000 to 300 000 $L_{\odot}$, and radii up to 1500 $R_{\odot}$ (Levesque et al. 2005). These stars exhibit variations in integrated brightness, surface features, and the depths, shapes, and Doppler shifts of spectral lines; as a consequence, stellar parameters and abundances are difficult to determine. Progress has been made using 1D hydrostatic models revising the $T_{\rm eff}$-scale and reddening both at solar and Magellanic Clouds metallicities (Levesque et al. 2005, 2006; Massey et al. 2007; Levesque et al. 2007; Levesque 2010) but problems still remain, e.g. the blue-UV excess that may be caused by scattering by circumstellar dust or an insufficiency in the models, and the visual-infrared effective temperature mismatch (Levesque et al. 2006). Finally, RSGs eject massive amounts of mass back to the interstellar medium with an unidentified process that may be related to acoustic waves and radiation pressure on molecules (Josselin & Plez 2007), or to the dissipation of Alfvén waves from magnetic field, recently discovered on RSGs (Aurière et al. 2010; Grunhut et al. 2010), as early suggested by Hartmann & Avrett (1984); Pijpers & Hearn (1989); Cuntz (1997).

The dynamical convective pattern of RSGs is then crucial for the understanding of the physics of these stars that contribute extensively to the chemical enrichment of the Galaxy. There is a number of multiwavelength imaging examples of RSGs (e.g. α Ori) because of their high luminosity and large angular diameter. Several research teams (Buscher et al. 1990; Wilson et al. 1992; Tuthill et al. 1997; Wilson et al. 1997; Young et al. 2000) detected time-variable inhomogeneities on the surface of α Ori with WHT and COAST; Haubois et al. (2009)

reported a reconstructed image in the H-band with two large spots; Ohnaka et al. (2009, 2011) detected possible convective motions in CO line formation layers, but it is not obvious whether this strong convective motion can be present in these layers (detected up to 1.3–1.4 stellar radii), where the convective energy flux is low; Kervella et al. (2009) resolved α Ori using diffraction-limited adaptive optics in the near-infrared and found an asymmetric envelope around the star with a bright plume extending in the southwestern region. Tuthill et al. (1997) reported bright spots on the surface of the supergiants α Her and α SCO using WHT, and Chiavassa et al. (2010c) on VX Sgr using VLTI/AMBER.

The effects of convection and non-radial waves can be represented by numerical multi-dimensional time-dependent radiation hydrodynamics (RHD) simulations with realistic input physics. Three-dimensional radiative hydrodynamics simulations are no longer restricted to the Sun (for a review on the Sun models see Nordlund et al. 2009) but cover a substantial portion of the Hertzsprung-Russell diagram (Ludwig et al. 2009). Moreover, they have been already extensively employed to study the effects of photospheric inhomogeneities and velocity fields on the formation of spectral lines and on interferometric observables in a number of cases, including the Sun, dwarfs and subgiants (e.g. Asplund et al. 1999; Asplund & García Pérez 2001; Asplund et al. 2009; Caffau et al. 2010; Behara et al. 2010; Sbordone et al. 2010), red giants (e.g. Chiavassa et al. 2010a; Collet et al. 2007, 2009; Wende et al. 2009), asymptotic giant branch stars (Chiavassa et al. 2010c), and RSG stars (Chiavassa et al. 2009, 2010b, 2011). In particular, the presence and the characterization of the size of convective cells on α Ori has been shown by Chiavassa et al. (2010b) by comparing an extensive set of interferometric observations ranging from the optical to the infrared wavelengths.

This paper is the fourth in a series aimed to present the numerical simulations of RSG stars with CO^{5}BOLD and to introduce the new generation of RSG simulations with a more sophisticated opacity treatment. These simulations are very important for an accurate quantitative analysis of observed data.

2. 3D numerical simulations with CO^{5}BOLD

2.1. Basic equations

The code solves the coupled equations of compressible hydrodynamics and non-local radiation transport

$$\frac{\partial \rho}{\partial t} + \nabla \cdot (\rho \boldsymbol{v}) = 0 \tag{1}$$

$$\frac{\partial \rho \boldsymbol{v}}{\partial t} + \rho \left(\boldsymbol{v} \cdot \nabla\right) \boldsymbol{v} + \nabla P = -\rho \boldsymbol{\nabla} \Phi \tag{2}$$

$$\frac{\partial \rho e_{\rm ikg}}{\partial t} + \nabla \cdot \left(\left[\rho e_{\rm ikg} + P \right] \boldsymbol{v} + F_{\rm rad} \right) = 0. \tag{3}$$

They describe the inviscid flow of density ρ, momentum $\rho \boldsymbol{v}$, and total energy $e_{\rm ikg}$ (including internal, kinetic, and gravitational potential energy). Further quantities are the velocity vector $\boldsymbol{v}$, pressure P, and radiative energy flux $F_{\rm rad}$. The latter is computed from the frequency-integrated intensity I for the gray treatment of opacity and for each wavelength group in the non-gray approach (Sect. 2.3).

The gravitational potential is spherical,

$$\Phi = -GM_{\rm pot} \left(r_0^4 + r^4 / \sqrt{1 + (r/r_1)} \right)^{-1/4}, \tag{4}$$

where $M_{\rm pot}$ is the mass of the star to be modeled (see Fig. 3, bottom right panel); r_0 and r_1 are free smoothing parameters: when $r_0^4 \ll r^4 \ll r_1^4$, $\Phi = -\frac{GM_{\rm pot}}{r}$; while when $r \to 0$, $\Phi \to \Phi = -\frac{GM_{\rm pot}}{r_0}$; and for $r \to \infty$, $\Phi \to \Phi = -\frac{GM_{\rm pot}}{r_1}$. Typically, $r_0 \approx 0.2\ R_\star$ and $r_1 \approx 1.2\ R_\star$ for RSG simulations (Freytag et al. 2002).

2.2. The code

The numerical simulations described here are performed with CO^{5}BOLD (COnservative COde for the COmputation of COmpressible COnvection in a BOx of L Dimensions, $L = 2, 3$). It uses operator splitting (Strang 1968) to separate the various (explicit) operators: the hydrodynamics, the optional tensor viscosity, and the radiation transport.

The hydrodynamics module is based on a finite-volume approach and relies on directional splitting to reduce the 2D or 3D problem to one dimension. In the 1D steps an approximate Riemann solver of Roe-type (Roe 1986) is applied, modified to account for a realistic equation of state, a non-equidistant Cartesian grid, and the presence of source terms due to an external gravity field. In addition to the stabilizing mechanism inherent in an upwind-scheme with a monotonic reconstruction method (typically a piecewise-linear van Leer interpolation), a 2D or 3D tensor viscosity can be activated. This step eliminates certain errors of Godunov-type methods dealing with strong velocity fields aligned with the grid (Quirk 1994).

The equation of state uses pre-tabulated values as functions of density and internal energy ($\rho, e_i \to P, \Gamma_1, T, s$). It accounts for H , H , H_2, He , He , He and a representative metal for any prescribed chemical composition. The equation of state does not account for the ionization states of metals, but it uses only one neutral element to achieve the appropriate atomic weight (in the neutral case) for a given composition. Two different geometries can be used with CO^{5}BOLD, which are characterized by different gravitational potentials, boundary conditions, and modules for the radiation transport:

- The - - - setup is used to model a statistically representative volume of the stellar atmosphere with a constant gravitation, where the lateral boundaries are periodic, and the radiation transport module relies on a Feautrier scheme applied to a system of long rays (Freytag et al. 2002; Wedemeyer et al. 2004, and for analysis, e.g., Caffau et al. 2010).
- The - - - setup is used to model RSG stars of this work. The computational domain is a cubic grid equidistant in all directions, and the same open boundary condition is employed for all sides of the computational box.

Because the outer boundaries are usually either hit at some angle by an outgoing shockwave, or let material fall back (mostly with supersonic velocities), there is not much point in tuning the formulation for an optimum transmission of small-amplitude waves. Instead, a simple and stable prescription, that lets the shocks pass is sufficient. It is implemented by filling typically two layers of ghost cells where the velocity components and the internal energy are kept constant. The density is assumed to decrease exponentially in the ghost layers, with a scale height set to a controllable fraction of the local hydrostatic pressure scale height. The control parameter allows us to account for the fact that the turbulent pressure plays a significant role for the average pressure stratification. The acceleration through gravity is derived from Eq. (4). Within a radius r_0 the potential is smoothed (Eq. (4)). In this sphere a source term to the internal

Table 1. Simulations of red supergiant stars used in this work.

model	Simulated relaxed time [years]	grid [grid points]	grid [$R_\odot$]	$M_{\rm pot}$ [$M_\odot$]	$M_{\rm env}$ [$M_\odot$]	L [$L_\odot$]	$T_{\rm eff}$ [K]	$R_\star$ [$R_\odot$]	$\log g$ [cgs]	comment
st35gm03n07[a]	5.0	235^3	8.6	12	3.0	91 932 ± 1400	3487 ± 12	830.0 ± 2.0	−0.335 ± 0.002	gray
st35gm03n13	7.0	235^3	8.6	12	3.0	89 477 ± 857	3430 ± 8	846.0 ± 1.1	−0.354 ± 0.001	non-gray
st36gm00n04	6.4	255^3	3.9	6	0.4	24 211 ± 369	3663 ± 14	386.2 ± 0.4	0.023 ± 0.001	gray
st36gm00n05	3.0	401^3	2.5	6	0.4	24 233 ± 535	3710 ± 20	376.7 ± 0.5	0.047 ± 0.001	gray, highest resolution

Notes. [(a)] Used and thoroughly analyzed in Chiavassa et al. (2009, 2010b). Note that a sequence of 1.5 stellar years has been added with respect to this paper. All models have solar chemical composition. The table reports the simulated time used to average the stellar parameters; the numerical resolution in grid points and $R_\odot$; the mass used to compute the potential in Eq. (4); total mass actually included in the model (the rest is assumed to sit in the unresolved stellar core); the luminosity, effective temperature, radius and surface gravity averaged over both spherical shells and simulated time (second column), the errors are one standard deviation fluctuations with respect to the average over time; comment.

energy provides the stellar luminosity. Motions in the core are damped by a drag force to suppress dipolar oscillations. The hydrodynamics and the radiation transport scheme ignore the core completely and integrate right through it.

The code is parallelized with Open Multi-Processing (OpenMP) directives.

2.3. Radiation transport and opacities tables

The radiation transport step for RSGs' simulations uses a short-characteristics method. To account for the short radiative time scale several (typically 6 to 9) radiative sub−steps are performed per global step. Each sub-step uses only three rays (e.g. in the directions (1,1,0), (1,−1,0), (0,0,1) or (1,0,1), (1,0,−1), (0,1,0) or (0,1,1), (0,1,−1), (1,0,0) or four rays (along the space diagonals (±1,±1,±1)). The different orientation sets are used cyclically. The radiation transport is solved for a given direction for both orientations. More irregular directions (and more rays) are possible but are avoided in the models presented here to save computational time. The radiation transport operator is constructed to be stable in the presence of strong jumps in opacity and temperature (even on a coarse grid).

The frequency dependance of the radiation field in the CO5BOLD models can be calculated with two approaches:

- the gray approximation, which completely ignores the frequency dependence, is justified only in the stellar interior and it is inaccurate in the optically thin layers. The Rosseland mean opacities are calculated as a function of pressure and temperature ($T, P \rightarrow \kappa_{\rm Ross}$) and are available in a 2D table. The necessary values are found by interpolation in a 2D table. It has been merged at around 12 000 K from high-temperature OPAL (Iglesias et al. 1992) data and low-temperature PHOENIX (Hauschildt et al. 1997) data by Hans-Günter Ludwig. The models that use these opacities are reported in Table 1.
- the more elaborate scheme accounting for non-gray effects, which is based on the idea of *opacity binning* (Nordlund 1982; Nordlund & Dravins 1990). The basic approximation is the so called multi-group scheme (Ludwig et al. 1994; Vögler et al. 2004). In this scheme, the frequencies that reach monochromatic optical depth unity within a certain depth range of the model atmosphere will be put into one frequency group. The opacity table used in this work is sorted to five wavelengths groups according to the run of the monochromatic optical depth in a corresponding MARCS (Gustafsson et al. 2008) 1D model. The corresponding logarithmic Rosseland optical depths are $+\infty, 0.0, -1.5, -3.0, -4.5, -\infty$. In each group there is a smooth transition from a Rosseland average in the optically thick regime to a Planck average in the optically thin regime, except for the group representing the highest opacities, where the Rosseland average is used throughout. The implementation of non-gray opacities tables has been carried out by Hans-Günter Ludwig and we computed one non-gray model (Table 1).

3. Modeling RSG stars

The most important parameters that determine the type of the modeled star are

- the input luminosity into the core;
- the stellar mass that enters in Eq. (4) for the gravitational potential;
- the abundances that are used to create the tables for the equation-of-state and the opacities.

In addition, there are a number of parameters that influence the outcome of a simulation to some extent, i.e. the detailed formulation of the boundary conditions, the smoothing parameters of the potential, the numerical resolution, detailed settings of the hydrodynamics scheme and the additional tensor viscosity, choice of ray directions for the radiation transport, and the time-step control. The model presented in Freytag et al. (2002) relies on the same assumptions as the current ones. In the meantime, modifications of the code (e.g. restrictions to rays only along axes and diagonals avoiding some interpolations in the radiation transport module) and faster computers allow models with higher resolution, frequency-dependent opacity tables, and various stellar parameters. These new models show a significant increase in the number of small convective cells on the stellar surface.

The initial model is produced starting from a sphere in hydrostatic equilibrium with a weak velocity field inherited from a previous model with different stellar parameters (top left panel of Fig. 1). The temperature in the photosphere follows a gray $T(\tau)$ relation. In the optically thick layers it is chosen to be adiabatic. The first frame of Fig. 1, taken just after one snapshot, displays the limb-darkened surface without any convective signature but with some regular patterns due to the coarse numerical grid and the correspondingly poor sampling of the sharp temperature jump at the bottom of the photosphere. The central spot,

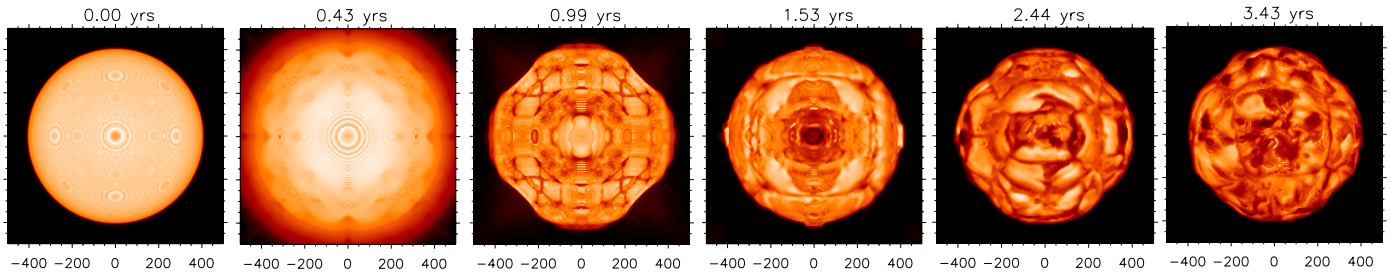

Fig. 1. Gray intensity on one side of the computational cube from the initial sequence of the model st35gm00n05 in Table 1. The axes are in solar radii. The artifacts caused by the mismatch between the spherical object and the Cartesian grid become less evident with time passing.

quite evident at the beginning of the simulation, vanishes completely when convection becomes strong. A regular pattern of small-scale convection cells develops initially and then, as the cells merge, the average structure becomes big and the regularity is lost. The intensity contrast grows. After several years, the state is relaxed and the pattern becomes completely irregular. All memory from the initial symmetry is lost. The influence of the cubical box and the Cartesian grid is strongest in the initial phase onset of convection. At later stages, there is no alignment of structures with the grid nor a tendency of the shape of the star to become cubical.

4. Model structure

Table 1 reports the simulations analyzed in this work. These models are the result of intensive calculations on parallel computers: the oldest simulation, st35gm03n07, used so far in the other papers of this series, took at least a year (this time may be difficult to estimate because of the queuing system and different machines used) on machines with 8–16 CPUs to provide nine years of simulated stellar time; more recently, we managed to compute the other simulations of Table 1 on a shorter time scale on a machine with 32 CPUs. The model st36gm00n04, which is slightly higher in numerical resolution, needed about two months to compute more than 20 stellar years, while st36gm00n05 (the highest numerical resolution so far) about six months for about three stellar years. Eventually, st35gm03n13 needed about eight months to compute ten years of stellar time despite its lower numerical resolution. The CPU time needed for non-gray runs does scale almost linearly with the number of wavelength groups.

4.1. Global quantities

Three-dimensional simulations start with an initial model that has an estimated radius, a certain envelope mass, a certain potential profile, and a prescribed luminosity as described above. During the run, the internal structure relaxes to something not to far away from the initial guess. We needed several trials to get the correct initial model for the latest set. The average final stellar parameters are determined once the simulation has ended (Fig. 2). For this purpose, we adopted the method reported in (Chiavassa et al. 2009, hereafter Paper I). The quantities are averages over spherical shells and over time, and the errors are one-sigma fluctuations with respect to the average over time. We computed the average temperature and luminosity over spherical shells, $T(r)$, and $L(r)$. Then, we searched for the radius R for which

$$L(R)/(4\pi R^2) = \sigma T^4, \quad (5)$$

where σ is the Stefan-Boltzmann constant. Eventually, the effective temperature is $T_{\rm eff} = T(R)$. As already pointed out in Paper I, the gray model st35gm03n07 (top row of Fig. 2) shows a drift in the first two years (−0.5% per year) before stabilisation in the last 2.5 years. This drift is also visible in the radius of the non-gray model st35gm03n13 (second row) even though it is weaker (less than 0.3%). The luminosity fluctuations are on the order of 1% and the temperature variations <0.3% for both simulations. It must be noted that the last snapshot of the gray simulation was used as the initial snapshot for the non-gray model. The two hotter models, st36gm00n04 and st36gm00n05, are also somehow related because they both use a gray treatment of opacities and st36gm00n05 has been started using the last snapshot of st36gm00n04. The temperature (0.5%) and luminosity (2.2%) fluctuations of the higher resolution model are slightly higher than the temperature (0.4%) and luminosity (1.5%) fluctuations of st36gm00n04. None of the simulations shows a drift of the radius in the last years of evolution.

The bottom row in Fig. 2 shows the ratio between the turbulent pressure and the gas pressure (defined as in Sect. 4.2). This quantity shows that in the outer layers, just above the stellar radius, the turbulent pressure plays a significant role for the average pressure stratification and the radial velocities resulting from the vigorous convection are supersonic.

Figure 3 displays some quantities spatially averaged over spherical shells for a snapshot of the gray simulation st35gm03n07 in Table 1. Figure 4 shows three-dimensional views of some quantities for the same snapshot and simulation. Radiation is of primary importance for many aspects of convection and the envelope structure in a RSG. It does not only cool the surface to provide a somewhat unsharp outer boundary for the convective heat transport. It also contributes significantly to the energy transport in the interior (top left panel of Fig. 3), where convection never carries close to 100% of the luminosity. In the optically thick part the stratification is slightly far from radiative equilibrium and the entropy jump from the photosphere to the layers below is fairly large (entropy s in Figs. 3 and 4). The He /He ionization zone is visible in the entropy structure as a small minimum near the surface before the normal steep entropy decrease. The opacity peak at around $T = 13\,000$ K just below the photosphere causes a very steep temperature jump (temperature T and opacity κ in Fig. 4), which is very prominent on top of upflow regions (opacity κ in Fig. 3). This causes a density inversion (density ρ in Figs. 4 and 8), which is a sufficient condition of convective instability resolved, the entropy drop occurs in a very thin layer, while the smearing from the averaging procedure over nonstationary up- and downflows leads to the large apparent extent of the mean superadiabatic layer.

The local radiative relaxation time scale in the photosphere is much shorter than a typical hydrodynamical time scale (time

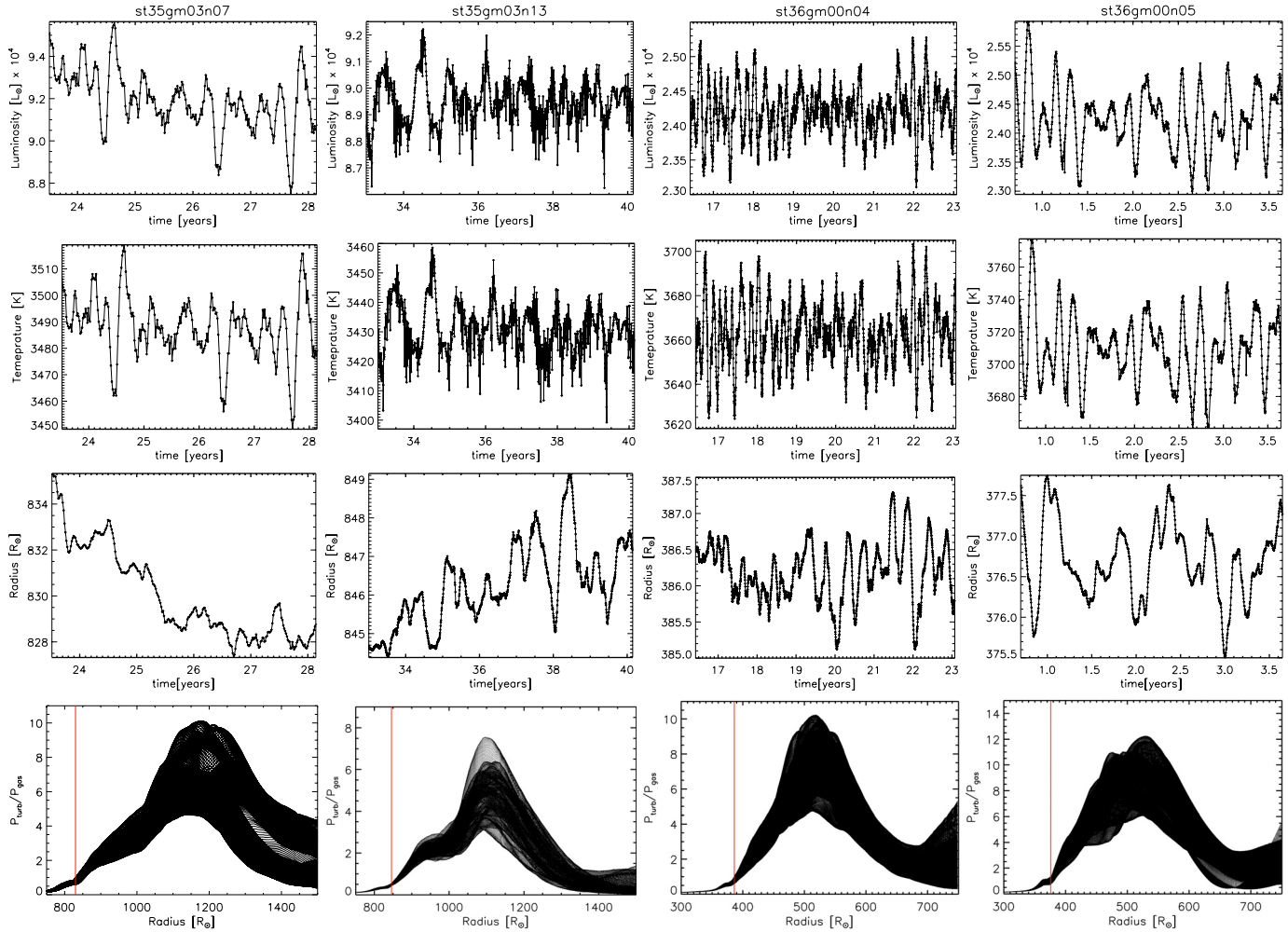

Fig. 2. Luminosity, temperature, and radius as a function of time for the simulations of Table 1: from *left to right columns* st35gm03n07, st35gm03n13, st36gm00n04, and st36gm00n05. The *bottom panels* are the ratio between turbulent pressure and gas pressure for different snapshots. The red vertical lines in *all the panels* is the approximative position of the radius from Table 1.

in Fig. 3). Numerically, the radiative energy exchange terms are quite stiff and prevent large deviations from a radiative equilibrium stratification. These terms enforce very short time steps (about 600 s per individual radiation transport step) and are responsible for the relatively high computational cost of this type of simulations. Local fluctuations in opacity, temperature (source function), and heat capacity pose high demands on the stability of the radiation transport module. This is true to a lesser degree for the hydrodynamics module due to shocks, high Mach numbers, and small scale heights. A side effect of the steep and significant temperature jump is the increase in pressure scale height from small photospheric values to values that are a considerable fraction of the radius in layers just below the photosphere (pressure scale heigh H_P in Fig. 3). The non-gray model has systematically shorter time scales (Fig. 3, bottom row), which causes the increased smoothing efficiency of temperature fluctuations.

4.2. Temperature and density structures

The temperature structure for the 3D simulations is displayed in Fig. 5 as a function of the optical depth at $\lambda = 5000$ Å for all simulations used in this work. We also computed classical 1D, LTE, plane-parallel, hydrostatic marcs model atmospheres (Gustafsson et al. 2008) with identical stellar parameters, input data, and chemical compositions as the 3D simulations (Table 2). It should be noted that the MARCS models do not have identical input data and numerical scheme as 3D simulations but they are a good benchmark for a quantitative comparison. The optical depth scale in Fig. 5 has been computed with the radiative transfer code O 3D (see Paper I, and Sect. 5.2)

Table 2. 1D MARCS models used in this work.

$T_{\rm eff}$ [K]	M [$M_\odot$]	log g [cgs]	Corresponding 3D simulation	Surface gravity
3490	12	−0.35	st35gm03n07	g
3490	12	−0.58	st35gm03n07	$g_{\rm eff}$
3430	12	−0.35	st35gm03n13	g
3700	12	−0.35	st35gm03n13	g
3430	12	−0.65	st35gm03n13	$g_{\rm eff}$
3660	6	0.02	st36gm00n04	g
3660	6	−0.22	st36gm00n04	$g_{\rm eff}$
3710	6	0.05	st36gm00n05	g
3710	6	−0.22	st36gm00n05	$g_{\rm eff}$

Notes. All 1D models are spherical and were computed with solar metallicity. The effective surface gravity ($g_{\rm eff}$) is given at the positions of the radii from Fig. 7 and using Eq. (8). The last column displays weather the surface gravity used to compute 1D model is $g_{\rm eff}$ or g. For g we took the same values as in the 3D simulations of Table 1.

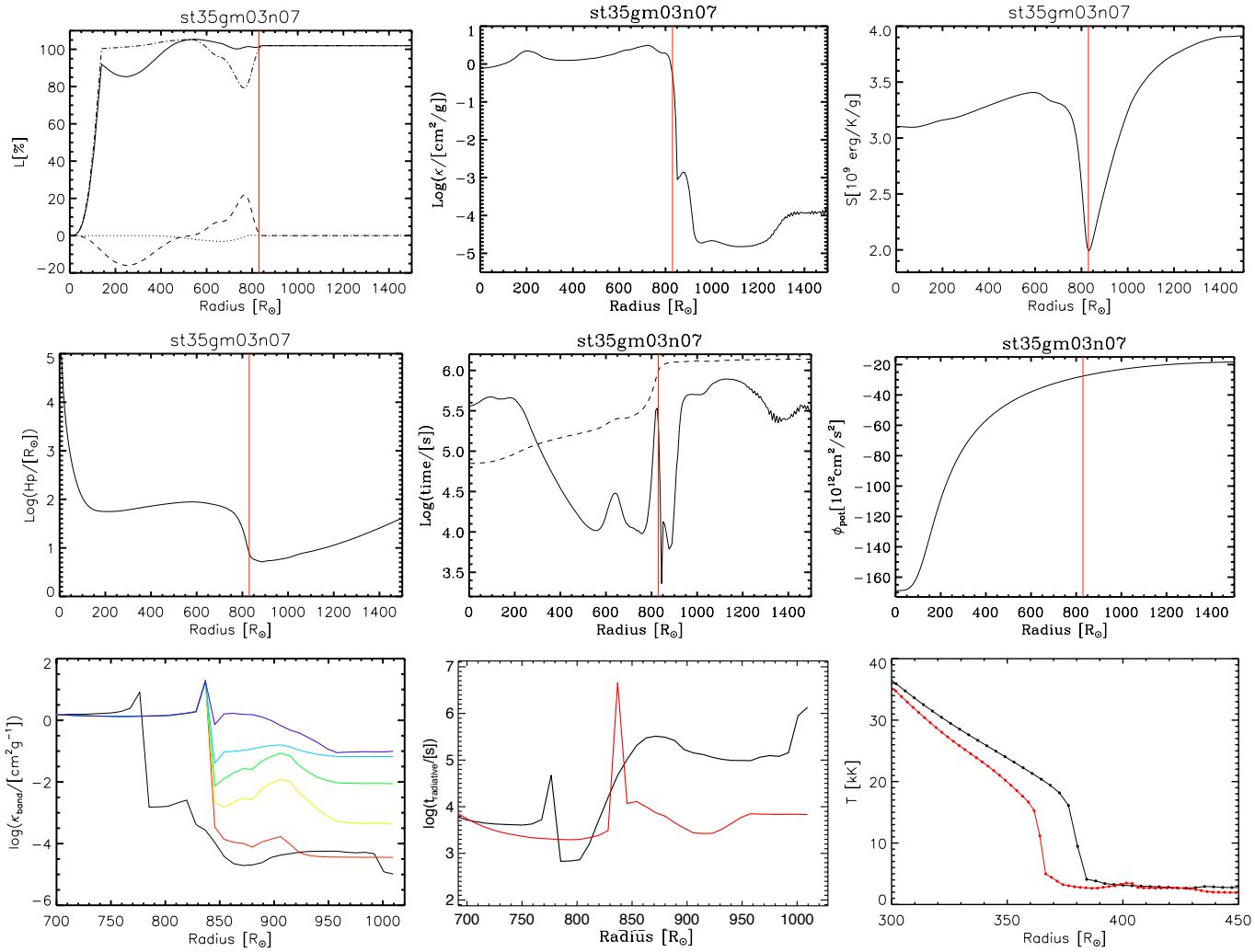

Fig. 3. Some spatially average quantities (i.e., spherical shells) for a snapshot of st35gm03n07 (Table 1). The red vertical line is the location of the radius. *Top row, left panel*: luminosities as function of radius in solar radii: continuous curve is the total luminosity; the dashed curve is the luminosity owing to pressure work; the dotted curve is the luminosity of kinetic energy; and the dash-dotted curve is the radiative luminosity. *Top row, center*: opacity. *Top row, right*: specific entropy. *Central row, left panel*: pressure scale height. *Central row, center*: characteristic radiative (continuous line) and hydrodynamical (dotted line) time scales. *Central row, right*: gravitational potential $\Phi_{\rm pot}$. *Bottom row, left panel*: random column opacity and radiative time scale for a given snapshot of the gray model st35gm03n07 (black) and non-gray model st35gm03n13 (red). The five colored curves correspond to the opacity groups. The radiative time scale is estimated for temperature fluctuations with spatial scales on the order of the grid size. *Bottom row, center*: characteristic radiative time scale for the gray (black) and non-gray (red) models. *Bottom row, right*: temperature profiles for the st36g00n04 (255^3 grid points, black) and st36g00n05 (401^3 grid points, red).

for all rays parallel to the grid axes with a $x-y$ positions $\leq(x_{\rm center}, y_{\rm center}) \pm (G * 0.25)$ (i.e., a small square at the center of the stellar disk), where $x_{\rm center}$ and $y_{\rm center}$ are the coordinate of the center of one face of the numerical box, G is the number of grid points from Table 1, and 0.25 was chosen to consider only the central rays of the box.

The models using a frequency-independent gray treatment show stronger temperature fluctuations compared to the non-gray case (top right panel in Fig. 5), as was already pointed out in Ludwig et al. (1994) for local hydrodynamical models, because the frequency-dependent radiative transfer causes an intensified heat exchange of a fluid element with its environment tending to reduce the temperature differences. Moreover, the temperature structure in the outer layers of the non-gray simulation tends to remain significantly cooler than the gray case (up to ∼200 hundreds K, Fig. 6), close to the radiative equilibrium. The thermal gradient is then steeper in the non-gray model and this is crucial for the formation of the spectral lines (see Sect. 5.2). This effect has already been pointed out in the literature and a more recent example is Vögler (2004), who pointed out that the non-gray treatment of opacities is mandatory to compare solar magneto-convective simulations with the M code to the observations.

It is also striking all gray simulations largely diverge from 1D MARCS models, while the case of the thermal structure of the non-gray model is more complicated. The outer layers agree very well with a cool 1D MARCS model at 3430 K (Fig. 5, top right panel). At $\lg \tau_{5000} \sim 1$ (i.e., where the continuum flux comes from) the mean 3D temperature is warmer than the 1D: a hot 1D MARCS model at 3700 K is then necessary to reach a better agreement but, however, this 1D profile diverges strongly for $\lg \tau_{5000} < 1$.

While turbulent pressure is naturally included in the RHD simulations, it is modeled in 1D models assuming a parameterisation as

$$P_{\rm turb} = \beta \rho v_{\rm t}^2, \quad (6)$$

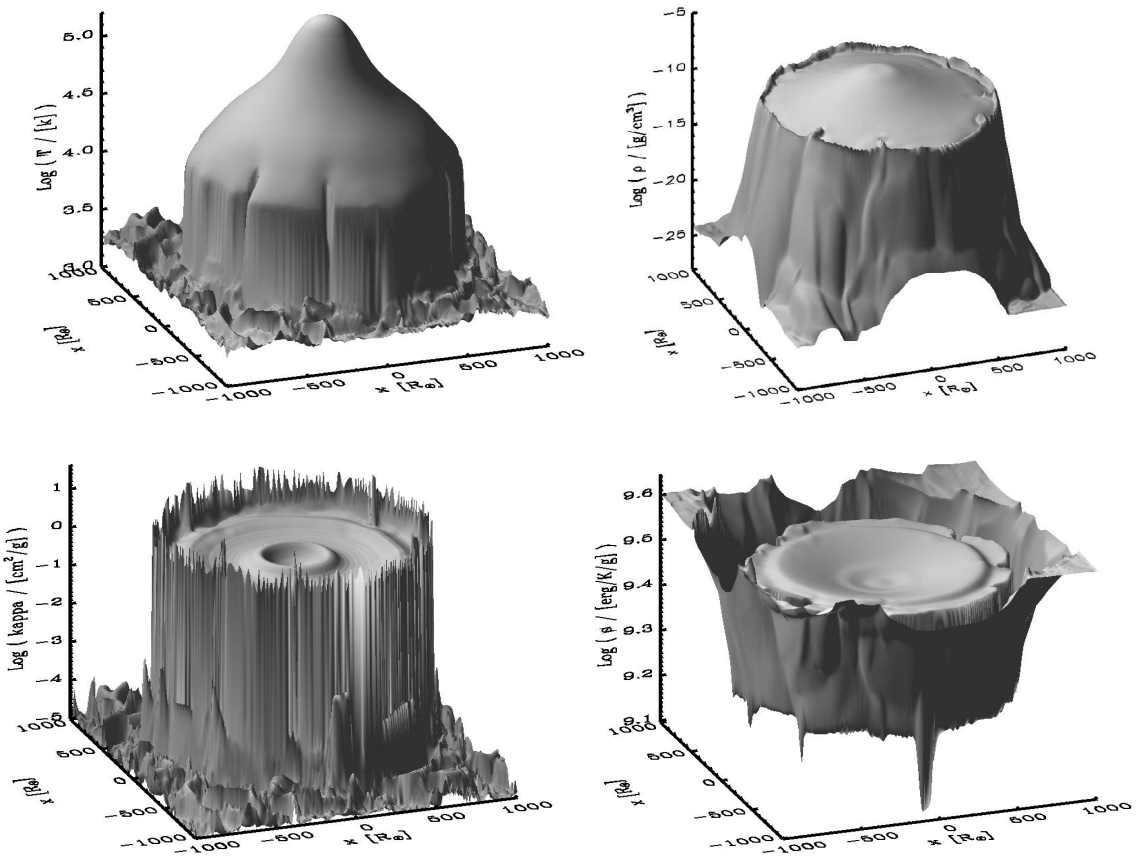

Fig. 4. Logarithm of temperature (*top left panel*), density (*top right*), opacity (*bottom left*) and entropy (*bottom right*) of a slice through the center from a snapshot of the RSG simulation st35gm03n07 in Table 1.

where ρ is the density, v_t the characteristic velocity, and β is approximately 1 and depends on whether the motions occur more or less isotropically. This pressure is measuring the force produced by the kinetic movements of the gas, whether caused by convective or other turbulent gas motions. In 1D models, assuming spherical symmetry, the equation of hydrostatic equilibrium is solved for

$$\nabla P_{\rm tot} = \nabla P_{\rm g} + \nabla P_{\rm turb} + \nabla P_{\rm rad} = -\rho g, \tag{7}$$

where $g(r) = \frac{GM}{r^2}$ (being r the radius, M the mass of the star and G the Newton's constant of gravity), $P_{\rm g} = \Re\rho T/\mu_{\rm mol}$ the gas pressure ($\Re$ being the gas constant, $\mu_{\rm mol}$ the molecular weight, and T the temperature), and $P_{\rm rad}$ the radiative pressure. Gustafsson et al. (2008) and Gustafsson & Plez (1992) showed that assuming $P_{\rm rad} = 0$ like in 3D simulations, they could mimic the turbulent pressure on the models by using models with those effects neglected with an adjusted gravity:

$$g_{\rm eff} = g\left(\frac{1}{1+\beta\frac{\mu_{\rm mol}}{\Re T}v_t^2}\right), \tag{8}$$

Eventually, Gustafsson et al. (2008) chose to set $v_t = 0$ for all 1D models in their grid, advising those who would have liked a different choice to use models with a different mass or gravity, according to the recipe given in Eq. (8).

After averaging all necessary thermodynamical quantities in 3D simulations averaged over spherical shells, we computed $g_{\rm eff}$ using Eq. (8) with $\mu_{\rm mol} = 1.3$ (appropriate value for the atmosphere of RSGs). Figure 7 shows the behavior of $g/g_{\rm eff}$ for 3D simulations of Table 1. We used the effective surface gravity at the the radius position (red vertical lines in the figure) to compute new 1D models (see Table 2). Figure 8 shows the comparison of the 3D density structures with 1D models. The models with the new effective gravity agree better with the 3D mean profiles than the models with v_t set to zero (i.e., $g_{\rm eff} = g$). The effects on the temperature structures of 1D models with different surface gravity and equal effective temperature is negligible as displayed in all panels of Fig. 5.

We conclude that 1D simulation of RSG stars must have a turbulent velocity that is not equal to zero, which accordingly to Eq. (8) gives the correct value of surface gravity. The effect of the turbulent pressure is a lowering of the gravity that can be calibrated on 3D simulations in the same way as in to Fig. 7.

5. Non-gray versus gray simulations

We used the 3D pure-LTE radiative transfer code O 3D described in Paper I to compute spectra and intensity maps from the gray simulation st35gm03n07 and the non-gray simulation st35gm03n13 (Table 1). The code takes into account the Doppler shifts caused by convective motions. The radiative transfer equation is solved monochromatically using extinction coefficients pre-tabulated as a function of temperature, density, and wavelength. The lookup tables were computed for the solar chemical compositions (Asplund et al. 2006) using the same extensive atomic and molecular opacity data as the latest generation of MARCS models (Gustafsson et al. 2008). We assumed a zero micro-turbulence because the velocity fields inherent in 3D models are expected to self-consistently and adequately account for non-thermal Doppler broadening of spectral lines.

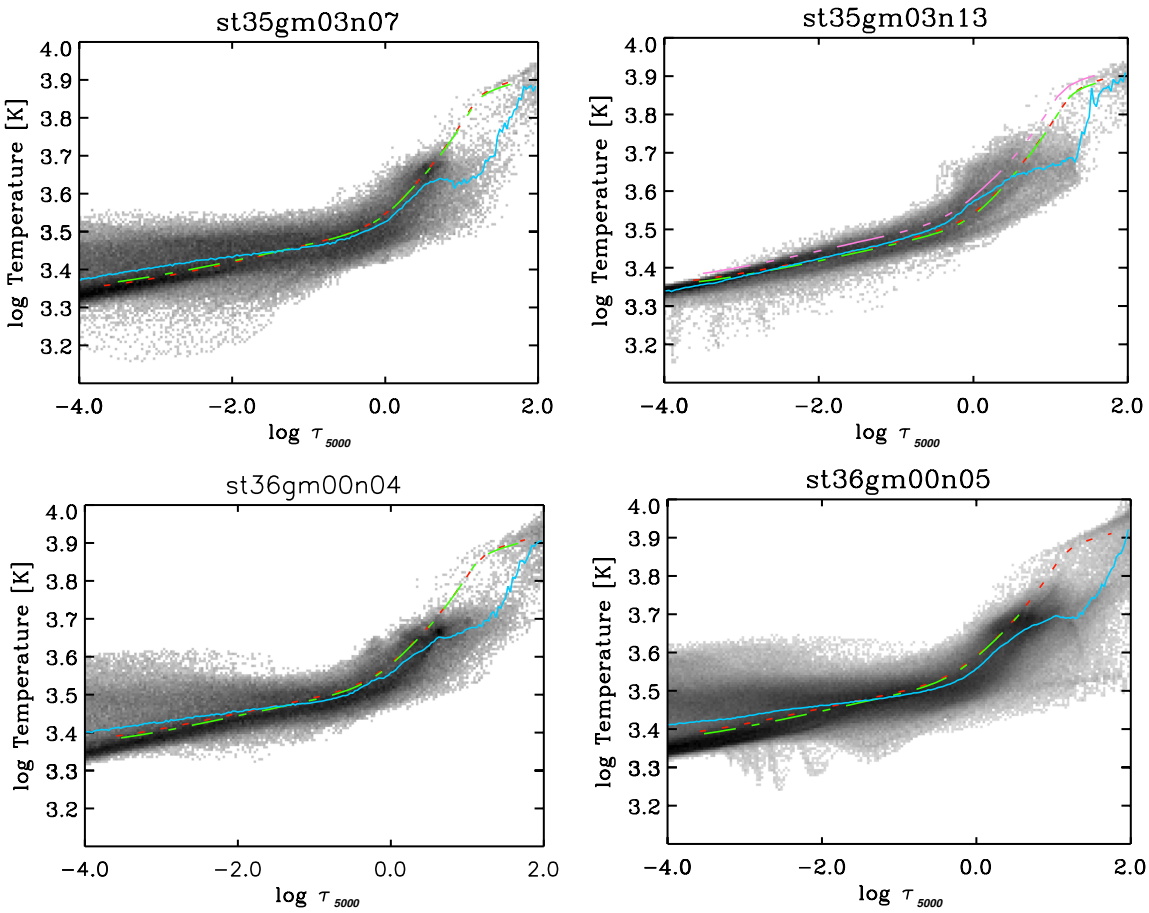

Fig. 5. Thermal structures of the simulations in Table 1 as a function of the optical depth at λ = 5000 Å. Darker areas indicate temperature values with higher probability. The solid light blue curve is the average temperature, the red dashed line is the 1D MARCS model profile with surface gravity g (Table 2) and the green dotted-dashed line is the 1D MARCS model with surface gravity $g_{\rm eff}$ (see text). In the top right panel the 3D mean thermal profile is compared to a cool MARCS model at 3430 K for the outer layers and a hot one with 3700 K (magenta dotted-triple dashed line) for the continuum-forming region (see text).

5.1. From one- to three- dimensional models: determination of micro- and macroturbulence

Radiation hydrodynamics simulations provide a self-consistent ab-initio description of the non-thermal velocity field generated by convection, shock waves and overshoot that are only approximated in 1D models by empirical calibrations. Thus, the comparison between 1D and 3D spectra requires the determination of ad hoc parameters like microturbulence ($\xi_{\rm mic}$) and macroturbulence ($\xi_{\rm mac}$) velocities that must be determined for the 1D spectra.

For this purpose, we used a similar method as Steffen et al. (2009). Standard 1D radiative transfer codes usually apply $\xi_{\rm mic}$ and $\xi_{\rm mac}$ broadening on spectral lines isotropically, independently of depth, and identically for both atomic and molecular lines. Hence, to achieve a good representation of the conditions throughout the 3D atmosphere, we selected a set of 12 real Fe I lines in the 5000–7000 Å range (see Table 3) such that (i) their equivalent width on the 3D spectrum range between few mÅ to 150 mÅ; and (ii) with two excitation potentials, low (∼1.0 eV) and high (∼5.0 eV). Using the 1D MARCS models with the same stellar parameters (plus the effective surface gravity, $g_{\rm eff}$) of the corresponding 3D simulations (see Table 2), we first derived the abundance from each line using Turbospectrum (Plez et al. 1993; Alvarez & Plez 1998; and further improvements by Plez) from the 3D equivalent width. For the non-gray model we used the 1D MARCS model corresponding to the lower temperature (i.e., 3430 K) because its thermal structure is more similar to the 3D mean temperature profile in the outer layers where spectral lines form (see top right panel of Fig. 5). Note that we computed the 3D spectra using O 3D with negligible expected differences (less than 5%; Paper I) with respect to Turbospectrum. The microturbulence velocity was then

Table 3. Parameters of the Fe I lines used to extract 1D microturbulence and macroturbulence and equivalent width, W, computed for the gray simulation st35gm03n07 and non-gray st35gm03n13 of Table 1

Wavelength Å	χ eV	lg (gf)	W gray mÅ	W non-gray mÅ
5853.148	1.485	−5.280	112.7	104.0
5912.690	1.557	−6.605	46.1	39.8
6024.058	4.548	−0.120	128.4	129.8
6103.186	4.835	−0.770	78.6	81.1
6214.182	1.608	−7.250	13.9	14.6
6364.366	4.795	−1.430	52.7	57.8
6569.216	4.733	−0.420	106.7	107.1
6581.210	1.485	−4.679	147.3	140.7
6604.583	4.835	−2.473	11.4	14.5
6712.438	4.988	−2.160	13.6	18.4
6717.298	5.067	−1.956	13.8	17.4
6844.667	1.557	−6.097	78.9	71.8

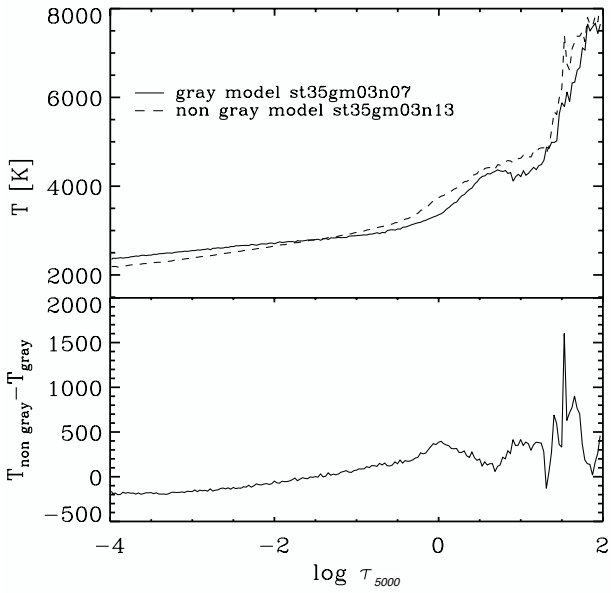

Fig. 6. Mean profiles (*top*) and temperature difference (*bottom*) of the gray and non-gray simulations from Fig. 5.

Table 4. 1D microturbulence (ξ_{mic}) and macroturbulence (ξ_{mac}) velocities determined to match the 3D spectra characteristics.

	Gray model st35gm03n07		Non-gray model st35gm03n13	
	ξ_{mic} (km s^{-1})			
	1.45 ± 0.09		1.28 ± 0.33	
	Logϵ (Fe)$_{3D}$ −Logϵ (Fe)$_{1D}$			
	0.14		−0.02	
	ξ_{mac}			
Profile	Velocity (km s^{-1})	χ^2	Velocity (km s^{-1})	χ^2
Radtan	6.7 ± 0.9	1.15	6.4 ± 2.7	1.17
Gauss	10.1 ± 1.2	1.19	9.7 ± 3.5	1.14
Exp	5.5 ± 0.9	1.21	5.2 ± 2.2	1.22

Notes. 3D−1D corrections to Fe abundances derived for the selected iron lines with the best-matching ξ_{mic}, are also indicated.

derived by requiring no trend of the abundances against the equivalent widths. The error on the microturbulence velocity was estimated from the uncertainties on the null trend. Once the microturbulence was fixed, the macroturbulence velocity was determined by minimizing the difference between the 3D and the 1D line profiles, and this for three profile types: radial-tangential, Gaussian and exponential. The error on the macroturbulence velocity is calculated from the dispersion of the macroturbulence from line to line. The reduced χ^2 is also determined on the best-fitting 1D to 3D line profiles. Hence, the automatic nature of the determination ensures an objective determination.

Table 4 presents the derived values of the microturbulence and macroturbulence respectively for the 3D gray and non-gray models. The dispersion of the microturbulent velocities is reasonably low, so that the depth-independent microturbulence is a fairly good approximation. Note also that the microturbulence velocity for the gray and non-gray model are quite close. Although the macroturbulence profile varies from one to another, the reduced χ^2 show that all of them give about the same value. Note that the micro and macroturbulence standard deviations from the average velocities are systematically higher in the non-gray model. We found that the non-gray spectral lines

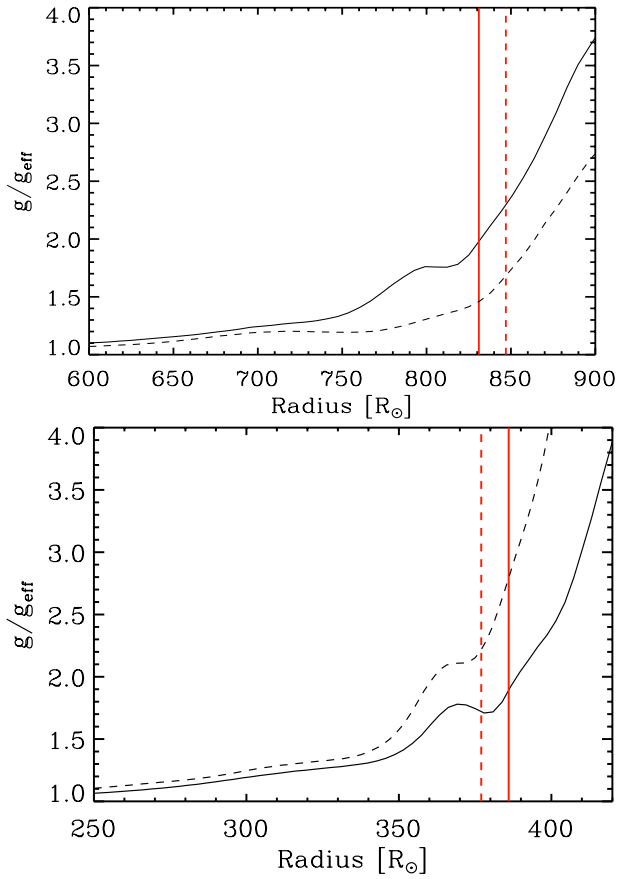

Fig. 7. Ratio between the g and g_{eff} from Eq. (8) for simulations st35gm03n07 (solid line) and st35gm03n13 (dotted line) in *top panel*, and st36gm00n04 (solid line) and st36gm00n05 (dotted line) in *the bottom panel*. We used the same snapshots as in Fig. 5 and 8. The vertical red lines are the approximate positions of the radii from Table 1.

generally show a more complex profile that affect the line fitting with 1D models, which causes higher standard deviations. An example for the non-gray model is shown in Fig. 9: the spectral lines look shifted and broadened. The line asymmetries are caused by the inhomogeneous velocity field emerging from optical depths where lines form. The lower temperature in the outer layers of non-gray model (Fig. 6) could cause lower pressure and density scale heights and consequently a faster density drops and stronger shocks. These shocks would complicate the shape of the non-gray spectral lines. The macroturbulence parameter used for the convolution of 1D spectra reproduces only partly the complex profile with larger differences in line wings.

On a wavelength scale of the size of a few spectral lines, the differences between 3D and 1D models are caused by the velocity field in 3D simulations that affect the spectral lines in terms of broadening and shift. A 1D model does not take into account velocity fields, and ad hoc parameters for micro- and macroturbulence are used to reproduce this effect. The microturbulence and macroturbulence calibration results are pretty similar for gray and non-gray simulations even if the 3D-1D corrections of the resulting iron abundances are smaller for the non-gray model. The microturbulence values obtained in this work are comparable, albeit a little bit lower, with Carr et al. (2000) who found $1.7 \lesssim \xi_{mic} \lesssim 3.5$ km s^{-1} with a different method based on observed CO lines. Our values also generally agree to what Steffen et al. (2009) found for their RHD Sun and Procyon simulations ($0.8 \lesssim \xi_{mic} \lesssim 1.8$).

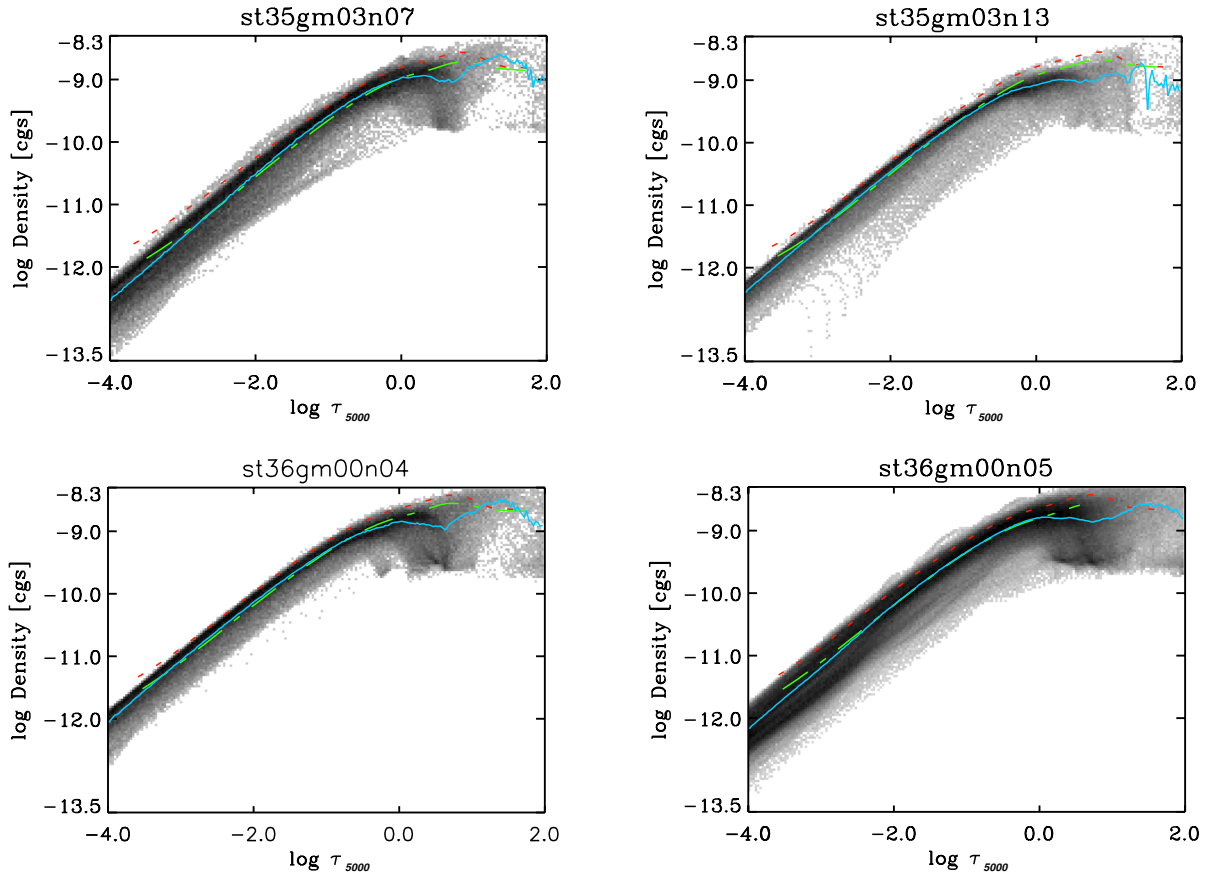

Fig. 8. Density structures of the simulations in Table 1. Darker areas indicate temperature values with higher probability. The colored curves have the same meaning as in Fig. 5).

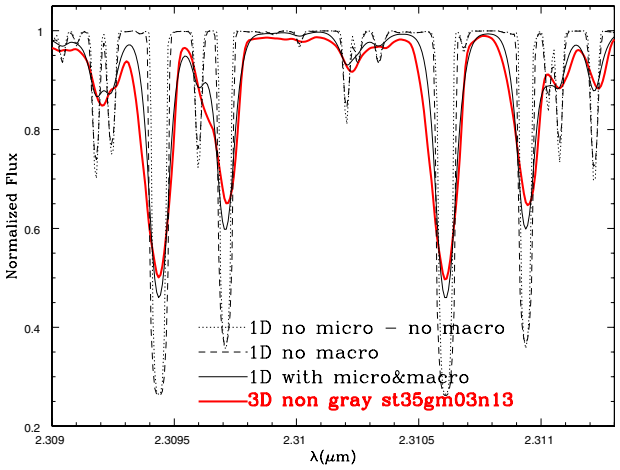

Fig. 9. Example of CO first overtone lines computed for the 3D non-gray simulation and the corresponding 1D MARCS model of Table 2. The $\xi_{\rm mic}$ turbulent velocity used is 1.5 km s^{-1} and the $\xi_{\rm mac}$ is 6.4 km s^{-1} with a radial-tangential profile (see Table 3).

5.2. Spectral energy distribution

The cooler outer layers encountered in the convection simulations are expected to have a significant impact on the temperature sensitive features. This is the case for, in particular, molecular lines (e.g., TiO) and strong low-excitation lines of neutral metals, the line-formation regions of which are shifted outwards because of the lower photospheric temperatures (Gustafsson et al. 2008; Plez et al. 1992). The importance of opacity from molecular electronic transition lines of TiO are crucial in the spectrum of M-type stars. Figure 10 (top row) shows the synthesis of a TiO band. The strength of the transition depends on the mean thermal gradient in the outer layers ($\tau_{5000} < 1$), where TiO has a significant effect, which is more pronounced in the non-gray model with respect to the gray one Fig. 6. A shallow mean thermal gradient weakens the contrast between strong and weak lines and this is visible in the molecular band strength, which is much stronger for the non-gray model.

The top right panel of Fig. 10 also shows that the TiO band strength of non-gray model is more similar to the cool 1D MARCS model at 3430 K than the hot one at 3700 K. This reflects the fact that the 3D mean thermal structure in the outer layers is very similar to 1D-3430 K model (Fig. 5, top right panel).

The approximation of gray radiative transfer is justified only in the stellar interior and it is inaccurate in the optically thin layers. So far, this approximation was the best we could do because the RHD simulations have been constrained by execution time. However, with the advent of more powerful computers, the frequency-dependent treatment of radiative transfer is now possible and, on a wavelength scale of one or more molecular bands, the use of this method is big step forward for a quantitative analysis of observations.

The shape of the spectral energy distribution (SED) reflects the mean thermal gradient of the simulations. The absolute flux plots in the bottom row of Fig. 10 display that at lower resolution two important conclusions can be retrieved: (i) the spectrum based on the gray model is very different from the 1D spectra; (ii) the non-gray model shows that the SED, compared to the 1D MARCS model with the hot temperature (3700 K), displays

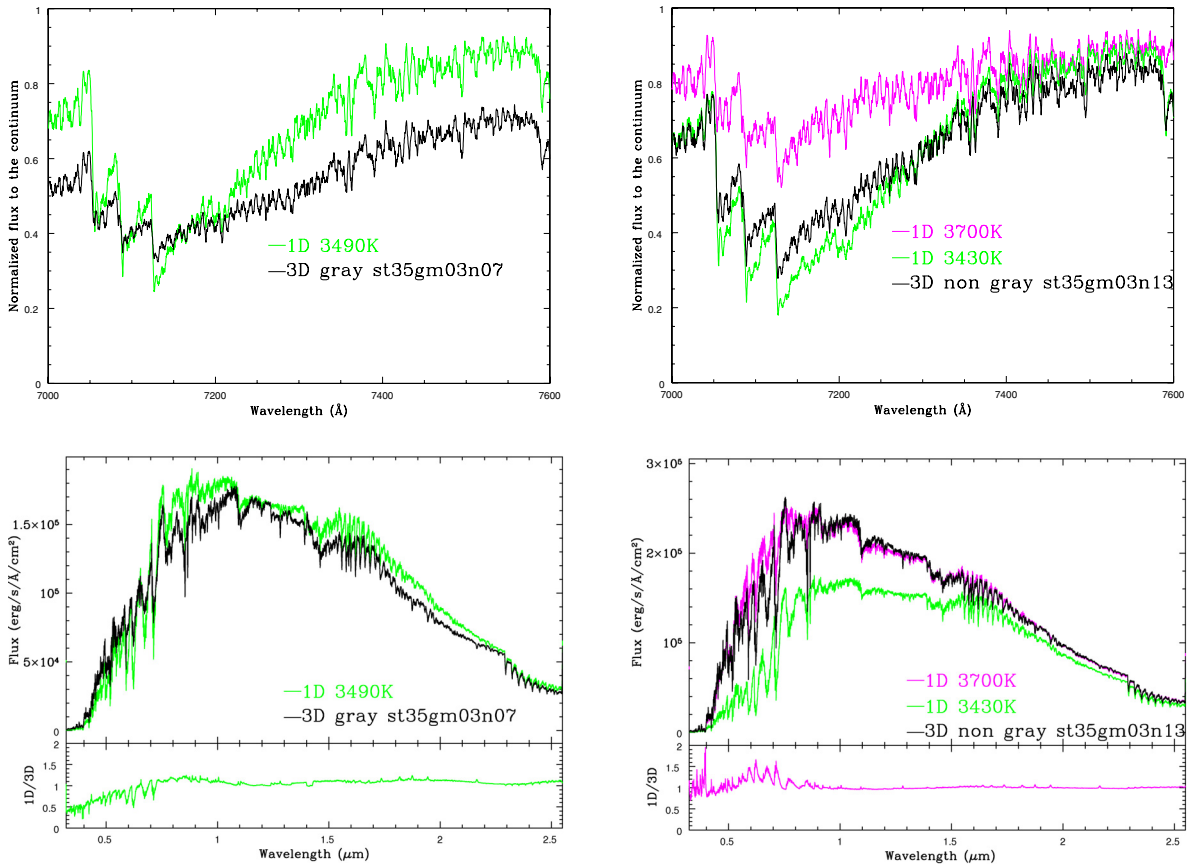

Fig. 10. *Top panel*: spectral synthesis of TiO band transition $A^3\Phi - X^3\Delta\,(\gamma)$ (*top row*) and spectral energy distribution (*bottom row*) for the same snapshots of the gray, st35gm03n07, and non-gray, st35gm03n13, simulations of Fig. 5. 3D spectra are compared to the corresponding 1D MARCS models (Table 2) with $\xi_{\rm mic}$ and $\xi_{\rm mac}$ from Table 4 (radial-tangential profile).

Table 5. Photometric colors for RHD simulations of Table 1 and for the corresponding 1D models of Table 2. Δ(3D−1D) shows the 3D/1D difference for each index.

Model	$B-V$	$V-R$	$V-K$	$J-H$	$J-K$	$H-K$
3D gray, st35gm03n07	1.680	0.955	4.751	0.859	1.153	0.293
1D, $T_{\rm eff}$ = 3490 K, $\log g = -0.58$	1.881	1.125	5.070	0.931	1.200	0.269
Δ(3D−1D)	−0.201	−0.170	−0.319	−0.072	−0.047	0.024
3D non-gray, st35gm03n13	1.661	0.886	4.356	0.807	1.064	0.258
1D, $T_{\rm eff}$ = 3700 K, $\log g = -0.35$	1.850	0.962	4.202	0.854	1.080	0.226
Δ(3D−1D)	−0.189	−0.076	0.154	−0.047	−0.016	0.032

almost no distinction in the infrared region, and a weaker distinction in molecular bands in the visible region and in the near-ultraviolet region. Using the prescriptions by Bessell et al. (1998) for the filters *BVRJHK*, we computed the expected colors for the gray and non-gray models as well as the corresponding MARCS models (Table 5). The non-gray 3D model shows smaller differences to the 1D model than the gray one. The stronger radiative efficiency in the non-gray case forces the temperature stratification to be closer to the radiative equilibrium than in the gray case, where convection and waves have a larger impact on it.

Josselin et al. (2000) probed the usefulness of the index $V-K$ as a temperature indicator for Galactic RSGs, but Levesque et al. (2006), fitting TiO band depths, showed that $V-K$ and $V-R$ provides systematic higher effective temperatures in Galactic and Magellan clouds RSGs (an average +170 K and +30 K, respectively) than the spectral fitting with 1D MARCS models. Levesque et al. (2006) concluded that the systematic offset was probably caused by the limitations of static 1D models. Using the radius definition of Eq. (5), we find that the effective temperature from the SED of 3D non-gray spectrum is $T_{\rm eff}$ = 3700 K. However, in the optical the spectrum looks more like a 3500 K 1D model (judging from the TiO bandheads of Fig. 10, top right panel). Assuming that the 3D non-gray model spectrum is close to real star spectra and using $V-K$, this leads to a $T_{\rm eff}$ that is higher by about 200 K than the $T_{\rm eff}$ from TiO bands. This goes in the right direction considering the results of Levesque et al. (2006).

5.3. Interferometry: visibility fluctuations

Chiavassa et al. (2010b, 2011) showed that in the visible spectral region, the gray approximation in our modeling may significantly affect the intensity contrast of the granulation. Figure 11 (top row) shows the resulting intensity maps computed in a

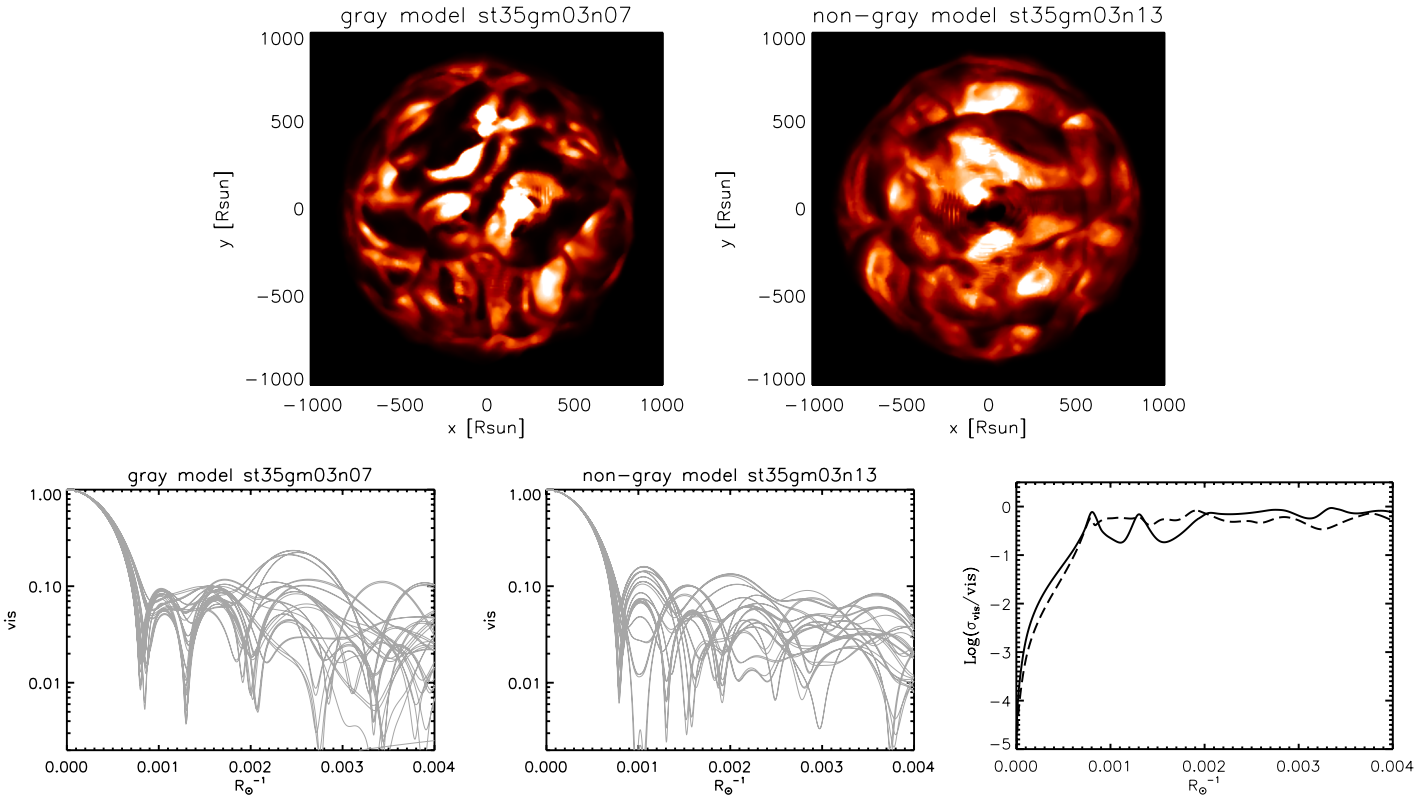

Fig. 11. *Top row*: map of the linear intensity in the TiO band transition $A^3\Phi - X^3\Delta\,(\gamma)$ of Fig. 10. The range is $[0; 3.5 \times 10^5]$ for the gray simulation st35gm03n07 of Table 1 and $[0; 4.5 \times 10^5]$ erg cm^{-2} s^{-1} Å^{-1} for the non-gray simulation st35gm03n13. *Bottom row*: visibility curves obtained from the maps above. The visibilities were computed for 36 different azimuth angles 5° apart. *Bottom right panel*: visibility fluctuations with respect to the average value for the gray (solid line) and non-gray (dashed line).

TiO electronic transition. The resulting surface pattern is connected throughout the granulation to dynamical effects. The emerging intensity is related to layers where waves and shocks dominate together with the variation in opacity through the atmosphere and veiling by TiO molecules.

The intensity fluctuations are linked with the temperature inhomogeneities, which are weaker in the thermal structure of the non-gray simulation (see Sect. 4.2 and Fig. 5). We analyzed the impact on the interferometric observables using the method described in Paper I. We computed visibility curves for 36 different rotation angles with a step of 5° from the intensity maps in Fig. 11. In the plots, we introduced a theoretical spatial frequency scale expressed in units of inverse solar radii ($R_\odot^{-1}$). The conversion between visibilities expressed in the latter scale and in the more usual scale is given by $['']^{-1} = [R_\odot^{-1}] \cdot d\,[\mathrm{pc}] \cdot 214.9$. The resulting visibility curves are plotted in the bottom row of Fig. 11 together with the one σ visibility fluctuations, F, with respect to the average value $\overline{vis}$ ($F = \sigma/\overline{vis}$). The visibility fluctuations of the non-gray model are lower than the gray model ones for spatial frequencies lower than the first null point (approximately 0.0075 $R_\odot^{-1}$), as a consequence the uncertainty on the radius determination (the first null point of the visibility curves is sensitive to the stellar radius, Hanbury Brown et al. 1974) is smaller: ∼10% in the gray model versus ∼4% in the non-gray one. At higher frequencies, the visibility fluctuations are higher in the non-gray model between 0.0075 and 0.002 $R_\odot^{-1}$, then the non-gray model fluctuations are systematically lower between ∼0.002 and 0.004 $R_\odot^{-1}$. However, it must be noted that after 0.03 $R_\odot^{-1}$ (corresponding to 33 $R_\odot$, i.e., ∼4 pixels), the numerical resolution limit is reached and visibility curves can be affected by numerical artifacts (Paper I and Sect. 6).

6. Study on the increase of the numerical resolution of simulations

We presented two simulations with approximately the same stellar parameters but with an increase of the numerical resolution. We analyzed the effect of increasing the resolution from 255^3 grid points of simulation st36gm00n04 to 401^3 grid points of st36gm00n05 (Table 1). Owing to the long computer time needed for the high-resolution model, the better way to proceed is to compute a gray model with the desired stellar parameters first, then the numerical resolution can be increased, and eventually the frequency-dependent non-gray treatment can be applied. With the actual computer power and the use of the OpenMP method of parallelization in CO^{5}BOLD, this process may take several months.

We computed intensity maps at 5000 Å. This spectral region, as for the TiO band, is interspersed by a granulation pattern with high-intensity contrast. Figure 12 displays the intensity maps permeated by a variety of convection-related structures; while the large structures are visible in both images, the higher resolution model resolves the details much better and smaller-scale structures appear within the large ones (as already shown in a previous work, Chiavassa et al. 2006). Artifacts owing to Moire-like patterns show up in the maps of the higher numerical resolution simulation. They are composed of thin ripples up to 40% brighter than the surrounding points and have already been pointed out in Paper I. They are caused by high opacities, large variations in opacity, and significant changes in optical depth between two successive columns in the numerical box (see κ in Fig. 3). To overcome this problem, we computed visibility curves from these images and compared the visibility curves for

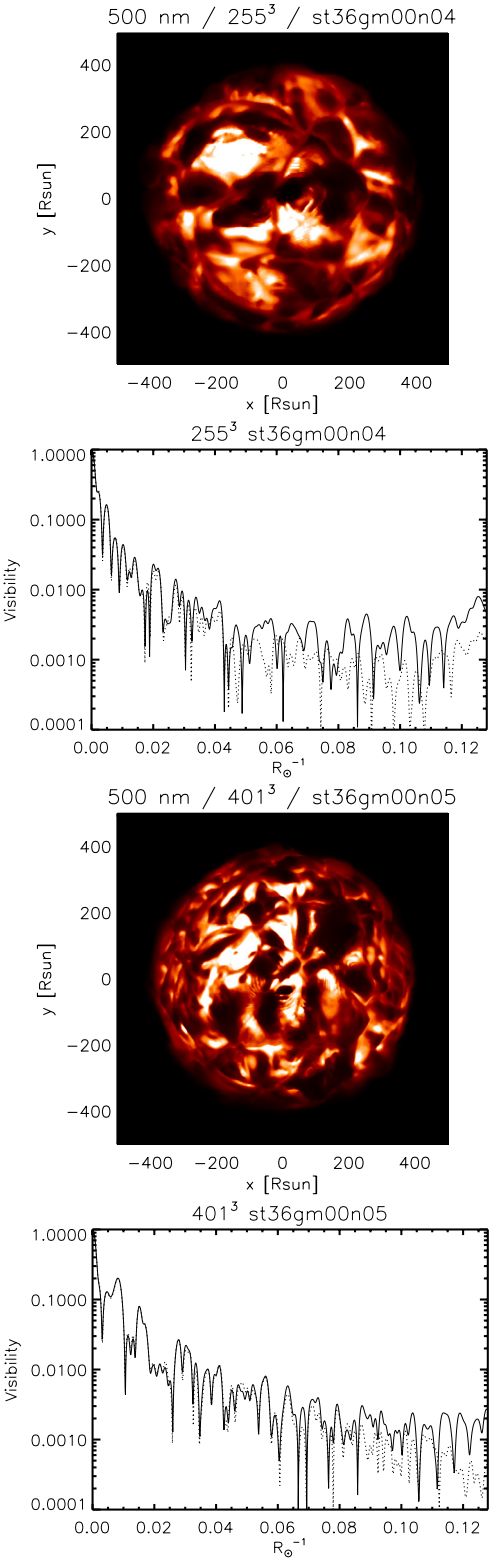

Fig. 12. Maps of the square root intensity (to better show the structure in the higher resolution simulation) of st36gm00n04 and st36gm00n05 (Table 1) at 5000 Å together with a visibility curve extracted for a particular angle (solid curve) and the the same visibility's angle after applying a [3 × 3] median smoothing (dashed curve). The intensity range in the maps is [0; 547.7] erg cm^{-2} s^{-1} Å^{-1}.

one particular projected baseline from the raw image, and after applying a median [3 × 3] smoothing that effectively erases the artifacts. The visibility curves in Fig. 12 show that the signal from the low-resolution st36g00n04 simulation is stronger than st36g00n05 for spatial frequencies higher than about 0.07 $R_\odot^{-1}$. A weaker signal at a particular frequency means better spatial resolution: therefore very small structures (corresponding to roughly ≤ 15–20 $R_\odot$) are better resolved in st36g00n05.

Moreover, the visibility curves are mostly affected by the numerical artifacts for frequencies higher than ∼0.05 $R_\odot^{-1}$ (corresponding to 25 $R_\odot$, i.e., ∼5 pixels) for st36g00n04 and 0.09 $R_\odot^{-1}$ (corresponding to 11 $R_\odot$, i.e., ∼4 pixels) for st36g00n05. The increase of numerical resolution reduces only partly the problem in the intensity maps and therefore the cosmetic median filter must be still applied. This will not affect the visibilities at lower frequencies, which are the only ones observable in practice with modern interferometers.

Apart for the problems in the Moire-like patterns of intensity maps, the number of convection related surface structures seems to visually increase and possibly change size passing from 255^3 to 401^3 grid points (Fig. 12). In addition to this, the bottom right panel of Fig. 3 shows that going from 255^3 to 401^3 grid points the resolution of the temperature jump does not change so much. This means that the numerical resolution limit has not been reached yet. The principal limitation to the computation of an even more extended numerical simulation is the computer power. A more complete study concerning the impact of numerical resolution on the number and size of granules is necessary and will be addressed in a forthcoming paper, where a series of simulations with the same stellar parameters and increasing numerical resolution will be analyzed.

7. Conclusions

We presented the radiation hydrodynamical simulations of red supergiants with the code CO5BOLD together with the new generation of models based on a more sophisticated opacity treatment, and higher effective temperature and surface gravity.

The actual pattern and the mean temperature structure of RSGs simulations are influenced by (i) differences in the relative efficiency of convective and radiative energy transport and by the efficiency of radiation to smooth out temperature fluctuations; (ii) the optical depth of the upper boundary of the convection zone; (iii) the extent of convective overshoot.

The main difference between RSG and Sun-like granulation (except for geometrical scales) comes from the altered role of radiation: it is much more efficient in transporting energy in an RSG than in the Sun. This strongly influences the stratification and keeps it closer to the case of radiative equilibrium than its inefficient counterpart in the deeper layers of the Sun. Moreover, the strong entropy gradient causes a high buoyancy and renders the convective motions, which compete with the radiative energy transport, more violent in a relatively limited region over which the sub-photospheric entropy jump occurs (compared to a typical size of a convective element). Eventually, higher velocities are accompanied by higher pressure fluctuations and a stronger influence of shockwaves on the photosphere.

The most important improvement of our work is the relaxation of the assumption of gray opacities through multigroup frequency-dependent opacities. The non-gray simulation shows (i) a steeper mean thermal gradient in the outer layers that affect strongly the molecular and line strengths that are deeper in the non-gray case; (ii) that the general shape of the spectrum of the 3D non-gray simulation is similar to the 1D model, while the 3D gray simulation is very different. Hence, we concluded that the frequency-dependent treatment of radiative transfer with 5 bins represents a good approximation of the more complex

profile of 1D based on ∼110 000 frequency points. Moreover, the lower temperature fluctuations of the non-gray model, caused by the intensified heat exchange of a fluid element with its environment, affect the surface intensity contrast and consequently the interferometric observables, which in turn reduces the uncertainty on the stellar radius determination.

We also showed that 1D models of RSGs must include a turbulent velocity calibrated on 3D simulations to obtain the effective surface gravity that mimics the effect of turbulent pressure on the stellar atmosphere.

We provided a calibration of the ad hoc micro- and macroturbulence parameters for 1D models using the 3D simulations, which have a self-consistent ab initio description of the non-thermal velocity field generated by convection, shock waves and overshoot. We found that the microturbulence velocity for the gray and non-gray model are quite close and the depth-independent microturbulence assumption in 1D models is a fairly good approximation, even if the 3D–1D corrections of the resulting iron abundances are smaller for the non-gray model. We also assessed that there is no clear distinction between the different macroturbulent profiles needed in 1D models to fit 3D synthetic lines; nevertheless, we noticed that micro and macroturbulence standard deviations on the average velocities are systematically larger in the non-gray model, which shows more complex line profiles than the gray simulation. This may be caused by stronger shocks in the outer layers of the non-gray models where the pressure and density scales heights are smaller.

While simulations with more sophisticated opacity treatment are essential for the subsequent analysis, models with a better numerical resolution are desirable to study the impact of the numerical resolution on the number and size of granules. We provided a first investigation showing that the number of convection related surface structures seems to increase and change size passing from 255^3 to 401^3 grid points, therefore the numerical resolution limit has not been reached yet. Future work will focus on a series of simulations with the same stellar parameters and increasing numerical resolution.

Acknowledgements. The ULB team is supported in part by an *Action de recherche concertée* (ARC) grant from the *Direction générale de l'Enseignement non obligatoire et de la Recherche scientifique – Direction de la Recherche scientifique – Communauté française de Belgique*. A.C. is supported by the F.R.S.-FNRS FRFC grant 2.4513.11, T.M. by the F.R.S.-FNRS FRFC grant 2.4533.09. A.C. thanks the Rechenzentrum Garching (RZG) and the CINES for providing the computational resources necessary for this work. A.C. also thanks Pieter Neyskens and Sophie Van Eck for enlightening discussions. B.F. acknowledges financial support from the *Agence Nationale de la Recherche* (ANR), the "*Programme National de Physique Stellaire*" (PNPS) of CNRS/INSU, and the "*École Normale Supérieure*" (ENS) of Lyon, France, and the *Istituto Nazionale di Astrofisica/Osservatorio Astronomico di Capodimonte* (INAF/OAC) in Naples, Italy.

References

Alvarez, R., & Plez, B. 1998, A&A, 330, 1109
Asplund, M., & García Pérez, A. E. 2001, A&A, 372, 601
Asplund, M., Nordlund, Å., Trampedach, R., & Stein, R. F. 1999, A&A, 346, L17
Asplund, M., Grevesse, N., & Sauval, A. J. 2006, Commun. Asteroseismol., 147, 76
Asplund, M., Grevesse, N., Sauval, A. J., & Scott, P. 2009, ARA&A, 47, 481
Aurière, M., Donati, J., Konstantinova-Antova, et al. 2010, A&A, 516, L2
Behara, N. T., Bonifacio, P., Ludwig, H., et al. 2010, A&A, 513, A72
Bessell, M. S., Castelli, F., & Plez, B. 1998, A&A, 333, 231
Buscher, D. F., Baldwin, J. E., Warner, P. J., & Haniff, C. A. 1990, MNRAS, 245, 7P
Caffau, E., Ludwig, H., Steffen, M., Freytag, B., & Bonifacio, P. 2010, Sol. Phys., 66
Carr, J. S., Sellgren, K., & Balachandran, S. C. 2000, ApJ, 530, 307
Chiavassa, A., Plez, B., Josselin, E., & Freytag, B. 2006, in EAS Publ. Ser. 18, ed. P. Stee, 177
Chiavassa, A., Plez, B., Josselin, E., & Freytag, B. 2009, A&A, 506, 1351
Chiavassa, A., Collet, R., Casagrande, L., & Asplund, M. 2010a, A&A, 524, A93
Chiavassa, A., Haubois, X., Young, J. S., et al. 2010b, A&A, 515, A12
Chiavassa, A., Lacour, S., Millour, F., et al. 2010c, A&A, 511, A51
Chiavassa, A., Pasquato, E., Jorissen, A., et al. 2011, A&A, 528, A120
Collet, R., Asplund, M., & Trampedach, R. 2007, A&A, 469, 687
Collet, R., Nordlund, Å., Asplund, M., Hayek, W., & Trampedach, R. 2009, Mem. Soc. Astron. Ital., 80, 719
Cuntz, M. 1997, A&A, 325, 709
Freytag, B., Steffen, M., & Dorch, B. 2002, Astron. Nachr., 323, 213
Grunhut, J. H., Wade, G. A., Hanes, D. A., & Alecian, E. 2010, MNRAS, 408, 2290
Gustafsson, B., & Plez, B. 1992, in Instabilities in Evolved Super- and Hypergiants, ed. C. de Jager, & H. Nieuwenhuijzen, 86
Gustafsson, B., Edvardsson, B., Eriksson, K., et al. 2008, A&A, 486, 951
Hanbury Brown, R., Davis, J., Lake, R. J. W., & Thompson, R. J. 1974, MNRAS, 167, 475
Hartmann, L., & Avrett, E. H. 1984, ApJ, 284, 238
Haubois, X., Perrin, G., Lacour, S., et al. 2009, A&A, 508, 923
Hauschildt, P. H., Baron, E., & Allard, F. 1997, ApJ, 483, 390
Iglesias, C. A., Rogers, F. J., & Wilson, B. G. 1992, ApJ, 397, 717
Josselin, E., & Plez, B. 2007, A&A, 469, 671
Josselin, E., Blommaert, J. A. D. L., Groenewegen, M. A. T., Omont, A., & Li, F. L. 2000, A&A, 357, 225
Kervella, P., Verhoelst, T., Ridgway, S. T., et al. 2009, A&A, 504, 115
Levesque, E. M. 2010, New Astron. Rev., 54, 1
Levesque, E. M., Massey, P., Olsen, K. A. G., et al. 2005, ApJ, 628, 973
Levesque, E. M., Massey, P., Olsen, K. A. G., et al. 2006, ApJ, 645, 1102
Levesque, E. M., Massey, P., Olsen, K. A. G., & Plez, B. 2007, ApJ, 667, 202
Ludwig, H., Jordan, S., & Steffen, M. 1994, A&A, 284, 105
Ludwig, H., Caffau, E., Steffen, M., et al. 2009, Mem. Soc. Astron. Ital., 80, 711
Massey, P., Levesque, E. M., Olsen, K. A. G., Plez, B., & Skiff, B. A. 2007, ApJ, 660, 301
Nordlund, A. 1982, A&A, 107, 1
Nordlund, A., & Dravins, D. 1990, A&A, 228, 155
Nordlund, Å., Stein, R. F., & Asplund, M. 2009, Living Rev. Sol. Phys., 6, 2
Ohnaka, K., Hofmann, K., Benisty, M., et al. 2009, A&A, 503, 183
Ohnaka, K., Weigelt, G., Millour, F., et al. 2011, A&A, 529, A163
Pijpers, F. P., & Hearn, A. G. 1989, A&A, 209, 198
Plez, B., Brett, J. M., & Nordlund, A. 1992, A&A, 256, 551
Plez, B., Smith, V. V., & Lambert, D. L. 1993, ApJ, 418, 812
Quirk, J. J. 1994, Int. J. Num. Meth. Fluids, 18, 555
Roe, P. L. 1986, Ann. Rev. Fluid Mech., 18, 337
Sbordone, L., Bonifacio, P., Caffau, E., et al. 2010, A&A, 522, A26
Steffen, M., Ludwig, H., & Caffau, E. 2009, Mem. Soc. Astron. Ital., 80, 731
Strang, G. 1968, SIAM J. Numer. Anal., 5, 506
Tuthill, P. G., Haniff, C. A., & Baldwin, J. E. 1997, MNRAS, 285, 529
Vögler, A. 2004, A&A, 421, 755
Vögler, A., Bruls, J. H. M. J., & Schüssler, M. 2004, A&A, 421, 741
Wedemeyer, S., Freytag, B., Steffen, M., Ludwig, H., & Holweger, H. 2004, A&A, 414, 1121
Wende, S., Reiners, A., & Ludwig, H. 2009, A&A, 508, 1429
Wilson, R. W., Baldwin, J. E., Buscher, D. F., & Warner, P. J. 1992, MNRAS, 257, 369
Wilson, R. W., Dhillon, V. S., & Haniff, C. A. 1997, MNRAS, 291, 819
Young, J. S., Baldwin, J. E., Boysen, R. C., et al. 2000, MNRAS, 315, 635

A&A 506, 1351–1365 (2009)
DOI: 10.1051/0004-6361/200911780

Astronomy & Astrophysics

Radiative hydrodynamics simulations of red supergiant stars

I. interpretation of interferometric observations

A. Chiavassa[1,2], B. Plez[2,4], E. Josselin[2], and B. Freytag[3,4]

[1] Max-Planck-Institut für Astrophysik, Karl-Schwarzschild-Str. 1, Postfach 1317, 85741 Garching b. München, Germany
e-mail: chiavass@mpa-garching.mpg.de
[2] GRAAL, Université de Montpellier II - IPM, CNRS, Place Eugéne Bataillon, 34095 Montpellier Cedex 05, France
[3] Centre de Recherche Astrophysique de Lyon, UMR 5574: CNRS, Université de Lyon, École Normale Supérieure de Lyon, 46 allée d'Italie, 69364 Lyon Cedex 07, France
[4] Department of Physics and Astronomy, Division of Astronomy and Space Physics, Uppsala University, Box 515, 75120 Uppsala, Sweden

Received 3 February 2009 / Accepted 14 July 2009

ABSTRACT

Context. It has been proposed that convection in red supergiant (RSG) stars produces large-scale granules causing observable surface inhomogeneities. This convection is also extremely vigorous and is suspected to be one of the main causes of mass-loss in RSGs. It should thus be understood in detail. Evidence has accumulated of asymmetries in the photospheres of RSGs, but detailed studies of granulation are still lacking. Interferometric observations provide an innovative way of addressing this question, but they are still often interpreted using smooth symmetrical limb-darkened intensity distributions, or simple, spotted, ad hoc models.
Aims. We explore the impact of the granulation on visibility curves and closure phases using the radiative transfer code OPTIM3D. We simultaneously assess how 3D simulations of convection in RSG with CO^{5}BOLD can be tested by comparing with these observations.
Methods. We use 3D radiative hydrodynamical (RHD) simulations of convection to compute intensity maps at various wavelengths and time, from which we derive interferometric visibility amplitudes and phases. We study their behaviour with time, position angle, and wavelength, and compare them to observations of the RSG α Ori.
Results. We provide average limb-darkening coefficients for RSGs. We describe the prospects for the detection and characterization of granulation (i.e., contrast, size) on RSGs. We demonstrate that our RHD simulations provide an excellent fit to existing interferometric observations of α Ori, in contrast to limb darkened disks. This confirms the existence of large convective cells on the surface of Betelgeuse.

Key words. stars: supergiants – stars: atmospheres – hydrodynamics – radiative transfer – techniques: interferometric

1. Introduction

Massive stars with masses between roughly 10 and 25 $M_\odot$ spend some time as red supergiant (RSG) stars, which represent the largest stars in the universe. They have effective temperatures, $T_{\rm eff}$, ranging from 3450 to 4100 K, luminosities of between 20 000 and 300 000 $L_\odot$ and radii up to 1500 $R_\odot$ (Levesque et al. 2005). Their luminosities imply that they are among the brightest stars, visible to very large distances. However, a number of open issues remain. They shed large amounts of mass back to the interstellar medium, but their mass-loss mechanism is unidentified, although Alfvén and acoustic waves have been proposed (Hartmann & Avrett 1984; Pijpers & Hearn 1989; Cuntz 1997), as well as acoustic waves and radiation pressure on molecules (Josselin & Plez 2007). Their chemical composition is largely unknown, despite the work of e.g. Carr et al. (2000), and Cunha et al. (2007), because of difficulties in analysing their spectra, which contain broad, asymmetric lines that according to a convection pattern of large granules and (super-)sonic velocities (Josselin & Plez 2007; Gray 2008). Their $T_{\rm eff}$-scale has been revised both at solar and Magellanic Cloud metallicities using 1D hydrostatic models (Levesque et al. 2005, 2006; Massey et al. 2007; Levesque et al. 2007). Although these MARCS models (Gustafsson et al. 2008) provide an accurate fit to the optical spectra allowing the derivation of $T_{\rm eff}$ and reddening, problems remain. There is a blue-UV excess in many of the observed spectra, which may be related to either scattering by circumstellar dust or to an insufficiency in the models. There is also some disagreement in the IR colours, which may be related to atmospheric temperature inhomogeneities that are characteristic of convection (Levesque et al. 2006).

Hydrodynamical modeling of convection in RSGs has lagged behind that of solar type stars because of the need to include the entire star in the simulation box. Freytag et al. (2002) managed to develop numerical simulations of a typical RSG. We thus attempted to improve our understanding and description of RSGs using detailed numerical simulations and a large set of observational material.

This paper is the first in a series exploring the granulation pattern of RSGs and its impact on interferometric observations.

2. 3D radiative transfer in a radiative hydrodynamical simulation

2.1. 3D hydrodynamical simulations with CO^{5}BOLD

The numerical simulations employed in this work were developed using CO^{5}BOLD (Freytag et al. 2002; Freytag & Höfner 2008) in the *star-in-a-box* configuration: the computational

domain is a cube, and the grid is equidistant in all directions. All six faces of the cube use the same open boundary conditions for material flows and emergent radiation. In addition, there is an "inner boundary condition": in a small spherical region in the centre of the cube, a source term to the internal energy provides the stellar luminosity and a drag force brakes dipolar flows through it. Otherwise, the hydrodynamics and the radiative transfer scheme are unaffected by the core and an integration can be completed without problem. Radiation transport is strictly in LTE. The grey Rosseland mean opacity is a function of both gas pressure and temperature. The necessary values are derived by interpolating in a table derived for temperatures around 12 000 K from high-temperature OPAL data (Iglesias et al. 1992) and low-temperature PHOENIX data (Hauschildt et al. 1997) by Hans-Günter Ludwig. Some more technical information can be found in Freytag & Höfner (2008), the CO^{5}BOLD Online User Manual[1], and in a forthcoming paper by Freytag (2009).

The 12 $M_\odot$ model that we use in this paper, called st35gm03n07, was produced by of intensive calculations corresponding to about 7.5 years of simulated stellar time. It has a numerical resolution of 8.6 $R_\odot$ within a cube of 235^3 grid points. The model parameters are a luminosity of $L = 93\,000 \pm 1300\,L_\odot$, an effective temperature of $T_{\rm eff} = 3490 \pm 13$ K, a radius of $R = 832 \pm 0.7\,R_\odot$, and correspondingly a surface gravity of $\log g = -0.337 \pm 0.001$. These values are averages over both spherical shells and time (over the past year), and the errors are one standard deviation fluctuations with respect to the average over time. We define the stellar radius, R, and the effective temperature, $T_{\rm eff}$, as follows. First, we compute the average temperature and luminosity over spherical shells, $T(r)$, and $L(r)$. We then search the radius R for which $L(R)/(4\pi R^2) = \sigma T^4(R)$, where σ is the Stefan-Boltzmann constant. The effective temperature is then $T_{\rm eff} = T(R)$. Figure 1 shows the value of the radius, temperature, and luminosity over the past 3.5 years. The radius drifts by about −0.5% per year and seems to have stabilised to $R = 832\,R_\odot$ in the last year. Over the entire sequence $T_{\rm eff}$ fluctuates by ±1%, and has a constant average value. The luminosity fluctuations are of the order of ±4%, reflecting the temperature variations, with a decrease of about 1% per year in the first few years, reflecting the radius decrease. These drifts indicate that the simulation has not completely converged in the first few years. In this work, we consider the entire 3.5 year sequence, despite the small radius drift, to obtain better statistics. The preceding 4 years of the simulation are not considered here, since they show larger drifts. The interferometric observables derived in this work are insensitive to the drift in the parameters.

This is our most successful RHD simulation so far because it has stellar parameters closest to those of real RSGs (e.g., 3650 K for α Ori, Levesque et al. 2005). We are developing additional simulations with different stellar parameters and will present the analysis of these simulations in a forthcoming paper.

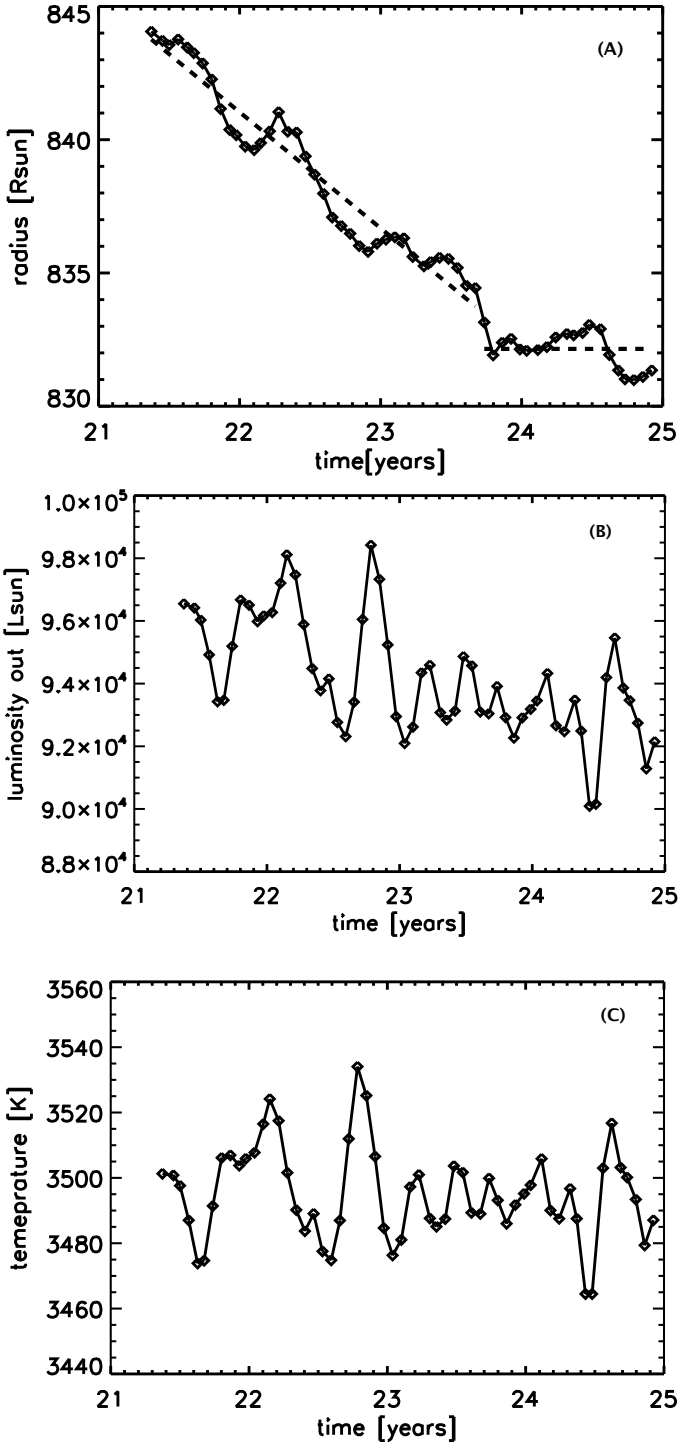

Fig. 1. Radius (Panel **A**), luminosity (Panel **B**) and temperature (Panel **C**) as a function of time for the simulation used in this work. The radius is fitted with the law: $R(t) = 936.9 - 4.3 \times t$ for $t \leq 23.8$ yrs and $R = 832\,R_\odot$ for $t > 23.8$ yrs.

2.2. Radiative transfer code: OPTIM3D

We developed a 3D pure LTE radiative transfer code, OPTIM3D, to generate synthetic spectra and intensity maps from snapshots of the 3D hydrodynamical simulations, taking into account the Doppler shifts caused by the convective motions. The radiation transfer is calculated in detail using pre-tabulated extinction coefficients generated with the MARCS code (Gustafsson et al. 2008). These tables are functions of temperature, density, and wavelength, and were computed by assuming the solar composition of Asplund et al. (2006). The tables include the same extensive atomic and molecular data as the MARCS models. They were constructed with no micro-turbulence broadening and the temperature and density distribution was optimized to cover the values encountered in the outer layers of the RHD simulations. The wavelength resolution is $R = \lambda/\Delta\lambda = 500\,000$ and we checked that this resolution is sufficient to ensure an accurate

[1] www.astro.uu.se/~bf/co5bold_main.html

calculation of broadened line profiles of RSGs even after interpolation of the opacity at the Doppler shifted wavelengths.

The monochromatic intensity emerging towards the observer at a given position on the simulation can be computed by integrating the source function along a ray perpendicular to a face of the cube, at that position. In LTE it is given by:

$$I_\lambda(0) = \int_0^{\tau_\lambda} S_\lambda(t_\lambda)\, e^{-t_\lambda} dt_\lambda, \quad (1)$$

where I_λ is the intensity, t_λ is the optical depth along the ray increasing inwards, τ_λ is the maximum optical depth reached along the line-of-sight, and $S_\lambda = B_\lambda(T)$, the Planck function at the temperature T, is the source function. A Gauss-Laguerre quadrature of order n can be performed to evaluate the integral, Eq. (1), when $\tau_\lambda \to \infty$. This method is much faster than a detailed integration along the discretized ray, because it uses only the value of the source function at n depth points weighted with n predetermined weights. This method is reliable as long as the source function is sufficiently smooth along the optical depth scale, and is well known at the quadrature points. This is not always the case in our simulations, where the optical depth scale may jump by large amounts between 2 successive cells, e.g., from $\tau = 1$ to $\tau = 300$ for extreme cases. The source function must then be interpolated at intermediate optical depths, and the result is largely dependent on the way this interpolation is performed. We note however that this is also the case for a detailed integration, where too large jumps in the source function or optical depth scale will cause uncertainties in the resulting intensity. We checked for differences between a Gauss-Laguerre quadrature and a detailed summation of the contributions from all cells, with different kinds of interpolations, and found differences in intensities emerging from a single ray of less than 10% on average, although there were some extreme cases that reached more than 100% because of a particularly significant illconditioning of the source function. The average differences were within an acceptable range, we therefore rely on the Gauss-Laguerre quadrature, with a linear interpolation of the source function on the logarithmic τ-scale. The quadrature points and weights that we use are listed in Table 1 (Abramowitz & Stegun 1972). For the rays where the optical depth does not reach sufficiently high values, we complete a detailed summation of the contribution from all cells along the ray.

In practice, once the input simulation is read, OPTIM3D interpolates the opacity tables in temperature and logarithmic density for all the simulation grid points using a bi-linear interpolation. The interpolation coefficients are computed only once, and stored. Bi-linear interpolation was chosen instead of spline interpolation because: (i) spline interpolation is significantly more time consuming, and (ii) comparisons with other codes do not indicate that great improvements can be achieved using splines (see below). The logarithmic extinction coefficient is then linearly interpolated at each Doppler-shifted wavelength in each cell along the ray, and the optical depth scale along the ray is calculated. Equation (1) is then integrated, inferring the intensity emerging towards the observer at that wavelength and position. This calculation is performed for every line-of-sight that is perpendicular to the face of the computational box, for all the required wavelengths.

Comparisons with existing codes were carried out. The spectral synthesis code Turbospectrum (Plez et al. 1993; Alvarez & Plez 1998, and further improvements by Plez) was used with one-dimensional MARCS models, where the source function was very well sampled on the τ-scale. OPTIM3D computations completed with bi-linear interpolation deviate by less than 5%, and the deviation decreases to 0.2% with spline interpolation. We also checked OPTIM3D against Linfor3D (Cayrel et al. 2007 for the Non-LTE version, and[2] for the LTE version) using 3D CO^{5}BOLD local models. We compared synthetic spectra computed for three artificial iron lines (of increasing strength) centered on a laboratory wavelength of 5500 Å using the same abundances. The discrepancy between the results of the codes was less than 3% and was even less than 0.2% when a spline interpolation of the opacity tables was used in OPTIM3D (with a significant increase in the CPU time). Finally, comparisons were made with the spectral line formation code used by, e.g., Asplund (2000) for 3D local convection simulations carried out with the code by Stein & Nordlund (1998) for giant stars (Collet et al. 2007). The tests were carried out on the [OI] line at 6300.3 Å and various Fe I and Fe II lines around 5000 Å. The discrepancies between the resulting synthetic spectra were less than 2%, and became even less than 0.6% when a spline interpolation of the opacity tables is used in OPTIM3D. Thus, the interpolation is the main source of error. In conclusion, if only a few lines are computed for, e.g., accurate abundance determinations, Linfor3D or the Asplund code are superior because they mostly avoid interpolations into opacity tables. The code used by Asplund performs bi-cubic interpolations of both the continuum opacity and the individual number densities, whereas we interpolate the total opacity from all lines contributing at a given wavelength, which is in principle less accurate. Therefore, when a large wavelength range must be calculated by taking into account many molecular and atomic lines simultaneously, OPTIM3D is superior, faster choice, which still provides results with an accuracy of a few percent.

Table 1. Gauss-Laguerre quadrature weights for $n = 10$.

Abscissa	Weight
0.137793470540	3.08441115765E-01
0.729454549503	4.01119929155E-01
1.808342901740	2.18068287612E-01
3.401433697855	6.20874560987E-02
5.552496140064	9.50151697518E-03
8.330152746764	7.53008388588E-04
11.843785837900	2.82592334960E-05
16.279257831378	4.24931398496E-07
21.996585811981	1.83956482398E-09
29.920697012274	9.91182721961E-13

3. Simulated images in the H and K bands: giant convective cells

We analyze the properties of the simulations in the H and K bands, where many interferometric observations were completed, and existing interferometers, e.g., VLTI/AMBER, operate routinely. We calculated intensity maps for a series of snapshots about 23 days apart covering 3.5 years of the model described above. We used the transmission curve of the four K band filters mounted on FLUOR (Fiber Linked Unit for Optical Recombination; Coude Du Foresto et al. 1998), and the H band filter mounted on IONIC (Integrated Optics Near-infrared Interferometric Camera; Berger et al. 2003) at the IOTA

[2] http://www.aip.de/~mst/Linfor3D/linfor_3D_manual.pdf

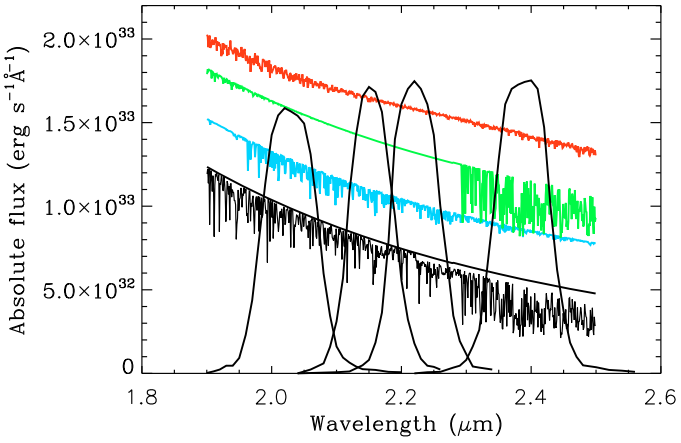

Fig. 2. The transmission curves of the 4 narrow band filters mounted on the FLUOR instrument at IOTA together with the K band synthetic spectrum of a snapshot of the simulation and the corresponding continuum (bottom black curve). From the top, the spectra computed with only H_2O (red), only CO (green), and only CN (blue) are shown with an offset of, respectively, 0.9×10^{33}, 0.6×10^{33}, and 0.3×10^{33} erg cm^{-2} s^{-1} Å^{-1}.

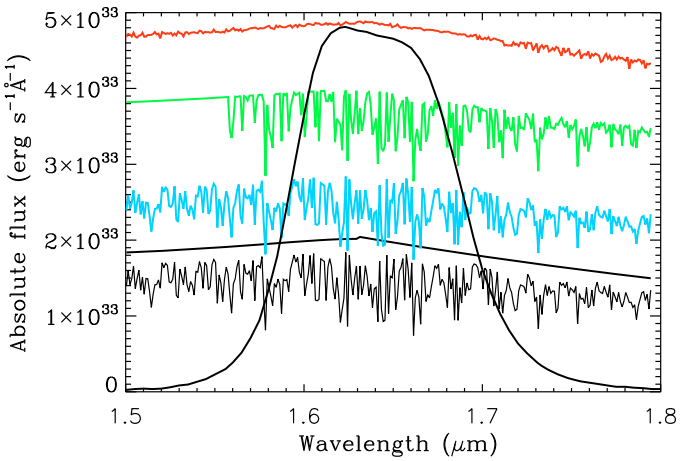

Fig. 3. The transmission curve of the filter mounted on IONIC at IOTA together with the H band synthetic spectra computed as in Fig. 2. From the top, the offset of the spectra is 3×10^{33}, 2×10^{33}, and 1×10^{33} erg cm^{-2} s^{-1} Å^{-1}.

interferometer (Traub et al. 2003). The K band filters (Fig. 2) are: K203 (with a central wavelength of 2.03 μm), K215 (2.15 μm), K222 (2.2 μm), and K239 (2.39 μm). The H band filter has a central wavelength of 1.64 μm (Fig. 3). The resulting intensities reported in this work are normalized to the filter transmission as $\frac{\int I_\lambda T(\lambda) \mathrm{d}\lambda}{\int T(\lambda) \mathrm{d}\lambda}$ where I_λ is the intensity and $T(\lambda)$ is the transmission curve of the filter at a certain wavelength. The intensity maps are showed after applying a median [3 × 3] smoothing (see Sect. 5).

It can be seen from our simulations (see Fig. 4) that the surface of the stellar model is covered by a few large convective cells of size between about 400 and 500 $R_\odot$ that evolve on a timescale of years. These cells have strong downdrafts that can penetrate to the stellar core (Freytag et al. 2002, 2009, in preparation). Close to the surface, there are short-lived (a few months to one year) small-scale (50 to 100 $R_\odot$) granules (bottom panels of Fig. 4). Freytag et al. (1997) found a relation between the mean horizontal size of convective granules $x_{\rm gran}$ and the atmospheric pressure scale-height defined as $H_{\rm p0} = \frac{kT_{\rm eff}}{g\mu m_{\rm H}}$ for GK dwarfs and subgiants. It is unclear if this relation can be extrapolated to 3D simulations of RSGs. Using it we find that $x_{\rm gran}/R_\star = 10 \times H_{\rm p0}/R_\star = 0.1$, for parameters appropriate to a RSG atmosphere dominated by gas pressure. Obviously, this leads to a size much smaller than can be seen in Fig. 4. Freytag et al. (1997) found that a value of $x_{\rm gran}/H_{\rm p0} = 10$ would fit 2D simulations for GK dwarfs and subgiants, but they also showed that A-type and F-type stars lie above the curve indicating that they have larger granules. These stars have high turbulent pressure that may dominate over the gas pressure in turbulent convective layers. Following Gustafsson et al. (2008), we write $P_{\rm turb} = \beta\rho v_{\rm turb}^2$, where $v_{\rm turb}$ is the turbulent velocity, ρ is the gas density, and β is a parameter close to one, whose value depends on the anisotropy of the velocity field. A clearer way to express $H_{\rm p0}$ is thus $H_{\rm p0} = \frac{kT_{\rm eff}}{g\mu m_{\rm H}}\left(1 + \beta\gamma(\frac{v_{\rm turb}}{c_{\rm s}})^2\right)$, where γ is the adiabatic exponent, and $c_{\rm s}$ the sound speed. If $v_{\rm turb}$ is only a factor of 2 larger than $c_{\rm s}$, $H_{\rm p0}$ is increased by a factor of about 5. This is the case for our RSG simulation, where $P_{\rm turb}/P_{\rm gas} \sim 2$ at the surface, R_*, as determined in Sect. 2.1. This implies then that $x_{\rm gran}/R_\star = 0.5$, after extrapolating Freytag et al. (1997) formula. This is more consistent with the properties of the large granules visible on intensity maps in Fig. 4. Additional mechanisms might influence the size of the granules: (i) in RSGs, most of the downdrafts will not grow fast enough to reach any significant depth before they are swept into the existing deep and strong downdrafts enhancing the strength of neighboring downdrafts; (ii) radiative effects and smoothing of small fluctuations can cause an enhancement in the growth time for small downdrafts, while the granule crossing time is short because of the large horizontal velocities; (iii) sphericity effects, see for example (Freytag & Ludwig 2007; Steffen & Freytag 2007); (iv) Freytag et al. (1997) use both the effective temperature and the pressure scale height at the bottom of the photosphere as a reference, although layers below the photosphere also matter; and (v) numerical resolution (or lack of it) could also have an effect.

4. Intensity profiles

The simulated RSG atmospheres appear very irregular both in their structure and dynamics. The surface inhomogeneities and their temporal evolution induce strong variations in the emerging spectra, and intensity profiles. In this section, we analyse the average centre-to-limb intensity profiles, and their time variations.

4.1. Surface inhomogeneities and temporal evolution

The top left panel of Fig. 5 shows a three-dimensional image representation of the intensity emerging from one face of a snapshot of the simulation in the H band. The K band appearance is similar. This image shows very sharp intensity peaks, two to three pixels wide. This is also evident in the top right panel of the figure as small bright (up to 40% brighter than the surrounding points) patches. These patches reflect the ill-conditioning of the source function, because of a lack of spatial resolution around $\tau_\lambda = 1$ along some lines of sight, where the source function may have a significant discontinuity (see Sect. 2.2). Attempts were made to solve this problem by interpolating the source function and opacity inside CO^{5}BOLD, although this led to numerical instabilities. The only possible solution is to increase the number of grid points, which would require larger and faster computers.

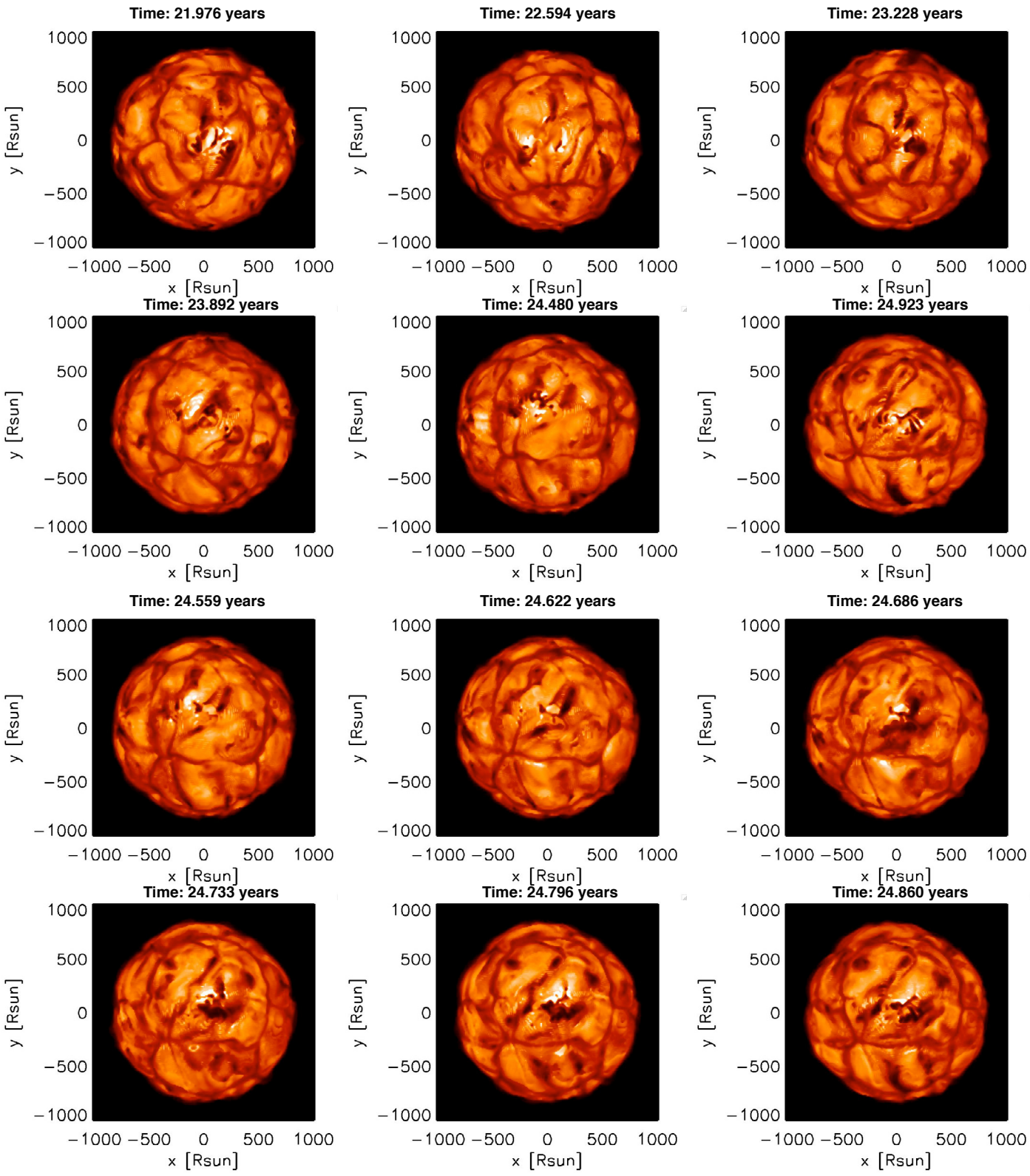

Fig. 4. *Top 6 panels*: maps of the intensity in the IONIC filter (linear scale with a range of $[0;2.5 \times 10^5]$ erg cm^{-2} s^{-1} Å^{-1}). The different panels correspond to snapshots separated by 230 days (~3.5 years covered). *Bottom 6 panels*: successive snapshots separated by 23 days (~140 days covered).

Radial intensity profiles within a given snapshot exhibit large variations with position angle in their radial extension of about 10% (see bottom left panel of Fig. 5). The variation with time in the intensity profiles are of the same order of magnitude (10%, see bottom right panel of figure).

4.2. The limb darkening law

Despite the large azimuthal variations in the intensity profiles, and their temporal variations, it is interesting to derive radially averaged intensity profiles for each snapshot. These may be be

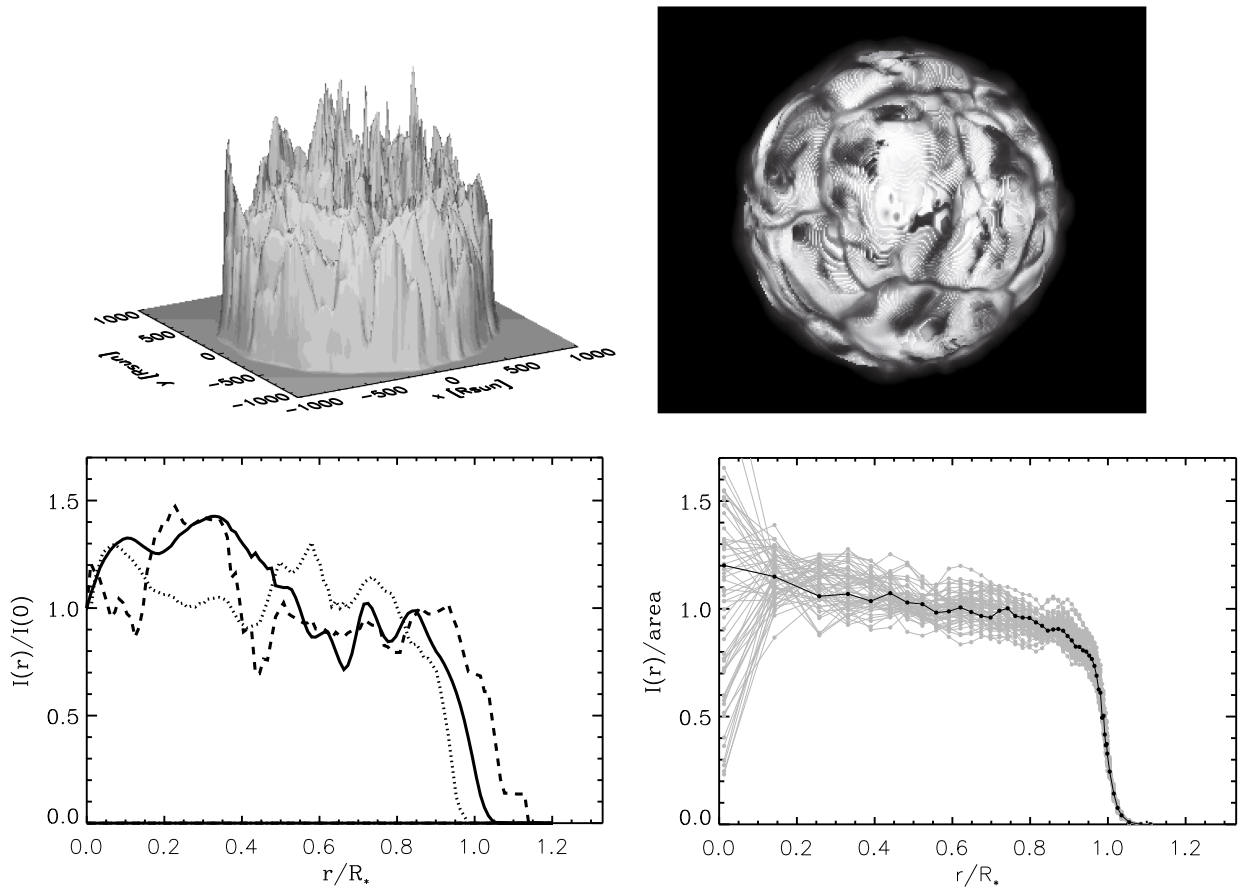

Fig. 5. *Top left panel*: three-dimensional image of a snapshot from Fig. 4. *Top right panel*: intensity map of the same snapshot represented using the histogram equalization algorithm to underline the thin bright patches because of the undersampling of the τ scale. *Bottom left panel*: intensity profiles for three position angles of the same snapshot. The numerical box edge is at impact parameter $r/R_\star \sim 1.3$. The intensity is normalized to the intensity at disk center. *Bottom right panel*: radially averaged intensity profiles for all the snapshots of the simulation (grey); one snapshot of the simulation is emphasized with a solid black line. The intensity is normalized to the area subtended by the curve, area $= \int_0^{1.3} I\,(r/R_\star)\,\mathrm{d}r/R_\star$.

used, e.g., as a first approximation when interpreting interferometric observations, instead of limb-darkening (LD) laws computed from hydrostatic models (Claret 2000). The bottom right panel of Fig. 5 shows all the radially averaged intensity profiles obtained from the simulation.

We use a LD law of the form

$$\frac{I(\mu)}{I(1)} = \sum_{k=0}^{3} a_k\,(1-\mu)^k\,, \tag{2}$$

where $I(\mu)$ is the intensity, a_k are the LD coefficients, and $\mu = \cos\theta$, where θ is the angle between the line of sight and the radial direction. μ is related to the impact parameter $r/R_\star$ by means of $r/R_\star = \sqrt{1-\mu^2}$, where $R_\star$ is the stellar radius determined as Sect. 2.1. The average intensity profiles were constructed by using rings regularly spaced in μ for $\mu \leq 1$ (i.e., $r/R_\star \leq 1$), and adding a few points for $r > R_\star$ up to the numerical box limit. The standard deviation of the average intensity, $\sigma_{I(\mu)}$, was computed within each ring. There is a small tail at $r > R_\star$, which provides a minor contribution to the total flux (less than 1%, see bottom right panel of Fig. 5), and cannot be fitted with Eq. (2). We fitted the radially averaged profiles of all the snapshots of the simulation (57 profiles, 23 days apart covering 3.5 years). The fit was weighted by $1/\sigma_{I(\mu)}$ to decrease the importance of central points with poor statistics. The fit was first made to $I(\mu)/I_{\rm norm}$, where $I_{\rm norm}$ the intensity normalized to the area subtended by the curve: $I_{\rm norm} = \frac{I(r/R_\star)}{\int_0^{1.3} I(r/R_\star)\mathrm{d}r/R_\star}$. This was done to diminish the impact of intensity fluctuations between snapshots on the fitting coefficients.

Table 2. Time-averaged limb-darkening coefficients for the RHD simulation.

λ (μm)	a_0	σ (%)	a_1	σ (%)	a_2	σ (%)	a_3	σ (%)
1.64[a]	1.00	5	–0.93	50	2.03	50	–1.98	55
2.22[b]	1.00	5	–0.85	50	2.12	45	–2.13	45

[a] central wavelength of the corresponding *IONIC* filter;
[b] central wavelength of the corresponding *K222-FLUOR* filter.
(see Eq. (2), where σ is the standard deviation over time (57 profiles covering 3.5 years)).

In Table 2, we present the values of the four LD coefficients averaged over all 3.5 years, renormalized to the disk center, for both the IONIC *H*-band filter, and the K222 filter (because the sensitivity of the FLUOR instrument is always superior in the continuum than in the molecular bands (Perrin et al. 2004b), and it samples the maximum transmission region of the *K* band). Figure 6 shows an example of a LD fit. The intensity profiles for different position angles in the same snapshot are very different (see Fig. 5, bottom left panel), the fitting coefficients having large scatter. The time averaged LD fits provides, however,

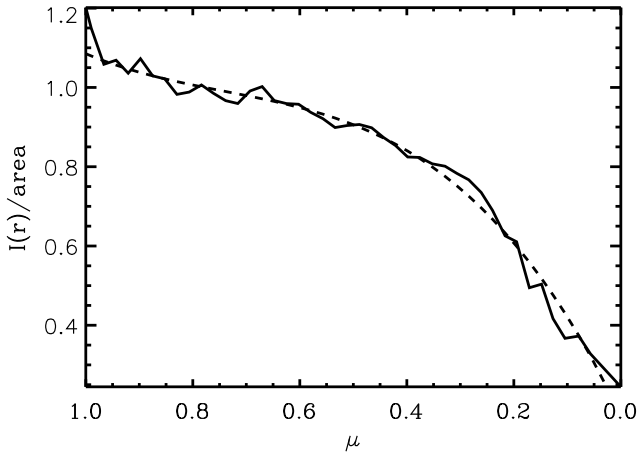

Fig. 6. Example of a LD fit (dashed line) using the LD law described in the text for the radially averaged intensity profile (solid line) emphasized in Fig. 5 (bottom right panel). The intensity is normalized to the area subtended by the curve. This best-fit model has a $\chi^2 = 0.02$.

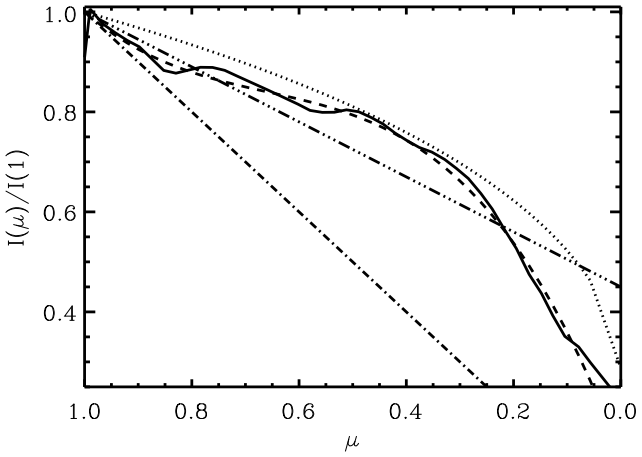

Fig. 7. The time-averaged H-band radial intensity profile of our simulation (solid line), and the fit of Table 2 (dashed line). A fully LD (dash-dotted line), a partially LD (triple dot-dashed line), and a LD fit from Claret (2000, dotted line) for comparable RSG parameters are plotted for comparison.

an indication of the shape of the intensity profile in the H and K bands (we note that they are very similar). They differ of course very much from simple first order LD laws. They also differ from LD laws calculated by Claret (2000) for parameters appropriate to RSGs (see Fig. 7). When comparing with observations of RSGs, we recommend the use of our fits. Ideally, one should use single snapshots, as we do below in our analysis of Betelgeuse, because they may deviate from the average LD fit by large amounts (see Table 2).

5. Visibility curves and phases

The granulation pattern has a significant impact on the interferometric visibility curves and phases. We attempted here to derive their characteristic signature.

5.1. Computation

We computed visibilities and phases using the IDL data visualization and analysis platform. For each image, a discrete Fourier

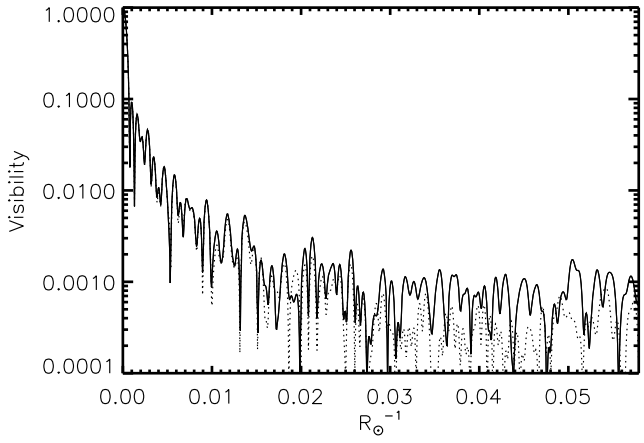

Fig. 8. The solid line is the visibility curve for the IONIC filter intensity map of Fig. 5 (top right). The dotted line is computed for the same map after applying a [3 × 3] median smoothing.

transform was calculated. To reduce the problems caused by the finite size of the object and avoid edge effects, the resolution in the Fourier plane was increased by resampling the input 235 × 235 pixel image to a grid size of 2048 × 2048 pixels. The visibility V was defined as the modulus $|z|$ of the complex Fourier transform, $z = x + iy$, normalized to the modulus at the origin of the frequency plane, $|z_0|$, with the phase $\tan\theta = \Im(z)/\Re(z)$. When dealing with observations, the natural spatial frequency (ν) unit is arcsec^{-1}. Since we study theoretical models, we instead use $R_\odot^{-1}$ units. The conversion factor between these is

$$\nu\,[\mathrm{arcsec}^{-1}] = \nu\,[R_\odot^{-1}] \cdot d\,[\mathrm{pc}] \cdot 214.9, \quad (3)$$

where 214.9 is the astronomical unit expressed in solar radii, and d is the distance of the observed star. The relation between the baseline, B (in m), of an interferometer, and the spatial frequency ν (in arcsec^{-1}) observed at a wavelength λ (in μm) is $\nu = B/\lambda/0.206265$. Since our calculated images are affected by source function discontinuities, we investigated how the visibility curves are affected by the resulting bright spikes (Fig. 5). In Fig. 8, we compare the visibility curves computed for one projected baseline from the raw image, and after applying a median [3×3] smoothing that effectively erases the artifacts. The visibility curves are affected by these artifacts mostly for frequencies higher than 0.03 $R_\odot^{-1}$ (corresponding to 33 $R_\odot$, i.e., ∼4 pixels). We can therefore apply this cosmetic median filter, because it will not affect the visibilities at lower frequencies, which are the only ones observable in practice with modern interferometers.

We now study the first few lobes of the visibility curves of our simulations, and how they are affected by asymmetries and surface structure.

5.2. The first lobe

The first lobe of the visibility curve is mostly sensitive to the radial extension of the observed source. Figure 9 (bottom panel) shows the visibility curves computed for 36 different angles from the intensity map of one snapshot in the IONIC filter (top panel). A dispersion of the visibility curves (thin grey lines in Fig. 9) is noticeable. This behavior is similar for all the snapshots. These synthetic visibilities have been compared with a uniform disk (UD) model (solid line in Fig. 9), and with limb-darkened (LD) models. We use both a fully limb-darkened disk ($I_\mu/I_1 = \mu$, dotted-dashed line in the figure), and a partially limb-darkened

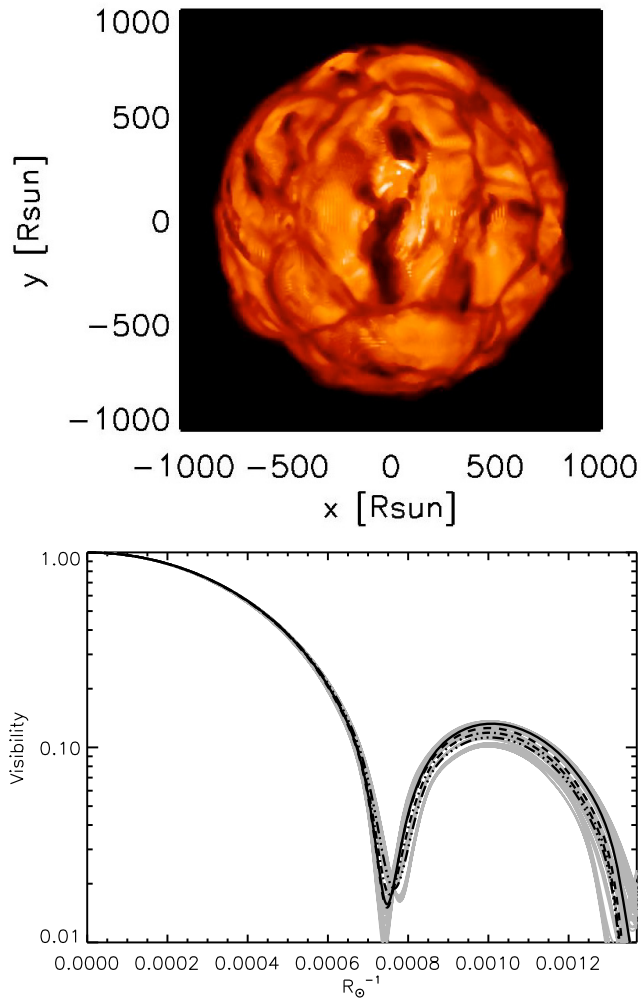

Fig. 9. *Top panel*: intensity map in the IONIC filter (the range is [0; 2.5×10^5] erg cm^{-2} s^{-1} Å^{-1}). *Bottom panel*: visibility curves from the above snapshot computed for 36 different angles, 5° apart (thin grey lines). Note the logarithm visibility scale. The solid black curve is a UD model, with a radius of 810 $R_\odot$. The dashed black line is a partially LD disk with a radius of 822 $R_\odot$. The dot-dashed line is a fully LD disk with a radius of 830 $R_\odot$. the triple-dot-dashed line is our average LD law (cf. Table 2) for a radius of 842 $R_\odot$. The stellar parameters of this snapshot are: $L = 98\,400\,L_\odot$, $R_* = 836.5\,R_\odot$, $T_{\rm eff} = 3534$ K, and $\log g = -0.34$.

model with $a_1 = -0.5$ ($I_\mu/I_1 = 0.5 + 0.5 \cdot \mu$, dashed line in the figure). The radius determined by fitting a UD disk model to the computed visibilities ranges from 794 to 845 $R_\odot$ for the 36 angles, and is up to 5% smaller than $R_\star = 836.5\,R_\odot$, the radius of the simulation determined as described in Sect. 2.1. The partially-, and fully-darkened models are respectively ∼2%, and only ∼1% smaller than $R_\star$. In Fig. 9, we also show the visibility amplitude resulting from our average LD fit of Table 2. The resulting diameter is then 842 $R_\odot$, very close to the simulation radius. We note, that Nardetto et al. (2006) also found that the UD radius is about 4 to 5% smaller than the photospheric radius in their simulation of Cepheids, and that the LD radius is much closer to the radius of their simulation. Stellar diameters determined with UD or LD fits to the observed first visibility lobe of RSGs will be affected by these systematic errors. As shown below, observations of higher spatial frequencies will greatly improve the knowledge of both limb-darkening and asymmetries, thus helping the radius to be more tightly constrained.

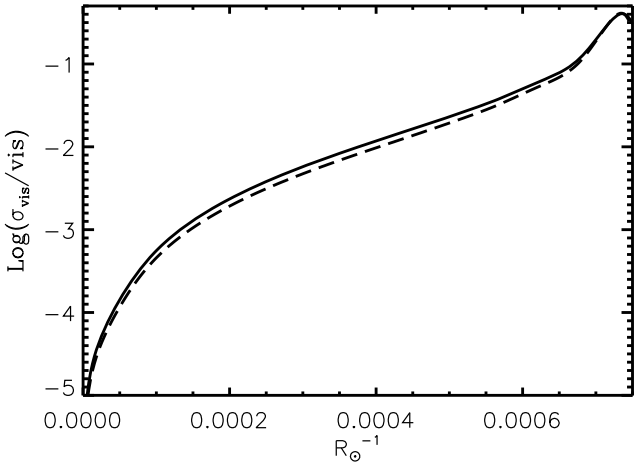

Fig. 10. Standard deviation of the visibility normalized to the visibility in the first lobe. The solid line indicates the temporal fluctuations for one fixed angle over 3.5 years. The trend is similar for all other angles. The dashed curve corresponds to the angular fluctuations of the snapshot in Fig. 9.

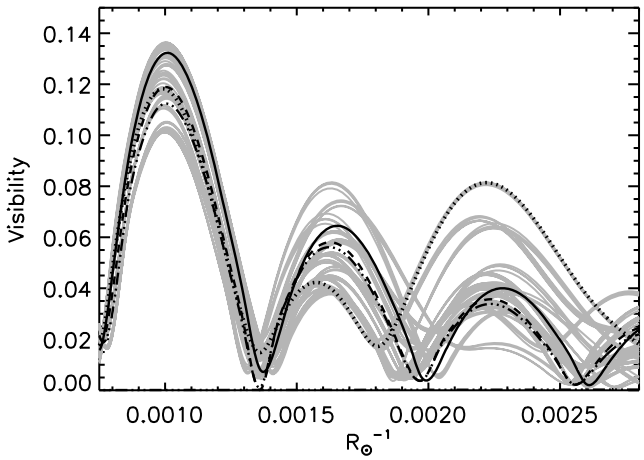

Fig. 11. Same as Fig. 9 for the second, third, and fourth lobes. In addition, the dotted line is the visibility curve for the particular azimuth parallel to the x-axis of the IONIC intensity map of Fig. 9.

It is interesting to compare the angular and temporal visibility fluctuations at one standard deviation, defined as $F = \sigma_{\rm vis}/{\rm vis}$, where vis is the visibility: (i) the *temporal evolution*, fixing one angle and following the RHD simulation for 3.5 years with a time-step of ∼23 days; (ii) the *angular evolution*, considering a single snapshot and computing the visibilities for 36 different angles 5° apart. In the first lobe, Fig. 10 shows that temporal and angular fluctuations have the same order of magnitude. The fluctuations are less than 1% at frequency ∼0.00040 $R_\odot^{-1}$ (at this frequency, the visibility is greater than 50%), they are ∼3% at frequency 0.00057 $R_\odot^{-1}$, and are close to ∼10% at 0.00069 $R_\odot^{-1}$.

5.3. The second, third, and fourth lobes: signature of convection

As in Sect. 5.2, we analyze the angular and temporal visibility fluctuations at one sigma with respect to the average value in the H band (IONIC filter). Figure 11 shows an enlargement of the second, third, and fourth lobes of the visibility curves computed for different position angles. The dispersion clearly increases with spatial frequency, and visibilities deviate significantly from

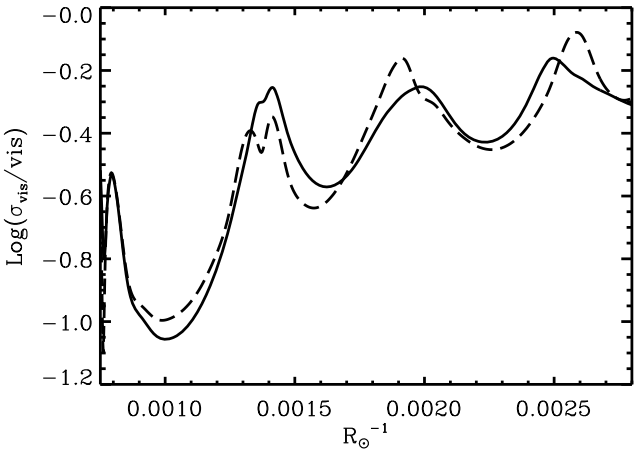

Fig. 12. Same as Fig. 10 for the second, third, and fourth lobe.

the UD or LD cases, because of the small scale structure in the model stellar disk. The same is true for temporal fluctuations of the visibility at a given position angle. Figure 12 shows the temporal fluctuations of the visibilities for one fixed position angle, as well as the angular fluctuations for the snapshot of Fig. 9. As for the first lobe, there is no clear distinction between angular and temporal fluctuations. Relative fluctuations are of course large around the minima of visibility, where visibilities are also more difficult to measure. However, with the precision of current interferometers (e.g., 1% for visibilities of ∼5–10% for VLTI-AMBER), it should be possible to characterize the granulation pattern of RSGs. This requires observing the third and the fourth lobes and not limiting the observation at the first and second lobes, which only provide information about the radius and LD. The signal to be expected in these lobes is higher than the UD or LD predictions (see dashed line in Fig. 11). Efforts should therefore be directed toward observing at these frequencies.

It may however be that approximations in our model (e.g., limited spatial resolution, grey radiative transfer) significantly affect the intensity contrast of the granulation. The radiation transfer in our RHD models indeed uses a frequency-independent grey treatment to speed up the calculations. This approximation leads to errors in the mean temperature structure within the optically thin layers that are difficult to quantify. The implementation of non-grey opacities can decrease the temperature fluctuations compared to the grey case (e.g., Ludwig et al. 1994, for local RHD models). As a consequence, the intensity contrast will decrease, reducing the visibility fluctuations. To investigate its impact on visibilities, we artificially decrease the intensity contrast in one of our images, and use the snapshot with its nominal intensities as reference. We first fit a LD law (as in Sect. 4) to the radially average intensity profile. After subtracting this average profile from the intensity map, we obtain the fluctuations caused by granulation, and measure the contrast $C_{\rm ref}=\frac{I_{\rm max}-I_{\rm min}}{I_{\rm max}+I_{\rm min}}$. It is then easy to scale this contrast before again adding the LD profile, to produce a reduced contrast image. An example of the resulting intensities is shown in Fig. 13 (top row). With a contrast of only 1% with respect to the nominal value, small surface structures are hardly visible. As previously, we determine $\sigma_{\rm vis}$/vis for all the images with various contrasts, around the top of the second (∼0.0010 $R_\odot^{-1}$), third (∼0.0016 $R_\odot^{-1}$), and fourth lobes (∼0.0022 $R_\odot^{-1}$). The bottom left panel of Fig. 13 shows that when the contrast is reduced, and the surface structures fade, the resulting visibility fluctuations similarly decrease in all the lobes (almost in proportion to the intensity contrast decrease). Reducing the contrast of course brings the visibility curves towards the visibility of the LD profile (Fig. 13, bottom right panel). This proportionality can be used to determine the granulation contrast from observations of the visibility fluctuations with time or position angle.

5.4. Importance of spectral resolution in interferometry: the H and K bands

Interferometric observations completed with a broad-band filter combine information about the lines and continuum. Higher spectral resolution allows us to recover for more information, about both visibility moduli and phases. The VLTI-AMBER interferometer provides spectral resolutions of R = 35, 1500, and 12 000. To illustrates the differences between these resolutions, we compute intensity maps around the CO first overtone line at 23041.75 Å ($\log(gf)$ = −5.527 and $\chi_{\rm ex}$ = 0.180 eV) for the three resolutions (Fig. 14). The resulting images are shown in the central row of the figure, and the spectrum in the top row. The contrast, defined as in the previous section, is similar for the low and medium resolution images but is ∼30% lower in the high resolution image, at the CO line wavelength. Large fluctuations are visible in all lobes, but they are smaller than those seen in the H band *IONIC* filter (see Fig. 12). The visibility fluctuations in the high spectral resolution image of the CO line are larger (second, third, and fourth lobes; see dotted line in bottom panel), in spite of a lower intensity contrast, presumably because of the darkening of large patches of the simulated stellar surface.

We also computed wavelength-dependent visibility curves in the H band for the high and medium VLTI-AMBER resolutions. Figure 15 displays a three-dimensional view of the visibility curves with a resolution of 12 000 and 1500 (top panels). The simulated star was scaled to an apparent diameter of ∼43.6 mas (the observed diameter of α Ori, Perrin et al. 2004a). The displacement of the zeropoints with wavelength is easily seen, as well as the amplitude variations in the higher frequency lobes.

To simulate differential observations with an interferometer at medium and high spectral resolution, in Fig. 15, we also show the variation in the visibility modulus with wavelength for a fixed baseline (15 m, i.e., in the second lobe, at ν = 45 arcsec^{-1}). The visibility shows variations related to the flux spectrum, which decreases in absorption lines. At these wavelengths, wiggles and dark spots appear on intensity maps (Fig. 14, central right panel) increasing the visibility signal at frequencies higher than the second lobe. The visibility variations are attenuated significantly at lower spectral resolution. Observations at wavelengths of a spectral line and the nearby continuum probe different atmospheric depths, and thus layers at different temperatures. They thus provide important information about the wavelength dependence of limb darkening. Since the horizontal temperature and density fluctuations depend on the atmospheric depth, differential observations with relative phase determination provide unique constraints on the granulation pattern. The visibility variations in Fig. 15, such as the steep visibility jump from 0.123 to 0.107 between 1.5975 and 1.5980 μm, could be measured in differential interferometric mode at high spectral resolution with the current precision of VLTI-AMBER (1% for visibilities of ∼5–10%), with optimal sky conditions.

5.5. Closure phase: departure from circular symmetry

Since terrestrial atmospheric turbulence affects the phases of the complex visibilities with random errors, it is impossible to derive

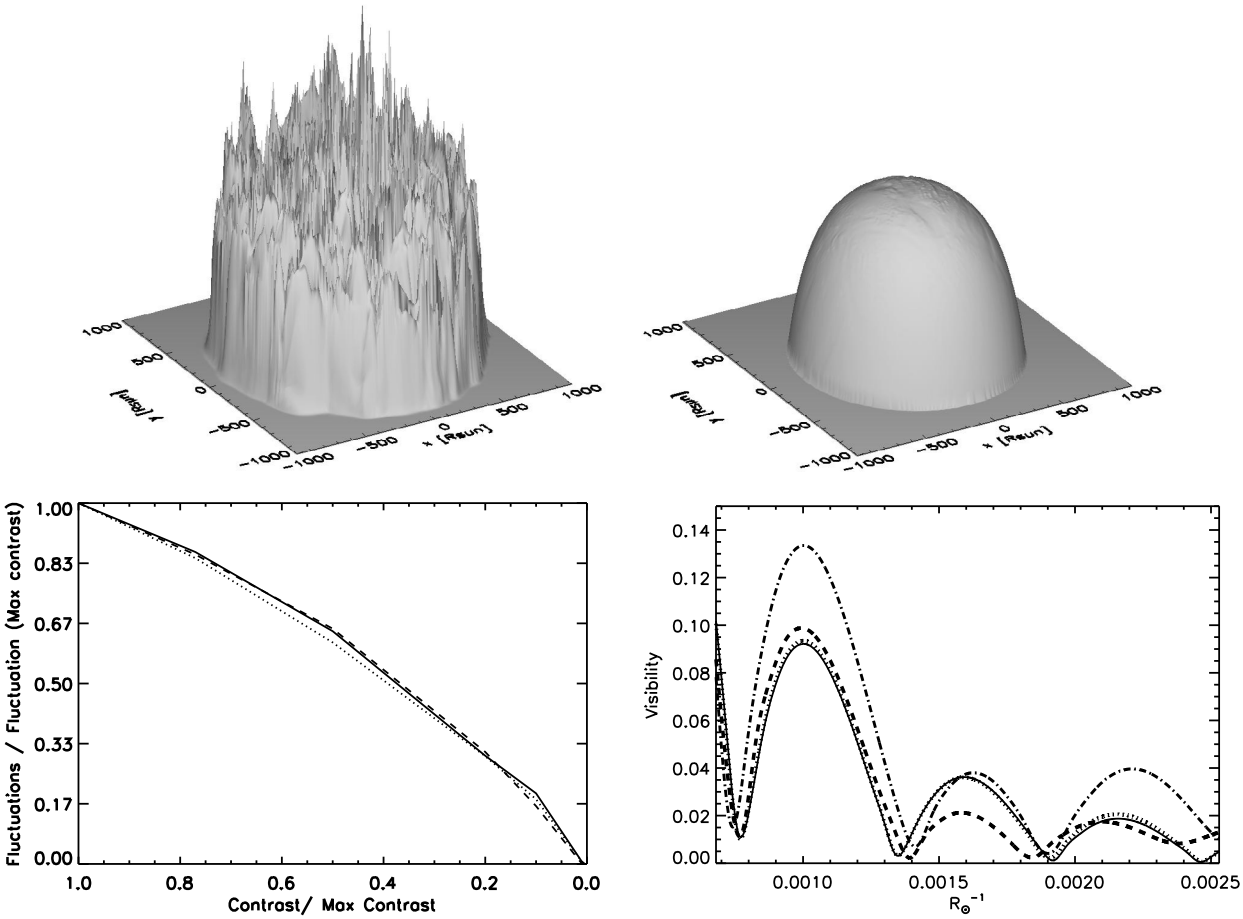

Fig. 13. *Top left panel*: three-dimensional image of a snapshot with nominal intensities. *Top right panel*: same snapshot with a feature contrast reduced to 1%. *Bottom left panel*: standard deviation of the visibility curves at 36 angles 5°) apart, for decreasing feature contrast. Solid line is for the top of the second lobe (~0.0010 $R_{\odot}^{-1}$), dashed line is for the top of the third lobe (~0.0016 $R_{\odot}^{-1}$), and dotted line is for the top of the fourth lobe (~0.0022 $R_{\odot}^{-1}$). *Bottom right panel*: visibility in the second, third, and fourth lobes for one particular position angle. The dot-dashed line shows the original simulation contrast. The dashed line, and the dotted line show the visibility with a feature contrast reduced to 50%, and 1% respectively. The solid line is the fitted LD profile computed for this snapshot.

them for individual pairs of telescopes. One instead uses closure phase between three telescopes, because the sum of all phase differences removes the atmospheric contribution,but not the phase information of the object visibility (see e.g., Monnier 2007). The closure phase is thus an important complementary piece of information, which can detect asymmetries in the RSG atmospheres. Figure 16 shows the scatter plot of the closure phase of one snapshot of the RHD model computed in the IONIC filter (the scatter is similar for the K222 filter). The behavior is similar for all snapshots. We used 500 random baseline triangles with a maximum linear extension of 40 m, and plot the closure phase as a function of the triangle maximum baseline. The closure phases deviate from zero or $\pm\pi$ already at ~10 m (0.0008 $R_{\odot}^{-1}$, if we scale the model to an apparent diameter of 43.6 mas at a distance of 174.3 pc). At higher baselines, it clearly differs from zero or $\pm\pi$, values that are indicating of a point symmetric brightness distribution. This is a clear signature of surface inhomogenities. The characteristic size distribution on the stellar surface can also be derived from the closure phase: the contribution of small-scale convection-related surface structures increases with frequency. The first deviation at ~0.0008 $R_{\odot}^{-1}$ (just beyond the first zero, see Fig. 11) corresponds to the deviation of the stellar disk from circular symmetry. It may be very efficient to constrain the level of asymmetry of RSG atmospheres by accumulating statistics on closure phase at short and long baselines, since they are easily measured to high precision. A small departure from zero immediately inters a departure from symmetry.

We also computed the closure phase for the different K band VLTI-AMBER spectral resolution intensity maps of Fig. 14. The large deviations from circular symmetry are already noticeable at low spectral resolution (Fig. 17, left panels) and the closure phase scatter does not differ much from that at high spectral resolution (right panel). This provides the possibility of detecting asymmetries caused by granulation without being compelled to observe at high spectral resolution.

6. Comparison with interferometric observations of α Ori

A preliminary comparison of our model predictions with true observations is possible for α Ori. We compare the synthetic visibilities derived from our RHD simulations in the continuum filter K222 (Fig. 2) with the observation of α Ori by Perrin et al. (2004a) that reach the third lobe in the K band. The absolute model dimensions were scaled to match the interferometric observation in the first lobe. This corresponds to an apparent diameter of 43.6 mas at a distance of 179 pc. These values agree with those of Perrin et al., who found a diameter of 43.64 ± 0.10 mas, and Harper et al. (2008), who reported a distance of 197 ± 45 pc.

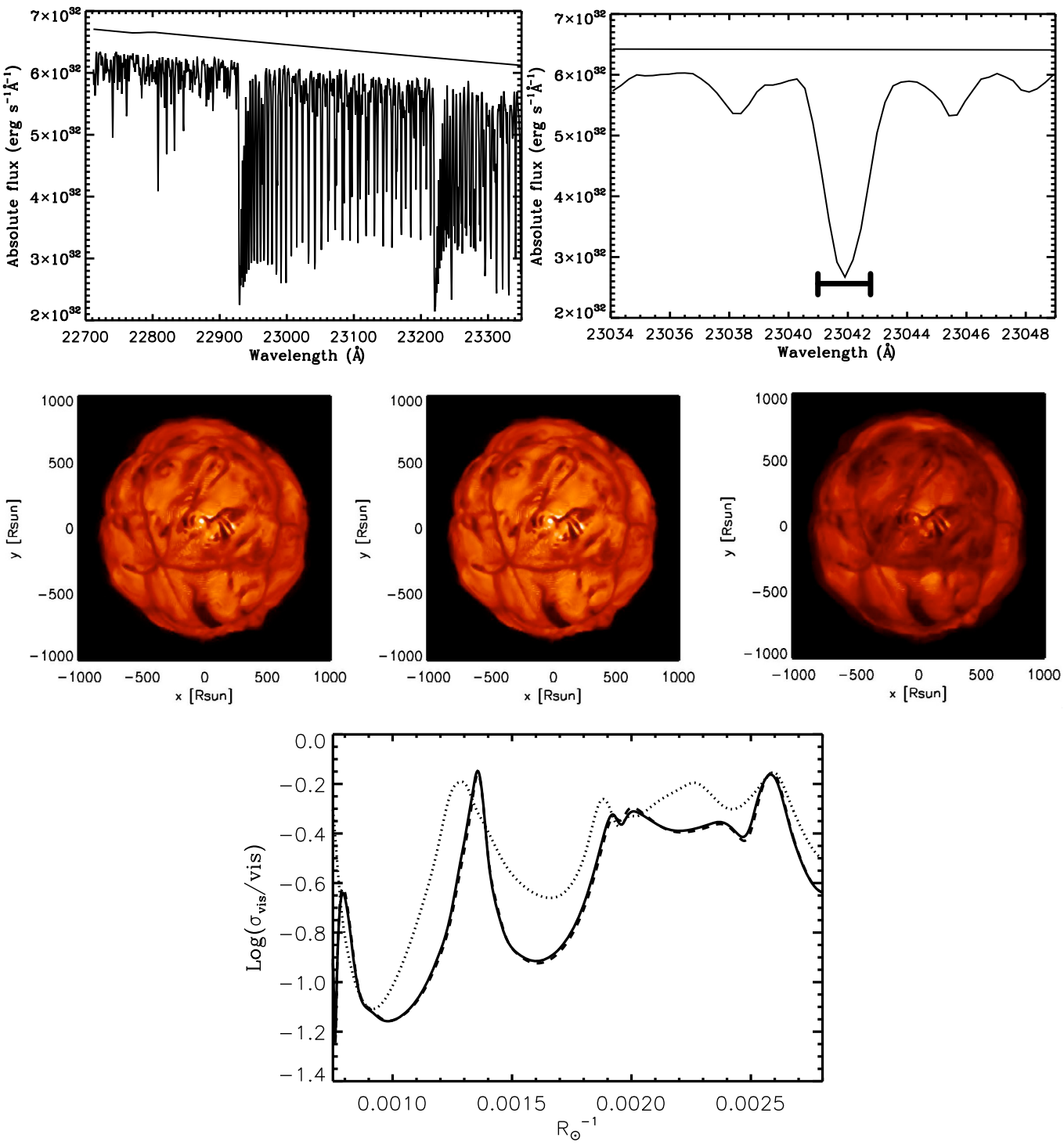

Fig. 14. *Top row*: synthetic spectrum centered on the CO first overtone band head. *The left panel* shows the range of wavelengths spanned by one resolution element at the VLTI-AMBER low spectral resolution of 35. *The right panel* shows the same for the VLTI-AMBER medium spectral resolution of 1500, and the high spectral resolution of 12 000 (thick mark). *Central row*: intensity maps for those three spectral resolution elements. The intensity range is $[0;10^5]$ erg cm^{-2} s^{-1} Å^{-1}. *Bottom row*: standard deviation of the visibility in the second, third, and fourth lobes. Solid and dashed lines correspond to low and medium resolution, respectively, and the dotted line to high resolution.

We computed over 2000 visibility curves and we found that the data can be described by visibility fluctuations caused by the granulation of the simulation (Fig. 18), as already shown in Chiavassa et al. (2007). Among this large number of visibility curves, we find some that match all the observational datapoints with greater accuracy than the uniform disk (with a diameter of 43.33 mas; Perrin et al. 2004a), or limb-darkened disk model (linear-limb darkening law, $I(\mu) = 1 - a(1-\mu)$, with a diameter of 43.64 mas and $a = 0.09$ also in Perrin et al., see Fig. 18). The best-fit model solution corresponded to a reduced $\chi^2 = 0.21$, and all the visibility curves fall within a χ^2 range of [0.21, 18.1]. Our RHD simulations represent a great improvement over parametric models (the UD model with reduced $\chi^2 = 19.9$, and the LD model with $\chi^2 = 22.3$) when interpreting these interferometric

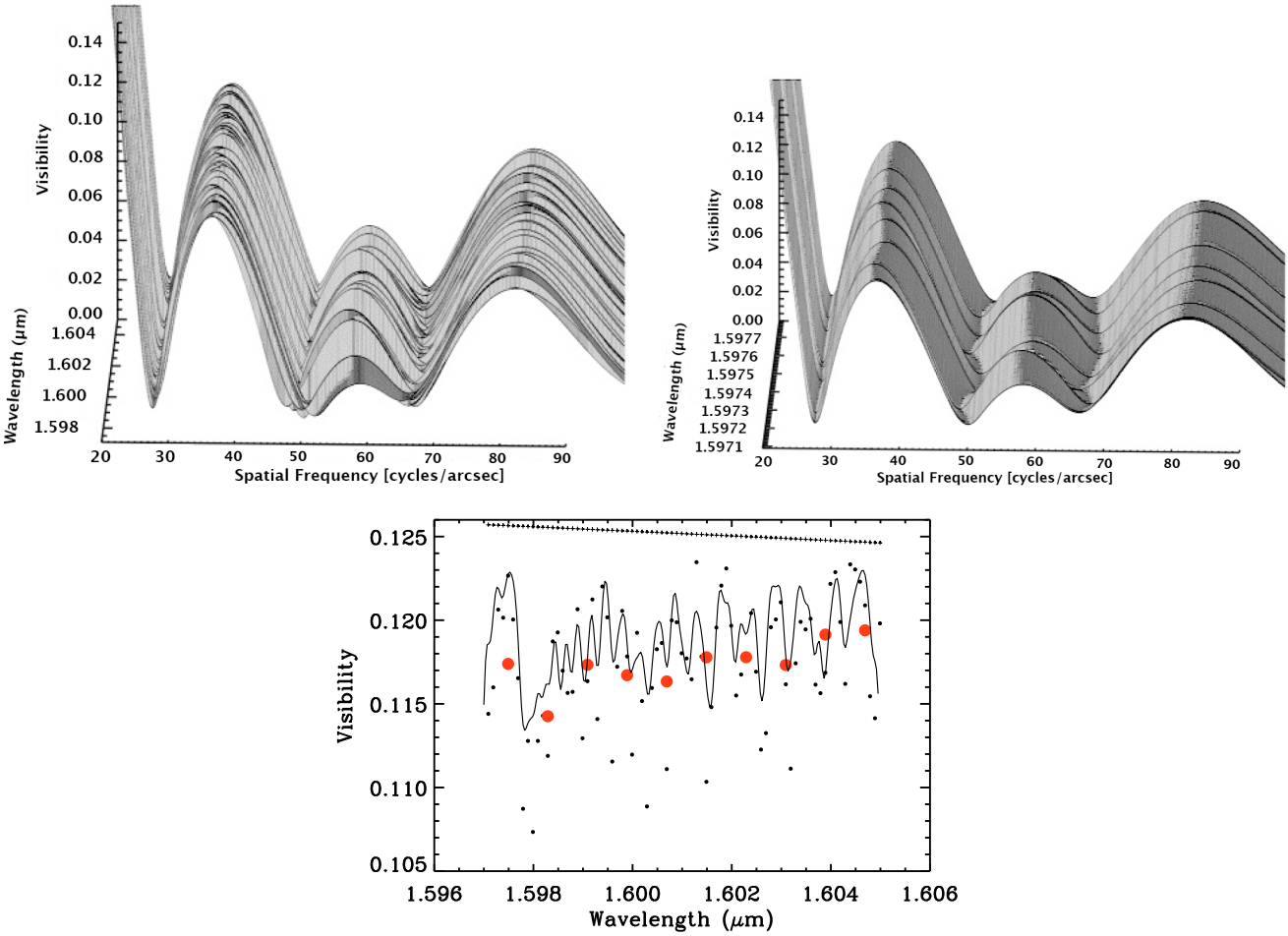

Fig. 15. *Top left panel*: three-dimensional view of the visibility curves as a function of wavelength for a particular position angle. The spectral resolution is 12 000. *Top right panel*: same as in top left panel at a spectral resolution of 1 500. *Bottom panel*: visibility as a function of wavelength for a baseline of ∼15 m, i.e., the top of the second lobe, at one particular position angle. The simulation has been scaled to an apparent diameter of ∼43.6 mas. The synthetic spectrum convolved to a resolution of 12 000 is overplotted (thin solid line). The small black dots correspond to the highest resolution with AMBER (12 000), while the large red dots correspond to medium resolution (1500). The crosses show the uniform disk of 43.6 mas. When changing the position angle, the expected standard deviation is about 10% of the visibility (see Fig. 12).

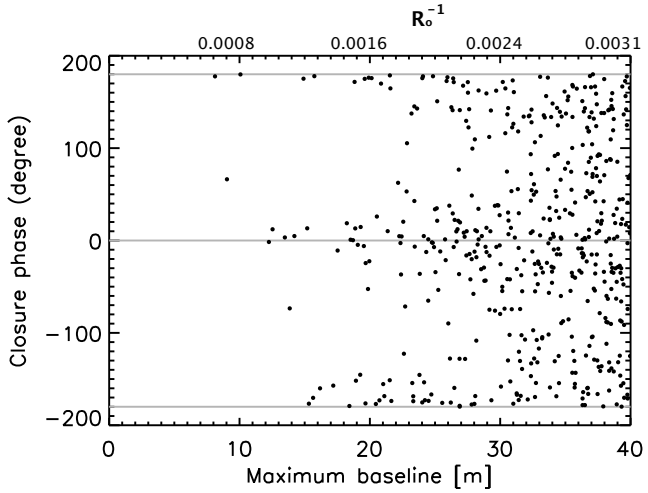

Fig. 16. Scatter plot of closure phases in the IONIC filter centered on 1.64 μm of 500 random baseline triangles with a maximum linear extension of 40 m. Closure phases are plotted against the longest baseline of the triangle. The upper x-axis corresponds to synthetic observations of the simulation at an apparent diameter of 43.6 mas (which corresponds to α Ori at a distance of 174.3 pc). The axisymmetric case is represented by the grey lines.

observations. The observation datapoints in the first, second, and third lobes can be reproduced by a single visibility curve, from the projection at a particular position angle of one of our snapshots (see Fig. 18). There is one observed point in the first lobe at 24.5 arcsec^{-1} that is difficult to reproduce. Adjustments to the absolute model dimensions of the star required to reproduce this datapoint, would lead to mismatch of the other observations at higher frequencies. However, this may be a problem when calibrating the observation.

A more detailed comparison with α Ori data in the H band (Haubois et al. 2006) will be presented in a forthcoming paper (Chiavassa et al. 2009, in prep.)

7. Conclusions

Our radiation hydrodynamical simulations have confirmed that only a few large granules cover the surfaces of RSG stars. The granules in the simulation that we analyze here are 400–500 $R_\odot$ in diameter, and have lifetimes of years. Smaller scale structures develop and evolve within these large granules, on shorter timescales (of a month).

We have demonstrated that RHD simulations are essential to a proper quantitative analysis of interferometric observations

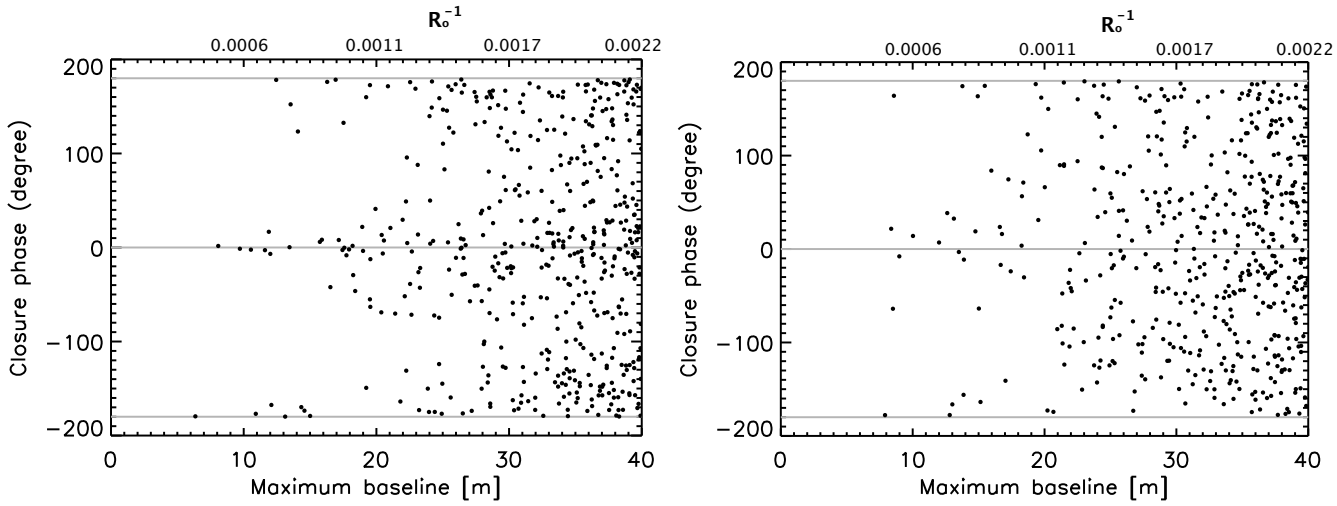

Fig. 17. Scatter plot of closure phases (cf. Fig. 16 for details) obtained from the VLTI-AMBER *K* band low, and high spectral resolution intensity maps (Fig. 14, central left, and right panels).

of the surface of RSGs beyond the smooth, symmetrical, limb-darkened intensity profiles. We present new average limb darkening coefficients within the *H* and *K* bands, which differ significantly from those commonly used in UD or LD profiles. However, these LD coefficients fluctuate with time, and the average is only indicative. Our model surface granulation causes angular and temporal variations in both visibility amplitudes and phases. In the first lobe, which is sensitive to radius, fluctuations can be as high as 5%, and radii determinations can be affected to this extent: the radius determined with a UD fit is 3–5% smaller than the radius of the simulation, while the radius determined with a fully LD model is 1% smaller.

The second, third, and fourth lobes, which carry a signature of both limb-darkening and smaller scale structure, are very different from the simple LD case. The visibility amplitudes can be greater than the UD or LD case, and closure phases differ significantly from 0 and $\pm\pi$, because of a departure from circular symmetry. The visibilities also show fluctuations with both position angle and time, which are directly related to the granulation contrast. We also want to emphasize that data at high spectral resolution provides extremely valuable information. The stellar surface differs dramatically between images of absorption line and its nearby continuum, and differential observations should be easier to carry out with high precision. At lower resolution (e.g. $R = 1500$), continuum and line information become mixed and there is a considerable loss of differential signal.

We conclude that the detection of the signature of granulation, as predicted by our simulation, is measurable with todays interferometers, if observations of both amplitude and closure phase are made at high spatial frequencies (second, third, and fourth lobes, or even higher if possible). These observations will provide direct information about the timescale of the variation, and the size and contrast of granulation.

A few RSGs are prime targets for interferometry, because of their large diameter, proximity, and high infrared luminosity. Only 4 or 5 are sufficiently close and bright for imaging to be possible, but a larger number (10–20) are within reach of less ambitious programs, such as closure phase measurements.

Three approaches can be combined to characterize the granulation pattern by

- searching for angular visibility variations, observing with the same telescope configuration (covering high spatial frequencies) and using the Earth's rotation to study 6–7 different position angles in one night, should be sufficient, if measurement errors can be kept below 10%, for visibilities of the order of between 5 and 10%. One or two other telescope configurations would provide more frequency points, but the change of configuration would then have to be made within days, which is possible at VLTI;
- looking for temporal visibility fluctuations by observing at two (preferably more) epochs ∼1 month apart with the same telescope configuration. This can easily be scheduled with existing interferometers, such as CHARA or the VLTI;
- looking for visibilities as a function of wavelength, at high spectral resolution, in different spectral regions belonging to both spectral features and continuum. If measurement errors can be kept close to 1%, for visibility of the order of ∼10%, variations in the visibility correlated with the flux spectrum could be detected, indicating variations in the radius, the limb-darkening, or the granulation pattern. These relative measurements are more easily completed at the required precision than absolute visibility measurements.

These observations provide a wealth of information about both the stars and our RHD models. which we know are affected by the limitations. Comparisons with observations will help us decide which approximations must be relaxed. The simulations are primarily constrained by execution time, which requires several approximations, the most important ones being the limited spatial resolution and the complete lack of wavelength resolution, i.e., grey radiative transfer. This speeds up the simulations to managable execution times of between several months and one year of intensive calculations for about seven years of stellar time. A higher numerical resolution shows smaller scale structures appearing within the granules that are already present in lower resolution simulations (Chiavassa et al. 2006, Fig. 10). However, this should not affect the first few visibility lobes.

The approximation of grey radiative transfer is only justified in the stellar interior and is inappropriate in the optically thin layers. The implementation of non-grey opacities (e.g., five wavelength groups employed to describe the wavelength dependency of the radiation field within a multigroup radiative transfer scheme, see Nordlund 1982, for details) would provide an important improvement to the hydrodynamical simulations. For local RHD simulations, Ludwig et al. (1994) found that

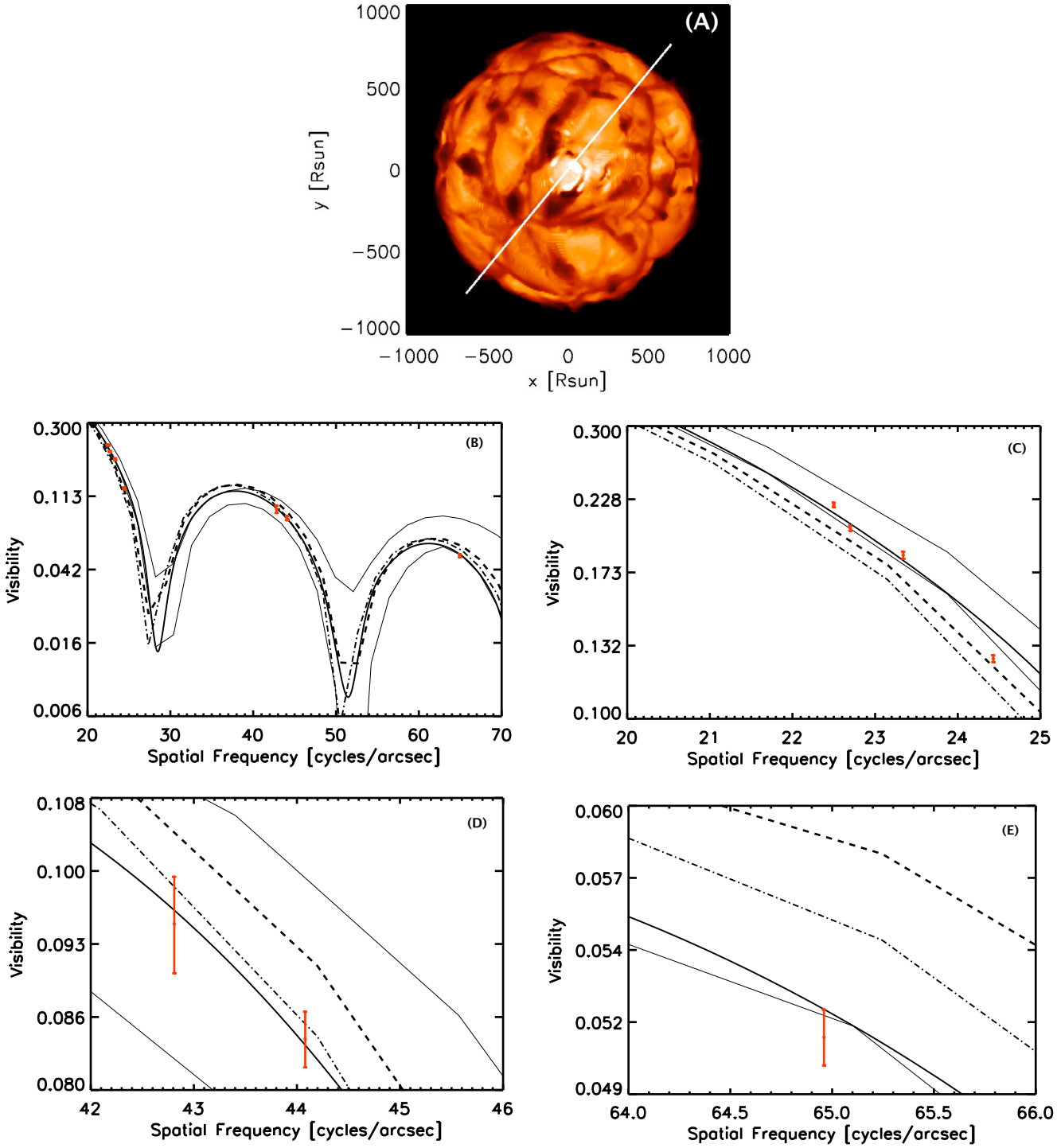

Fig. 18. Comparison of the RHD simulation with the α Ori observations (red dots with error bars) by Perrin et al. (2004a). *Top panel*: intensity map in the K222-FLUOR filter of the snapshot that most closely matches the interferometric data. The range is $[0; 10^5]$ erg cm^{-2} s^{-1} Å^{-1}. The stellar parameters of this snapshot are: $L = 93\,480\,L_\odot$, $R = 833\,R_\odot$, $T_{\rm eff} = 3497$ K, and log $g = -0.34$. The simulation has been scaled to an apparent diameter of 43.6 mas at a distance of 179 pc. The white line indicates the position angle of the projected baselines. *Other panels*: synthetic visibilities from the simulation, compared with observations. Panel B covers the entire observational range, and panels C-E are close-ups of clusters of observations. The thick, solid line corresponds to the most closely matching visibility curve(reduced $\chi^2 = 0.21$). The thin solid lines show the minimum and maximum extent of variations in the visibilities. The dot-dashed, and the dashed lines are the LD, and the UD models used by Perrin et al. (reduced $\chi^2 = 22.3$, and 19.9). Note the logarithmic visibility scale.

frequency-dependent radiative transfer causes an intensified heat exchange of a fluid element with its environment, which tends to reduce the temperature differences. Consequently, the temperature fluctuations in the non-grey local models are smaller than in the grey case. This is also expected for global RSG models, and the result of such a decrease in the temperature fluctuations, would be a decrease in both the intensity contrast and the visibility fluctuations.

Acknowledgements. This project was supported by the French Ministry of Higher Education through an ACI (PhD fellowship of Andrea Chiavassa, postdoc

fellowship of Bernd Freytag, and computational resources). Present support is ensured by a grant from ANR (ANR-06-BLAN-0105). We are also grateful to the PNPS and CNRS for their financial support through the years. We thank the CINES for providing some of the computational resources necessary for this work. We thank Michel Belmas and Philippe Falandry for their help. Part of this work was made while BPz was on sabbatical at Uppsala Astronomical Observatory. We thank Bengt Gustafsson, Hans-Gunter Ludwig, John Monnier, Martin Asplund, Nik Piskunov, and Nils Ryde for enlightening discussions.

References

Abramowitz, M., & Stegun, I. A. 1972, Handbook of mathematical functions, 9th edn. (New York: Dover publications, INC.)
Alvarez, R., & Plez, B. 1998, A&A, 330, 1109
Asplund, M. 2000, A&A, 359, 755
Asplund, M., Grevesse, N., & Sauval, A. J. 2006, Commun. Asteroseismol., 147, 76
Berger, J.-P., Haguenauer, P., Kern, P. Y., et al. 2003, in Interferometry for Optical Astronomy II, ed. W. A. Traub. Proc. SPIE, 4838, 1099
Carr, J. S., Sellgren, K., & Balachandran, S. C. 2000, ApJ, 530, 307
Cayrel, R., Steffen, M., Chand, H., et al. 2007, A&A, 473, L37
Chiavassa, A., Plez, B., Josselin, E., & Freytag, B. 2006, in EAS Publ. Ser. 18, ed. P. Stee, 177
Chiavassa, A., Plez, B., Josselin, E., & Freytag, B. 2007, in SF2A-2007: Proceedings of the Annual meeting of the French Society of Astronomy and Astrophysics held in Grenoble, France, ed. J. Bouvier, A. Chalabaev, & C. Charbonnel, 447
Claret, A. 2000, A&A, 363, 1081
Collet, R., Asplund, M., & Trampedach, R. 2007, A&A, 469, 687
Coude Du Foresto, V., Perrin, G., Ruilier, C., et al. 1998, in Astronomical Interferometry, ed. R. D. Reasenberg, Proc. SPIE, 350, 856
Cunha, K., Sellgren, K., Smith, V. V., et al. 2007, ApJ, 669, 1011
Cuntz, M. 1997, A&A, 325, 709
Freytag, B., & Höfner, S. 2008, A&A, 483, 571
Freytag, B., & Ludwig, H.-G. 2007, in SF2A-2007: Proceedings of the Annual meeting of the French Society of Astronomy and Astrophysics held in Grenoble, France, ed. J. Bouvier, A. Chalabaev, & C. Charbonnel, 481
Freytag, B., Holweger, H., Steffen, M., & Ludwig, H.-G. 1997, in Science with the VLT Interferometer, ed. F. Paresce, 316
Freytag, B., Steffen, M., & Dorch, B. 2002, Astron. Nachr., 323, 213
Gray, D. F. 2008, AJ, 135, 1450
Gustafsson, B., Edvardsson, B., Eriksson, K., et al. 2008, A&A, 486, 951
Harper, G. M., Brown, A., & Guinan, E. F. 2008, AJ, 135, 1430
Hartmann, L., & Avrett, E. H. 1984, ApJ, 284, 238
Haubois, X., Perrin, G., Lacour, S., et al. 2006, in SF2A-2006: Semaine de l'Astrophysique Française, ed. D. Barret, F. Casoli, G. Lagache, A. Lecavelier, & L. Pagani, 471
Hauschildt, P. H., Baron, E., & Allard, F. 1997, ApJ, 483, 390
Iglesias, C. A., Rogers, F. J., & Wilson, B. G. 1992, ApJ, 397, 717
Josselin, E., & Plez, B. 2007, A&A, 469, 671
Levesque, E. M., Massey, P., Olsen, K. A. G., et al. 2005, ApJ, 628, 973
Levesque, E. M., Massey, P., Olsen, K. A. G., et al. 2006, ApJ, 645, 1102
Levesque, E. M., Massey, P., Olsen, K. A. G., & Plez, B. 2007, ApJ, 667, 202
Ludwig, H.-G., Jordan, S., & Steffen, M. 1994, A&A, 284, 105
Massey, P., Levesque, E. M., Olsen, K. A. G., Plez, B., & Skiff, B. A. 2007, ApJ, 660, 301
Monnier, J. D. 2007, New Astron. Rev., 51, 604
Nardetto, N., Fokin, A., Mourard, D., & Mathias, P. 2006, A&A, 454, 327
Nordlund, A. 1982, A&A, 107, 1
Perrin, G., Ridgway, S. T., Coudé du Foresto, V., et al. 2004a, A&A, 418, 675
Perrin, G., Ridgway, S. T., Mennesson, B., et al. 2004b, A&A, 426, 279
Pijpers, F. P., & Hearn, A. G. 1989, A&A, 209, 198
Plez, B., Smith, V. V., & Lambert, D. L. 1993, ApJ, 418, 812
Steffen, M., & Freytag, B. 2007, Astron. Nachr., 328, 1054
Stein, R. F., & Nordlund, A. 1998, ApJ, 499, 914
Traub, W. A., Ahearn, A., Carleton, N. P., et al. 2003, in Interferometry for Optical Astronomy II, ed. W. A. Traub, Proc SPIE, 4838, 45

2

A journey cross Hertzsprung-Russel diagram

THERE are a few hundred billion stars in our Galaxy, and billions of galaxies in the Universe. One important technique in science is to try and sort/classify things into groups and seek out trends or patterns. This is done using stars. These can be plotted to form what is one of the most useful plots for stellar astronomy, the Hertzsprung-Russell (or H-R) diagram. Hertzsprung (Hertzsprung 1905) and later independently Russell (Russell 1919) realized that the knowledge of the absolute brightness of stars together with their spectral type or surface temperature allowed fundamentally different types of stars to be distinguished. Both astronomers already realized that the apparent stellar brightness was insufficient to draw conclusions, and that the absolute magnitude (i.e., distance) was a crucial need to properly order the stars in the H-R diagram. They also pointed out that the diagram contains important information about the stellar radii, with the giant sequence to be found at a larger brightness but similar surface temperatures to the cools stars of the dwarf or main sequence. Underlining a clear link with the qualitative determination of a stellar radius using the Stefan-Boltzmann law. The H-R diagram is an essential diagnostic diagram for stellar structure and evolution, which has now been in use for more than 100 years (Nielsen 1964).

The H-R diagram is an essential diagnostic diagram

With the advent of stellar model atmospheres, it has been possible to calculate accurately the surface gravity, e.g. Auer & Mihalas (1972) , that allowed to order the stars in the surface gravity-effective temperature (i.e., Kiel diagram). The main advantage of this digram is that stars can be compared to stellar evolution predictions without prior knowledge of their distances, e.g., a first example is in Kudritzki (1976). However, the comparison is often negatively affected by the relatively large uncertainties of the spectroscopic gravity determinations. In addition to this, the ra-

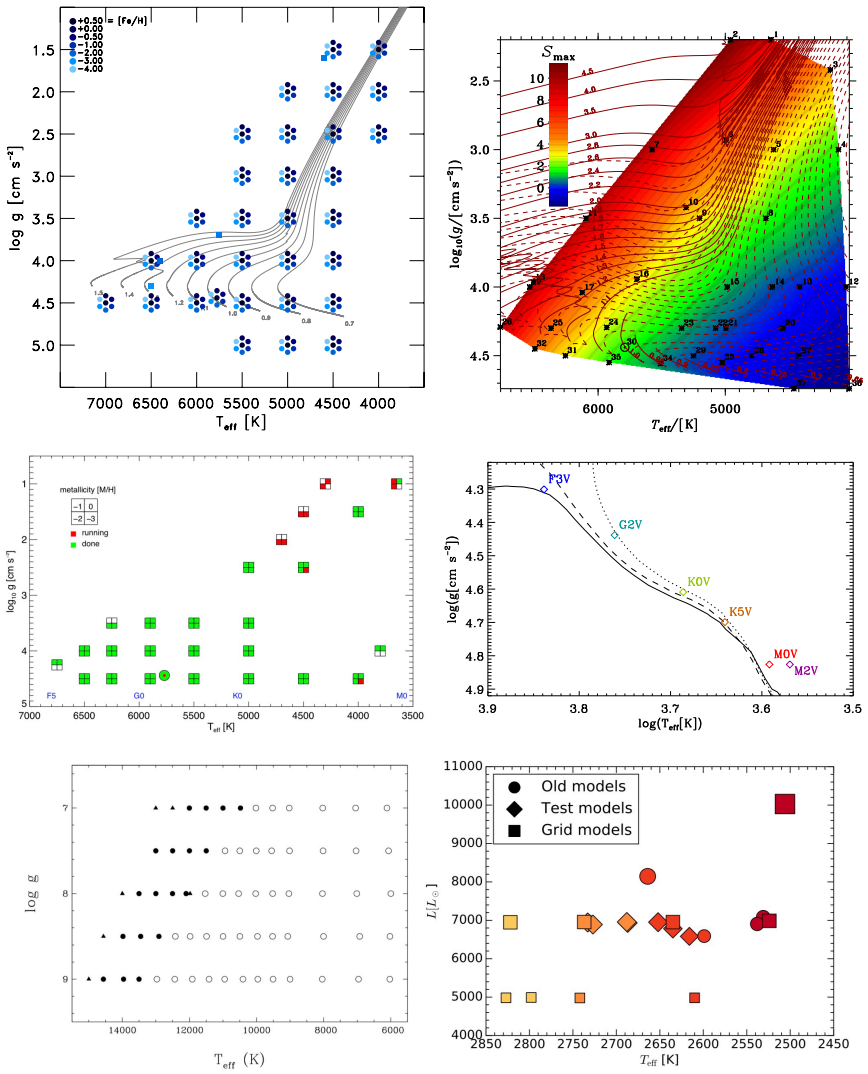

Figure 2.1: 3D RHD simulation-grid in the H-R diagram. *Top panels:* simulations computed with Stagger-code or similar branches (Section 1.3), Stagger-grid (left, Magic et al. 2013b) and "Trampedach" grid (right, Trampedach et al. 2013). *Central panels:* the CIFIST grid (left, (Ludwig et al. 2009) computed with CO^{5}BOLD code, and the grid (right, Beeck et al. 2013) computed with MURaM core (Vögler et al. 2005). *Bottom panels:* the White Dwarf grid (left, Tremblay et al. 2013b) and the AGB one (right, Freytag et al. 2017) computed with CO^{5}BOLD code (Section 1.3).

dius or any other stellar parameters cannot be directly retrieved from this approach

and other technique are needed, e.g., interferometry (Kervella et al. 2004) and asteroseismology (Stello et al. 2009).

3D RHD simulations of cool stars across the H-R diagram

In recent years, with increased computational power, it has been possible to compute grids of 3D RHD simulations (Section 1.3) covering largely the H-R diagram. Fig. 2.1 displays how the different codes available attack this problem. The computational time required for each simulation varies largely with stellar parameters, the numerical resolution, the physical ingredients included, the numerical approaches and the directive of parallelization taken into account. For a detailed comparison between the different codes, the reader may refer to Beeck et al. (2012). All these grids are constantly developing and some of the figures displayed may be out of date. Grids with limited number of simulations exist for particular stars: e.g., Cepheids stars (Vasilyev et al. 2017) , Red Supergiant stars (Chiavassa et al. 2011b), M-dwarf (Wedemeyer et al. 2013), Brown dwarf (Allard et al. 2013).

2.1 Main Sequence stars up to RGB phase

I START the review of my results with main sequence stars. In 2013, I participated in the publication of the Stagger-grid (Magic et al. 2013b). This grid is intended for various applications in addition to stellar convection studies and atmospheres themselves, including stellar parameter determination, stellar spectroscopy and abundance analysis, asteroseismology, calibration of stellar evolution models, interferometry, and characterisation of extrasolar planets. The surface structures and dynamics of cool stars are characterised by the presence of convective motions and turbulent flows which shape the emergent spectrum and the size of granules depends on the stellar parameters of the star and, as a consequence, on the extension of their atmosphere (Fig. 2.4).

2.1.1 Stellar fundamental parameters with spectroscopy

A first application of this grid is the library of high-resolution stellar synthetic fluxes obtained from these 3D simulations (Chiavassa et al. 2018a). These spectra are calculated spectra from 1000 to 200 000 Å with a constant resolving power of $\lambda/\Delta\lambda$=20 000 (Fig. 2.2, top panels) and from 8470 and 8710 Å (Gaia Radial Velocity Spectrometer - RVS - spectral range) with a constant resolving power of $\lambda/\Delta\lambda$=300 000. I used the synthetic spectra to compute theoretical colours in the Johnson-Cousins UBV(RI)C, SDSS, 2MASS, Gaia, SkyMapper, Strömgren, and HST-WFC3 systems.

The 3D stellar synthetic grid

The synthetic magnitudes are compared with those obtained using 1D hydrostatic models. 1D versus 3D differences are limited to a small percent ($< 5\%$) except for the narrow filters that span the optical and UV region of the spectrum (up to $\approx 10\%$). All the spectra publicly available on POLLUX database[1]. 3D Bolomentric corrections are available on CDS database.

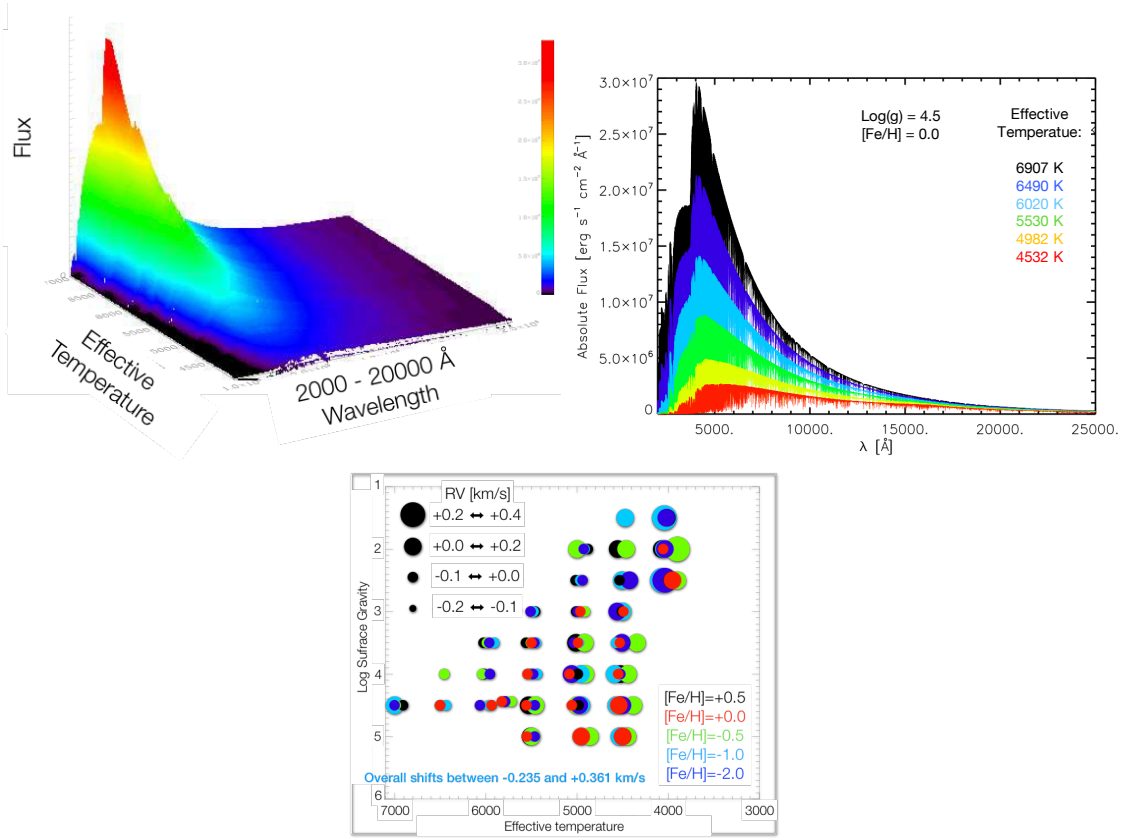

Figure 2.2: *Top left:* Surface rendering for all the synthetic spectra computed for the 3D RHD simulations (Chiavassa et al. 2018a). For clarity, the wavelength range has been reduced to 0.2 – 2.5 μm. *Top right:* Example of different spectra for RHD simulations with fixed surface gravity and metallicity, and varying effective temperature. *Bottom left*: Convective shifts predicted by the 3D RHD simulations for the Gaia RVS spectral range and the Fe I lines.

Radial velocities

Measurements of stellar radial velocities are fundamental in order to determine stellar spacevelocities. This is needed, for example to investigate the kinematic struc-

[1] http://pollux.graal.univ-montp2.fr

ture of stellar populations in the Galaxy or to monitor for radial velocity variations, either of which would point to the presence of unseen companion(s). Convection plays a crucial role in the formation of spectral lines and deeply influences the shape, shift, and asymmetries of lines in late-type stars (Asplund et al. 2000). Absorption lines may be blueshifted as a result of convective movements in the stellar atmosphere: bright and rising convective elements contribute more photons than the cool dark shrinking gas, and as a consequence, the absorption lines appear blueshifted (Dravins 1982). However, the convective line shift is not the same for all the spectral lines. Each line has a unique fingerprint in the spectrum that depends on line strength, depth, shift, width, and asymmetry across the granulation pattern depending on their height of formation and sensitivity to the atmospheric conditions. In Chiavassa et al. (2018a), we determined the convective shift (cross-correlation of each 3D spectrum with the corresponding 1D) considering only few unblended Fe I and only Ca II triplet lines in the Gaia RVS range (8470 to 8710 Å). The values for the Fe I are in the range between -0.235 and +0.361 km/s while the Ca II lines are strongly redshifted (Fig. 2.2, bottom left panel).

Despite the very recent publication in march 2018, the 3D spectral grid has been used in several works. I report here few examples:

- Maxted (2018) used the spectra from Magic et al. (2015) and Chiavassa et al. (2018a) to compute the power-2 limb-darkening for several passbands (UBVRI, CHEOPS, TESS, Kepler). He finds a very good agreement between observations (exoplanet systems and binary stars) and limb-darkening constructed on 3D intensity profiles. He proposes a new powerful analysis of light curves for transiting exoplanet systems and binary stars for stars with stellar parameters within the Stagger-grid range.

- Zwitter et al. (2018) used the spectra to extract accurate radial velocities for GALAH DR2 data release. They achieved a typical accuracy of 0.1 km/s for about 212 000 stars in the well-populated regions of the HR diagram for stars with metallicity between -0.6 and +0.3. The level of accuracy achieved is adequate for studies of dynamics within stellar clusters, associations and streams in the Galaxy.

- Gaia-DR3 release will provide accurate radial velocities from RVS. These values needs an appropriate wavelength calibration from convective shifts. This is directly processed in RVS pipeline using 3D synthetic spectra (Gaia consortium-CU6).

The paper, "The Stagger-grid: A grid of 3D stellar atmosphere models V. Synthetic stellar spectra and broad-band photometry" by Chiavassa et al. 2018, is attached at the end of the chapter..

2.1.2 Stellar fundamental parameters with interferometry

The radius of a star is not a well-defined quantity since stars are gaseous spheres and do not have a well-defined edge (Davies et al. 2013). Optical and infrared interferometry has already proven to be a powerful tool for stellar astrophysics, in particular by providing fundamental stellar parameters such as Center to limb variations (CLVs) and radius as well as masses (e.g. with CHARA interferometer Creevey et al. 2012), which are compared to predictions by models of stellar evolution and stellar atmospheres.
Interferometric observables such as CLVs and stellar radii can also be obtained by the use of 3D RHD simulations. First, one needs to have an image of the stellar disk as a nearby observer would see it as required to extract the interferometric observables. However, the computational domain of each simulation only represents a small portion of the stellar surface (Fig. 1.3). To overcome this limitation, and at the same time account for limb darkening effects (Fig. 2.3, left), we developed a technique (Chiavassa et al. 2010a) that consists into computing intensity maps for different inclinations angles (with respect to the line of sight) and tile them onto a spherical surface (Fig. 2.3, top right). In addition to this, the statistical tile-to-tile fluctuations in the number of granules and in their shape is also taken into consideration. We used this method in several papers (Chiavassa et al. 2010a, 2012, 2014, 2015, 2017a).

Procyon and RGBs' stellar fundamental parameters

I report here two results concerning the RGB stars and the sub-giant star Procyon.

- Red giant branch stars have evolved from the main sequence and are powered by hydrogen burning in a thin shell surrounding their helium core. Determine their fundamental parameters is very important because they are used as tracers of the morphology and evolution of the Galaxy in the framework of the GAIA mission and they are extensively used for spectroscopic elemental abundance analyses of distant stellar populations. In Chiavassa et al. (2010a), we provided average limb darkening coefficients for different metallicities and wavelengths ranges (Fig. 2.3, bottom right). We found that the effect of convective-related surface structures depends on metallicity and surface gravity. Finally, we estimate 3D vs 1D corrections to stellar radii determination: RHD simulations are $\sim$ 3.5% smaller to $\sim$ 1% larger in the optical than 1D, and roughly 0.5 to 1.5%

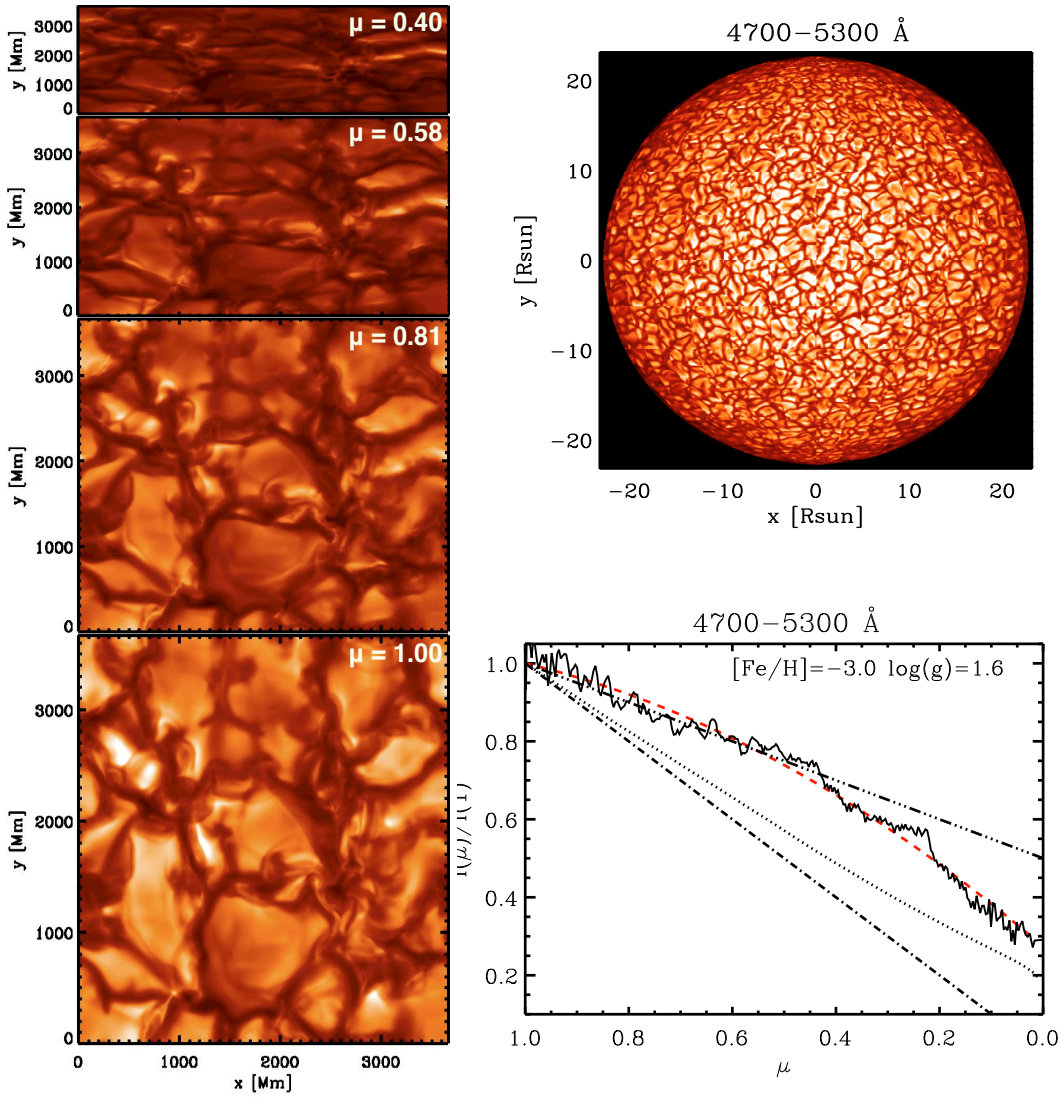

Figure 2.3: *Left:* Intensity maps at different inclined angles for a metal poor RGB star. *Top right:* Synthetic stellar disk image obtained by tiling the intensity maps (left panel) ont a spherical surface (Chiavassa et al. 2010a). *Bottom right:* CLV profiles from different models: RHD image (top right panel) azimuthal average (solid black line) with its numerical fit (red dashed line), a full limb darkened disk (dash-dotted line), and a partial limb darkened disk (triple dotted dashed line).

smaller in the IR. Even if these corrections are small, they are needed to prop-

erly set the zero point of effective temperature scale derived by interferometry and to strengthen the confidence of existing red giant catalogs of calibrating stars for interferometry.

- Procyon is one of the brightest stars in the sky and one of our nearest neighbours. It is therefore an ideal target for stellar astrophysics studies. The atmospheric parameters and the interferometric radius, which are used to define the stellar evolution model and the analysis of frequencies, depend strongly on the realism of the atmosphere and the exactness of the temperature gradient in the surface layers. In Chiavassa et al. (2012), we re-analyzed the interferometric and spectroscopic data at the different wavelengths to derive a new radius and provided limb-darkening coefficients in the optical as well as in the infrared. In addition to this, we computed also the asteroseismic radius. Eventually, we provided also the resulting effective temperature and surface gravity.

2.1.3 Granulation and interferometry

The size of the convective cells is correlated to the pressure scale height at optical-depth unity (Freytag 2001), confirmed later by Tremblay et al. (2013a). The pressure scale height is defined as

$$\mathcal{H}_{\rm p} = \frac{k_B T_{\rm eff}}{mg}, \tag{2.1}$$

where g is the surface gravity, k_B is the Boltzmann constant and m is the mean molecular mass ($m = 1.31 \times m_{\rm H} = 1.31 \times 1.67 \times 10^{-24}$ grams, for temperatures lower than 10000 K). In the above expression, $\mathcal{H}_{\rm p}$ has the dimension of length. Stars with low surface gravity have more diluted atmosphere and lower surface temperature while more compact objects are hotter. Fig. 2.4 shows the synthetic images of stars with different stellar parameters and thus different granulation pattern. Connected to this, also the turnover timescales are also related to the granulation pattern as displayed in the Figure.

Interferometric closure phases

The role of long-baseline interferometric observations is to investigate the dynamics of granulation as a function of stellar parameters: thanks to the higher angular resolution, interferometry is the ideal tool for exploring stellar convection in term of cells size, intensity contrast and temporal variations. In Chiavassa et al. (2014), we characterised the granulation on different type of stars using interferometric observables. For this purpose, we used the interferometric observable called ”closure

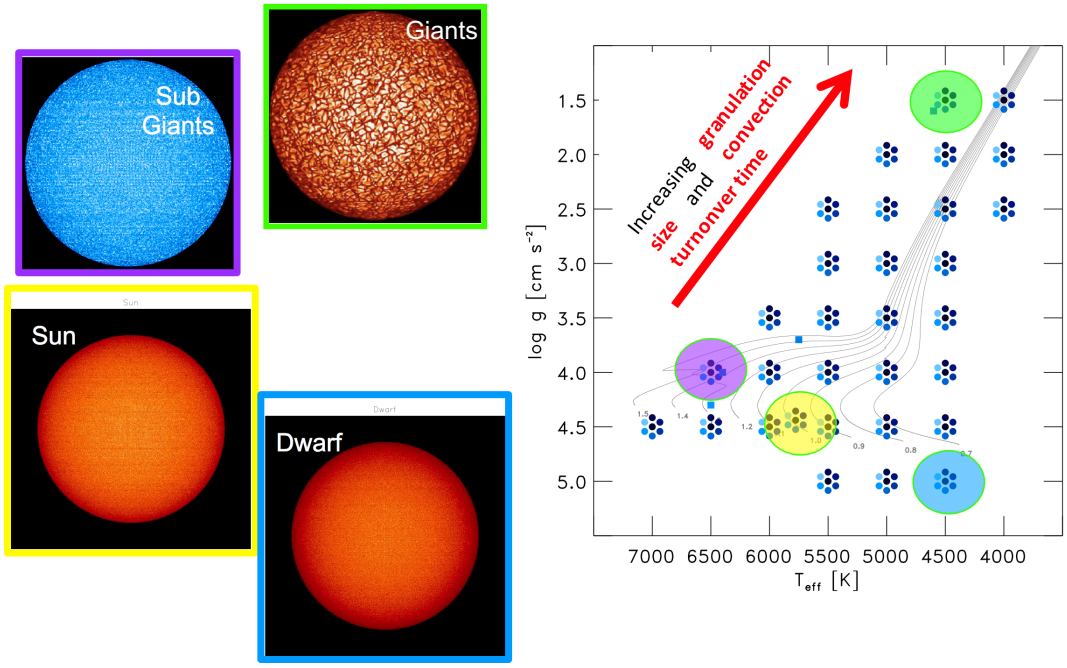

Figure 2.4: *Left:* Synthetic images of the stellar disk for some 3D RHD simulations (Chiavassa et al. 2017a, 2014, 2012, 2010a) associated with their positions in Hertzsprung-Russell diagram (*right*).

phase", which is defined as the phase of the triple product (or bispectrum) of the complex visibilities on three baselines that form a closed loop joining (at least) three stations. This procedure removes the atmospheric contribution, leaving the phase information of the object morphology unaltered (Monnier 2007). To sum up, values of closure phases different from zero° or ±180° means that the observed object is not centrosymmetric.

At the end, the characteristic size distribution on the stellar surface can be derived from the closure phase: the contribution of small-scale convection-related surface structures increases with frequency (see Section 2.2.4, Chiavassa et al. 2010b). Chiavassa et al. (2014) reported that the granulation has a very clear signature in all type stars and for different interferometric instruments depending on the wavelength range sampled and on the UV-coverage used. In particular, MIRC instrument mounted at CHARA interferometer is the most appropriate instrument because it combines good UV-plane coverage and long baselines (ie, high spatial resolving power together with very good coverage of the stellar surface). The signature of the convective-related surface structures stars to be relevant from spatial frequencies corresponding to the

third lobe (i.e., structures up to about 1/10 of the stellar radius).
The first confirmation of our predictions came with MIRC observations of three red giant branch (RGB) stars: HD 197989, HD 189276, and HD 161096. All of them with apparent radius between 2 and 4.5 mas. We detected departures from the centrosymmetric case for all three stars with the tendency of a greater effect for the stars with lower surface gravity, even though our sample is limited. This qualitatively means that the more the star evolves, the more significant the size of the granules becomes with respect to the disk size. This idea is supported by previous work showing even larger departures from centrosymmetry for very evolved stars such as AGBs (Ragland et al. 2006; Chiavassa et al. 2010c; Wittkowski et al. 2016) and RSGs (Chiavassa et al. 2010b; Montargès et al. 2018).

2.1.4 Exoplanet transits

Among the different methods used to detect exoplanets, the transit method is a very successful technique: 2487 over 3021 transit candidates have been confirmed with this technique (as of November 2018 from http://exoplanets.org, Wright et al. 2011). A transit event occurs when the planet crosses the line of sight between the star and the observer, thus occulting part of the star. This creates a periodic dip in the brightness of the star. The typical stellar light blocked is $\sim$ 1%, 0.1%, and 0.01% for Jupiter-, Neptune- and Earth-like planets transiting in front of a Sun-like star, respectively (Borucki & Summers 1984), making the detection very challenging, in particular for Earth-like planets. During the transit, the flux decrease is proportional to the squared ratio of planet and stellar radii. For sufficiently bright stars, the mass can also be measured from the host star's radial velocity semi-amplitude (Mislis et al. 2012). When the mass and radius of an exoplanet are known, its mean density can also be deduced and provide useful information for the physical formation processes. Today and in the near future, the prospects for planet detection and characterization with the transiting methods are excellent with access to a large amount of data coming, for instance, from the NASA missions Kepler (Borucki et al. 2010), TESS (Transit Exoplanet Survey Satellite, Ricker et al. 2010), and JWST[2] or from the ESA missions PLATO 2.0 (PLAnetary Transits and Oscillation of stars, Rauer et al. 2014) and CHEOPS (CHaracterizing ExOPlanet Satellite, Broeg et al. 2013).

Granulation noise in planet transits

[2]https://www.jwst.nasa.gov/

However, with improved photometric precision, additional sources of noise that are due to the presence of stellar surface inhomogeneities such as granulation, will become relevant, and the overall photometric noise will be less and less dominated by pure photon shot noise. I carried out an in-depth study of a very particular transit, that of Venus in 2004. To do this, I used the spherical tile imaging method (see Section 2.1.2, Chiavassa et al. 2010a) to construct the semi-global model of the Sun and then we modelled the light curve of the Venus transit, seen from the ACRIMSAT satellite (Fig. 2.5, top left panel), using several realizations of the solar disk (to represent the temporal variation of the granulation). Then, we compared the synthetic curves with the observations and found a very good agreement, both in terms of depth and entry/exit slopes of the transit (top right panel). In the end, the granulation pattern causes fluctuations in the transit light curve that can cause intrinsic uncertainty (due to stellar variability) on accurate measurements of transits (Chiavassa et al. 2015).
Following the method described for the transit of Venus, I evaluated the impact of granulation at different wavelengths (from optical to IR) for several planet/star systems: I simulated the transits of three prototype planets a hot Jupiter, a hot Neptune, and a terrestrial planet, orbiting around a solar and K-dwarf type stars. For the first time from the point of view of the star (Fig. 2.5, bottom panels). We demonstrated that granulation has a significant effect on the depth of the light curve during the transit, and consequently on the determination of the planetary radius (up to 0.90% and ∼0.5% for terrestrial and gaseous planets, respectively). We also showed that larger (or smaller) orbital inclination angles with respect to values corresponding to transit at the stellar center display a shallower transit depth and longer ingress and egress times, but also granulation fluctuations that are correlated to the center-to-limb variation: they increase (or decrease) the value of the inclination, which amplifies the fluctuations.

In conclusion, the granulation has to be considered as an intrinsic uncertainty (as a result of stellar variability) on the precise measurements of exoplanet transits of planets. The full characterization of the granulation is essential for determining the degree of uncertainty on the planet parameters. In this context, the use of 3D RHD simulations is important to measure the convection-related fluctuations. This can be achieved by performing precise and continuous observations of stellar photometry and radial velocity, as we explained with RHD simulations, before, after, and during the transit periods (Chiavassa et al. 2017a).

The paper, "Measuring stellar granulation during planet transits" by Chiavassa et al. 2017, is attached at the end of the chapter..

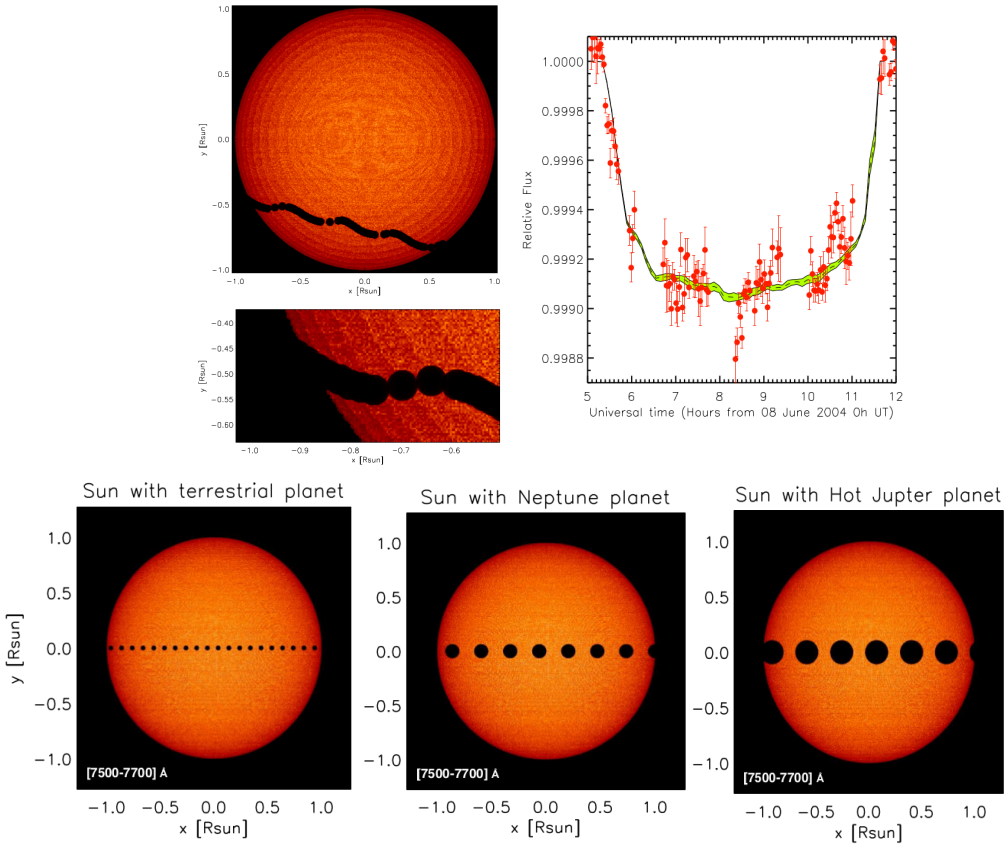

Figure 2.5: *Top left panel*: Synthetic image (with enlargement) of the solar disk in the visible and the different positions of the transit of Venus in 2004 as seen from the ACRIMSAT satellite. Venus' unusual trajectory is induced by the satellite's orbit. *Top right panel*: Light curve of the Venus transit, photometric observations are reported in red with error bars (Schneider et al. 2006), the dotted black line is the best matching curve from 3D simualtions, and the green color indicates the highest and lowest values due to the changes in granulation in the synthetic Sun (Chiavassa et al. 2015). *Bottom panels:* Synthetic transits in front of the Sun for several types of planets to study the impact of granulation on the measurement of the planetary radius (Chiavassa et al. 2017a).

2.2 Evolved cool stars

We now move to the results concerning the evolved stellar branch of the H-R diagram.

2.2.1 Let's compute a RSG simulation

In CO5BOLD (see Section 1.3), the most important parameters (Chiavassa et al. 2011b) that determine the type of the simulated star are:

- the input luminosity into the core
- the stellar mass that enters in the equation for the gravitational potential
- the abundances that are used to create the tables for the equation-of-state and the opacities.

The initial model is produced starting from a sphere in hydrostatic equilibrium with a weak velocity field inherited from a previous model with different stellar parameters (Fig. 2.6). After some time, the limb-darkened surface without any convective signature appears but with some regular patterns due to the numerical grid. The central spot, quite evident at the beginning of the simulation, vanishes completely when convection becomes strong. After several years of stellar time, a regular pattern of small-scale convection cells develops and, after cells merge the average structures, it becomes big and the regularity (due to the Cartesian grid) is lost. The intensity contrast grows with time.

Radiation transport in RHD simulations

The radiation transport for the simulations of evolved stars employs a short-characteristics method, and, to account for the short radiative time scale, several (typically 6 to 9) radiative sub−steps are performed per global step. The simulations can be computed: (i) either using a gray frequency dependance of the radiation field, which ignores the frequency dependence, based on Rosseland mean opacities calculated merging high-temperature OPAL (Iglesias et al. 1992) data and low-temperature PHOENIX (Hauschildt et al. 1997) at around 12 000K; (ii) or using a multi-group scheme (Ludwig et al. 1994; Vögler et al. 2004), where the frequencies that reach monochromatic optical depth unity within a certain depth range of the model atmosphere will be put into one frequency group. The RHD simulations employing the latter method have typically five wavelengths groups sorted according to the run of the monochromatic optical depth in a corresponding MARCS (Gustafsson et al.

2008) 1D model with a smooth transition to the Rosseland mean (OPAL opacities) in the optically thick regime.

Once the RHD simulation is relaxed, the snapshots are used for detailed post-processing treatment to extract interferometric, spectrophotometric, astrometric, and imaging observables using OPTIM3D.

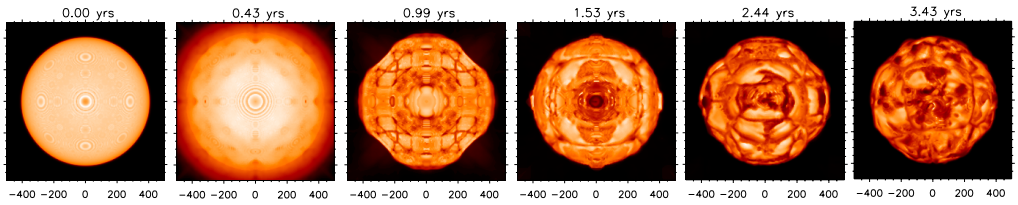

Figure 2.6: Gray intensity on one side of the computational cube from the initial sequence of a 3D RHD simulation of an RSG. The axes are in solar radii. The artifacts caused by the mismatch between the spherical object and the Cartesian grid become less evident with time passing (Chiavassa et al. 2011b).

2.2.2 Simulations characteristics and timescales

RHD simulations of evolved stars show a very heterogeneous surface caused by the dynamical granulation. The emerging intensity is related to layers where waves and shocks dominate together with the variation in opacity through the atmosphere. Small-amplitude acoustic waves are produced in the convective envelope by non-stationary convective flows with significant Mach numbers (e.g., 5 or even larger). These waves can travel outward in the convective envelope and even into the convectively stable atmosphere where they are compressed and amplified (due to the lower temperature and sound speed) and further amplified (due to the lower density). Here, they turn into shocks giving rise to a dynamical pressure larger than the gas pressure (Chiavassa et al. 2011b; Freytag et al. 2017).

RHD simulations pulsate by themselves and do not have any dynamic boundary condition, the hydrodynamical equations include the advection of momentum, which, after averaging over space and time, gives the dynamical pressure (Freytag et al. 2017). AGB models show more extend and varying structures in the near-surface than RSG (i.e., this is a consequence of the higher mass), and, convective velocities in RSGs are too low to reach escape velocity and contribute to the mass-loss mechanism. RSG and AGB simulations are both characterized by large convec-

tive cells and strong shocks, however, AGBs have in general even larger scales with shocks pushing the mass much further out.

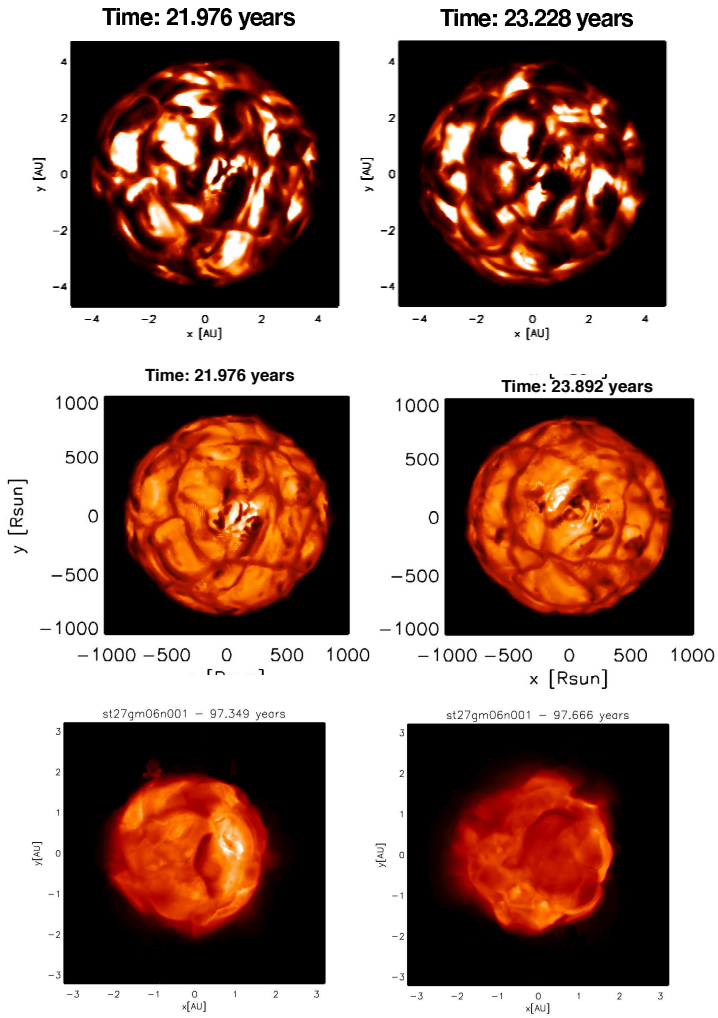

Figure 2.7: *Top panels:* Maps of the linear intensity of an RSG simulation in the Gaia *G* band (Evans et al. 2018). Each panel corresponds to a different snapshot whose time is indicated (Chiavassa et al. 2011c). *Central panels:* Maps of the linear intensity of the same simulation above but in the H band (IONIC filter, ∼1.6 μm, Chiavassa et al. 2009). *Bottom panels:* Squared root intensity maps of an AGB simulation in the Gaia *G* band (Chiavassa et al. 2018b).

Two main temporal scales depending on wavelength probed

The temporal timescales of the granulation pattern are different with respect to the spectral range probed. An example is reported in Fig. 2.7. The wavelength de-

Table 2.1: Typical stellar parameters for RHD simulations of RSG (Chiavassa et al. 2011b) and AGB (Freytag et al. 2017) stars.

Type	Numerical resolution	$M_{\rm pot}$ [$M_\odot$]	L [$L_\odot$]	$T_{\rm eff}$ [K]	
RSG	up to 401^3	5–12	≈30000–90000	≈3300–4000	
AGB	up to 401^3	1	≈5000–10000	≈2500–2900	
Type	$R_\star$ [$R_\odot$]	$\log g$ [cgs]	Rotation simulations?	Longest simulation [y]	Detected Pulsation?
RSG	≈400-900	≈−0.45 – 0.00	yes	30	not yet
AGB	≈300–550	≈−1.00 – −0.50	yes	30	yes

pendence is striking, but it is also important to note that going from the infrared to the optical, there is a relevant increase of the intensity contrast[3] as well as the number and complexity of surface structures. Concerning the timescales, the simulations are characterized by two principal characteristic time scales linked directly to the stellar dynamical effects:

- the surface is covered by a few large convective cells with a size of ≈ 60% of the stellar radius (top row of Fig. 2.7) that evolve on a time scale of years (Chiavassa et al. 2009). This is visible in the infrared, and particularly in the H band where the H^- continuous opacity minimum occurs and consequently the continuum-forming region is more evident;

- in the optical region (central and bottom row of the Figure, and Chiavassa et al. 2011c; Freytag et al. 2017; Chiavassa et al. 2018b), short-lived (a few weeks to a few months) small-scale structures appear. They result from the opacity contribution and dynamics at optical depths smaller than 1 (i.e., further up in the atmosphere with respect to the continuum-forming region), as well as from the higher sensitivity of the blackbody radiation to the temperature inhomogeneities. It must be noted that also the numerical resolution of the simulation plays a role for the size and number of these small structures.

[3]In average, the brightest areas exhibit an intensity ∼50 times or larger than the dark ones in the optical and up to ∼10 times in the infrared. Probing very narrow wavelength filters close to particular spectral line centers may increase these values.

2.2.3 Spatially unresolved surfaces: measuring convection cycles with velocity fields at high spectral resolution

RHD simulations provide a self-consistent ab-initio description of the non-thermal velocity field generated by convection, shock waves, and overshoot that manifests itself in spectral line shifts and changes in the equivalent width (Fig. 2.8, left panel). The shape of the optical Ti I line at 6261.11 Å , taken as an example here, constitutes of more than one velocity component that contributes through the different atmospheric layers where the line forms. As a consequence, the line bisector[4] is not straight and span values up to 5 km/s on a temporal scale of few weeks (as qualitatively seen in the prototypical RSG star α Ori by Gray 2008). As the vigorous convection is prominent in the emerging flux, the radial velocity measurements for evolved stars are very complex and need a sufficiently high spectral resolution to possibly disentangle all the sources of macro-turbulence.
In this context, Kateryna Kravchenko (the PhD student I co-supervise with S. Van Eck) is working on the tomographic method in the framework of evolved stars. The method allows to recover the distribution of the component of the velocity field projected on the line of sight at different optical depths in the stellar atmosphere (Alvarez et al. 2000, 2001b,a). Kravchenko et al. (2018) introduces the recently updates to the method as well as the implementation in Optim3D for the calculation of the contribution function in 3D RHD simulation of RSG stars. Kateryna successfully managed to show that in 3D simulations, the spectral lines do not form in a restricted range of reference optical depths as in 1D model atmospheres, but they spread over different optical depths due to the non-radial convective mouvements characterising the stellar atmosphere. In addition to this, she managed also to recover RHD simulation velocity field dependance across the atmosphere with this method.
The latter opens a new doorway for the study of stellar dynamical cycles in evolved stars, and in particular RSGs. A first example is reported in Kravchenko et al. 2018 (to be submitted) where the tomographic method help to interpret the long-term monitoring (almost 7 years with HERMES spectrograph) photometric variability of the RSG μ Cep. The tomographic method denoted, in the observations, the characteristic of the convective turn-over of the material in the stellar atmosphere (also knows as hysteresis loop Gray 2008, Fig. 2.8, right panel) and RHD simulations qualitatively explain this behaviour: the velocity maps in (same Figure) reveal upward and downward motions of matter extending over large portions of the stellar surface. The

Convective turn-over time in observations

[4]It is the locus of the midpoints of the line. A symmetric profile has a straight vertical bisector, while the "C"-shaped line bisector reveals asymmetries.

relative fraction of upward and downward motions is what distinguishes the upper from the lower part of the hysteresis loop, its top part (zero velocity) being characterized by equal surfaces of rising and falling material. The bottom part of the hysteresis loop occurs, as expected, when the stellar surface is covered mostly by downfalling material.

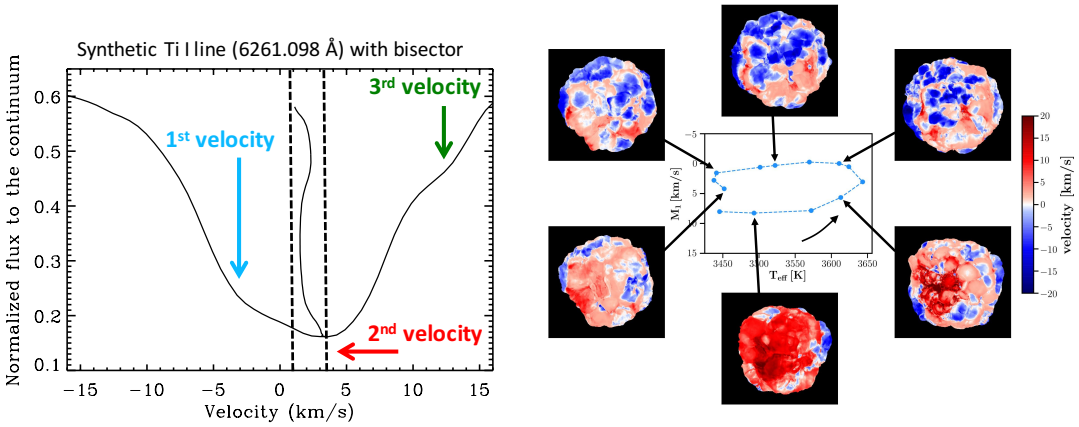

Figure 2.8: *Left panel:* Synthetic spectrum of the Ti I line at 6261.11 Å for one snapshot of a 3D RHD simulation of an RSG star (Chiavassa & Freytag 2015). The vertical dashed line shows the spanned velocities of the line bisector. The different arrow and colors displays the positions of different velocity components which contribute to the shape of the line. *Right panel:* Velocity maps for different snapshots of a RSG simulation during a convection cycle (central part of the panel). The velocity is weighted with the contribution function and red/blue colors correspond to falling/approaching material, respectively (Kravchenko, Chiavassa, Van Eck et al., to be submitted).

2.2.4 Spatially resolved surfaces: probing stellar parameters and surface details

Interferometry importance for evolved stars is two-folds: (i) it allows the determination of their stellar parameters, and (ii) affords the direct detection and characterization of the convective pattern related to the surface dynamics.

- Point (i). The direct measurement of stellar angular diameters has been the principal goal of most attempts with astronomical interferometers since the pioneering work (Michelson & Pease 1921). Nowadays with the advent of Gaia,

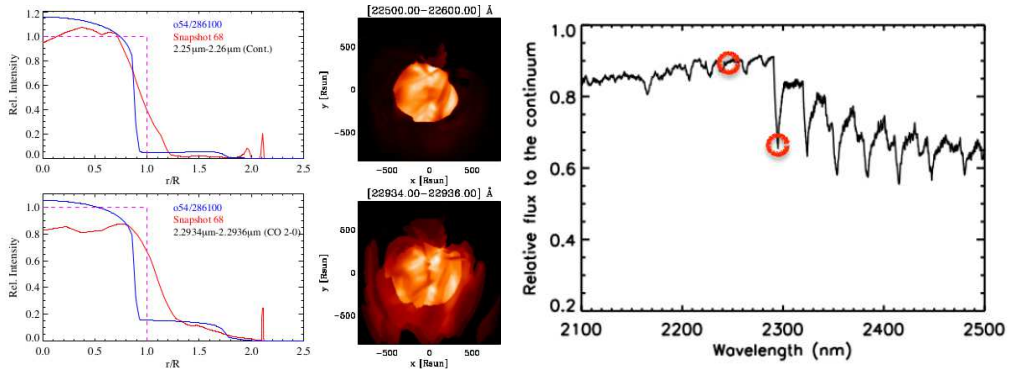

Figure 2.9: *Left panel:* Intensity profiles (in red) and intensity maps of a 3D RHD simulation of an AGB star in two spectral intervals in the K band (Wittkowski et al. 2016). *Right panel:* flux calculated for the same simulation. The red circles represent approximately the position of the selected intervals in the K-band.

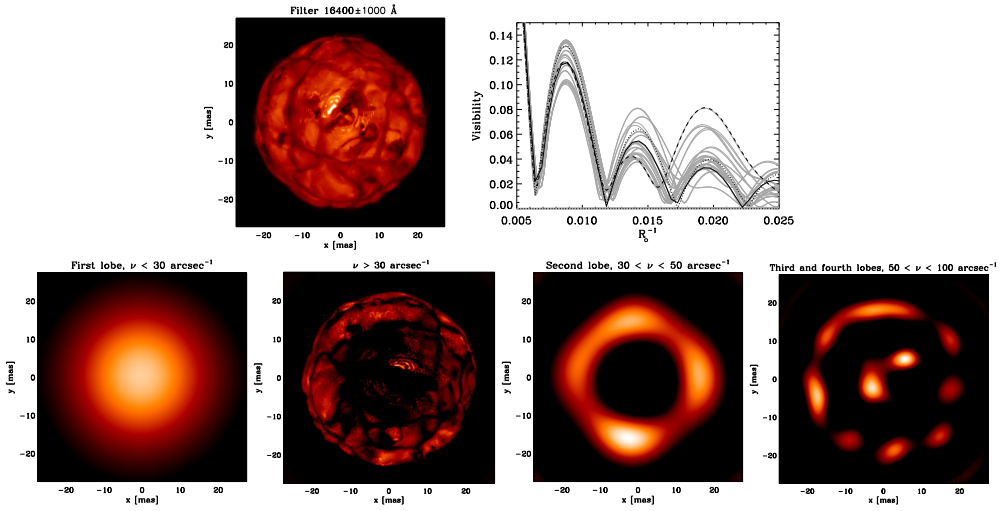

Figure 2.10: Characteristic size of convective cells on the prototypical RSG Betelgeuse (Chiavassa et al. 2009, 2010b). *Top left panel:* Synthetic intensity map in the H-band (Chiavassa et al. 2009). *Top right panel:* visibility curves (grey and black lines) computed from the image on the left for different rotation angles (36 in total with a step of 5 degrees). The dashed curve is the LD visibility while the black curve is the visibility for an uniform disc. *Low panels:* Filtered intensity maps at different spatial frequencies corresponding to the different lobes of the visibility curve (Chiavassa et al. 2010b).

for stars of known distance the angular diameter becomes of paramount importance to yield the stellar radius and eventually to the absolute magnitude. These quantities are essential links between the observed properties of stars and the results of theoretical calculations on stellar structure and evolution. Recent pioneering survey works (Wittkowski et al. 2012; Cruzalèbes et al. 2013; Arroyo-Torres et al. 2014, 2015; Wittkowski et al. 2017b), in which I took part, characterized the fundamental parameters and atmospheric extensions of evolved stars in our neighbourhood using AMBER instrument (now decommissioned) at VLTI. In particular, the last two papers observed a linear correlation between the visibility ratios of observed RSGs and the luminosity and surface gravity, indicating an increasing atmospheric extension with increasing luminosity and decreasing surface gravity, indirectly supporting a mass-loss scenario of a radiatively driven extension caused by radiation pressure on Doppler-shifted molecular lines. These results are confirmed for AGB stars (Fig. 2.9, Wittkowski et al. 2016) where the atmospheric extension are detected and explained by the RHD simulations for a sample of interferometric observations. The latter support the mass-loss scenario of pulsation- and shock-induced dynamics that can levitate the molecular atmospheres of Mira/AGB variables to extensions that are consistent with observations.

- Point (ii). Two main observables are used in interferometry: the visibility and the closure phases. The combination of both, plus a good enough coverage of the Fourier plane, contributes to the image reconstruction of the observed targets. Visibilities measure the surface contrast of the source and are primarily used to determine the fundamental stellar parameters and the limb-darkening. Closure phases combine the phase information from three (or more) telescopes and provide direct information on the morphology of the source. For a correct interpretation of the observations, it is necessary to simultaneously explain both observables with the same model. Chiavassa et al. (2009, 2010b) detected and measured the characteristic sizes of convective cells on the RSG star α Ori (Fig. 2.10) using visibility measurements in the infrared and managing to explain the observation of α Ori from the optical to the infrared region using RHD simulations. They showed that its surface is covered by a granulation pattern that, in the H and K bands, shows structures with small to medium scale granules (5-15 mas, while the size of the star at these wavelengths is ∼44 mas) and a large convective cell (∼30 mas). Another result concerns the first reconstructed images with AMBER/VLTI of the massive evolved star VX Sgr

Observing the details of the large granule means to understand the mass-loss

(Chiavassa et al. 2010c). The authors used RHD simulations of RSG and AGB to probe the presence of large convective cells on its surface. Since these publications, several other publications in which I participated actively, came out (Montargès et al. 2014, 2016; Chiavassa et al. 2017b; Montargès et al. 2017; Wittkowski et al. 2017a; Montargès et al. 2018; Paladini et al. 2018). With increasing observational power and analysis we can now probe the details on the stellar surfaces of different kind of stars. However also the temporal evolution (at different wavelengths) in a key point in the understanding of stellar dynamics: to tackle all the different astrophysical problems related to the evolved stars, today and future interferometers have to challenge the combination of high spectral and spatial resolution as well as the time monitoring on relatively short timescales (weeks/month) of these objects (e.g., Montargès et al. 2018).

The paper, "Radiative hydrodynamics simulations of red supergiant stars: II. simulations of convection on Betelgeuse match interferometric observations" by Chiavassa et al. 2010, is attached at the end of the chapter..

2.2.5 Evolved stars in the Gaia era: probing distances

Gaia (Gaia Collaboration et al. 2016) is an astrometric, photometric, and spectroscopic space-borne mission. It performs a survey of a large part of the Milky Way. The second data release (Gaia DR2) in April 2018 (Gaia Collaboration et al. 2018) brought high-precision astrometric parameters (i.e. positions, parallaxes, and proper motions) for over 1 billion sources brighter that $G \approx 20$. Among all the objects that have been observed, the complicated atmospheric dynamics of AGB and RSG stars is affect the photocentric position and, in turn, their parallaxes. The convection-related variability, in the context of Gaia astrometric measurements, can be considered as 'noise' that must be quantified in order to better characterise any resulting error on the parallax determination. However, important information about stellar properties, such as the fundamental stellar parameters, may be hidden behind the Gaia measurement uncertainty.
Chiavassa et al. (2011c, 2018b) explored the effect of convection-related surface structures on the photocentre to estimate its impact on the Gaia astrometric measurements. The surface of the deep convection zone has large and small convective cells. The visible fluffy stellar surface is made of shock waves that are produced in the interior and are shaped by the top of the convection zone as they travel outward (Freytag et al. 2017). In addition to this, at the wavelengths in Gaia G-band (Fig. 2.7,

top panel, for the RSGs; and bottom panel for the AGBs), molecules (e.g., TiO) produce strong absorption. Both effects modify the position of the photocentre and cause temporal fluctuations during the nominal 5 years of the Gaia mission.

The position of the photocentre for each snapshot of a simulation (i.e. as a function of time) can be computed as the intensity-weighted mean of the $x - y$ positions of all emitting points tiling the visible stellar surface according to

$$P_x = \frac{\sum_{i=1}^{N}\sum_{j=1}^{N} I(i,j) * x(i,j)}{\sum_{i=1}^{N}\sum_{j=1}^{N} I(i,j)} \tag{2.2}$$

$$P_y = \frac{\sum_{i=1}^{N}\sum_{j=1}^{N} I(i,j) * y(i,j)}{\sum_{i=1}^{N}\sum_{j=1}^{N} I(i,j)}, \tag{2.3}$$

where $I\,(i,\,j)$ is the emerging intensity for the grid point $(i,\,j)$ with coordinates $x(i,\,j)$, $y(i,\,j)$ of the simulation, and N is the total number of grid points in the simulated box. In the presence of surface brightness asymmetries, the photocentre position will not coincide with the barycentre of the star and its position will change as the surface pattern changes with time. This is displayed in the photocentre excursion plots of Fig. 2.11. The fact that $\langle P_x \rangle$ and $\langle P_y \rangle$ do not average to zero means that the photocentre tends not to be centred most of the time on the nominal centre of the star, because of the presence of a large convective cell.

First Gaia result on AGBs: correlation between the photocentre displacement and the pulsation

While Chiavassa et al. (2011c) denoted the first predictions for RSG stars, in (Chiavassa et al. 2018b), we showed that the convection-related variability accounts for a substantial part of the Gaia DR2 parallax error of a sample of semi-regular variables. In addition to this, we presented evidence for a correlation between the mean photocentre displacement and the stellar fundamental parameters: surface gravity and stellar pulsation. This is the first Gaia result on AGB' stars (INSU press release news in November 2018).

The paper, "Heading Gaia to measure atmospheric dynamics in AGB stars" by Chiavassa et al. 2018, is attached at the end of the chapter..

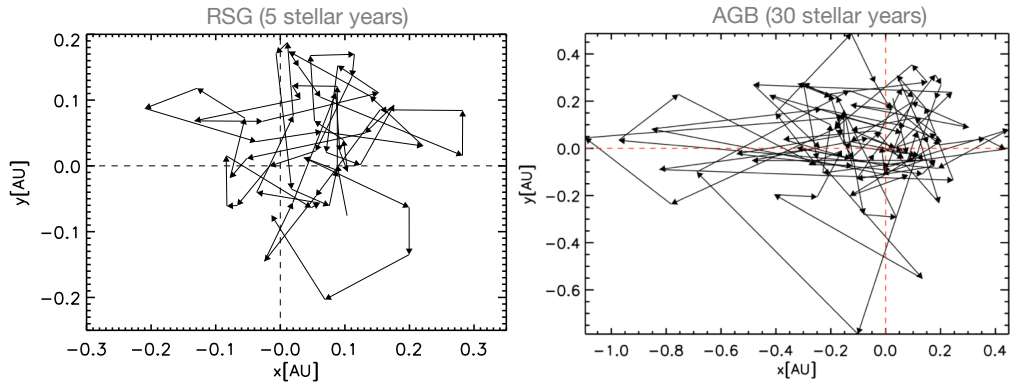

Figure 2.11: Photocentre position computed from 3D RHD simulation of a RSG (*left panel*, the radius is ∼4 AU Chiavassa et al. 2011c) and an AGB (*right panel*, the radius is 1.87 AU Chiavassa et al. 2018b) star. The different snapshots are connected by the line segments; the total time covered is reported above each panel and the snapshots are ∼23 days apart. The dashed lines intersect at the position of the geometrical centre of the images.

A&A 611, A11 (2018)
https://doi.org/10.1051/0004-6361/201732147

Astronomy & Astrophysics

The STAGGER-grid: A grid of 3D stellar atmosphere models

V. Synthetic stellar spectra and broad-band photometry⋆

A. Chiavassa[1], L. Casagrande[2], R. Collet[3], Z. Magic[4,5], L. Bigot[1], F. Thévenin[1], and M. Asplund[2]

[1] Université Côte d'Azur, Observatoire de la Côte d'Azur, CNRS, Lagrange, CS 34229, 06300 Nice, France
e-mail: andrea.chiavassa@oca.eu
[2] Research School of Astronomy & Astrophysics, Australian National University, Cotter Road, Weston, ACT 2611, Australia
[3] Stellar Astrophysics Centre, Department of Physics and Astronomy, Aarhus University, Ny Munkegade 120, 8000 Aarhus C, Denmark
[4] Niels Bohr Institute, University of Copenhagen, Juliane Maries Vej 30, 2100 Copenhagen, Denmark
[5] Centre for Star and Planet Formation, Natural History Museum of Denmark, University of Copenhagen, Øster Voldgade 5-7, 1350 Copenhagen, Denmark

Received 20 October 2017 / Accepted 4 January 2018

ABSTRACT

Context. The surface structures and dynamics of cool stars are characterised by the presence of convective motions and turbulent flows which shape the emergent spectrum.
Aims. We used realistic three-dimensional (3D) radiative hydrodynamical simulations from the STAGGER-grid to calculate synthetic spectra with the radiative transfer code OPTIM3D for stars with different stellar parameters to predict photometric colours and convective velocity shifts.
Methods. We calculated spectra from 1000 to 200 000 Å with a constant resolving power of $\lambda/\Delta\lambda = 20\,000$ and from 8470 and 8710 Å (*Gaia* Radial Velocity Spectrometer – RVS – spectral range) with a constant resolving power of $\lambda/\Delta\lambda = 300\,000$.
Results. We used synthetic spectra to compute theoretical colours in the Johnson-Cousins $UBV(RI)_C$, SDSS, 2MASS, *Gaia*, SkyMapper, Strömgren systems, and HST-WFC3. Our synthetic magnitudes are compared with those obtained using 1D hydrostatic models. We showed that 1D versus 3D differences are limited to a small percent except for the narrow filters that span the optical and UV region of the spectrum. In addition, we derived the effect of the convective velocity fields on selected Fe I lines. We found the overall convective shift for 3D simulations with respect to the reference 1D hydrostatic models, revealing line shifts of between −0.235 and +0.361 km s^{-1}. We showed a net correlation of the convective shifts with the effective temperature: lower effective temperatures denote redshifts and higher effective temperatures denote blueshifts. We conclude that the extraction of accurate radial velocities from RVS spectra need an appropriate wavelength correction from convection shifts.
Conclusions. The use of realistic 3D hydrodynamical stellar atmosphere simulations has a small but significant impact on the predicted photometry compared with classical 1D hydrostatic models for late-type stars. We make all the spectra publicly available for the community through the POLLUX database.

Key words. stars: atmospheres – stars: fundamental parameters – techniques: photometric – techniques: radial velocities – hydrodynamics – radiative transfer

1. Introduction

The stellar atmosphere is the boundary to the opaque stellar interior, and serves as the link between observations and the models of stellar structure and evolution. The phenomena of stellar evolution manifest themselves in the stellar surface as changes in chemical composition and in fundamental stellar parameters such as radius, surface gravity, effective temperature, and luminosity. The information we use to study distant stars comes from the flux they have emitted. However, the atmospheric layers where this flux forms is the transition region between convective and radiative regime. Thus, the surface structures and dynamics of cool stars are characterised by the presence of convective motions and turbulent flows. Convection manifests in the surface layers as a particular pattern of downflowing cooler plasma and bright areas where hot plasma rises (Nordlund et al. 2009). The size of granules depends on the stellar parameters of the star and, as a consequence, on the extension of their atmosphere (e.g. Magic et al. 2013). Eventually, the convection causes an inhomogeneous stellar surface that changes with time. They affect the atmospheric stratification in the region where the flux forms and also affect the emergent spectral energy distribution (SED), with potential effects on the precise determinations of stellar parameters (e.g. Bigot et al. 2011; Creevey et al. 2012; Chiavassa et al. 2012), radial velocity (e.g. Bigot & Thévenin 2008; Chiavassa et al. 2011; Allende Prieto et al. 2013), chemical abundance (e.g. Asplund et al. 2005, 2009; Caffau et al. 2011), photometric colours (Bonifacio et al. 2017), and on planet detection (Magic et al. 2015; Chiavassa et al. 2017).

Convection is a difficult process to understand because it is non-local, and 3D, and it involves non-linear interactions over many disparate length scales. In this context, the use of numerical 3D radiative hydrodynamical simulations of stellar convection is extremely important. In recent years, with

⋆ Tables 5–8 are only available at the CDS and Table B.1 is also available at the CDS and via anonymous ftp to cdsarc.u-strasbg.fr (130.79.128.5) or via http://cdsarc.u-strasbg.fr/viz-bin/qcat?J/A+A/611/A11

increased computational power, it has been possible to compute grids of 3D simulations that cover a substantial portion of the Hertzsprung–Russell diagram (Magic et al. 2013; Trampedach et al. 2013; Ludwig et al. 2009). With these tools it is possible to predict reliable synthetic spectra for several stellar types.

Photometric systems and filters are designed to be sensitive to temperature, gravity, and metal abundance indicators and thereby to complement spectroscopic determinations of the fundamental properties of stars. In addition, the integrated magnitudes and colours of stars can be used to infer the ages, metallicities, and other properties of the underlying stellar populations (e.g. Casagrande & VandenBerg 2014). For these purposes, several broad-band, or intermediate- and/or narrow-band filters have been designed to probe different regions of stellar spectra sensitive to different atmospheric parameters (Bessell & Murphy 2012; Gunn et al. 2006; Cohen et al. 2003). Additionally, there are the photometric systems used by the *Gaia* mission.

Gaia (Gaia Collaboration 2016) is an astrometric, photometric, and spectroscopic spaceborne mission of a large part of the Milky Way. Apart from the astrometric instrument, *Gaia* carries on board two low-resolution spectrophotometers (Blue and Red Prism, BP/RP, Bailer-Jones et al. 2013) and the Radial Velocity Spectrometer (RVS; Katz et al. 2004). The photometric instrument measures the SED over 120 pixels of all detected objects at the same angular resolution and at the same epoch as the astrometric observations. The BP operates in the range 3300–6800 Å, while the RP uses the range 6400–10 500 Å. The main aims of this instrument are to provide proper classifications (e.g. distinguish between stars, galaxies, and quasars) and characterisations (e.g. reddenings and stellar parameters), and to enable chromatic corrections of the astrometric centroid data. Finally, the integral-field spectrograph RVS provides spectra between 8470 and 8710 Å at a spectral resolving power of ≈11 200. The RVS is expected to produce radial velocities through Doppler-shift measurements; interstellar reddening, atmospheric parameters, and projected rotational velocities; and individual element abundances for some elements.

In this work, we calculated synthetic stellar spectra and photometry for broad-band and *Gaia* systems obtained using realistic 3D radiative hydrodynamical simulations of stellar convection from the STAGGER-grid. The predicted photometric 3D colours and the 3D spectra are publicly available for the community through the POLLUX database. The spectra corresponding to the *Gaia* RVS spectral range will be used for the calibration of the instrument to preserve the measured radial velocities from the convection shift (see forthcoming paper of GaiaDataRelease2/RVS).

2. Methods

2.1. Stellar model atmospheres

Magic et al. (2013) described the STAGGER-grid of realistic 3D radiative hydrodynamical simulations of stellar convection for cool stars using the STAGGER-code (originally developed by Nordlund & Galsgaard[1], and continuously improved over the years by its user community), a state-of-the-art (magneto)hydrodynamic code that solves the time-dependent hydrodynamic equations for mass-, momentum-, and energy-conservation, coupled with the 3D radiative transfer equation in order to account correctly for the interaction between the radiation field and the plasma. The code uses periodic boundary conditions horizontally and open boundaries vertically. At the bottom of the simulation, the inflows have a constant entropy. The outflows are not tightly constrained and are free to pass through the boundary. The code is based on a sixth-order explicit finite-difference scheme and a fifth-order interpolation. The considered large number over wavelength points is merged into 12 opacity bins (Nordlund 1982; Skartlien 2000; Magic et al. 2013). STAGGER simulations are based on a realistic equation of state that accounts for ionisation, recombination, and dissociation (Mihalas et al. 1988); continuous absorption and scattering coefficients listed in Hayek et al. (2010); and the line opacities listed in Gustafsson et al. (2008). These are in turn based on the VALD-2 database (Stempels et al. 2001) of atomic lines and the SCAN-base (Jørgensen 1997) of molecular lines.

2.2. Three-dimensional radiative transfer

We used the 3D pure-LTE radiative transfer code OPTIM3D (Chiavassa et al. 2009) to compute synthetic spectrum from the snapshots of the radiative-hydrodynamical (RHD) simulations of the STAGGER-grid (see Fig. 1 in Magic et al. 2013). The code takes into account the Doppler shifts due to convective motions. The radiative transfer equation is solved monochromatically using pre-tabulated extinction coefficients as a function of temperature, density, and wavelength.
The lookup tables were computed for the same chemical compositions as the RHD simulations using the same extensive atomic and molecular continuum and line opacity data as the latest generation of MARCS models (Gustafsson et al. 2008) with the addition – with respect to Table 2 of Gustafsson's paper – of the SiS molecule (Cami et al. 2009), which is particularly important for the far-infrared region of the spectrum. While the sources of line opacities used in the RHD simulations of Magic et al. (2013) and in OPTIM3D are the same, the data for the continuum opacities are almost the same: Hayek et al. (2010) reported that the data used in RHD simulations are mostly identical to those used in the MARCS models, but include additional bound-free data from the Opacity Project and the Iron Project (Trampedach et al., priv. comm.) as well as some opacities of the second ionisation stage for many metals.

For the computation of the spectra from RHD simulations, the assumed microturbulence is equal to zero since the velocity fields inherent in RHD models are expected to self-consistently and adequately account for non-thermal Doppler broadening of spectral lines (Asplund 2000). The temperature and density ranges spanned by the tables are optimised for the values encountered in the RHD simulations. The detailed methods used in the code are explained in Chiavassa et al. (2009, 2010). OPTIM3D has already been employed in synergy with the STAGGER simulations in several works (Chiavassa et al. 2010, 2011, 2012, 2014a, 2015, 2017; Magic et al. 2015) either concerning the extraction of synthetic spectra or interferometric observables.

2.3. One-dimensional radiative transfer

For all the following comparisons with 3D simulations, we used plane-parallel, hydrostatic, 1D atmosphere models computed with a similar physical treatment to the MARCS code and the same equation of state and opacities as in the individual 3D simulations (ATMO; Magic et al. 2013). Moreover, we used a 1D version of OPTIM3D, and the chemical compositions, the opacities, and numerics of the radiative transfer calculations for the emergent intensities are the same as used in the 1D and 3D approaches.

[1] http://www.astro.ku.dk/~kg/Papers/MHDcode.ps.gz

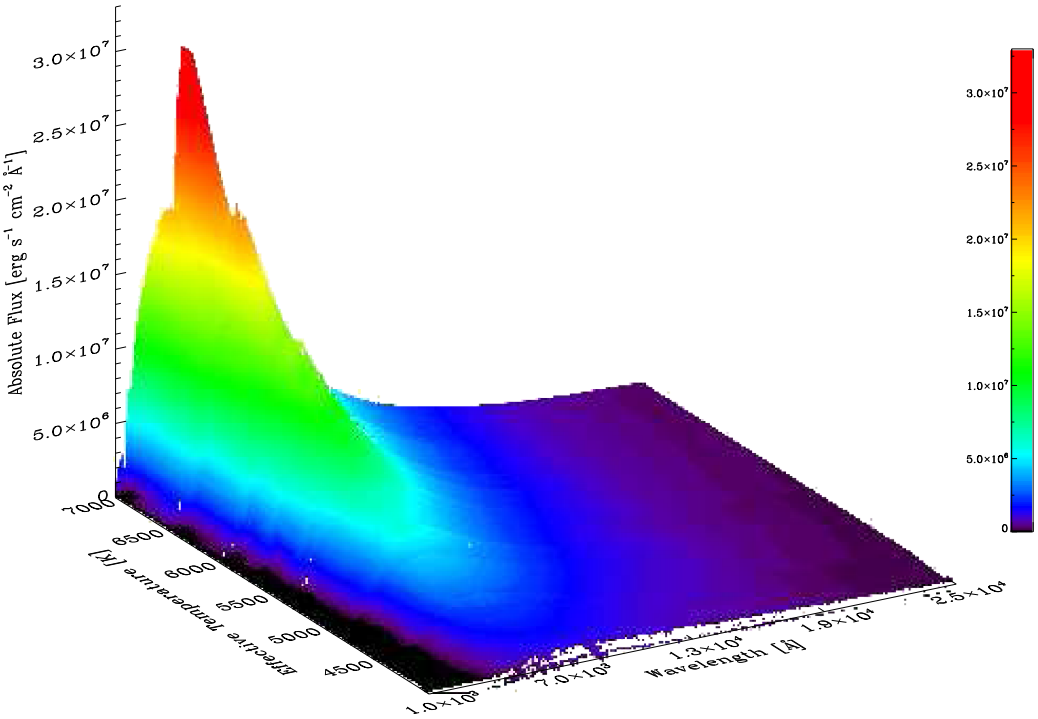

Fig. 1. Surface rendering for all the synthetic spectra computed for the 3D RHD simulations in Table B.1. The vertical bar on the right displays the colour scale for the emerging flux in erg s^{-1} cm^{-2} Å^{-1}. For clarity, the wavelength range has been reduced to 1000–25 000 Å.

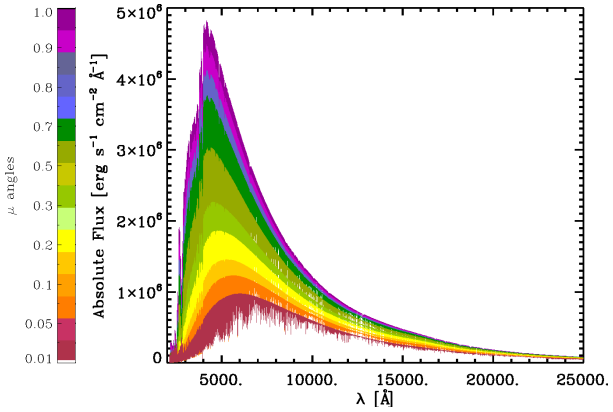

Fig. 2. Synthetic spectra of the solar simulation in the spectral range 2000–25 000 Å and for the different $\mu = \cos(\theta)$ inclination angles used in the computation, where θ is the angle with respect to the line of sight (vertical axis).

3. Synthetic spectra from 0.1 to 20 μm

The STAGGER-grid includes 3D stellar atmosphere simulations with metallicities [Fe/H] $= +0.5$, 0.0, -0.5, -1.0, -2.0, -3.0, and -4.0; surface gravity $\log g$ between 1.5 and 5.0 in steps of 0.5 dex; and effective temperature $T_{\rm eff}$ from 4000 to 7000 K in steps of 500 K (Fig. 1 of Paper I). In this work we present the synthetic spectra computed for the STAGGER-grid for a total of 181 simulations (Table B.1). The spectra have been calculated with a constant resolving power of $\lambda/\Delta\lambda = 20\,000$ ($n_\lambda = 105\,767$ wavelength points) from 1000 to 200 000 Å. OPTIM3D computes the emerging intensities for vertical rays cast through the computational box for all required wavelengths. The procedure is repeated after tilting the computational box by an angle θ with respect to the line of sight (vertical axis) and rotating it azimuthally by an angle ϕ. The final result is a spatially resolved intensity spectrum at different angles. In addition, a temporal average is also performed. We performed the calculations for ten snapshots of the 3D RHD simulations of Table B.1, adequately spaced so as to capture several convective turnovers, for ten different inclination angles $\mu = \cos(\theta) = [1.00, 0.90, 0.80, 0.70, 0.50, 0.30, 0.20, 0.10, 0.05, 0.01]$ (see Fig. 4), and four ϕ-angles [0°, 90°, 180°, 270°]. The strongest decline in the limb darkening is usually found towards the limb; therefore, we decided to resolve with more μ-angles at the limb instead of having an equidistant scale in μ. We tested the discrepancy between the temporal average using a large number of snapshots (e.g. 20) and using only 10 snapshots is lower than 0.3%. The number of ten snapshots was chosen because it represents the best compromise in terms of computational time and accuracy among the whole set of stellar parameters. All things considered, we computed 400 spectra in the range 1000–200 000 Å for every simulation.

Figure 1 displays the set of all synthetic spectra computed. We determined the $T_{\rm eff}$ from the integration of the SED of the spectra from 0.1 to 20 μm. The effective temperature has been computed using Stefan–Boltzmann law as

$$T_{\rm eff\ spectra} = \left\{ \left[\int_{\lambda_1}^{\lambda_2} f(\lambda)\, {\rm d}\lambda \right] / \sigma \right\}^{0.25}, \quad (1)$$

where $\lambda_1 = 1010$Å and $\lambda_2 = 199\,960$ Å, $f(\lambda)$ is the synthetic flux, and σ is the Stefan–Boltzmann constant. The values of the effective temperature are listed in Table B.1.

Figure 1 shows that increasing $T_{\rm eff}$ returns higher radiated energy per surface area and the peak of the radiation curve moves to shorter wavelengths, as expected by Planck law. Pereira et al. (2013) provided excellent agreement of their 3D solar simulation of the STAGGER-grid with the continuum observation of the Sun. As they did, we used the Kurucz (2005) irradiance[2] and normalised flux atlases for the Sun between 3000 and 10 000 Å and found a good agreement (Fig. 3), reinforcing the view that the simulation of thermodynamic structure

[2] Available at http://kurucz.harvard.edu/sun.html

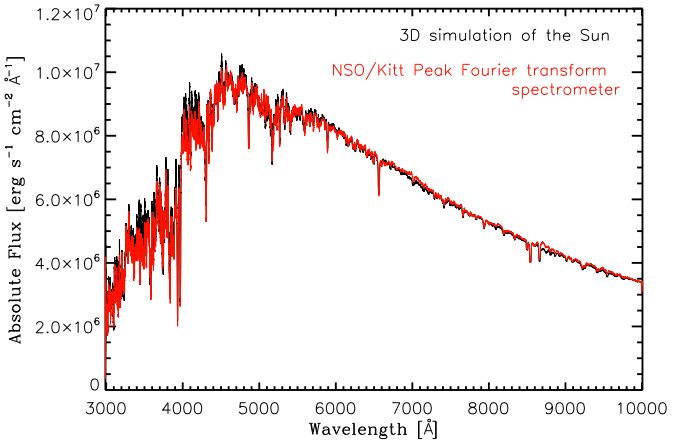

Fig. 3. Comparison of the solar simulation (black) with the observed flux of the Sun (red, Kurucz 2005). The solar irradiance is converted to flux at the solar surface using the multiplicative factor of $[(1\mathrm{AU})/R_\odot]^2 = 46\,202$. For clarity, the spectra have been resampled to a lower spectral resolution with fewer frequency points ($n_\lambda = 2115$).

Table 1. Photometric systems used in this work and overplotted on the synthetic spectra in Fig. 4.

Photometric system name	Filters
Johnson-Cousins[a]	$UBV(RI)_C$
Sloan Digital Sky Survey (SDSS)[b]	*ugriz*
2MASS[c]	J, H, K_S
Gaia[d]	G, BP, RP
SkyMapper[e]	$u_s, v_s, g_s, r_s, i_s, z_s$
Strömgren[f]	*uvby*
HST-WFC3[g]	*F*218*W*, *F*225*W*, *F*275*W*, *F*336*W*, *F*350*W*, *F*390*M*, *F*390*W*, *F*438*W*, *F*475*W*, *F*547*M*, *F*555*W*, *F*606*W*, *F*625*W*, *F*775*W*, *F*814*W*, *F*850*LP*

References. [(a)] Bessell & Murphy (2012), [(b)] Doi et al. (2010), [(c)] Cohen et al. (2003), [(d)] Jordi et al. (2010), [(e)] Bessell et al. (2011), [(f)] Bessell (2011), [(g)] Deustua et al. (2016).

and post-processing detailed radiative transfer are realistic. This conclusion was also reported by Hayek et al. (2012), who determined that the numerical resolution of the STAGGER 3D RHD models and the spectral resolution for the flux computations are sufficient to predict realistic observables. In particular, some of the RHD simulations presented in this work and for a limited spectral region between 2000 and 10 000 Å have been used in Magic et al. (2015) to provide appropriate coefficients for various bi-parametric and non-linear limb darkening laws.

4. Photometric synthetic observables

Photometric systems and filters are designed to probe fundamental physical parameters, such as the effective temperature, surface gravity, and metallicity of stars. Colour and magnitude relations are used for a variety of purposes: interpreting the observed distribution of stars in colour–colour and colour–magnitude diagrams, deriving distances to stars and star clusters, and testing stellar evolutionary theory by comparing with observations to name just a few. Thus, it is important to have realistic model fluxes to generate colours which match the observed values. In addition to synthetic model fluxes, details on the photometric standardisation are also a part of this quest.

In essence, photometry condenses the information encoded in a spectrum $f(\lambda)$ over a system response function $T(\lambda)$, i.e. $\int f(\lambda)\,T(\lambda)\,\mathrm{d}\lambda$. Each existing photometric system then varies in the details. Most notably, $T(\lambda)$ will depend on the filter under consideration and the response function of the detector. This means that a distinction must be made between photo-counting and energy-integration detectors, meaning that a measurement of energy $\int f(\lambda)\,T(\lambda)\,\mathrm{d}\lambda$ will correspond to $(hc)^{-1}\int f(\lambda)\,\lambda T(\lambda)\,\mathrm{d}\lambda$ photons (see e.g. Bessell 2000). Another aspect that often varies among different photometric systems is how their standardisation (zero-point and absolute calibration) is achieved. Here, for all systems but *Gaia* we adopted the exact same procedure as used by Casagrande & VandenBerg (2014), where details on the adopted filter transmission curves, the photo-counting and energy-integration formalism, and zero-points and absolute calibration can be found[3]. We computed synthetic colours in the Johnson-Cousins, SDSS, 2MASS, *Gaia*, SkyMapper, Strömgren, HST-WFC3, and *Gaia* systems (Table 1 and Fig. 4 for a comparison of the solar spectrum with the filter transmission curves studied here). For the HST-WFC3 systems our tables are provided in the VEGA, ST, and AB systems.

A full characterisation of the *Gaia* photometric system, including zero-points and standardisation is expected to be released in 2018. In this work, we used the transmission curves available from the ESA website[4], and computed *Gaia* colours following Jordi et al. (2010). We fixed Vega's magnitudes to be G = BP = RP = 0.03, and for the absolute calibration used a Kurucz synthetic Vega spectrum rescaled to the measured flux value at 5556 Å from Megessier (1995).

Similarly to Casagrande & VandenBerg (2014), instead of colour indices we provide bolometric corrections in different bands (Table B.1 and 4–7, available at the CDS) because they are more versatile and can be rearranged in any colour combination, as follows from Eqs. (3) and (4). The bolometric magnitude is defined as

$$M_{\mathrm{Bol}} = -2.5\log\frac{L}{L_\odot} + M_{\mathrm{Bol},\odot}, \tag{2}$$

where we adopt $M_{\mathrm{Bol},\odot} = 4.74$. It follows that the bolometric correction in a given band BC_ζ is

$$BC_\zeta = m_{\mathrm{Bol}} - m_\zeta = M_{\mathrm{Bol}} - M_\zeta, \tag{3}$$

where the lower and upper cases refer to apparent and absolute magnitudes, respectively. From this it follows that colour indices can be obtained from the difference in bolometric corrections, where ζ and η are two given bands:

$$\zeta - \eta = m_\zeta - m_\eta = BC_\eta - BC_\zeta. \tag{4}$$

Thus, in the rest of the paper when we talk about synthetic colours, these have been obtained as differences in bolometric corrections from our tables.

[3] The only difference with respect to Casagrande & VandenBerg (2014) is that here we have adopted $M_{\mathrm{Bol}\odot} = 4.74$.

[4] https://www.cosmos.esa.int/web/gaia/transmissionwithoriginal

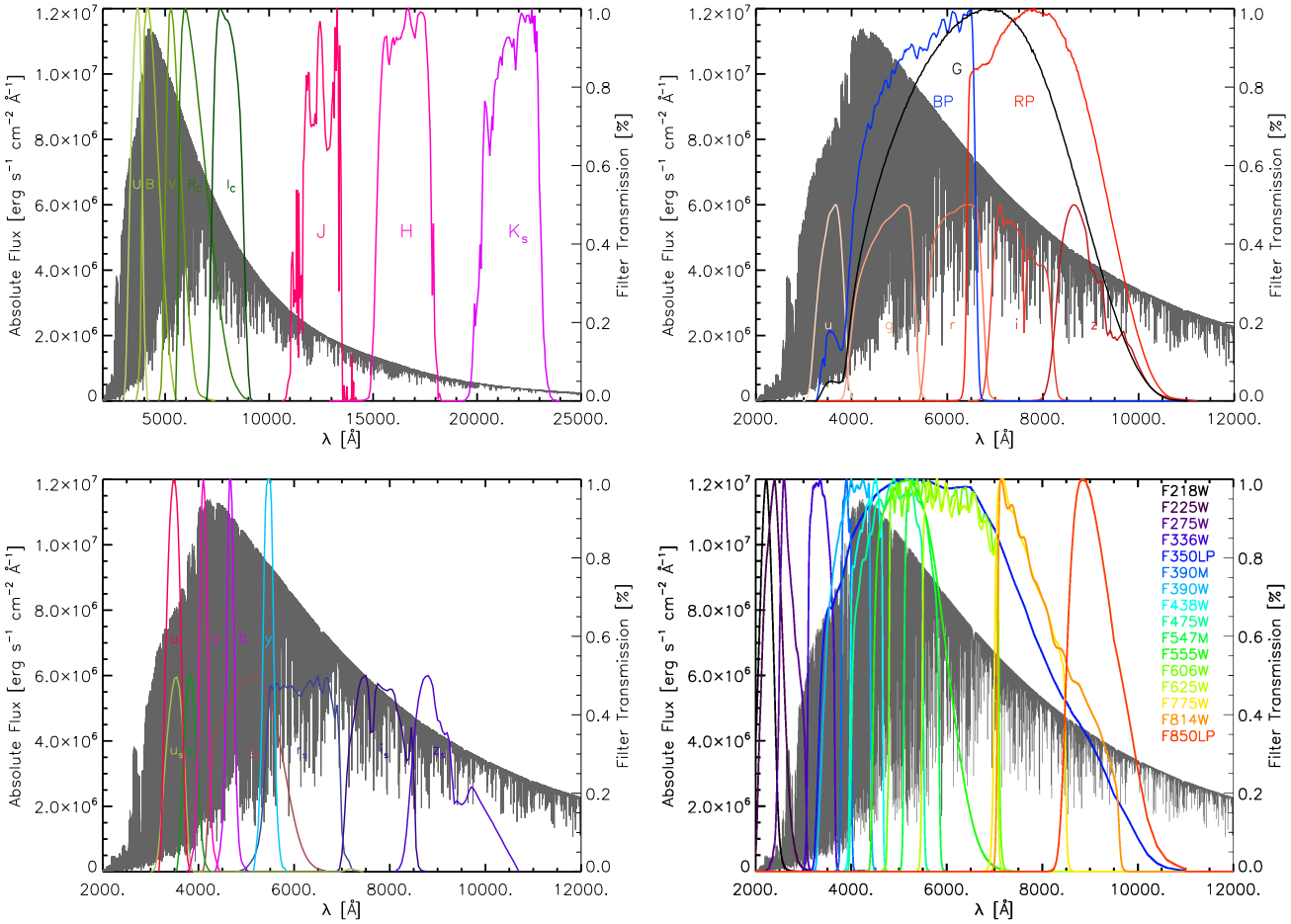

Fig. 4. Synthetic spectrum of the solar simulation at full spectral resolution in the spectral range 2000–25 000 Å (grey, *top panel*) and 2000–12 000 Å (*central* and *bottom* panels). Several system response functions (Table 1), from which synthetic colours have been computed, are overplotted. Johnson-Cousins system response functions (U, B, V, Rc, Ic) are plotted in green and 2MASS in pink-violet (*top left panel*); SDSS (u, g, r, i, z) in yellow-red and *Gaia* (BP, RP, G) (*top right panel*); Strömgren ($uvby$) in red-blue and SkyMapper ($u_s, v_s, g_s, r_s, i_s, z_s$) (*bottom left panel*); and the 15 filters of the HST-WFC3 (*bottom right panel*). For clarity, SDSS and SkyMapper functions are normalised to 0.5.

4.1. Microturbulence

The stellar surface convection produces a velocity field where the emerging spectral lines form. The Doppler broadening of these lines is a direct consequence of the velocity field in these crucial layers (Asplund et al. 2000b; Nordlund et al. 2009). In traditional 1D models, this effect can be accounted for by the use of arbitrary micro- and macroturbulence parameters. Full 3D line formation calculations using 3D RHD simulations have demonstrated that in late-type stars the required non-thermal Doppler line broadening is fully included in the convection-related motions of the stellar atmosphere (e.g. Collet et al. 2007). One-dimensional microturbulence represents the small-scale end of turbulent motions and is applied to the spectral line absorption coefficient. It affects the strong lines to a greater extent, reducing their saturation, and to a lesser extent the widths of weak lines. For 1D-based SEDs, microturbulence partly redistributes the flux in spectral regions probed by the photometric systems, in particular in regions crowded with lines towards the blue and the ultraviolet, and in filters with smaller wavelength coverages (Casagrande & VandenBerg 2014).

The values of the microturbulence parameters are usually determined by comparing synthetic and observed spectral line profiles and line strengths and often using a depth-independent value. For reference, a typical value for dwarfs and subgiants is around 1−1.5 km s^{-1}, which increases to 2−2.5 km s^{-1} for stars on the red giant branch (e.g. Gray et al. 2001). A constant value of 2 km s^{-1} is usually assumed in large grids of synthetic stellar spectra (Castelli & Kurucz 2004; Brott & Hauschildt 2005). To compute our 1D hydrostatic comparison models, we explored different values of microturbulence: 0, 1, and 2 km s^{-1}. We found that there is no clear and no unique relation between microturbulence and the stellar parameters, as reported by Casagrande & VandenBerg (2014). For clarity we adopted, as a guiding example, a value of 1 km s^{-1} when performing 1D calculations.

4.2. Three-dimensional versus one-dimensional bolometric differences in correction

The figures in the Appendix display the bolometric corrections between 3D simulations and the corresponding 1D hydrostatic models with microturbulence = 1 km s^{-1}. The values of BC are reported in Table B.1 to Table 8 for all the filters and, to retrieve the absolute colours, Eqs. (3) and (4) should be used. Considering the SDSS, SkyMapper, 2MASS, and HST-WFC3 systems, the overall deviations are limited to small fraction (less than 5%) from BC_r to BC_{Ks}, but they increase to 10% for BC_u and in BC_g (SDSS) and for $BC_g sky$, $BC_v sky$, and $BC_u sky$ (SkyMapper) where the optical and line crowded region of the spectrum is probed with rather narrow filters (Fig. 4, bottom); these differences decline with increasing effective temperature.

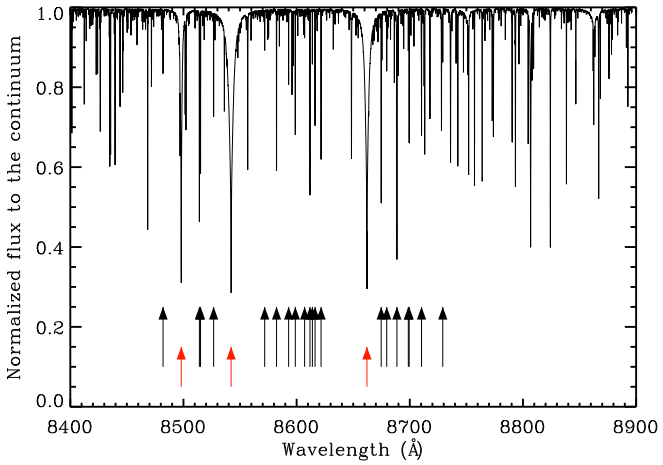

Fig. 5. Flux normalised to the continuum for the solar simulation (Table B.1) in the RVS range (8400–8900 Å). The Fe I lines (black arrows) are from Bigot & Thévenin (2006), while the Ca II triplet are indicated with red arrows.

This behaviour is more or less visible for all the photometric systems; there is no clear correspondence of ΔBC with the other stellar parameters. On a broad scale, the wide infrared photometric systems like 2MASS ($BC_{\rm H}$ and $BC_{\rm Ks}$) and optical *Gaia* ($BC_{\rm G}$) display a noticeable offset with respect to $\Delta BC = 0.0$. This is due to a redistribution of the spectral energy flux among the different filters and is a direct effect of the impact of 3D dynamics and thermodynamic structure on spectral line formation.

Gaia photometric systems return 3D and 1D deviations of less than 3% with higher values for the bluer system (BP). This effect may be not negligible and should become important for future releases of *Gaia* data. For this purpose, part of the spectra presented in this work have already been provided to *Gaia* consortium-CU8[5].

5. Convective velocity shifts for RVS

Measurements of stellar radial velocities are fundamental in order to determine stellar space velocities. This is needed, for example to investigate the kinematic structure of stellar populations in the Galaxy or to monitor for radial velocity variations, either of which would point to the presence of unseen companion(s). Convection plays a crucial role in the formation of spectral lines and deeply influences the shape, shift, and asymmetries of lines in late-type stars (e.g. Asplund et al. 2000a). These stars represent most of the objects that will be observed during the *Gaia* mission. Absorption lines may be blueshifted as a result of convective movements in the stellar atmosphere: bright and rising convective elements contribute more photons than the cool dark shrinking gas, and as a consequence, the absorption lines appear blueshifted (Dravins 1982). However, the convective line shift is not the same for all the spectral lines. Each line has a unique fingerprint in the spectrum that depends on line strength, depth, shift, width, and asymmetry across the granulation pattern depending on their height of formation and sensitivity to the atmospheric conditions. In this context, the line strengths play a major role (Asplund et al. 2000c).

[5] For more details, see the technical note "The 3D spectral library for BP/RP" (Chiavassa et al. 2014c).

Table 2. Central wavelength position, oscillator strength ($\log gf$), and excitation potential (χ) for the 20 Fe I in the spectral domain of RVS (Bigot & Thévenin 2006).

λ [Å]	($\log gf$)	χ [eV]
8481.985	−2.097	4.1860
8514.068	−2.250	2.1980
8515.109	−2.033	3.0180
8526.667	−0.675	4.9130
8571.803	−1.134	5.0100
8582.257	−2.198	2.9900
8592.951	−0.891	4.9560
8598.829	−1.285	4.3860
8607.078	−1.419	5.0100
8611.801	−1.900	2.8450
8613.939	−1.121	4.9880
8616.280	−0.935	4.9130
8621.601	−2.369	2.9490
8674.741	−1.780	2.8310
8679.639	−1.040	4.9660
8688.623	−1.249	2.1760
8698.706	−3.464	2.9900
8699.453	−0.480	4.9550
8710.391	−0.425	4.9130
8729.147	−2.933	3.4150

The aim of the present section is to derive the overall convective shift for 3D simulations. First, we computed the 1D and 3D spectra with a constant resolving power of $\lambda/\Delta\lambda = 300\,000$ from 8470 to 8710 Å for a limited number of 3D simulations (see Table B.1) covering stellar parameters observed by RVS (i.e. [Fe/H] ≥ -2.0). Then, from our spectra we selected only a series of non-blended Fe I lines and masked the others (Fig. 5). The oscillator strengths of these Fe I lines (Table 2) have been accurately determined by Bigot & Thévenin (2006) using 3D RHD simulation where the Fe I and Ca II lines are indicated. It should be noted that the synthetic spectra, when compared to the observations, have to be gravitationally redshifted (e.g. Pasquini et al. 2011) by a certain amount corresponding to the type of star considered (e.g. for the Sun it is $636.486 \pm 0.024\,{\rm m\,s^{-1}}$ Lindegren & Dravins 2003). Gravitational shifts for late-type dwarfs ($\log g \approx 4.5$) range between 0.7 and $0.8\,{\rm km\,s^{-1}}$ and they dramatically decrease with surface gravity down to 0.02–$0.03\,{\rm km\,s^{-1}}$ for K giant stars with $\log g \approx 1.5$ (Allende Prieto et al. 2013).

The velocity gradient through the photosphere sets the basic shape of the absorption lines in terms of asymmetry and position of the emerging intensity. One way to detect the asymmetries in the line is the bisector[6]. A symmetric profile has a straight vertical bisector (i.e. in the case of hydrostatic 1D spectra). The spectral lines with C-shape bisectors are formed mostly in the upflows (granules) and therefore blueshifted. The reverse C-shapes are generally formed in downflows (Dravins et al. 1981). Reversed C-shape bisectors can be explained by a combination of a steep decline in velocities with height with a flux deficit spanning only a fraction of the red wing of the line profiles (Gray 2010). Different articles show the presence of bisectors revealing asymmetries and wavelength shifts that indicate the presence of granulation for several kinds of stars (e.g. Ramírez et al. 2008; Gray 2009).

[6] Defined as the locus of the midpoints of the spectral line.

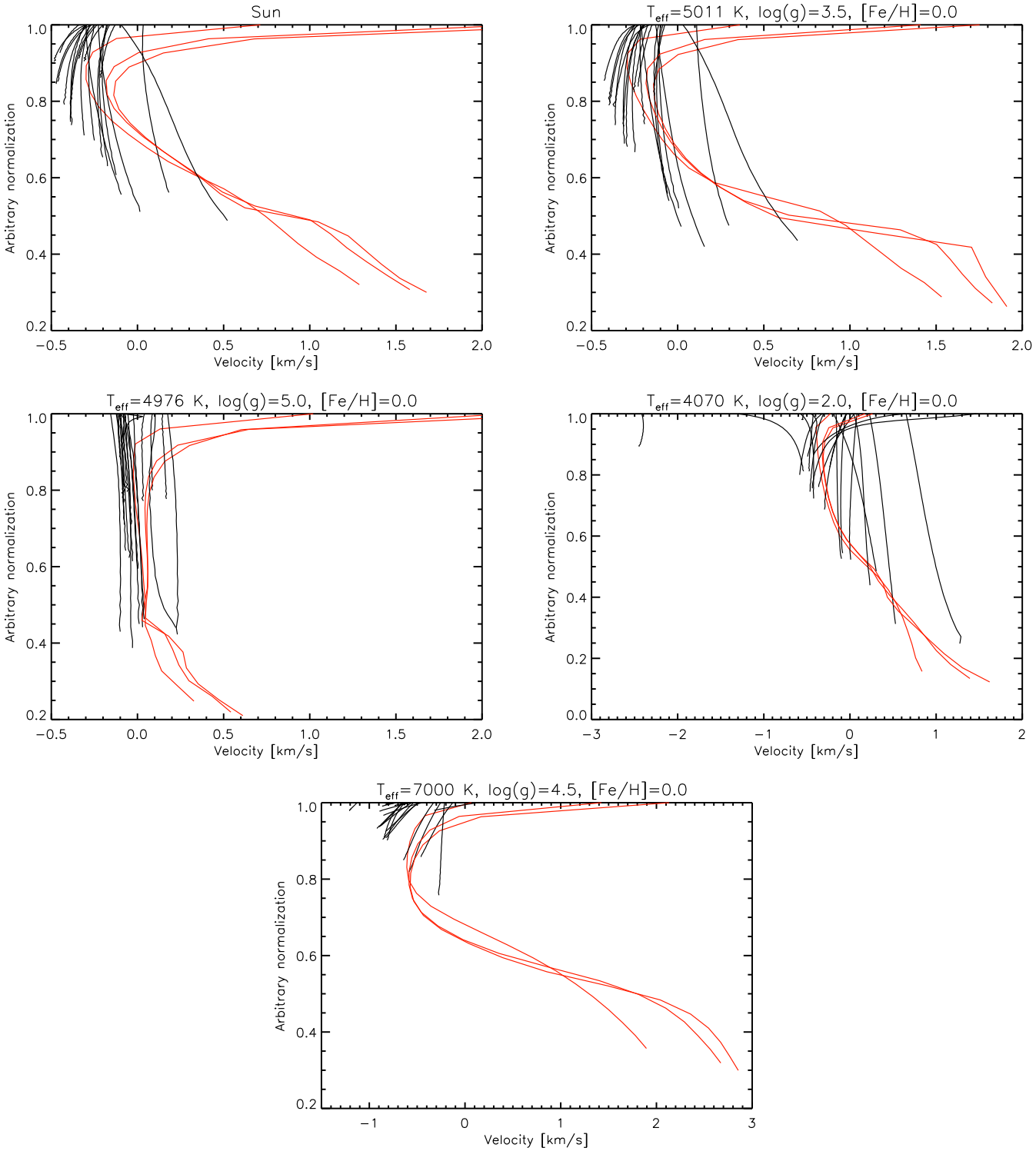

Fig. 6. Line bisectors of the 20 Fe I lines (black) from Bigot & Thévenin (2006) and Ca II triplet (red) for five 3D simulations in the grid.

Figure 6 shows the line bisectors for the Fe I and Ca II triplet lines for stars with different $T_{\rm eff}$ and $\log g$, but with the same metallicity. The gas is strongly horizontally divergent due to mass conservation and its velocities diminish with height. Weak lines (with typically high excitation potential), which form in deeper layers, are more blueshifted than strong lines whose core and part of the wings are formed in higher layers. This effect is particularly visible in Fig. 6 when comparing the solar bisector with the hottest $T_{\rm eff}$ = 7000 K simulations. In addition, the velocity field in 3D simulations of STAGGER-grid largely affects the overall shape of the iron lines in the range of RVS and for all the stars with the strongest effects for Ca II. This has already been shown for other spectral regions (e.g. Asplund et al. 2000b; Allende Prieto et al. 2002; Ramírez et al. 2009; Pereira et al. 2013; Magic et al. 2014).

We determined the convective shift considering only Fe I and only Ca II triplet lines, we cross-correlated each 3D spectrum with the corresponding 1D by using a lag vector corresponding

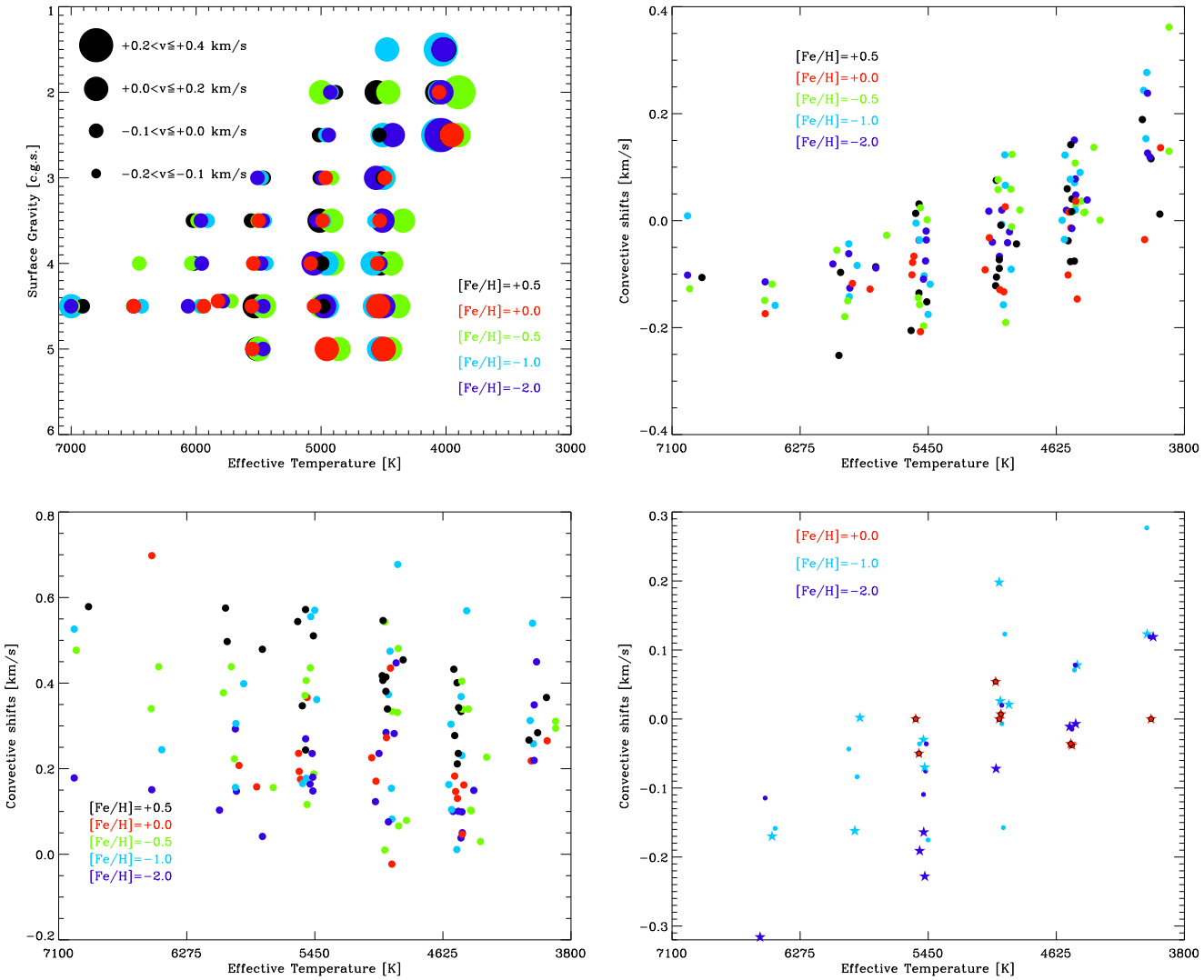

Fig. 7. *Top left panel*: convective shifts predicted by the 3D hydrodynamical simulations for the *Gaia* RVS spectral range and the Fe I lines (see text for details). *Top right panel*: convective shifts from Fe I lines as a function of the effective temperature of the 3D simulations in Table B.1. *Bottom left panel*: convective shifts from Ca II lines. *Bottom right panel*: comparison of convective shifts for a selected number of RHD simulations from this work (stars) with simulations with equivalent stellar parameters from Allende Prieto et al. (2013) (circles). See Table 3 for details.

to radial velocities (RV) in the range $-10 < v < +10\,\mathrm{km\,s^{-1}}$ for Fe I, and $-150 < v < +150\,\mathrm{km\,s^{-1}}$ for Ca II triplet lines, in steps of $0.3\,\mathrm{km\,s^{-1}}$. These velocity ranges were chosen to largely cover the wavelength frequency points of all the single lines. For each RV value, we Doppler-shifted the 1D spectrum and computed its cross-correlation function (CCF) with the 3D spectrum. The final step is to compute the weighted average to obtain the location of the CCF maximum, which corresponds to the actual 3D convective shifts (CS) with respect to 1D models:

$$CS = \frac{\int_{-10}^{+10} RV\,(v) \cdot CCF\,(v)\,\mathrm{d}v}{\int_{-10}^{+10} CCF\,(v)\,\mathrm{d}v} \quad (5)$$

Figure 7 displays the convective shifts for all the simulations either in the HR diagram (top left panel) or as a function of the $T_{\rm eff}$ for the Fe I of Table 2 (top right panel), and for the Ca II triplet lines (bottom left panel). We found that surface gravity and metallicity have a small effect on the convective shifts, as already noticed by Allende Prieto et al. (2013). The values for the Fe I are in the range between −0.235 and +0.361 $\mathrm{km\,s^{-1}}$. The convective shifts of Ca II lines are strongly redshifted (as shown by red bisectors in Fig. 6) and are between −0.023 and +0.698 $\mathrm{km\,s^{-1}}$. In Fig. 7 (top right panel), there is a net correlation of the convective shifts with the effective temperature: $T_{\rm eff} \lessapprox 4500$ K denotes redshifts, while $T_{\rm eff} \gtrapprox 5000$ K denotes blueshifts (except for the hottest $T_{\rm eff} \approx 7000$ K). This result is in agreement with Allende Prieto et al. (2013), who had performed the calculations for a different set of iron lines and found a milder correlation, where $T_{\rm eff}$ with warmer stars tend to exhibit larger blueshifts.

To quantify the differences in the convective shifts, we selected 26 simulations from Table B.1 with the same surface gravity, metallicity, and $\Delta T_{\rm eff} < 50$ K with respect to a subset of CIFIST-grid simulations from Allende Prieto et al. (2013). Convective shifts, as a function of metallicity (Table 3), from RHD simulations in this work are $CS_{\rm Stagger,[Fe/H]=0} = [-0.135, 0.142]$, $CS_{\rm Stagger,[Fe/H]=-1} = [-0.175, 0.277]$, and $CS_{\rm Stagger,[Fe/H]=-2} = [-0.114, 0.119]\,\mathrm{km\,s^{-1}}$, and from CIFIST-grid simulations $CS_{\rm CIFIST,[Fe/H]=0} = [-0.050, 0.054]$, $CS_{\rm CIFIST,[Fe/H]=-1} = [-0.170, 0.198]$, and $CS_{\rm CIFIST,[Fe/H]=-2} = [-0.316, 0.119]\,\mathrm{km\,s^{-1}}$. The spanned shift values from both grids are similar (Fig. 7,

Table 3. Selected convective shifts for Fe I only ($CS_{\rm Stagger}$ in km s^{-1}) from RHD simulations in this work and from CIFIST-grid simulations ($CS_{\rm CIFIST}$ in km s^{-1}) with equivalent stellar parameters from Allende Prieto et al. (2013).

$T_{\rm eff,Stagger}$	$T_{\rm eff,CIFIST}$	$\log g$	[Fe/H]	$CS_{\rm Stagger}$	$CS_{\rm CIFIST}$	$\Delta_{\rm CS}$
4014	4018	1.50	−0.0	0.116	0.000	0.116
4524	4480	4.00	−0.0	0.040	−0.038	0.078
4532	4509	4.50	−0.0	0.142	−0.036	0.178
5015	4968	2.50	−0.0	−0.122	0.054	−0.176
4992	4954	4.00	−0.0	−0.073	0.000	−0.073
4982	4982	4.50	−0.0	−0.009	0.007	−0.016
5509	5475	4.00	−0.0	−0.135	−0.050	−0.085
5530	5488	4.50	−0.0	0.014	0.000	0.014
4042	4040	1.50	−1.0	0.277	0.123	0.154
4508	4490	2.50	−1.0	0.071	0.078	−0.007
4965	4993	2.50	−1.0	−0.157	0.198	−0.355
4975	4930	3.50	−1.0	−0.007	0.021	−0.028
4956	4986	4.00	−1.0	0.123	0.026	0.097
5450	5481	3.50	−1.0	−0.175	−0.030	−0.145
5506	5473	4.50	−1.0	−0.036	−0.070	0.034
5907	5890	3.50	−1.0	−0.084	0.002	−0.086
5961	5923	4.50	−1.0	−0.043	−0.162	0.119
6435	6456	4.50	−1.0	−0.158	−0.170	0.012
4021	4001	1.50	−2.0	0.119	0.119	−0.000
4524	4500	4.00	−2.0	−0.015	−0.007	−0.008
4502	4539	4.50	−2.0	0.078	−0.011	0.089
4976	5013	4.50	−2.0	0.020	−0.072	0.092
5467	5505	3.50	−2.0	−0.075	−0.191	0.116
5480	5472	4.00	−2.0	−0.109	−0.228	0.119
5462	5479	4.50	−2.0	−0.036	−0.164	0.128
6500	6533	4.50	−2.0	−0.115	−0.316	0.201

Notes. The difference in $T_{\rm eff}$ is set to be smaller than 50 K.

bottom right panel), and show smaller deviations at solar metallicity ($\Delta_{\rm CS} \leqslant 0.195$ km s^{-1}) and slightly larger deviations at [Fe/H] = −1 ($\Delta_{\rm CS} \leqslant 0.370$ km s^{-1}) and [Fe/H] = −2 ($\Delta_{\rm CS} \leqslant 0.221$ km s^{-1}). Apart from the possible numerical differences in the simulations and in the radiative transfer, the shift deviations may also be due to the set of spectral lines considered.

The extraction of accurate radial velocities from RVS needs an appropriate wavelength calibration from convective shifts. This is directly processed in RVS pipeline using the synthetic spectra presented in this work and provided to *Gaia* consortium-CU6[7].

6. Conclusions

We provided synthetic spectra from the STAGGER-grid:

- low-resolution spectra from 1000 to 200 000 Å with a constant resolving power of $\lambda/\Delta\lambda = 20\,000$;
- high-resolution spectra from 8400 to 8900 Å (*Gaia* RVS spectral range), with a constant resolving power of $\lambda/\Delta\lambda = 300\,000$.

We used the low-resolution spectra to compute synthetic colours in the Johnson-Cousins $UBV(RI)_C$, SDSS, 2MASS, *Gaia* systems, SkyMapper, Strömgren, and HST-WFC3. We extracted the bolometric corrections for the 3D simulations and the corresponding 1D hydrostatic models. We probed that 1D versus 3D deviations are limited to small fraction (less than 5%) except for $BC_{\rm u}$ and to a lesser extent $BC_{\rm g}$, where the differences are larger than 10%. Systems *u* and *g* span the optical and line crowded region of the spectrum. Moreover, we showed that there is a clear correlation between effective temperature and 3D and 1D deviations (ΔBC): it decreases with increasing effective temperature.

The *Gaia* photometric system return 3D and 1D deviations of less than 3% with higher values for the bluer filter (BP). This effect should become important for future releases of *Gaia* data. For this purpose, part of the spectra presented in this work have already been provided to *Gaia* consortium-CU8.

We used the high-resolution spectra to denote the impact of the velocity gradient through the photosphere on the basic shape of the absorption lines. For this purpose, we reported the line bisectors of non-blended Fe I and Ca II triplet lines for different stars. We showed that weak lines (high excitation potential), which form in deeper layers, are more blueshifted than strong lines (low excitation potential), whose core and part of the wings are formed in higher layers.

As a final step to derive the overall convective shift for 3D simulations with respect to the reference 1D hydrostatic models, we cross-correlated each 3D spectrum with the corresponding 1D spectrum. The spanned values are between −0.235 and +0.361 km s^{-1}. We showed a net correlation of the convective shifts with the effective temperature: lower $T_{\rm eff}$ denotes redshifts and higher $T_{\rm eff}$ blueshifts; this result is in agreement with Allende Prieto et al. (2013). In addition, we quantified the differences in the convective shifts between a subset of the RHD simulations in this work and the corresponding CIFIST-grid simulations. The spanned shift values from the two grids are similar, and show smaller deviations at solar metallicity. The extraction of accurate radial velocities from RVS spectra need an appropriate wavelength calibration from convection shifts. The spectra presented in this work have been provided to *Gaia* consortium-CU6 to directly process the observed spectra in RVS pipeline.

We have made all the spectra publicly available for the community through the POLLUX database (Palacios et al. 2010). POLLUX[8] is a stellar spectra database proposing access to theoretical data including high-resolution synthetic spectra and spectral energy distributions from several model atmospheres. Continuous development either of the STAGGER-grid simulations or of the spectral synthesis calculations will be uploaded there in the future.

Acknowledgements. L.C. gratefully acknowledges support from the Australian Research Council (grants DP150100250, FT160100402). This work was granted access to the HPC resources of Observatoire de la Côte d'Azur – Mésocentre SIGAMM.

References

Allende Prieto, C., Asplund, M., García López, R. J., & Lambert, D. L. 2002, ApJ, 567, 544
Allende Prieto, C., Koesterke, L., Ludwig, H.-G., Freytag, B., & Caffau, E. 2013, A&A, 550, A103
Asplund, M. 2000, A&A, 359, 755
Asplund, M., Ludwig, H., Nordlund, Å., & Stein, R. F. 2000a, A&A, 359, 669
Asplund, M., Nordlund, Å., Trampedach, R., Allende Prieto, C., & Stein, R. F. 2000b, A&A, 359, 729
Asplund, M., Nordlund, Å., Trampedach, R., & Stein, R. F. 2000c, A&A, 359, 743

[7] For more details, see the technical note "3D spectral library for RVS radial velocities" (Chiavassa et al. 2014b) and the paper on CU6 design and performance (Sartoretti et al., in prep.).

[8] Available at http://pollux.oreme.org

Asplund, M., Grevesse, N., & Sauval, A. J. 2005, in Cosmic Abundances as Records of Stellar Evolution and Nucleosynthesis, eds. T. G. Barnes, III, & F. N. Bash, ASP Conf. Ser., 336, 25
Asplund, M., Grevesse, N., Sauval, A. J., & Scott, P. 2009, ARA&A, 47, 481
Bailer-Jones, C. A. L., Andrae, R., Arcay, B., et al. 2013, A&A, 559, A74
Bessell, M. S. 2000, PASP, 112, 961
Bessell M. S. 2011, PASP, 123, 1442
Bessell, M., & Murphy, S. 2012, PASP, 124, 140
Bessell, M., Bloxham, G., Schmidt, B., et al. 2011, PASP, 123, 789
Bigot, L., & Thévenin, F. 2006, MNRAS, 372, 609
Bigot, L., & Thévenin, F. 2008, in SF2A-2008, 3, eds. C. Charbonnel, F. Combes, & R. Samadi
Bigot, L., Mourard, D., Berio, P., et al. 2011, A&A, 534, L3
Bonifacio, P., Caffau, E., Ludwig, H.-G., et al. 2017, Mem. Soc. Astron. It., 88, 90
Brott, I., & Hauschildt, P. H. 2005, in The Three-Dimensional Universe with Gaia, ed. C. Turon, K. S. O'Flaherty, & M. A. C. Perryman, ESA SP, 576, 565
Caffau, E., Ludwig, H.-G., Steffen, M., Freytag, B., & Bonifacio, P. 2011, Sol. Phys., 268, 255
Cami, J., Sloan, G. C., Markwick-Kemper, A. J., et al. 2009, ApJ, 690, L122
Casagrande, L., & VandenBerg, D. A. 2014, MNRAS, 444, 392
Castelli, F., & Kurucz, R. L. 2004, ArXiv e-prints [arXiv:0405087]
Chiavassa, A., Plez, B., Josselin, E., & Freytag, B. 2009, A&A, 506, 1351
Chiavassa, A., Collet, R., Casagrande, L., & Asplund, M. 2010, A&A, 524, A93
Chiavassa, A., Bigot, L., Thévenin, F., et al. 2011, J. Phys. Conf. Ser., 328, 012012
Chiavassa, A., Bigot, L., Kervella, P., et al. 2012, A&A, 540, A5
Chiavassa, A., Ligi, R., Magic, Z., et al. 2014a, A&A, 567, A115
Chiavassa, A., Thévenin, F., Magic, Z., Collet, R., & Asplund, M. 2014b, 3D spectral library for RVS radial velocities, GAIA-C8-TN-OCA-AC-001-1, Tech. Rep.
Chiavassa, A., Thévenin, F., Magic, Z., Collet, R., & Asplund, M. 2014c, The 3D spectral library for BP/RP, GAIA-C8-TN-OCA-AC-002-1, Tech. Rep.
Chiavassa, A., Pere, C., Faurobert, M., et al. 2015, A&A, 576, A13
Chiavassa, A., Caldas, A., Selsis, F., et al. 2017, A&A, 597, A94
Cohen, M., Wheaton, W. A., & Megeath, S. T. 2003, AJ, 126, 1090
Collet, R., Asplund, M., & Trampedach, R. 2007, A&A, 469, 687
Creevey, O. L., Thévenin, F., Boyajian, T. S., et al. 2012, A&A, 545, A17
Deustua, S., Baggett, S., Brammer, G., et al. 2016, WFC3 Data Handbook. Version 3.0 (Baltimore: STScI) Tech. Rep.
Doi, M., Tanaka, M., Fukugita, M., et al. 2010, AJ, 139, 1628
Dravins, D. 1982, ARA&A, 20, 61
Dravins, D., Lindegren, L., & Nordlund, A. 1981, A&A, 96, 345
Gaia Collaboration (Prusti, T., et al.) 2016, A&A, 595, A1
Gray, D. F. 2009, ApJ, 697, 1032
Gray, D. F. 2010, ApJ, 721, 670
Gray, R. O., Graham, P. W., & Hoyt, S. R. 2001, AJ, 121, 2159
Gunn, J. E., Siegmund, W. A., Mannery, E. J., et al. 2006, AJ, 131, 2332
Gustafsson, B., Edvardsson, B., Eriksson, K., et al. 2008, A&A, 486, 951
Hayek, W., Asplund, M., Carlsson, M., et al. 2010, A&A, 517, A49
Hayek, W., Sing, D., Pont, F., & Asplund, M. 2012, A&A, 539, A102
Jordi, C., Gebran, M., Carrasco, J. M., et al. 2010, A&A, 523, A48
Jørgensen, U. G. 1997, IAU Symp., 178, 441
Katz, D., Munari, U., Cropper, M., et al. 2004, MNRAS, 354, 1223
Kurucz, R. L. 2005, Mem. Soc. Astron. It. Suppl., 8, 189
Lindegren, L., & Dravins, D. 2003, A&A, 401, 1185
Ludwig, H., Caffau, E., Steffen, M., et al. 2009, Mem. Soc. Astron. It., 80, 711
Magic, Z., Collet, R., Asplund, M., et al. 2013, A&A, 557, A26
Magic, Z., Collet, R., & Asplund, M. 2014, A&A, submitted [arXiv:1403.6245]
Magic, Z., Chiavassa, A., Collet, R., & Asplund, M. 2015, A&A, 573, A90
Megessier, C. 1995, A&A, 296, 771
Mihalas, D., Dappen, W., & Hummer, D. G. 1988, ApJ, 331, 815
Nordlund, A. 1982, A&A, 107, 1
Nordlund, Å., Stein, R. F., & Asplund, M. 2009, Liv. Rev. Sol. Phys., 6, 2
Palacios, A., Gebran, M., Josselin, E., et al. 2010, A&A, 516, A13
Pasquini, L., Melo, C., Chavero, C., et al. 2011, A&A, 526, A127
Pereira, T. M. D., Asplund, M., Collet, R., et al. 2013, A&A, 554, A118
Ramírez, I., Allende Prieto, C., & Lambert, D. L. 2008, A&A, 492, 841
Ramírez, I., Allende Prieto, C., Koesterke, L., Lambert, D. L., & Asplund, M. 2009, A&A, 501, 1087
Skartlien R. 2000, ApJ, 536, 465
Stempels, H. C., Piskunov, N., & Barklem, P. S. 2001, in 11th Cambridge Workshop on Cool Stars, Stellar Systems and the Sun, eds. R. J. Garcia Lopez, R. Rebolo, & M. R. Zapaterio Osorio, ASP Conf. Ser., 223, 878
Trampedach, R., Asplund, M., Collet, R., Nordlund, Å., & Stein, R. F. 2013, ApJ, 769, 18

Appendix A: One-dimensional versus three-dimensional bolometric corrections

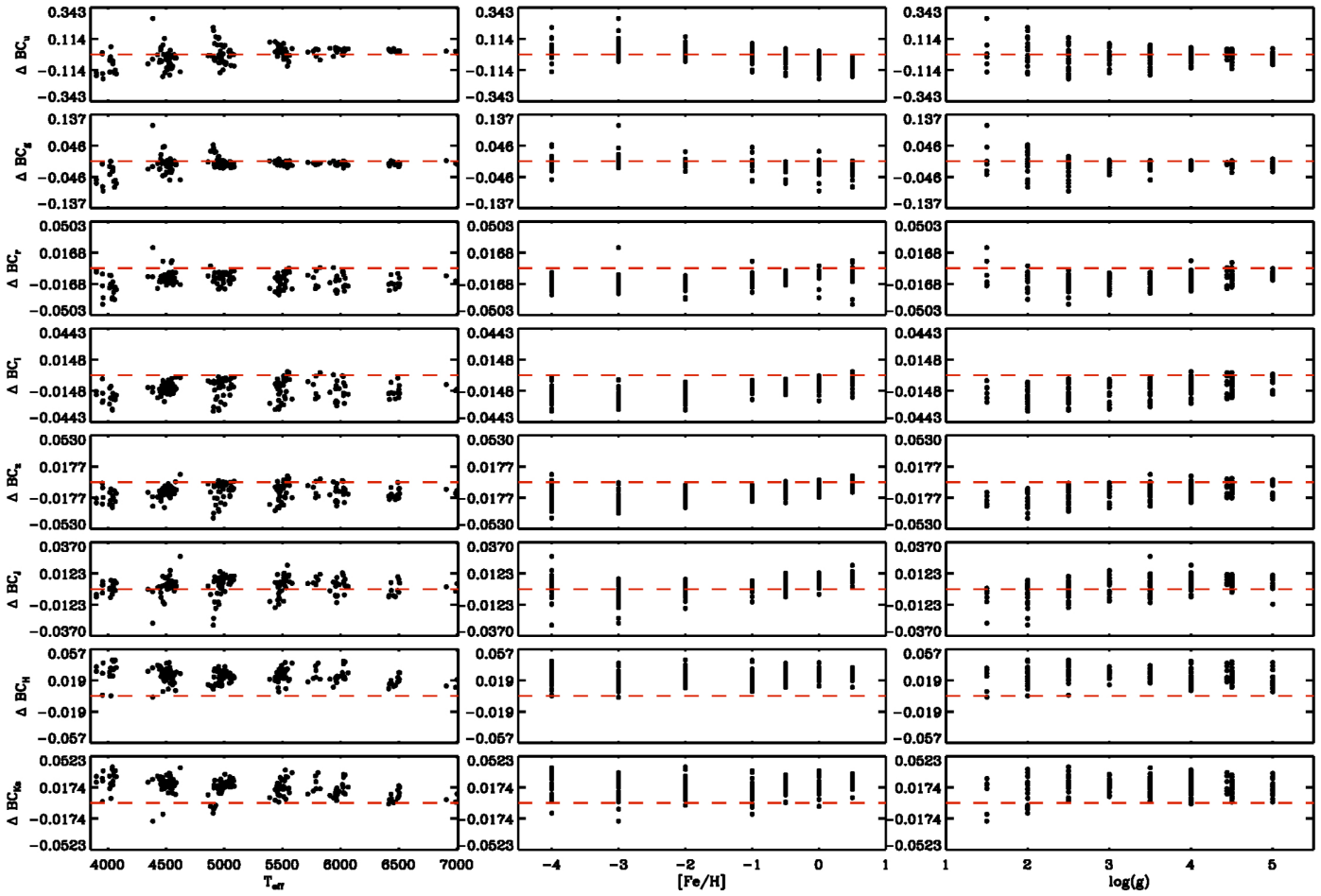

Fig. A.1. Bolometric correction (BC) differences computed for the photometric filters Johnson-Cousins and 2MASS with 3D simulations (Table B.1) and the corresponding 1D hydrostatic models with microturbulence = 1 km s^{-1}: $\Delta BC = BC_{1D} - BC_{3D}$. The red dashed line indicates $\Delta BC = 0.0$.

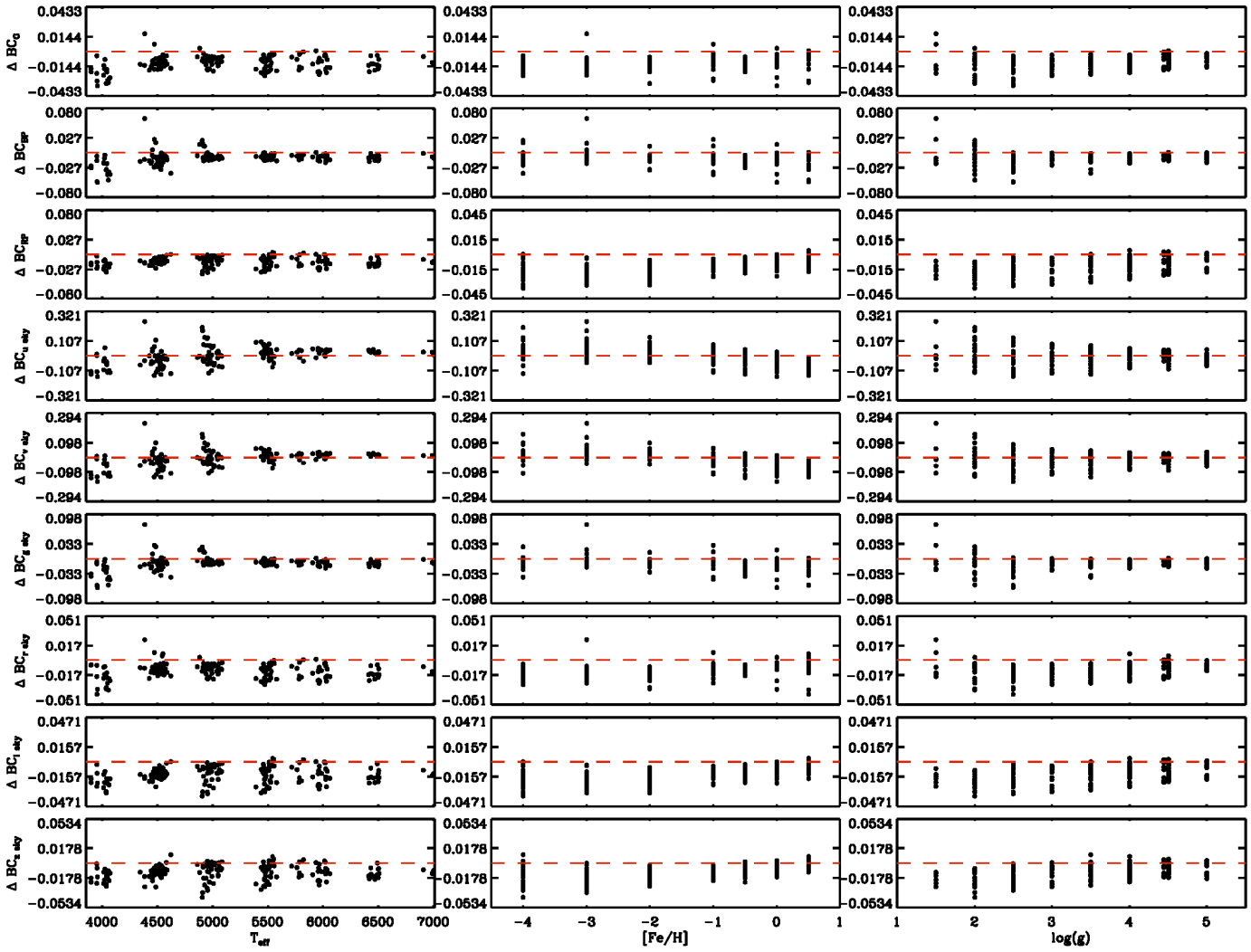

Fig. A.2. Bolometric correction differences for the SkyMapper and *Gaia* photometric filters (Table 1). The notation is the same as in Fig. A.1.

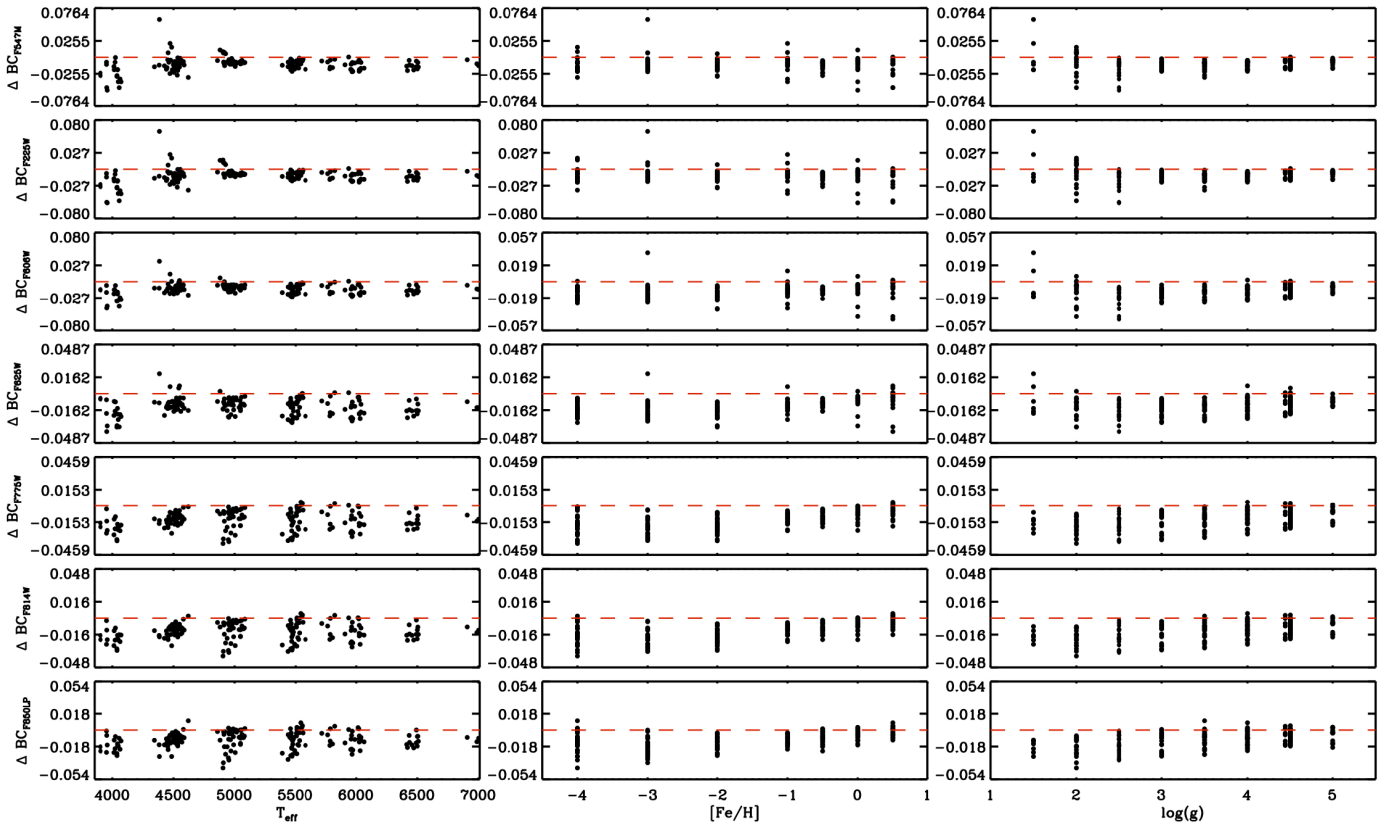

Fig. A.3. Bolometric correction differences for the HST-WFC3 provided in the VEGA system (for the ST and AB systems the differences are similar); first set of filters (Table 1). The notation is the same as in Fig. A.1.

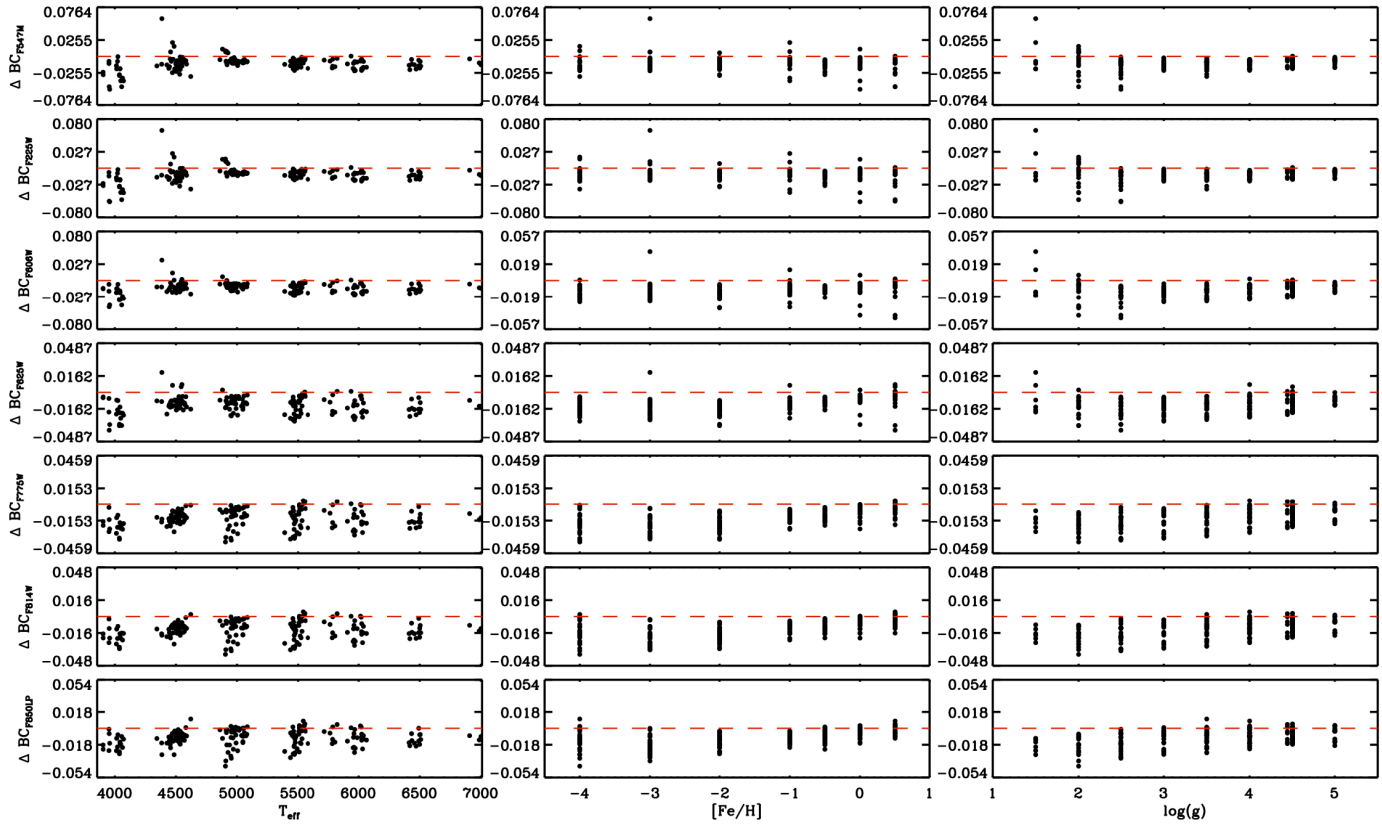

Fig. A.4. Bolometric correction differences for the HST-WFC3 provided in the VEGA system (for ST and AB systems the differences are similar); second set of filters (Table 1). The notation is the same as in Fig. A.1.

Appendix B

Table B.1. RHD simulations' stellar parameters (first three cols.), bolometric Magnitude (M_{bol}), and bolometric correction (*BC*) for Johnson-Cousins, 2MASS, SDSS, and *Gaia* systems (Table 1).

T_{eff}	log g	[Fe/H]	M_{bol}	BC_U	BC_B	BC_V	BC_R	BC_I	BC_J	BC_H	BC_{Ks}	BC_u	BC_g	BC_r	BC_i	BC_z	BC_G	BC_{BP}	BC_{RP}
4014.99	1.50	0.0	6.320	−3.75310	−2.26910	−0.90560	−0.14050	0.53170	1.58810	2.32330	2.53140	−4.67960	−1.63880	−0.43510	0.02130	0.31350	−0.42180	−1.17700	0.44010
4042.38	1.50	−1.0	6.291	−3.11690	−2.12650	−0.86970	−0.13680	0.52720	1.55730	2.32870	2.50310	−4.01150	−1.54990	−0.42970	0.02220	0.30510	−0.40820	−1.13330	0.43660
4021.90	1.50	−2.0	6.313	−3.24590	−2.23800	−0.90050	−0.14700	0.53780	1.56940	2.32730	2.50270	−4.17080	−1.62720	−0.44840	0.02840	0.32220	−0.42050	−1.17860	0.44480
3951.92	1.50	−3.0	6.389	−3.90090	−2.60760	−1.04190	−0.19200	0.56190	1.61550	2.33340	2.52470	−4.86820	−1.90680	−0.52040	0.03670	0.36450	−0.46890	−1.33700	0.46060
4070.69	2.00	0.0	6.260	−3.47470	−2.14830	−0.85400	−0.10740	0.54590	1.57170	2.29980	2.49240	−4.39490	−1.55290	−0.39570	0.04140	0.31920	−0.38850	−1.11670	0.45590
4056.19	2.00	0.5	6.276	−3.85400	−2.25760	−0.92060	−0.14870	0.56010	1.60690	2.29380	2.50930	−4.79910	−1.63670	−0.45150	0.03890	0.34310	−0.41620	−1.18640	0.45950
3899.43	2.00	−0.5	6.447	−3.49590	−2.36970	−1.05820	−0.25620	0.49620	1.59210	2.40180	2.59540	−4.40270	−1.78920	−0.57300	−0.03710	0.29980	−0.51130	−1.31650	0.39120
4047.76	2.00	−1.0	6.285	−2.91330	−2.07200	−0.87100	−0.14040	0.52420	1.55180	2.32650	2.49650	−3.79910	−1.52820	−0.43160	0.01740	0.30250	−0.40790	−1.12290	0.43260
4037.03	2.00	−2.0	6.296	−2.95540	−2.11670	−0.86700	−0.13370	0.53570	1.55820	2.31110	2.48410	−3.86190	−1.54730	−0.42860	0.02910	0.31640	−0.40330	−1.13120	0.44430
4013.24	2.00	−3.0	6.322	−3.35520	−2.30150	−0.90580	−0.12690	0.58160	1.58900	2.27120	2.46040	−4.30180	−1.66740	−0.43730	0.06690	0.36920	−0.40050	−1.19080	0.48470
4025.21	2.00	−4.0	6.309	−3.55980	−2.40540	−0.92680	−0.10890	0.63070	1.60940	2.21870	2.41580	−4.52770	−1.73930	−0.43200	0.10980	0.42170	−0.38300	−1.21920	0.52890
3958.11	2.50	0.0	6.382	−3.56660	−2.32010	−1.02810	−0.23570	0.51510	1.59780	2.37820	2.57360	−4.48420	−1.74370	−0.54840	−0.01940	0.31200	−0.48920	−1.28330	0.40730
3953.50	2.50	0.5	6.387	−3.80950	−2.40470	−1.11480	−0.30470	0.52780	1.63440	2.37350	2.58690	−4.74740	−1.81650	−0.64260	−0.02810	0.33840	−0.52750	−1.37160	0.40560
3899.65	2.50	−0.5	6.447	−3.38240	−2.35470	−1.08720	−0.28100	0.50300	1.60010	2.40430	2.59230	−4.28350	−1.80050	−0.60420	−0.04080	0.31030	−0.52270	−1.33810	0.39050
4063.17	2.50	−1.0	6.268	−2.78900	−2.03250	−0.86810	−0.13650	0.53330	1.55190	2.31450	2.48120	−3.66800	−1.51230	−0.42730	0.02380	0.31040	−0.40060	−1.11150	0.43930
4037.59	2.50	−2.0	6.296	−2.77250	−2.05380	−0.85520	−0.12540	0.53900	1.55450	2.29540	2.46930	−3.66430	−1.51240	−0.41780	0.03300	0.31850	−0.39290	−1.10840	0.44790
4042.85	2.50	−3.0	6.290	−2.93700	−2.11110	−0.83090	−0.09010	0.59520	1.57280	2.21440	2.40930	−3.85780	−1.52630	−0.39140	0.08580	0.37500	−0.35830	−1.10360	0.50040
3951.87	2.50	−4.0	6.389	−3.26910	−2.30040	−0.89860	−0.09830	0.63760	1.61510	2.16480	2.38120	−4.21420	−1.66940	−0.41890	0.11610	0.43080	−0.36630	−1.18290	0.53650
4472.00	1.50	−1.0	5.852	−2.21550	−1.56460	−0.51380	0.07860	0.62940	1.46770	2.05830	2.20120	−3.09040	−1.04910	−0.17990	0.15820	0.35350	−0.18650	−0.76800	0.55020
4384.64	1.50	−3.0	5.938	−2.61300	−1.81900	−0.61560	0.05090	0.66850	1.51840	2.07870	2.23480	−3.54550	−1.25530	−0.22970	0.18080	0.41100	−0.22330	−0.89270	0.57920
4554.69	2.00	0.0	5.772	−2.44380	−1.54790	−0.46730	0.13820	0.65260	1.46810	2.00720	2.16230	−3.33110	−1.01620	−0.11140	0.18970	0.36460	−0.14540	−0.71970	0.57920
4461.67	2.00	−0.5	5.862	−2.29270	−1.57500	−0.52280	0.08150	0.62970	1.47180	2.06290	2.20930	−3.16770	−1.06080	−0.17630	0.15810	0.35420	−0.18760	−0.77230	0.55100
4498.97	2.00	−1.0	5.826	−2.02690	−1.49220	−0.50110	0.07720	0.61920	1.45210	2.04650	2.18410	−2.89380	−1.00370	−0.17790	0.14940	0.34140	−0.18180	−0.74320	0.54090
4452.94	2.00	−2.0	5.871	−2.06200	−1.55860	−0.53160	0.06150	0.62690	1.46640	2.05450	2.19950	−2.94780	−1.06070	−0.20060	0.15090	0.35670	−0.19770	−0.78270	0.54490
4455.77	2.00	−3.0	5.868	−2.19880	−1.62250	−0.54530	0.07300	0.65900	1.48290	2.03060	2.18220	−3.10880	−1.11000	−0.19620	0.17840	0.39140	−0.19120	−0.80530	0.57330
4485.37	2.00	−4.0	5.839	−2.18230	−1.61150	−0.53590	0.08540	0.67470	1.48090	2.00600	2.15740	−3.10140	−1.10450	−0.18510	0.19360	0.40570	−0.17930	−0.79680	0.58790
4533.90	2.50	0.0	5.792	−2.42220	−1.54340	−0.48380	0.12230	0.64140	1.46840	2.02900	2.17920	−3.31120	−1.02400	−0.12760	0.17660	0.35660	−0.15770	−0.73070	0.56730
4470.97	2.50	0.5	5.853	−2.96950	−1.69780	−0.54020	0.11300	0.65080	1.50870	2.05830	2.22920	−3.89340	−1.13610	−0.14310	0.18090	0.37280	−0.17980	−0.79450	0.57530
4503.34	2.50	−0.5	5.822	−2.14420	−1.51100	−0.50420	0.08910	0.62890	1.45710	2.04320	2.18270	−3.01490	−1.01820	−0.16560	0.15940	0.34990	−0.17610	−0.74480	0.55090
4508.09	2.50	−1.0	5.817	−1.92660	−1.46250	−0.50400	0.07270	0.61160	1.44500	2.04480	2.17960	−2.78780	−0.99160	−0.18090	0.14210	0.33360	−0.18380	−0.73710	0.53370
4426.04	2.50	−2.0	5.897	−1.96700	−1.54550	−0.54940	0.04450	0.60950	1.46430	2.06960	2.21620	−2.84060	−1.06370	−0.21680	0.13270	0.34180	−0.21180	−0.79080	0.52790
4477.40	2.50	−3.0	5.847	−1.95290	−1.53210	−0.52230	0.07420	0.64670	1.46370	2.00770	2.16010	−2.84360	−1.04790	−0.19010	0.16890	0.37590	−0.18320	−0.77040	0.56270
4535.29	2.50	−4.0	5.791	−1.84490	−1.47630	−0.49410	0.09330	0.66230	1.45020	1.96320	2.11390	−2.74040	−1.00810	−0.16990	0.18550	0.38710	−0.16180	−0.73980	0.57780
4508.67	3.00	0.0	5.817	−2.43240	−1.55940	−0.50960	0.10690	0.63360	1.47190	2.05230	2.19880	−3.32140	−1.05050	−0.14450	0.16670	0.35230	−0.17220	−0.75060	0.55840
4490.40	3.00	0.5	5.834	−2.82400	−1.65450	−0.53470	0.11420	0.64960	1.49830	2.05480	2.21750	−3.74320	−1.11560	−0.14020	0.18030	0.37020	−0.17570	−0.78140	0.57380
4503.05	3.00	−1.0	5.822	−1.89600	−1.46140	−0.51820	0.06670	0.60620	1.44450	2.05290	2.18560	−2.75320	−1.00280	−0.18660	0.13630	0.32910	−0.19030	−0.74390	0.52820
4559.76	3.00	−2.0	5.768	−1.66470	−1.38800	−0.47670	0.08100	0.61510	1.42270	1.98970	2.12750	−2.52520	−0.93990	−0.17070	0.14680	0.33350	−0.16840	−0.70350	0.53670
4555.30	3.00	−3.0	5.772	−1.67820	−1.41150	−0.47620	0.09230	0.64410	1.43190	1.94970	2.10060	−2.55210	−0.95830	−0.16520	0.17160	0.36490	−0.15810	−0.71090	0.56230
4534.50	3.00	−4.0	5.792	−1.69370	−1.43200	−0.48720	0.09140	0.65760	1.43870	1.93500	2.09420	−2.57560	−0.98030	−0.17060	0.18120	0.38190	−0.15880	−0.72490	0.57340
4548.87	3.50	0.0	5.778	−2.35730	−1.52710	−0.49890	0.11790	0.64060	1.46320	2.03430	2.17580	−3.24060	−1.03220	−0.13180	0.17550	0.35520	−0.16090	−0.73350	0.56530
4531.27	3.50	0.5	5.795	−2.71390	−1.61440	−0.52540	0.12180	0.65650	1.48990	2.04020	2.19570	−3.62570	−1.09490	−0.13100	0.18760	0.37340	−0.16580	−0.76460	0.57940
4344.11	3.50	−0.5	5.978	−2.42410	−1.70320	−0.64420	0.02020	0.60920	1.50070	2.14480	2.29230	−3.29750	−1.21390	−0.24690	0.12480	0.34900	−0.25070	−0.87740	0.52410
4573.06	3.50	−1.0	5.755	−1.78470	−1.39920	−0.48670	0.08940	0.61390	1.42690	2.01210	2.14120	−2.63660	−0.95540	−0.15930	0.14840	0.32930	−0.16750	−0.70500	0.53750
4508.84	3.50	−2.0	5.816	−1.72960	−1.43710	−0.50780	0.07100	0.61480	1.43680	2.00740	2.15330	−2.58590	−0.98660	−0.18370	0.14390	0.33770	−0.18240	−0.73290	0.53540
4571.34	3.50	−3.0	5.757	−1.59330	−1.38170	−0.46480	0.10020	0.64940	1.42240	1.91350	2.07260	−2.45980	−0.93710	−0.15650	0.17770	0.36800	−0.14850	−0.69500	0.56760
4620.85	3.50	−4.0	5.710	−1.46630	−1.32610	−0.44540	0.10780	0.65470	1.40480	1.87300	2.03130	−2.33620	−0.90080	−0.14800	0.18350	0.37040	−0.13610	−0.67120	0.57240
4524.22	4.00	0.0	5.802	−2.43030	−1.57480	−0.53140	0.10760	0.64220	1.47270	2.05380	2.19560	−3.31140	−1.08310	−0.14460	0.17420	0.35930	−0.17440	−0.76270	0.56480
4549.22	4.00	0.5	5.778	−2.65660	−1.61150	−0.53480	0.11940	0.66340	1.48930	2.03670	2.18880	−3.56000	−1.10480	−0.13440	0.19200	0.37930	−0.16630	−0.76890	0.58340
4441.77	4.00	−0.5	5.881	−2.28050	−1.60600	−0.58340	0.06360	0.62690	1.47940	2.08810	2.22950	−3.14810	−1.13150	−0.19600	0.15070	0.35490	−0.20920	−0.81060	0.54490
4587.16	4.00	−1.0	5.742	−1.79580	−1.40010	−0.48760	0.09840	0.62010	1.42670	2.00310	2.13310	−2.64530	−0.96180	−0.14950	0.15580	0.33330	−0.16230	−0.70200	0.54390
4524.97	4.00	−2.0	5.801	−1.72580	−1.42910	−0.50050	0.08470	0.62750	1.43500	1.98070	2.13130	−2.57980	−0.98180	−0.16980	0.15730	0.34810	−0.17090	−0.72310	0.54790
4517.64	4.00	−3.0	5.808	−1.66100	−1.42450	−0.48450	0.09720	0.65910	1.43670	1.90820	2.08050	−2.52650	−0.97230	−0.16350	0.18420	0.38210	−0.15380	−0.71680	0.57570
4580.60	4.00	−4.0	5.748	−1.49510	−1.35310	−0.45580	0.10980	0.66660	1.41430	1.85260	2.02610	−2.36350	−0.92270	−0.14940	0.19310	0.38520	−0.13590	−0.68330	0.58300
4532.22	4.50	0.0	5.794	−2.46210	−1.59380	−0.54300	0.11020	0.65210	1.47610	2.04950	2.19140	−3.33990	−1.10600	−0.14280	0.18240	0.36800	−0.17400	−0.77120	0.57240
4543.15	4.50	0.5	5.783	−2.65550	−1.64110	−0.55840	0.11090	0.67100	1.49540	2.04080	2.19370	−3.55180	−1.14040	−0.14560	0.19540	0.38810	−0.17420	−0.78970	0.58690
4383.32	4.50	−0.5	5.939	−2.44210	−1.70270	−0.63540	0.04670	0.63370	1.49980	2.11150	2.25940	−3.31230	−1.22150	−0.21880	0.15100	0.36780	−0.23090	−0.86400	0.54770
4569.29	4.50	−1.0	5.759	−1.88740	−1.44200	−0.50720	0.10140	0.63080	1.43760	2.00870	2.14160	−2.73700	−1.00230	−0.14850	0.16470	0.34510	−0.16530	−0.72080	0.55310
4502.45	4.50	−2.0	5.823	−1.80750	−1.46400	−0.51140	0.09260	0.64530	1.44530	1.96500	2.12500	−2.66330	−1.01120	−0.16520	0.17310	0.36750	−0.16720	−0.73560	0.56420
4526.03	5.00	0.0	5.800	−2.53060	−1.63450	−0.56170	0.11040	0.66540	1.48360	2.04650	2.19060	−3.40670	−1.14470	−0.14510	0.19250	0.38170	−0.17640	−0.78950	0.58260

Table B.1. continued.

$T_{\rm eff}$	log g	[Fe/H]	$M_{\rm bol}$	$BC_{\rm U}$	$BC_{\rm B}$	$BC_{\rm V}$	$BC_{\rm R}$	$BC_{\rm I}$	$BC_{\rm J}$	$BC_{\rm H}$	$BC_{\rm Ks}$	$BC_{\rm u}$	$BC_{\rm g}$	$BC_{\rm r}$	$BC_{\rm i}$	$BC_{\rm z}$	$BC_{\rm G}$	$BC_{\rm BP}$	$BC_{\rm RP}$
4447.10	5.00	−0.5	5.876	−2.38690	−1.65720	−0.59700	0.08140	0.65580	1.48830	2.06250	2.21000	−3.25500	−1.17990	−0.18080	0.17770	0.38180	−0.19960	−0.82390	0.57090
4535.47	5.00	−1.0	5.791	−2.02130	−1.50860	−0.53300	0.10480	0.65280	1.45520	2.00600	2.14670	−2.87420	−1.06100	−0.14990	0.18190	0.36990	−0.16790	−0.74980	0.57140
4881.31	2.00	0.0	5.472	−1.85600	−1.25750	−0.31260	0.22580	0.68500	1.37760	1.81390	1.95050	−2.72730	−0.78050	−0.00840	0.23980	0.36540	−0.04640	−0.54830	0.61700
4915.99	2.00	−1.0	5.441	−1.44220	−1.13310	−0.30090	0.18660	0.65110	1.33750	1.79320	1.91320	−2.30660	−0.70420	−0.04620	0.20420	0.33450	−0.05710	−0.52190	0.58110
4926.40	2.00	−2.0	5.432	−1.34090	−1.10990	−0.30720	0.17860	0.65220	1.33030	1.77580	1.89650	−2.22010	−0.70160	−0.05610	0.20220	0.33790	−0.06010	−0.52350	0.57980
4907.94	2.00	−3.0	5.448	−1.33290	−1.11580	−0.31880	0.17220	0.65590	1.33580	1.77730	1.90090	−2.22150	−0.71570	−0.06510	0.20260	0.34500	−0.06540	−0.53470	0.58150
4905.26	2.00	−4.0	5.450	−1.31800	−1.11680	−0.32140	0.17000	0.65720	1.33590	1.77420	1.89900	−2.20890	−0.71960	−0.06810	0.20270	0.34730	−0.06690	−0.53770	0.58210
5015.94	2.50	0.0	5.353	−1.62160	−1.12750	−0.26400	0.24070	0.67640	1.33360	1.75120	1.87470	−2.48800	−0.68310	0.01380	0.23750	0.34640	−0.02060	−0.48580	0.61100
4950.97	2.50	−0.5	5.410	−1.46410	−1.12260	−0.28930	0.20120	0.65640	1.33150	1.77560	1.89620	−2.32290	−0.69250	−0.02930	0.21170	0.33560	−0.04630	−0.50820	0.58770
4965.89	2.50	−1.0	5.397	−1.30120	−1.07870	−0.29020	0.18260	0.63700	1.31510	1.77130	1.88540	−2.15760	−0.66800	−0.04680	0.19220	0.31700	−0.05470	−0.50120	0.56810
4939.03	2.50	−2.0	5.421	−1.22650	−1.08470	−0.30980	0.16770	0.63670	1.31660	1.76870	1.88800	−2.09240	−0.68770	−0.06530	0.18740	0.32160	−0.06650	−0.51850	0.56490
4948.74	2.50	−3.0	5.412	−1.18400	−1.07210	−0.31190	0.16680	0.64250	1.31290	1.74910	1.87140	−2.05810	−0.68720	−0.06770	0.19100	0.32840	−0.06530	−0.51850	0.56890
4953.38	2.50	−4.0	5.408	−1.15390	−1.06350	−0.31300	0.16320	0.64060	1.30950	1.74280	1.86550	−2.03030	−0.68490	−0.07170	0.18830	0.32720	−0.06690	−0.51840	0.56660
5010.39	3.00	0.0	5.358	−1.60350	−1.12280	−0.26930	0.23460	0.67050	1.33290	1.75990	1.88080	−2.46850	−0.68320	0.00800	0.23110	0.34180	−0.02510	−0.48820	0.60510
4963.15	3.00	0.5	5.399	−2.01830	−1.22030	−0.28690	0.25740	0.69550	1.37290	1.78610	1.92160	−2.90900	−0.74410	0.02810	0.25630	0.36760	−0.02140	−0.51540	0.63150
4912.91	3.00	−0.5	5.444	−1.48350	−1.14370	−0.31040	0.18750	0.64870	1.34060	1.80810	1.92460	−2.33910	−0.71470	−0.04420	0.20190	0.33170	−0.06000	−0.52690	0.57930
4990.00	3.00	−1.0	5.376	−1.23520	−1.05870	−0.28900	0.18010	0.63000	1.30440	1.76130	1.87240	−2.08530	−0.65640	−0.04790	0.18620	0.30840	−0.05510	−0.49430	0.56170
4991.62	3.00	−2.0	5.375	−1.10840	−1.04440	−0.29980	0.16590	0.62510	1.29330	1.73740	1.85460	−1.96400	−0.65950	−0.06400	0.17830	0.30590	−0.06390	−0.50080	0.55440
4970.32	3.00	−3.0	5.393	−1.08960	−1.05480	−0.31250	0.16100	0.63320	1.29860	1.72860	1.85230	−1.95230	−0.67740	−0.07250	0.18260	0.31770	−0.06820	−0.51360	0.56000
5005.01	3.00	−4.0	5.363	−1.02090	−1.02550	−0.30670	0.15890	0.62840	1.28370	1.70360	1.82670	−1.88520	−0.66040	−0.07370	0.17810	0.31130	−0.06660	−0.50360	0.55520
5011.53	3.50	0.0	5.357	−1.60830	−1.11830	−0.27140	0.23210	0.66630	1.33220	1.76670	1.88440	−2.47170	−0.68150	0.00630	0.22730	0.33790	−0.02680	−0.48760	0.60130
4988.91	3.50	0.5	5.377	−1.94540	−1.19200	−0.28030	0.25750	0.69200	1.36290	1.77640	1.90760	−2.83360	−0.72660	0.02990	0.25360	0.36300	−0.01820	−0.50420	0.62830
4917.82	3.50	−0.5	5.439	−1.47540	−1.13940	−0.31360	0.18630	0.64600	1.33880	1.81020	1.92450	−2.32810	−0.71460	−0.04500	0.19960	0.32890	−0.06120	−0.52660	0.57690
4975.93	3.50	−1.0	5.388	−1.23620	−1.06800	−0.29970	0.17470	0.62560	1.30730	1.77390	1.88400	−2.08140	−0.66750	−0.05340	0.18150	0.30520	−0.06130	−0.50220	0.55730
5036.62	3.50	−2.0	5.336	−1.03470	−1.01790	−0.29250	0.16610	0.61710	1.27520	1.71280	1.82790	−1.88270	−0.64050	−0.06150	0.17250	0.29440	−0.06140	−0.48780	0.54740
5047.83	3.50	−3.0	5.326	−0.96660	−1.00740	−0.29740	0.16210	0.62210	1.26750	1.68170	1.80270	−1.82030	−0.64280	−0.06790	0.17490	0.30090	−0.06260	−0.49050	0.55030
5047.65	3.50	−4.0	5.326	−0.92830	−1.00340	−0.30440	0.15450	0.61880	1.26280	1.67270	1.79580	−1.78380	−0.64680	−0.07650	0.17000	0.29900	−0.06810	−0.49560	0.54600
4992.30	4.00	0.0	5.374	−1.65750	−1.13970	−0.28430	0.22940	0.66690	1.33920	1.78180	1.89940	−2.51940	−0.70140	0.00290	0.22730	0.34010	−0.03200	−0.49910	0.60170
5083.68	4.00	0.5	5.295	−1.81620	−1.12350	−0.24970	0.27320	0.69200	1.33530	1.73100	1.85530	−2.69810	−0.67430	0.05010	0.25840	0.35530	0.00120	−0.46590	0.63020
4910.47	4.00	−0.5	5.446	−1.50710	−1.15360	−0.32320	0.18670	0.64700	1.34290	1.81920	1.93320	−2.35760	−0.72940	−0.04480	0.20080	0.33020	−0.06370	−0.53380	0.57810
4956.78	4.00	−1.0	5.405	−1.26990	−1.08980	−0.31280	0.17380	0.62680	1.31480	1.78840	1.89940	−2.11150	−0.68840	−0.05490	0.18240	0.30750	−0.06600	−0.51360	0.55850
5059.64	4.00	−2.0	5.316	−1.00690	−1.01250	−0.28900	0.16920	0.61650	1.26760	1.69860	1.81470	−1.84930	−0.63570	−0.05750	0.17320	0.29180	−0.05880	−0.48260	0.54730
5049.09	4.00	−3.0	5.325	−0.95400	−1.01840	−0.29950	0.16420	0.62660	1.26650	1.66930	1.79600	−1.80280	−0.65070	−0.06660	0.17910	0.30530	−0.06210	−0.49370	0.55430
5072.94	4.00	−4.0	5.304	−0.88740	−0.99970	−0.30200	0.15690	0.61980	1.25250	1.64710	1.77460	−1.73790	−0.64440	−0.07400	0.17170	0.29840	−0.06600	−0.49210	0.54710
4982.27	4.50	0.0	5.383	−1.72500	−1.16460	−0.29680	0.23170	0.67060	1.34610	1.79300	1.91140	−2.58520	−0.72470	0.00480	0.23130	0.34400	−0.03450	−0.50950	0.60550
5056.36	4.50	0.5	5.319	−1.88710	−1.15520	−0.26760	0.26980	0.69220	1.34570	1.75190	1.87680	−2.76700	−0.70440	0.04610	0.25810	0.35810	−0.00620	−0.48200	0.63050
4953.63	4.50	−1.0	5.408	−1.30860	−1.10260	−0.31920	0.17860	0.63060	1.31920	1.79400	1.90580	−2.14780	−0.70140	-0.05010	0.18690	0.31060	−0.06550	−0.51780	0.56260
4976.19	4.50	−2.0	5.388	−1.12990	−1.07590	−0.31240	0.17020	0.63070	1.29880	1.73600	1.86150	−1.97110	−0.68450	−0.06050	0.18430	0.31130	−0.06570	−0.51170	0.56000
5079.81	4.50	−3.0	5.299	−0.93440	−1.00930	−0.28990	0.17290	0.63270	1.25750	1.63920	1.77090	−1.78110	−0.64150	−0.05750	0.18640	0.30880	−0.05410	−0.48420	0.56050
4969.79	4.50	−4.0	5.394	−0.99560	−1.06860	−0.32560	0.15760	0.64080	1.28800	1.67600	1.81900	−1.84780	−0.69690	−0.07950	0.18760	0.32670	−0.07210	−0.52490	0.56540
4976.20	5.00	0.0	5.388	−1.80450	−1.18960	−0.30900	0.23590	0.67520	1.35290	1.80360	1.92170	−2.66340	−0.74840	0.00890	0.23660	0.34830	−0.03580	−0.51910	0.61050
4953.82	5.00	0.5	5.408	−2.06940	−1.26350	−0.32520	0.25260	0.69740	1.38040	1.81150	1.94240	−2.94810	−0.80270	0.02370	0.25750	0.37140	−0.03290	−0.54080	0.63250
4860.02	5.00	−0.5	5.491	−1.69170	−1.22730	−0.35980	0.18960	0.65750	1.36700	1.85490	1.97290	−2.54240	−0.79760	−0.04420	0.21030	0.34330	−0.07360	−0.56810	0.58820
4971.82	5.00	−1.0	5.392	−1.34160	−1.10480	−0.31670	0.18980	0.63850	1.31870	1.78420	1.89690	−2.17970	−0.70420	−0.03820	0.19630	0.31600	−0.05840	−0.51340	0.57090
4980.19	5.00	−2.0	5.385	−1.16660	−1.08500	−0.30950	0.18140	0.64380	1.30190	1.72070	1.85140	−2.00770	−0.69000	−0.05020	0.19760	0.32340	−0.05790	−0.51010	0.57260
5043.95	5.00	−3.0	5.329	−0.98540	−1.03600	−0.29540	0.17780	0.64540	1.27090	1.64160	1.78140	−1.83240	−0.66010	−0.05510	0.19740	0.32370	−0.05260	−0.49410	0.57210
4950.01	5.00	−4.0	5.411	−1.02750	−1.08610	−0.32710	0.16400	0.65270	1.29530	1.66540	1.81680	−1.88020	−0.70860	−0.07490	0.19850	0.33960	−0.06840	−0.52960	0.57640
5390.37	2.50	−2.0	5.041	−0.82020	−0.79850	−0.19050	0.20750	0.60490	1.16860	1.52300	1.62440	−1.69170	−0.46740	−0.00540	0.17540	0.25740	−0.00210	−0.36480	0.54180
5436.69	2.50	−3.0	5.004	−0.74360	−0.76850	−0.19050	0.19770	0.59290	1.14600	1.49030	1.59150	−1.61830	−0.45280	−0.01400	0.16340	0.24430	−0.00580	−0.35830	0.52960
5459.13	3.00	0.0	4.986	−1.08180	−0.83640	−0.13880	0.27850	0.65050	1.18980	1.51360	1.61770	−1.94170	−0.45620	0.07000	0.22980	0.28990	0.04550	−0.33170	0.59260
5479.60	3.00	−0.5	4.970	−0.90320	−0.79180	−0.14620	0.24700	0.62080	1.16170	1.49630	1.59370	−1.76010	−0.43380	0.03930	0.19900	0.26220	0.02950	−0.32920	0.56200
5476.23	3.00	−1.0	4.972	−0.81420	−0.78110	−0.16190	0.22670	0.60550	1.14950	1.48940	1.58670	−1.67100	−0.43750	0.01810	0.18220	0.24920	0.01520	−0.33830	0.54560
5509.14	3.00	−2.0	4.946	−0.69810	−0.75540	−0.18090	0.20020	0.58320	1.12170	1.45720	1.55500	−1.55960	−0.43710	−0.00860	0.15760	0.22820	−0.00280	−0.34620	0.52160
5459.30	3.00	−3.0	4.986	−0.67650	−0.77320	−0.20260	0.18300	0.57740	1.12910	1.47530	1.57530	−1.53840	−0.46070	−0.02840	0.14800	0.22770	−0.01860	−0.36700	0.51380
5469.82	3.00	−4.0	4.977	−0.65020	−0.77020	−0.20640	0.17690	0.57180	1.12170	1.46520	1.56580	−1.51210	−0.46190	−0.03460	0.14200	0.22230	−0.02310	−0.36940	0.50800
5560.38	3.50	0.0	4.906	−0.96890	−0.78500	−0.12210	0.27880	0.63790	1.15520	1.46520	1.56360	−1.82320	−0.41820	0.07400	0.22080	0.27090	0.05240	−0.30700	0.58140
5505.98	3.50	−0.5	4.949	−0.86310	−0.78730	−0.14720	0.24470	0.61600	1.15180	1.48590	1.58080	−1.71280	−0.43160	0.03770	0.19500	0.25570	0.02780	−0.32770	0.55740
5450.91	3.50	−1.0	4.992	−0.79730	−0.80110	−0.17530	0.21780	0.60060	1.15430	1.50760	1.60290	−1.64430	−0.45460	0.00820	0.17600	0.24610	0.00530	−0.35150	0.54010
5467.28	3.50	−2.0	4.979	−0.69010	−0.79070	−0.19890	0.19070	0.58080	1.13170	1.48070	1.57850	−1.54010	−0.46540	−0.02010	0.15330	0.22870	−0.01530	−0.36650	0.51820
5474.46	3.50	−3.0	4.974	−0.63520	−0.78550	−0.21190	0.17500	0.57030	1.11900	1.46290	1.56310	−1.48740	−0.47210	−0.03680	0.14080	0.22000	−0.02700	−0.37560	0.50640
5490.94	3.50	−4.0	4.960	−0.60100	−0.78120	−0.21870	0.16520	0.56060	1.10820	1.45220	1.55150	−1.45300	−0.47410	−0.04640	0.13060	0.21050	−0.03450	−0.37960	0.49650

Table B.1. continued.

$T_{\rm eff}$	log g	[Fe/H]	$M_{\rm bol}$	$BC_{\rm U}$	$BC_{\rm B}$	$BC_{\rm V}$	$BC_{\rm R}$	$BC_{\rm I}$	$BC_{\rm J}$	$BC_{\rm H}$	$BC_{\rm Ks}$	$BC_{\rm u}$	$BC_{\rm g}$	$BC_{\rm r}$	$BC_{\rm i}$	$BC_{\rm z}$	$BC_{\rm G}$	$BC_{\rm BP}$	$BC_{\rm RP}$
5509.78	4.00	0.0	4.946	−1.02250	−0.81670	−0.13570	0.27720	0.64210	1.17320	1.49830	1.59590	−1.87210	−0.44260	0.07070	0.22330	0.27800	0.04630	−0.32270	0.58500
5542.42	4.00	0.5	4.920	−1.21110	−0.83140	−0.11970	0.31630	0.67320	1.18930	1.48680	1.59160	−2.07400	−0.44380	0.10990	0.25810	0.30310	0.07120	−0.31040	0.61820
5513.71	4.00	−0.5	4.943	−0.85020	−0.78790	−0.14990	0.24220	0.61180	1.14860	1.48830	1.57990	−1.69360	−0.43210	0.03570	0.19130	0.25090	0.02550	−0.32850	0.55340
5437.76	4.00	−1.0	5.003	−0.79930	−0.81480	−0.18240	0.21510	0.59910	1.15810	1.52100	1.61420	−1.63930	−0.46520	0.00530	0.17420	0.24520	0.00110	−0.35840	0.53850
5480.60	4.00	−2.0	4.969	−0.66620	−0.79900	−0.20260	0.18810	0.57760	1.12580	1.47340	1.57090	−1.50870	−0.47140	−0.02270	0.15040	0.22470	−0.01870	−0.37010	0.51490
5582.06	4.00	−3.0	4.889	−0.55510	−0.76090	−0.20610	0.16940	0.55320	1.07930	1.40670	1.50300	−1.39990	−0.45430	−0.03940	0.12710	0.19680	−0.02900	−0.36420	0.49050
5523.51	4.00	−4.0	4.935	−0.56420	−0.78730	−0.22270	0.16140	0.55580	1.09460	1.43000	1.53000	−1.40920	−0.47970	−0.05020	0.12640	0.20410	−0.03890	−0.38300	0.49150
5530.74	4.50	0.0	4.929	−1.02080	−0.81610	−0.13430	0.28030	0.64200	1.16930	1.49320	1.58920	−1.86610	−0.44100	0.07450	0.22450	0.27660	0.04830	−0.32010	0.58560
5554.75	4.50	0.5	4.910	−1.21550	−0.83210	−0.11950	0.31850	0.67280	1.18760	1.48520	1.58870	−2.07540	−0.44380	0.11290	0.25850	0.30220	0.07240	−0.30890	0.61840
5457.22	4.50	−0.5	4.987	−0.91310	−0.82770	−0.16420	0.24350	0.62030	1.17060	1.52390	1.61650	−1.75180	−0.46190	0.03480	0.19810	0.26280	0.02050	−0.34640	0.56130
5506.04	4.50	−1.0	4.949	−0.75260	−0.79550	−0.17240	0.21990	0.59470	1.13760	1.48950	1.58030	−1.58720	−0.44910	0.01220	0.17280	0.23600	0.00660	−0.34520	0.53540
5462.38	4.50	−2.0	4.983	−0.67600	−0.82030	−0.20600	0.19180	0.58460	1.13500	1.48320	1.58370	−1.51290	−0.48530	−0.02000	0.15690	0.23250	−0.01870	−0.37670	0.52150
5517.41	4.50	−3.0	4.940	−0.58380	−0.80280	−0.21510	0.17620	0.57180	1.10550	1.43390	1.53740	−1.42380	−0.48440	−0.03610	0.14290	0.21930	−0.02900	−0.38030	0.50750
5531.84	4.50	−4.0	4.928	−0.54970	−0.80040	−0.22400	0.16470	0.56120	1.09390	1.42120	1.52480	−1.39030	−0.48890	−0.04770	0.13160	0.20920	−0.03820	−0.38650	0.49650
5509.50	5.00	0.0	4.946	−1.08990	−0.84050	−0.14030	0.28640	0.64890	1.18130	1.51060	1.60770	−1.93310	−0.45760	0.08000	0.23180	0.28430	0.04880	−0.32750	0.59300
5550.69	5.00	0.5	4.913	−1.27800	−0.84870	−0.12150	0.32560	0.67680	1.19420	1.49360	1.59840	−2.13540	−0.45410	0.12060	0.26370	0.30590	0.07460	−0.31120	0.62360
5528.91	5.00	−1.0	4.931	−0.75360	−0.79470	−0.16850	0.22590	0.59690	1.13360	1.48250	1.57240	−1.58430	−0.44640	0.01900	0.17650	0.23610	0.01080	−0.34060	0.53820
5463.42	5.00	−2.0	4.982	−0.68880	−0.82760	−0.20200	0.19950	0.59230	1.13890	1.48120	1.58480	−1.52290	−0.48740	−0.01270	0.16520	0.23950	−0.01350	−0.37490	0.52920
5468.24	5.00	−3.0	4.978	−0.62010	−0.83010	−0.21800	0.18420	0.58830	1.12600	1.45040	1.56140	−1.45890	−0.50250	−0.03070	0.15760	0.23840	−0.02570	−0.38900	0.52280
5474.24	5.00	−4.0	4.974	−0.58920	−0.83070	−0.22720	0.17450	0.58120	1.11790	1.43980	1.55230	−1.42960	−0.50960	−0.04100	0.14930	0.23230	−0.03390	−0.39620	0.51500
5787.92	4.44	0.0	4.732	−0.78450	−0.69460	−0.08850	0.28170	0.61220	1.08170	1.35950	1.44730	−1.62860	−0.34790	0.08430	0.20330	0.23130	0.06660	−0.25960	0.55930
5824.45	4.44	0.5	4.705	−0.95150	−0.69700	−0.06460	0.32440	0.64470	1.09800	1.34930	1.44350	−1.80570	−0.33820	0.12800	0.23980	0.25710	0.09610	−0.23970	0.59420
5718.03	4.44	−0.5	4.785	−0.69890	−0.70920	−0.11910	0.24620	0.59040	1.08200	1.38680	1.47140	−1.53790	−0.37120	0.04620	0.17730	0.21680	0.03870	−0.28650	0.53520
5765.80	4.44	−1.0	4.748	−0.58150	−0.69110	−0.13560	0.21880	0.56260	1.04910	1.35270	1.43610	−1.41840	−0.37060	0.01940	0.14930	0.18870	0.01960	−0.29400	0.50690
5787.32	4.44	−2.0	4.732	−0.48830	−0.69910	−0.16960	0.18280	0.53630	1.02020	1.31860	1.40570	−1.32680	−0.39640	−0.01850	0.11930	0.16560	−0.01080	−0.32100	0.47790
5784.22	4.44	−3.0	4.735	−0.44810	−0.70850	−0.18920	0.16320	0.52400	1.00940	1.30620	1.39610	−1.28770	−0.41440	−0.03960	0.10440	0.15600	−0.02780	−0.33820	0.46410
5806.41	4.44	−4.0	4.718	−0.42430	−0.70840	−0.19780	0.15190	0.51230	0.99560	1.29050	1.38030	−1.26420	−0.41940	−0.05080	0.09250	0.14430	−0.03730	−0.34470	0.45220
6025.18	3.50	0.0	4.557	−0.65120	−0.57750	−0.04410	0.28120	0.58140	1.00060	1.22820	1.31580	−1.51480	−0.25890	0.09210	0.18060	0.18840	0.08460	−0.20280	0.53280
5988.06	3.50	−0.5	4.584	−0.57750	−0.58350	−0.07320	0.24900	0.55910	0.99250	1.23880	1.32330	−1.43830	−0.27770	0.05810	0.15520	0.17090	0.05920	−0.22540	0.50860
5907.99	3.50	−1.0	4.643	−0.54850	−0.61340	−0.10640	0.22340	0.54840	1.00290	1.27030	1.35510	−1.40580	−0.31300	0.02910	0.14000	0.16690	0.03450	−0.25650	0.49540
5961.94	3.50	−2.0	4.603	−0.46090	−0.60220	−0.13650	0.18370	0.51050	0.96200	1.23060	1.31350	−1.32050	−0.32360	−0.01030	0.10040	0.13010	0.00410	−0.27540	0.45620
5965.56	3.50	−3.0	4.601	−0.43190	−0.60880	−0.15100	0.16700	0.49750	0.95080	1.21940	1.30400	−1.29060	−0.33570	−0.02760	0.08580	0.11870	−0.01000	−0.28800	0.44230
5971.49	3.50	−4.0	4.596	−0.41640	−0.61290	−0.16090	0.15610	0.48770	0.94320	1.21470	1.29850	−1.27470	−0.34340	−0.03860	0.07550	0.10960	−0.01950	−0.29620	0.43230
6014.61	4.00	0.0	4.565	−0.63510	−0.58990	−0.05210	0.27640	0.57840	1.00220	1.23980	1.32370	−1.48810	−0.26890	0.08670	0.17710	0.18510	0.07870	−0.21020	0.52910
6038.71	4.00	−0.5	4.548	−0.52650	−0.58300	−0.07750	0.24160	0.54800	0.97380	1.21950	1.29990	−1.37710	−0.27850	0.05150	0.14520	0.15670	0.05300	−0.22700	0.49760
5958.44	4.00	−1.0	4.606	−0.49750	−0.61480	−0.11210	0.21450	0.53610	0.98300	1.24910	1.33020	−1.34490	−0.31560	0.02090	0.12870	0.15190	0.02690	−0.25960	0.48310
5954.96	4.00	−2.0	4.608	−0.43750	−0.63070	−0.14980	0.17680	0.50850	0.96150	1.23400	1.31640	−1.28550	−0.34630	−0.01860	0.09720	0.12860	−0.00600	−0.29090	0.45310
6032.46	4.00	−3.0	4.552	−0.38350	−0.61880	−0.16300	0.15260	0.47990	0.92310	1.18800	1.26910	−1.23210	−0.34640	−0.04130	0.06930	0.09810	−0.02370	−0.29780	0.42470
6023.76	4.00	−4.0	4.558	−0.37830	−0.62430	−0.17300	0.14000	0.46860	0.91710	1.18740	1.26780	−1.22630	−0.35410	−0.05410	0.05720	0.08810	−0.03440	−0.30700	0.41290
6020.75	4.50	0.0	4.561	−0.62240	−0.60530	−0.05810	0.27690	0.58070	1.00290	1.24360	1.32550	−1.46690	−0.28070	0.08660	0.17920	0.18680	0.07610	−0.21670	0.53100
5938.44	4.50	0.5	4.620	−0.84350	−0.64830	−0.04780	0.32120	0.62900	1.05840	1.29200	1.38240	−1.69580	−0.30130	0.12840	0.22750	0.23520	0.10120	−0.21670	0.57990
5968.38	4.50	−0.5	4.598	−0.54580	−0.61870	−0.08980	0.24110	0.55630	0.99720	1.26070	1.33920	−1.38610	−0.30410	0.04870	0.15120	0.16850	0.04730	−0.24340	0.50460
5961.60	4.50	−1.0	4.603	−0.48430	−0.62810	−0.11610	0.21340	0.53520	0.98260	1.25350	1.33230	−1.32270	−0.32400	0.01960	0.12800	0.15040	0.02390	−0.26450	0.48210
6064.09	4.50	−2.0	4.529	−0.37850	−0.62070	−0.15140	0.16540	0.48750	0.92170	1.18240	1.26070	−1.21880	−0.33990	−0.02760	0.07910	0.10230	−0.01400	−0.28860	0.43310
6024.94	4.50	−3.0	4.557	−0.36240	−0.64300	−0.17340	0.14780	0.47970	0.92350	1.19060	1.27150	−1.20220	−0.36560	−0.04740	0.06810	0.09880	−0.03140	−0.31050	0.42350
6037.83	4.50	−4.0	4.548	−0.34920	−0.64840	−0.18370	0.13650	0.46920	0.91320	1.18030	1.26130	−1.18910	−0.37440	−0.05880	0.05710	0.08880	−0.04160	−0.31940	0.41280
6432.73	4.00	0.0	4.273	−0.44620	−0.45690	−0.01340	0.26040	0.51590	0.86370	1.03890	1.11640	−1.30920	−0.17170	0.08240	0.12760	0.10220	0.08700	−0.15010	0.47320
6455.69	4.00	−0.5	4.258	−0.39190	−0.46130	−0.04240	0.22580	0.48510	0.83560	1.01710	1.09260	−1.25390	−0.18890	0.04730	0.09550	0.07330	0.05920	−0.17200	0.44140
6413.03	4.00	−1.0	4.286	−0.36430	−0.48480	−0.07670	0.19490	0.46490	0.83130	1.03060	1.10340	−1.22350	−0.21990	0.01440	0.07170	0.05800	0.03080	−0.20200	0.41910
6419.24	4.00	−2.0	4.282	−0.32650	−0.50660	−0.11630	0.15370	0.43180	0.80570	1.01380	1.08600	−1.18510	−0.25300	−0.02810	0.03530	0.02860	−0.00560	−0.23610	0.38400
6470.07	4.00	−3.0	4.248	−0.30140	−0.51070	−0.13440	0.12860	0.40500	0.77640	0.98300	1.05410	−1.15920	−0.26380	−0.05250	0.00860	0.00150	−0.02610	−0.25050	0.35720
6491.09	4.00	−4.0	4.234	−0.29550	−0.51950	−0.14770	0.11380	0.38990	0.76180	0.96910	1.04010	−1.15280	−0.27510	−0.06720	−0.00660	−0.01350	−0.03980	−0.26240	0.34210
6491.63	4.50	0.0	4.234	−0.40280	−0.45840	−0.01840	0.25180	0.50340	0.84300	1.01850	1.09080	−1.25470	−0.17330	0.07470	0.11630	0.08580	0.07990	−0.15270	0.46050
6503.68	4.50	−0.5	4.225	−0.34200	−0.47480	−0.05660	0.21110	0.47040	0.81610	1.00130	1.07120	−1.19170	−0.20250	0.03260	0.08080	0.05620	0.04510	−0.18400	0.42590
6435.89	4.50	−1.0	4.271	−0.32460	−0.50900	−0.09030	0.18460	0.45760	0.82040	1.02180	1.09230	−1.17110	−0.24010	0.00320	0.06380	0.04950	0.01840	−0.21670	0.41060
6500.28	4.50	−2.0	4.228	−0.28230	−0.52190	−0.13210	0.13260	0.40680	0.77100	0.97710	1.04490	−1.12910	−0.26750	−0.04840	0.01150	0.00010	−0.02500	−0.25060	0.35880
6499.46	4.50	−3.0	4.228	−0.26620	−0.54150	−0.15330	0.11380	0.39330	0.76150	0.97070	1.03950	−1.11160	−0.29040	−0.06830	−0.00380	−0.01110	−0.04360	−0.27080	0.34440
6507.77	4.50	−4.0	4.223	−0.26320	−0.55210	−0.16540	0.10200	0.38280	0.75240	0.96260	1.03170	−1.10820	−0.30260	−0.08030	−0.01480	−0.02100	−0.05520	−0.28230	0.33360
6907.57	4.50	0.0	3.964	−0.29660	−0.36800	−0.00300	0.22060	0.43030	0.70520	0.82860	0.89670	−1.15810	−0.11040	0.05350	0.05490	−0.00540	0.07110	−0.11930	0.39350
6986.84	4.50	−0.5	3.914	−0.26030	−0.37800	−0.03960	0.17480	0.38420	0.65680	0.78140	0.84700	−1.12200	−0.13320	0.00820	0.00850	−0.05110	0.03340	−0.14820	0.34710
7000.57	4.50	−3.0	3.906	−0.23350	−0.45660	−0.13960	0.07470	0.30170	0.59740	0.74610	0.80810	−1.08970	−0.22660	−0.09490	−0.08060	−0.12520	−0.05990	−0.24050	0.26070

A&A 597, A94 (2017)
DOI: 10.1051/0004-6361/201528018

Astronomy & Astrophysics

Measuring stellar granulation during planet transits

A. Chiavassa[1], A. Caldas[2], F. Selsis[2], J. Leconte[2], P. Von Paris[2], P. Bordé[2], Z. Magic[3,4], R. Collet[5,6], and M. Asplund[5]

[1] Laboratoire Lagrange, Université Côte d'Azur, Observatoire de la Côte d'Azur, CNRS, Bd de l'Observatoire, CS 34229, 06304 Nice Cedex 4, France
e-mail: andrea.chiavassa@oca.eu
[2] Laboratoire d'Astrophysique de Bordeaux, Univ. Bordeaux, CNRS, B18N, allée Geoffroy Saint-Hilaire, 33615 Pessac, France
[3] Niels Bohr Institute, University of Copenhagen, Juliane Maries Vej 30, 2100 Copenhagen, Denmark
[4] Centre for Star and Planet Formation, Natural History Museum of Denmark, University of Copenhagen, Øster Voldgade 5-7, 1350 Copenhagen, Denmark
[5] Research School of Astronomy & Astrophysics, Australian National University, Cotter Road, Weston ACT 2611, Australia
[6] Stellar Astrophysics Centre, Department of Physics and Astronomy, Ny Munkegade 120, Aarhus University, 8000 Aarhus C, Denmark

Received 21 December 2015 / Accepted 25 September 2016

ABSTRACT

Context. Stellar activity and convection-related surface structures might cause bias in planet detection and characterization that use these transits. Surface convection simulations help to quantify the granulation signal.
Aims. We used realistic three-dimensional (3D) radiative hydrodynamical (RHD) simulations from the STAGGER grid and synthetic images computed with the radiative transfer code OPTIM3D to model the transits of three prototype planets: a hot Jupiter, a hot Neptune, and a terrestrial planet.
Methods. We computed intensity maps from RHD simulations of the Sun and a K-dwarf star at different wavelength bands from optical to far-infrared that cover the range of several ground- and space-based telescopes which observe exoplanet transits. We modeled the transit using synthetic stellar-disk images obtained with a spherical-tile imaging method and emulated the temporal variation of the granulation intensity generating random images covering a granulation time-series of 13.3 h. We measured the contribution of the stellar granulation on the light curves during the planet transit.
Results. We identified two types of granulation noise that act simultaneously during the planet transit: (i) the intrinsic change in the granulation pattern with timescale (e.g., 10 min for solar-type stars assumed in this work) is smaller than the usual planet transit (~hours as in our prototype cases); and (ii) the fact that the transiting planet occults isolated regions of the photosphere that differ in local surface brightness as a result of convective-related surface structures. First, we showed that our modeling approach returns granulation timescale fluctuations that are comparable with what has been observed for the Sun. Then, our statistical approach shows that the granulation pattern of solar and K-dwarf-type stars have a non-negligible effect of the light curve depth during the transit, and, consequentially on the determination of the planet transit parameters such as the planet radius (up to 0.90% and ~0.47% for terrestrial and gaseous planets, respectively). We also showed that larger (or smaller) orbital inclination angles with respect to values corresponding to transit at the stellar center display a shallower transit depth and longer ingress and egress times, but also granulation fluctuations that are correlated to the center-to-limb variation: they increase (or decrease) the value of the inclination, which amplifies the fluctuations. The granulation noise appears to be correlated among the different wavelength ranges either in the visible or in the infrared regions.
Conclusions. The prospects for planet detection and characterization with transiting methods are excellent with access to large amounts of data for stars. The granulation has to be considered as an intrinsic uncertainty (as a result of stellar variability) on the precise measurements of exoplanet transits of planets. The full characterization of the granulation is essential for determining the degree of uncertainty on the planet parameters. In this context, the use of 3D RHD simulations is important to measure the convection-related fluctuations. This can be achieved by performing precise and continuous observations of stellar photometry and radial velocity, as we explained with RHD simulations, before, after, and during the transit periods.

Key words. planet-star interactions – stars: activity – techniques: photometric – stars: atmospheres – hydrodynamics – radiative transfer

1. Introduction

Among the different methods used to detect exoplanets, the transit method is a very successful technique: 1147 planets and 3787 transit candidates have been confirmed with it (as of November 2015 from http://exoplanets.org, Wright et al. 2011). A transit event occurs when the planet crosses the line of sight between the star and the observer, thus occulting part of the star. This creates a periodic dip in the brightness of the star. The typical stellar light blocked is ~1%, 0.1%, and 0.01% for Jupiter-, Neptune- and Earth-like planets transiting in front of a Sun-like star, respectively (Borucki & Summers 1984), making the detection very challenging, in particular for Earth-like planets. During the transit, the flux decrease is proportional to the squared ratio of planet and stellar radii. For sufficiently bright stars, the mass can also be measured from the host star's radial velocity semi-amplitude (Mislis et al. 2012). When the mass and radius of an exoplanet are known, its mean density can also be deduced and provide useful information for the physical formation processes. Today and in the near future,

Table 1. 3D RHD simulations from STAGGER grid.

$\langle T_{\rm eff}\rangle^a$ [K]	[Fe/H]	$\log g$ [cgs]	x, y, z-dimensions [Mm]	x, y, z-resolution [grid points]	$M_\star$ [$M_\odot$]	$R_\star$ [$R_\odot$]	Granule size^b [10^{-3}]	Number of tiles^c over the diameter
5768 (Sun)	0.0	4.4	$7.76 \times 7.76 \times 5.20$	$240 \times 240 \times 240$	1.0	1.00	4.5	286
4516 (K dwarf)	0.0	4.5	$4.00 \times 4.00 \times 3.17$	$240 \times 240 \times 240$	0.7^d	0.78	5.1	427

Notes. $^{(a)}$ Horizontal and temporal average of the emerging effective temperatures from Magic et al. (2013). $^{(b)}$ Approximate granulation size from Magic & Asplund (2014) divided by the stellar radius. See also Fig. 1. $^{(c)}$ $N_{\rm tile} = \frac{\pi \cdot R_\star}{x,y-{\rm dimension}}$. $^{(d)}$ Figure 1 of Magic et al. (2013).

the prospects for planet detection and characterization with the transiting methods are excellent with access to a large amount of data coming, for instance, from the NASA missions *Kepler* (Borucki et al. 2010) and TESS (Transit Exoplanet Survey Satellite, Ricker et al. 2010), or from the ESA missions PLATO 2.0 (PLAnetary Transits and Oscillation of stars, Rauer et al. 2014) and CHEOPS (CHaracterizing ExOPlanet Satellite, Broeg et al. 2013).

Space- and ground-based telescopes used for transit photometry require high photometric precision to provide accurate planetary radii, masses, and ages. Moreover, transit photometry also needs continuous time series data over an extended period of time. Earth-sized planets are the most challenging targets: if the radius of the Earth is approximately 1/100 that of the Sun, then a transit of the Sun by Earth blocks $\sim 10^{-4}$ of the solar flux, in addition to the challenge of the limited number of photons arriving from a faint star. For all these reasons, it is necessary to go to space to monitor the target fields continuously with minimal interruptions.

However, with improved photometric precision, additional sources of noise that are due to the presence of stellar surface inhomogeneities such as granulation, will become relevant, and the overall photometric noise will be less and less dominated by pure photon shot noise. The Sun's total irradiance varies on all timescales relevant for transit surveys, from minutes to months (Aigrain et al. 2004). In particular, granulation analysis of SOHO quiet-Sun data shows that the photometric variability ranges from 10 to 50 part-per-million (ppm; Jenkins 2002; Frohlich et al. 1997). The granulation was observed for the first time on the Sun by Herschel (1801), but Dawes (1864) coined the term granules. The granulation pattern is associated with heat transport by convection, on horizontal scales on the order of a thousand kilometers (Nordlund et al. 2009). The bright areas on the stellar surfaces, the granules, are the locations of upflowing hot plasma, while the dark intergranular lanes are the locations of downflowing cooler plasma. Additionally, the horizontal scale on which radiative cooling drives the convective motions is linked with the granulation diameter (Nordlund & Dravins 1990). Stellar granulation manifests either on spatially resolved (e.g., images of the solar disk) or unresolved observables such as spectral line profiles in terms of widths, shapes, and strengths. The best observational evidence comes from unresolved spectral lines because they combine important properties such as velocity amplitudes and velocity-intensity correlations, which produce line broadening. This is interpreted as the Doppler shifts arising from the convective flows in the solar photosphere and solar oscillations (Asplund et al. 2000; Nordlund et al. 2009). Similarly, correlations of velocity and temperature cause characteristic asymmetries of spectral lines as well as net blueshifts for main-sequence stellar types (Dravins 1987; Gray 2005).

The purpose of this work is to study the impact of stellar granulation on the transit shape and retrieved planetary parameters (e.g., radius). We considered three prototypes of

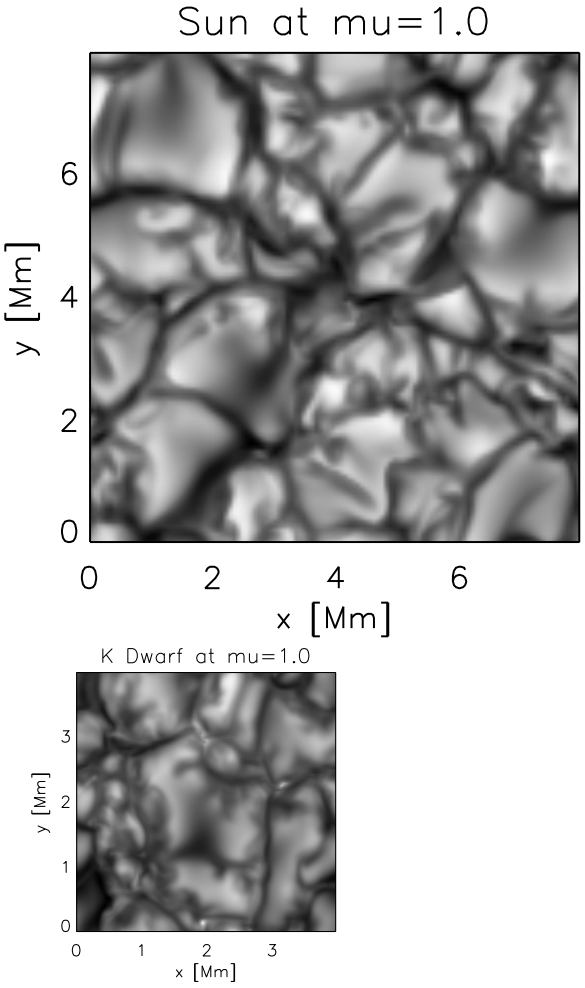

Fig. 1. Intensity maps computed at [7620–7640] Å (Table 2) of the 3D RHD simulations of Table 1 and for the vertical direction ($\mu = 1.0$). The intensity ranges from [1.56–2.76] $\times$ 10^6 erg cm^{-2} s^{-1} Å^{-1} for the Sun (*top*) and from [0.68–1.10] $\times$ 10^6 erg cm^{-2} s^{-1} Å^{-1} for the K dwarf (*bottom*). The size ratio between the two images corresponds approximatively to the numerical box sizes.

planets with different sizes and transit time lengths corresponding to a hot Jupiter, a hot Neptune, and a terrestrial planet. We used theoretical modeling of stellar atmospheres where the multidimensional radiative hydrodynamic equations are solved and convection emerges naturally. These simulations take surface inhomogeneities (i.e., the granulation pattern) and velocity fields into account in a self-consistent manner. They cover a substantial portion of the Hertzsprung-Russell diagram (Magic et al. 2013; Ludwig et al. 2009; Trampedach et al. 2013), including the evolutionary phases from the main sequence over the turnoff up to the red giant branch for low-mass stars.

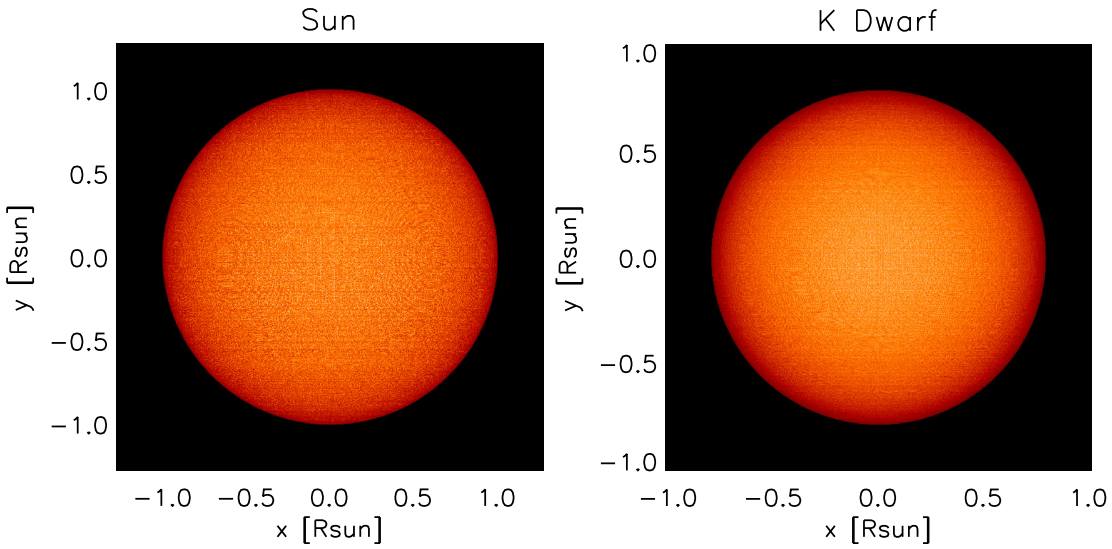

Fig. 2. Representative synthetic solar-disk image computed at [7620–7640] Å (Table 2) of the 3D RHD simulations of Table 1. The intensity range is [0.0–2.86] $\times$ 10^6 erg cm^{-2} s^{-1} Å^{-1} for the Sun and [0.0–1.82] $\times$ 10^6 erg cm^{-2} s^{-1} Å^{-1} for the K-dwarf star. We generated 80 different synthetic solar-disk images to account for a granulation time-series of 800 min (13.3 h).

2. Stellar atmospheres and radiative transfer

We used the simulations (Table 1) from the STAGGER grid of realistic three-dimensional (3D) radiative hydrodynamical (RHD) simulations of stellar convection for cool stars (Magic et al. 2013). This grid is computed using the STAGGER code (originally developed by Nordlund & Galsgaard, 1995[1], and continuously improved over the years by its user community). In a Cartesian box located around the optical surface (i.e., $\tau \sim 1$), the code solves the time-dependent equations for conservation of mass, momentum, and energy coupled to a realistic treatment of the radiative transfer. The simulation domains are chosen large enough to cover at least ten pressure scale heights vertically and to allow for about ten granules to develop at the surface; moreover, there are periodic boundary conditions horizontally and open boundaries vertically. At the bottom of the simulation, the inflows have a constant entropy, and the whole bottom boundary is set to be a pressure node for p-mode oscillations. The simulations employ realistic input physics: the equation of state is an updated version of the one described by Mihalas et al. (1988), and the radiative transfer is calculated for a large number over wavelength points merged into 12 opacity bins (Nordlund 1982; Skartlien 2000; Magic et al. 2013). They include continuous absorption opacities and scattering coefficients from Hayek et al. (2010) as well as line opacities described in Gustafsson et al. (2008), which in turn are based on the VALD-2 database (Stempels et al. 2001) of atomic lines. The abundances employed in the computation are the solar chemical composition by Asplund et al. (2009).

Theses simulations have been used to compute synthetic images with the pure-LTE radiative transfer code OPTIM3D (Chiavassa et al. 2009). The code takes into account the Doppler shifts that are due to convective motions. The radiative transfer equation is solved monochromatically using pre-tabulated extinction coefficients as a function of temperature, density, and wavelength. OPTIM3D uses lookup tables with the same chemical compositions as the 3D RHD simulations as well as the same extensive atomic and molecular continuum and line opacity data as the latest generation of MARCS models (Gustafsson et al. 2008). The microturbulence is assumed to be zero (i.e., the non-thermal Doppler broadening of spectral lines is the consequence of the self-consistent velocities in the simulations, Asplund et al. 2000) and the temperature and density ranges spanned by the tables are optimized for the values encountered in the RHD simulations. The detailed methods used in the code are explained in Chiavassa et al. (2009, 2010).

[1] http://www.astro.ku.dk/~kg/Papers/MHD_code.gz

Table 2. Integrated wavelength bands computed.

Wavelength range, [Å]	Number of bands	$\Delta\lambda$ per band [Å]
7500–7700	10	20
25 000–29 000	16	250
39 000–51 000	1	12 000

3. Stellar image disks to model the transits

We employed the tiling method explained in Chiavassa et al. (2010) and used in Chiavassa et al. (2012, 2014, 2015). We used OPTIM3D to compute intensity maps (see an illustrative image for $\mu = 1.0$ in Fig. 1 and more examples in Chiavassa et al. 2012) at different integrated wavelength bands (Table 2) covering spectral regions in the optical, which are characterized by a higher density of transition lines toward the infrared part of the spectrum (Fig. 3).

We performed the calculations for 30 snapshots of the 3D RHD simulations of Table 1, adequately spaced apart so as to capture several convective turnovers, and for 43 different inclination angles (θ) with respect to the line of sight (vertical axis): $\mu \equiv \cos(\theta)$ ranging from 1.000 to 0.1045 with a step of 0.0174. These synthetic images have been used to map them onto spherical surfaces to account for distortions especially at high latitudes and longitudes by cropping the square-shaped intensity maps when defining the spherical tiles. The total number of tiles ($N_{\rm tile}$) needed to cover half a circumference from side to side on the sphere is $N_{\rm tile} = \frac{\pi \cdot R_\star}{x,y-{\rm dimension}}$, where $R_\star$ (transformed into Mm), and the x, y-dimension are taken from Table 1. The computed

Table 3. Prototypes of planets chosen to represent the planet transits.

Planet type	Mass M_p [M_{Jup}]	Radius[a] R_p [R_{Jup}] Sun/K dwarf	Equilibrium temperature T_p [K]	Semi-major axis [AU]	*inc*[b] [°]	Transit duration Δt [h]
Terrestrial planet	0.006	0.219/0.173	400	0.2504	90	~7
Hot Neptune	0.360	0.654/0.510	1540	0.0431	90	~2
Hot Jupiter	7.570	1.090/0.850	1952	0.0269	90	~3

Notes. [(a)] R_p is different for the RHD simulation of the Sun and of the K dwarf, to keep the same ratio $R_p/R_\star$ for the transits. Moreover, the radius of the terrestrial planet is larger than Earth's radius. [(b)] The inclination orbit (*inc*) has been arbitrarily chosen to be equal to 90° to have a planet crossing at the center of the star.

value of the θ-angle used to generate each map depended on the position (longitude and latitude) of the tile on the sphere.

We aim to emulate the temporal variation of the granulation intensity, which shows a timescale on the order of ~10 min (Nesis et al. 2002) for the Sun. We generated 80 different synthetic stellar-disk images (Fig. 2) using, for each tile, synthetic maps chosen randomly among the snapshots in the time-series. This resulted in a simulated granulation time-series of 800 min (13.3 h). Since more tiles are necessary to cover the sphere than there are representative snapshots of the 3D RHD simulations, tiles randomly appear several times at different inclination angles θ, and adjacent tiles are not completely uncorrelated. However, we assumed that this statistical representation is good enough to represent the changing granulation pattern during the planet transit.

4. Granulation noise

The granulation pattern of the star may affect the photometric measurements during planet transit with two different types of noise: (i) the intrinsic timescale of the changes in granulation pattern (e.g., 10 min for solar-type stars assumed in this work) is shorter than the usual planet transit (~hours as in our prototype cases of Table 3); and (ii) the fact that the transiting planet occults isolated regions of the photosphere that differ in local surface brightness as a result of convection-related surface structures. These sources of noise act simultaneously during the planet transit, and we analyze them in the next sections.

4.1. Photon noise of the synthetic stellar disk with convection-related structures

The granulation pattern changes with time. Figure 4 displays the fluctuation of the intensity profiles for a particular cut in the synthetic disk images during a period corresponding to the transit duration of the prototype terrestrial planet (7 h, Table 3). In our approach, the solar disk intensity fluctuates during the transit by between $[2.68–2.80] \times 10^6$ erg cm^{-2} s^{-1} Å^{-1}, and for the K dwarf by between $[1.63–1.66] \times 10^6$ erg cm^{-2} s^{-1} Å^{-1}.

We calculated the number of photons from the granulation synthetic images ($\varphi_{\star\text{granulation}}$) and compared it with the image produced by a black body ($\varphi_{\star\text{BB}}$) with an effective temperature of 5768 K for the Sun and 4516 K for the K dwarf (same T_{eff} as in the RHD simulations of Table 1) at the different wavelength ranges of Table 2. The granulation images were averaged over the $N_{\text{terrestrial}} = 42$ different realizations, where $N = \frac{\Delta t}{\sigma_{\text{Sun}}}$, Δt is the transit duration and σ_{Sun} is the observed granulation fluctuation timescale for the Sun, which is ~10 min (Nesis et al. 2002). The number of photons reaching a telescope with a collecting area S, a net efficiency ϵ, and an integration time Δt is equal

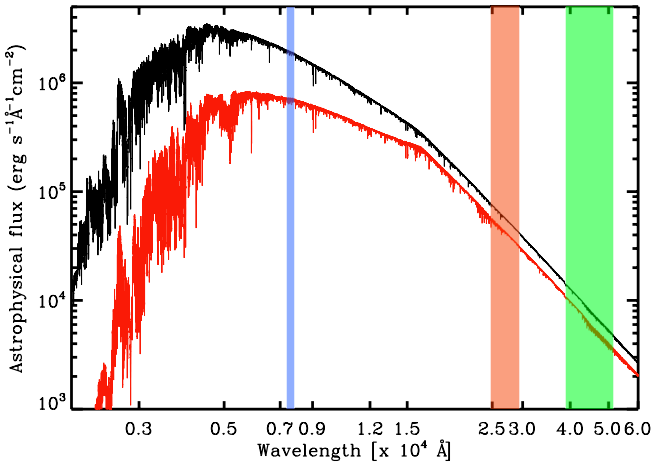

Fig. 3. Synthetic spectra computed for the Sun (black curve) and the K dwarf (red curve) from the optical to the infrared with a constant resolution of $\lambda/\Delta\lambda = 20\,000$. The blue shading indicates the [7500–7700] Å region used in Table 2, the red shading the [25 000–29 000] Å, and the green shading the [39 000–51 000] Å. Note the use of the astronomical flux (i.e., the flux divided by a factor π) such that the values of the flux and intensity are the same. Note also the logarithmic x- and y-axis scale.

to $\varphi_\star = I_\star(\lambda) \cdot \lambda / (h_{\text{Planck}} c) \cdot R \cdot S \cdot \epsilon \cdot \Delta t$, where λ is the central wavelength and R the spectral resolution of the ranges in Table 2, $I_\star(\lambda)$ the stellar intensity (either the averaged intensity of the granulation maps or the black body) at a certain wavelength and for a star at 100 pc, h_{Planck} is the Planck constant, and c the speed of light. In this work, we assumed a 100 cm diameter and thus a collecting area of $S = 7854$ cm^2; a net efficiency $\epsilon = 0.15$ electron/photon; and an integration time, Δt equal to the transit time of 7 h from Table 3. Figure 5 (top panel) shows the number of photons is larger for the visible region with respect to the infrared, as can be expected by the behavior of the Planck function at these wavelengths. Moreover, the central and bottom panels show a clear dependence of the intensity with respect to wavelength ranges used.

The noise is the fluctuation in the total number of detected photons, and it is $\sigma_{\varphi_{\star\text{granulation}}} = \sqrt{\varphi_{\star\text{granulation}}}$ for the granulation synthetic images and $\sigma_{\varphi_{\star\text{BB}}} = \sqrt{\varphi_{\star\text{BB}}}$ for the corresponding black body. Figure 6 shows the ratio between the photon noise of the granulation images and the one from the black body. In the optical, the value of $\sigma_{\varphi_{\star\text{granulation}}}$ of the Sun is alternatively lower and higher than $\sigma_{\varphi_{\star\text{BB}}}$, in particular, the granulation signal becomes important at the wavelength bin of [7620–7640] Å. On the other hand, the K-dwarf granulation photon noise is systematically lower than the corresponding black body, even if it follows the same trends as the solar one.

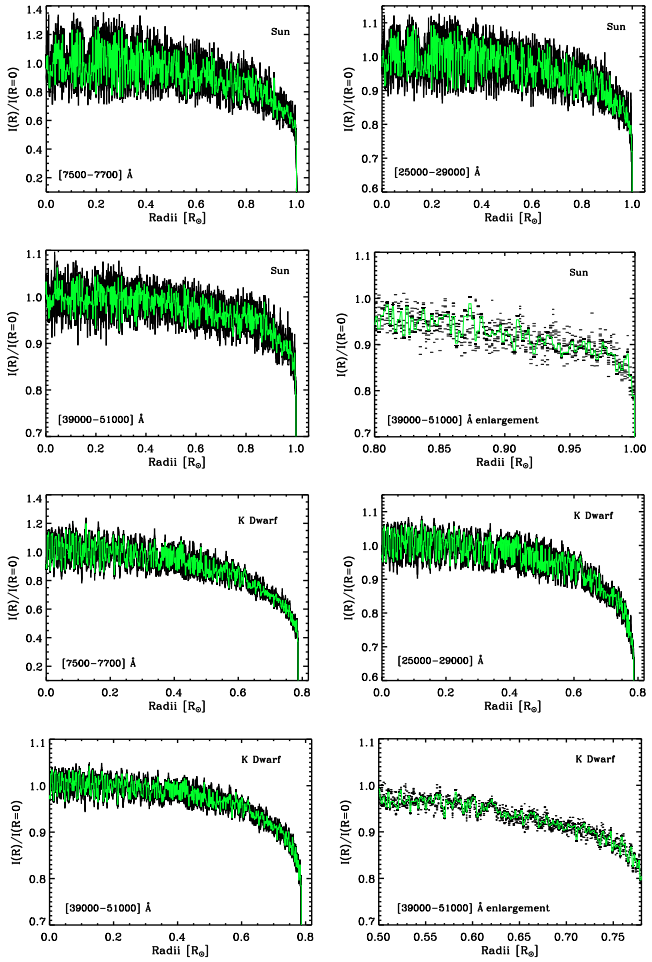

Fig. 4. Intensity profiles obtained from the cut at $x = 0$, $y > 0$ in the synthetic disk images of Fig. 2. The black curves are the overlap of $N = 42$ different images. The number N depends on the duration of the transit of *Kepler* 11-f (7 h, Table 3) and the observed granulation timescale for the Sun is ∼10 min (see text). The intensity profiles are normalized to the intensity at the disk center ($R = 0.0$). The green line is the temporal average profile.

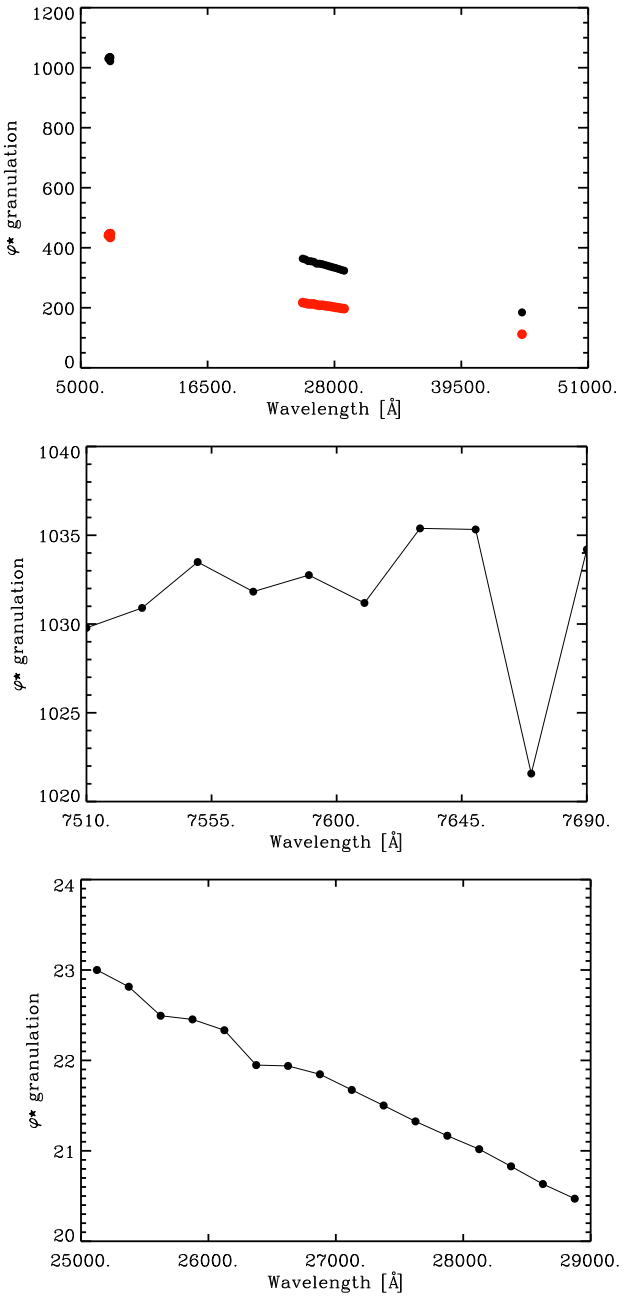

Fig. 5. *Top panel*: number of photons ($\varphi_{\star\text{granulation}}$ for the synthetic Sun (black) and K dwarf (red) calculated as described in the text and for the wavelengths of Table 2. *Central and bottom panels*: enlargements for the Sun in the optical and infrared.

In the infrared, the situation is different: for both the Sun and the K dwarf, the photon noise is greater than the black-body noise for all wavelength ranges; moreover, K dwarf values are higher than the Sun owing to the lower effective temperature of the star and the consequent displacement of the radiation peak. Furthermore, increasing the number of N realizations (up to $N = 80$) for the granulation average (i.e., $\Delta t = 13.3$ h) returns values very similar to Fig. 6.

Granulation significantly affects the photon noise in various wavelength ranges compared to the black-body approximation, so that transit uncertainties based on the black-body approximation can overestimate or underestimate the uncertainties, depending on the wavelength range considered. Furthermore, it is important to consider the change in the granulation pattern during the photometric measurements of transits like the one considered in this work, as developed in the next section.

4.2. Flux variations caused by the transiting planet

Chiavassa et al. (2015) modeled the transit light curve of Venus in 2004 assuming the 3D RHD simulation of the Sun (the same as we used here) for the background solar disk. They showed that in terms of transit depth and ingress/egress slopes as well as the emerging flux, the RHD simulation is well adapted to interpret the observed data. Furthermore, they reported that the granulation causes intrinsic changes in the total solar irradiance over the same time interval as the Venus transit, arguing that the granulation is a source of an intrinsic noise that may affect precise measurements of exoplanet transits.

In this work, we extended their analysis to the simulations of Table 1 (i.e., adding more calculations for the Sun and the K dwarf) and to the large set of wavelength bands of Table 2. We used the following procedure:

– we chose three prototypes of planets with different sizes and transit time lengths corresponding to a hot Jupiter, a hot

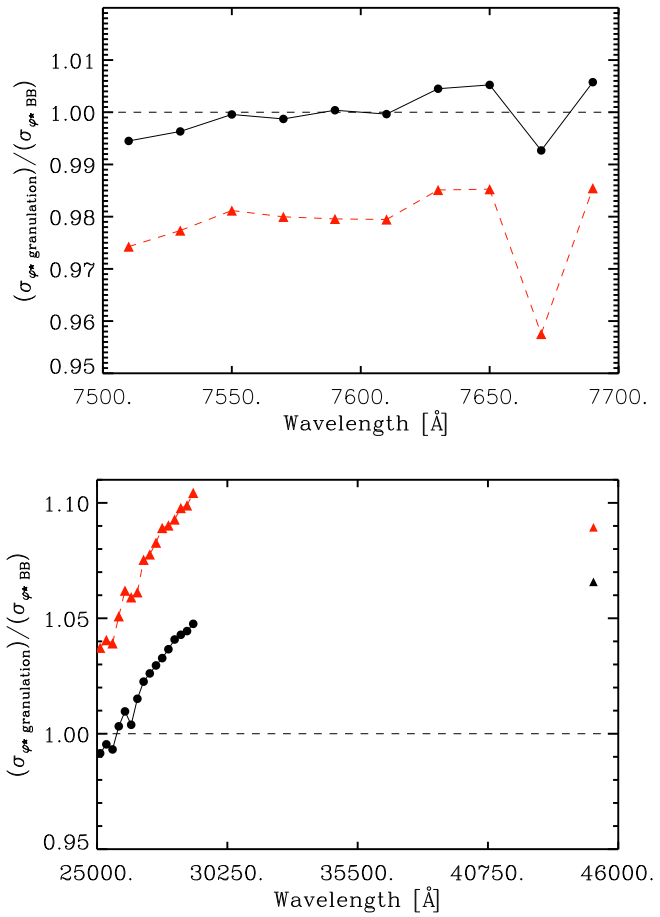

Fig. 6. Ratio between the photon noise computed for the synthetic images with granulation ($\sigma_{\varphi_{\star\text{granulation}}}$) and for the correspondent black body ($\sigma_{\varphi_{\star\text{BB}}}$) with the same effective temperature of the RHD simulations of the Sun (black circles) and K dwarf (red triangles). The wavelengths are taken from Table 2.

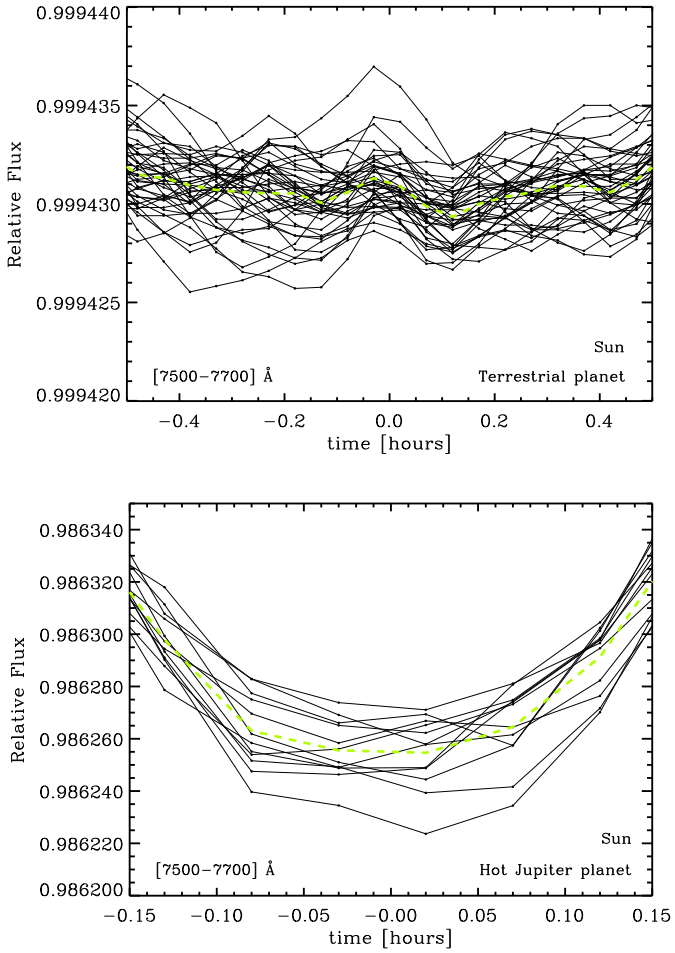

Fig. 7. Scatter plot of 42 (*top*) and 12 (*bottom*) different transit light curves for a terrestrial and hot Jupiter planet of Table 3, respectively. The green dashed line is the average light curve profile.

Table 4. Typical values of the stellar (either Sun or K dwarf) intensities, I_{star}, at its center ($\mu = 1$) for the synthetic images of the simulations (Fig. 2), and the planet integrated intensity, I_{planet}, for a few representative wavelength bands (Table 2).

λ band [Å]	[7620–7640]	[25 000–25 250]	[39 000–51 000]
$I_{\text{Sun}}/I_{\text{terrestrial}}$	4×10^{15}	360 000	6066
$I_{\text{Sun}}/I_{\text{Neptune}}$	75 270	187	86
$I_{\text{Sun}}/I_{\text{Jupiter}}$	4487	68	42
$I_{\text{Kdwarf}}/I_{\text{terrestrial}}$	10^{16}	262 000	4560
$I_{\text{Kdwarf}}/I_{\text{Neptune}}$	28 130	136	65
$I_{\text{Kdwarf}}/I_{\text{Jupiter}}$	7510	50	32

Neptune, and a terrestrial planet (Table 3) with the purpose of studying the resulting noise caused by the granulation on simulated transits. We did not aim to reproduce the exact conditions of the planet-star systems detected;

- we used the synthetic disk images as the background-emitting source for all the wavelength bands of Table 2;
- to model the flux of the planet, we used a black body with the planet equilibrium temperature reported in Table 3. The typical flux ratios are reported in Table 4;
- we simulated the transits using the exoplanet data reported in Table 3, and collected data points every 3 min. Synthetic images are reported in Fig. 8 for the Sun;
- the emerging intensity was collected for every transit step;
- we accounted for the variation of the granulation intensity using a set of N different synthetic stellar-disk images. We chose randomly $N_{\text{terrestrial}} = 42$, $N_{\text{Neptune}} = 18$, and $N_{\text{Jupiter}} = 12$ synthetic realizations from our 80 realizations.

Following this procedure, since we collected points every 3 min, that is, about one-third of 10 min (the granulation timescale for the Sun), to build a transit there are three adjacent time steps for which the same image was used (i.e., this corresponds to three different positions of the transiting planet). Then, a new synthetic image was chosen randomly and used for about three more times, and so on. This leads for a total of, for instance, $N_{\text{terrestrial}} = 42$ or $N_{\text{Jupiter}} = 12$ synthetic realizations as in the example of different transit curves superimposed in Fig. 7. The figure shows that the central phase of the terrestrial transit wiggles more strongly than that of the hot Jupiter, which looks smoother. Since the number of tiles needed to cover the sphere is smaller than the number of representative snapshots of the RHD simulations, tiles randomly appear several times along the transit trajectory and, consequentially, a correlated behavior between the different transit curves arises. This effect is more important for the terrestrial planet, which is more sensitive to the stellar inhomogeneities because of the convection-related surface structures because its apparent size is comparable to the RHD simulation box.

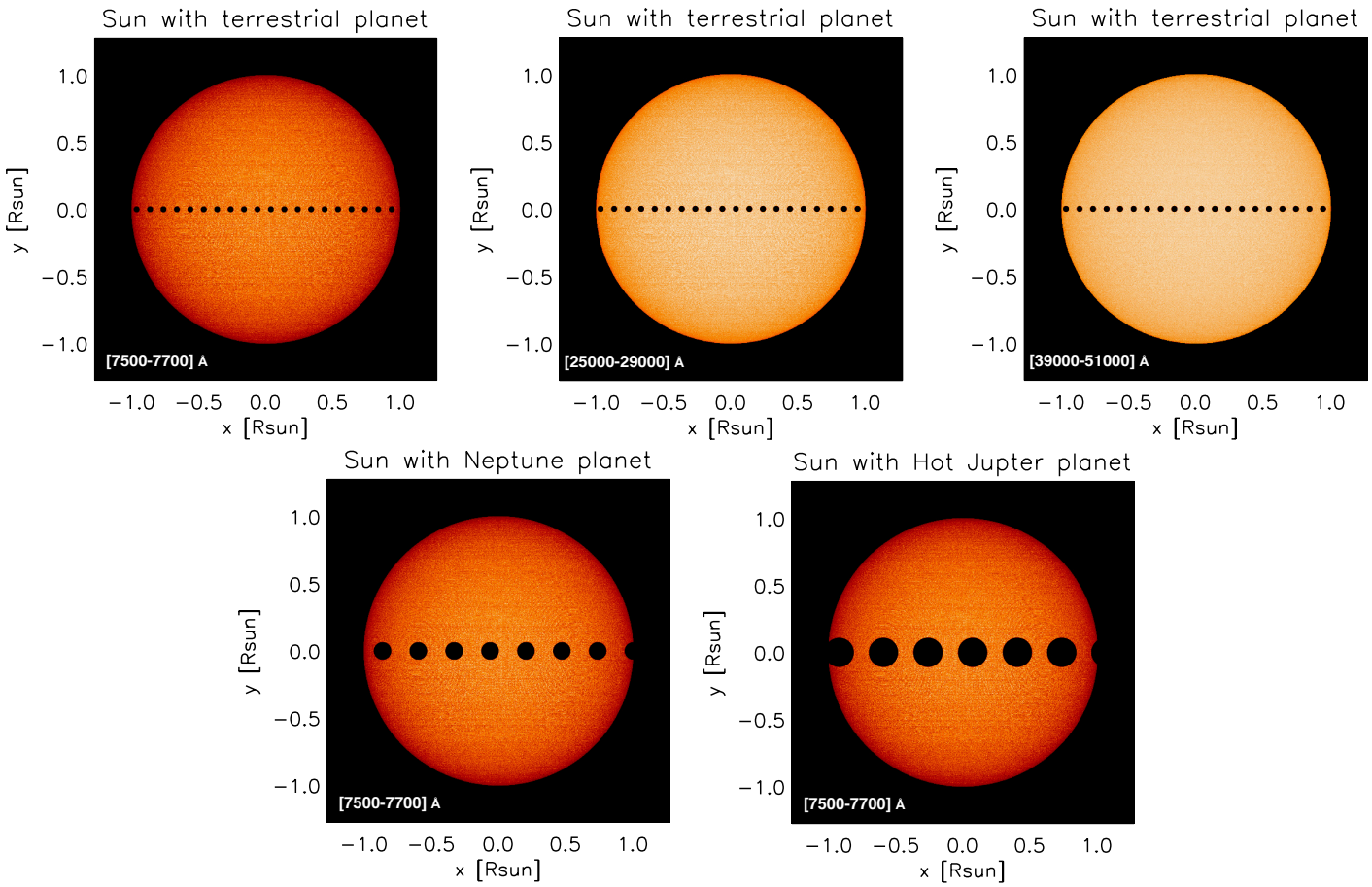

Fig. 8. *Top row*: synthetic solar disk images with transiting planet computed at [7620–7640] Å (*left*, see Table 2), [25 000–25 250] Å (*center*), [39 000–51 000] Å (*right*) for the Sun (Table 1). The prototype planet for the transit is the terrestrial planet (Table 3). For the sake of clarity, we assumed transit data measurements every 20 min in these plots. However, in the analysis (Figs. 9 and 10), we simulated transits measurements every 3 min. *Bottom row*: same as above with solar images computed at [7620–7640] Å and the prototype Neptune (*left*) and the hot Jupiter (*center*).

Figure 8 shows the simulated transits at different wavelength bands and prototype planets. The top row panel displays pronounced center-to-limb variations in the stellar disk from the optical toward the infrared bands, which is principally caused by the Planck function behavior at different wavelengths.

We computed light curves for the prototype planets of Table 3 and for all the wavelength bands of Table 2. Representative examples are shown in Figs. 9 and 10. During a transit, the planet blocks part of the radiation of its host star. The observed dim of light is directly proportional to the ratio of the planetary and the stellar projected areas as well as to the ratio of the brightness contrast. The latter depends on the wavelength probed, owing mainly to the different Planck functions in the optical and the infrared wavelength ranges (e.g., Chiavassa et al. 2012), and on the temporal variation of the granulation pattern (green shades in the transit plots and Fig. 7). Moreover, the depth of the curves depends of the size of the transiting planets (e.g., Borucki & Summers 1984) with the largest prototype planet (hot Jupiter) causing the largest transit depth (Table 5).

The envelope of the various computed transits (green shades) in Fig. 9 and is affected by the granulation noise, either because during the transit the planet occults isolated regions of the photosphere that differ in local surface brightness as a result of convection-related surface structures or by the photometric fluctuations of the stellar disk (as discussed in the previous section). These two sources of noise act simultaneously during the planet transit. In Table 5 we report the maximum depth value of the different transits and the root-mean-square (rms) of the light curves for values covering the central part of the transit periods. The rms is the direct signature of the granulation noise. It is present for all the wavelength bands used in this work and depends on the size of the planet (larger planets return stronger fluctuations) and the wavelength probed (the optical region is characterized by stronger fluctuations with respect to the infrared wavelengths). Compared to the terrestrial planet, hot Jupiter and Neptune planets occult larger regions of the stellar disk that differ in local surface brightness: this results in greater changes in the total stellar irradiance in the same time interval. The K-dwarf star returns weaker fluctuations than the Sun, at least at the spectral resolution considered for the calculations.

The granulation rms found for the terrestrial planet transit (3.5 and 2.7 ppm for the Sun and the K-dwarf star, respectively) is close to the observed photometric variability of the SOHO quiet-Sun data, which ranges between 10 to 50 ppm (Jenkins 2002; Frohlich et al. 1997). It should be noted that in our case we use narrower bands (e.g., 20 Å in the optical) with respect to the very broad filter of SOHO. The accuracy of ground-based telescopes (Table 6) is higher than the contribution of the granulation fluctuations. On the other hand, space-based telescopes show better precision, down to ∼10 ppm in the optical. These

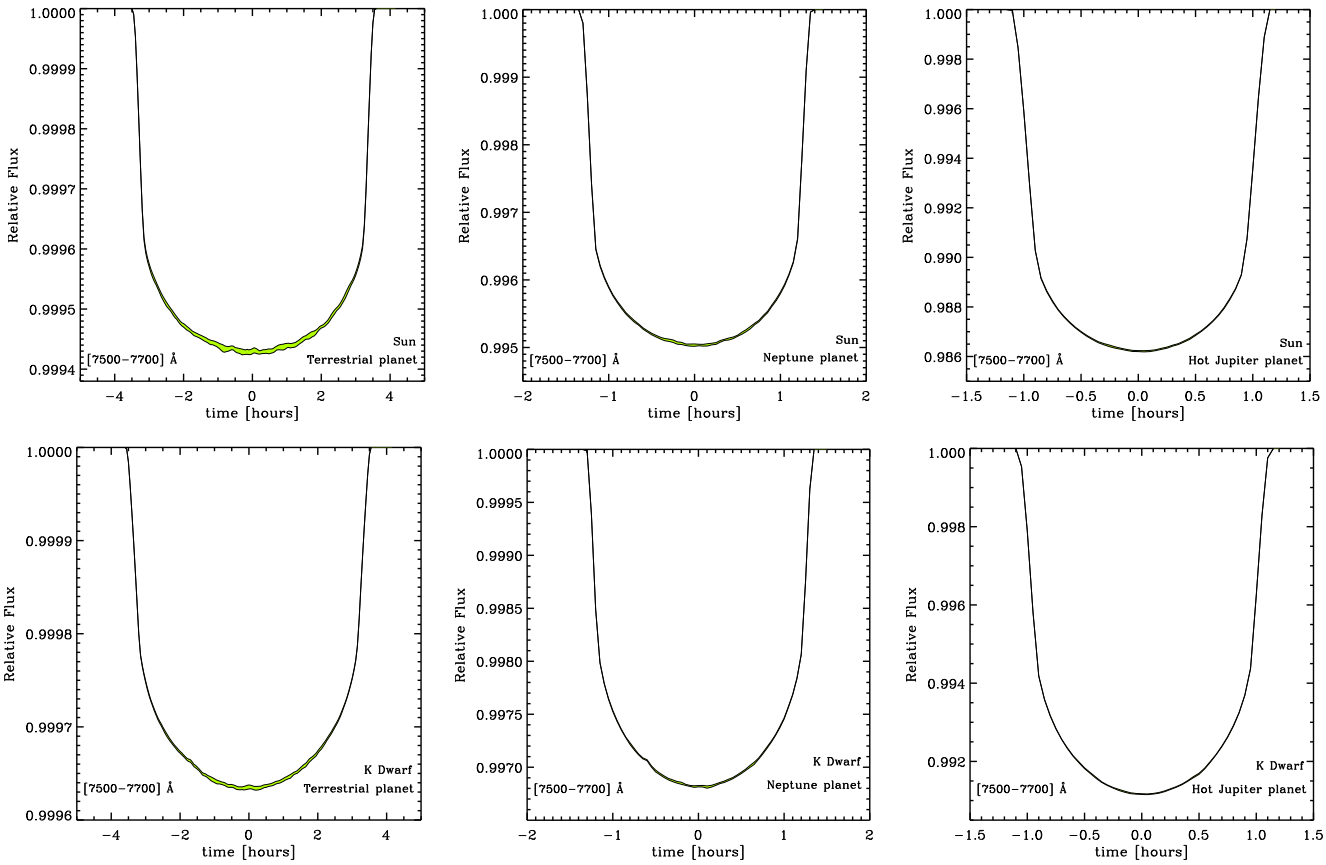

Fig. 9. Transit light curves (with the green shade denoting highest and lowest values) of 42 different synthetic Sun (*top row*) and K-dwarf star (*bottom row*) images to account for granulation changes during the transit time length for every planet (Table 3) and considering that the granulation timescale for the Sun is ∼10 min. The wavelength band shown is [7620–7640] Å (Table 2).

Table 5. Transiting curve data for the different prototype planets of Table 3 and 3D RHD simulations of Table 1.

Planet	Star	Wavelength [Å]	Depth[a]	rms [ppm]
terrestrial	Sun	[7600–7700]	0.999431	3.5
Neptune			0.995046	7.4
hot Jupiter			0.986251	15.9
terrestrial		[25 000–29 000]	0.999480	1.1
Neptune			0.995487	2.1
hot Jupiter			0.987509	4.6
terrestrial		[39 000–51 000]	0.999489	0.8
Neptune			0.995557	1.8
hot Jupiter			0.987660	3.5
terrestrial	K dwarf	[7600–7700]	0.999635	2.7
Neptune			0.996822	6.3
hot Jupiter			0.991180	9.8
terrestrial		[25 000–29 000]	0.999679	0.8
Neptune			0.997194	2.1
hot Jupiter			0.992244	2.7
terrestrial		[39 000–51 000]	0.999684	0.7
Neptune			0.997261	1.6
hot Jupiter			0.992391	2.1

Notes. The values reported in Col. 4 are the maximum transit depth and those in Col. 5 are the rms of a set of values covering the central part of the transit periods: [−1, +1] h for the terrestrial planet, [−0.15, +0.15] h for hot Neptune, and [−0.1, +0.1] h for the hot Jupiter. These values are representative for all the wavelength bands from Table 2.
[a] The depth is defined as the normalized flux minimum during transit.

Table 6. Photometric accuracy of different telescopes.

Name	Ground- or space-based	Accuracy [part-per-million]	Filter [Å]
HATNet[a]	ground	∼5000	*V* and *I* bands
NGTS[b]	ground	<1000	[6000–9000]
TRAPPIST[c]	ground	∼300	*V* band
WASP[d]	ground	∼4000	[4000–7000]
SPITZER[e]	space	29–143	[36 000–80 000]
CHEOPS[f]	space	∼10	*V* band
Kepler[g]	space	20–84	[4230–8970]
CoRoT[h]	space	∼100	[5000–10 000]
TESS[i]	space	∼60	[6000–10 000]
PLATO[j]	space	∼27	[5000–10 000]

References. [(a)] Bakos et al. (2004); [(b)] Wheatley et al. (2013); [(c)] Jehin et al. (2011); [(d)] Pollacco et al. (2006); [(e)] Gillon et al. (2010), Stevenson et al. (2010); [(f)] Broeg et al. (2013); [(g)] Koch et al. (2010); [(h)] Auvergne et al. (2009); [(i)] Ricker et al. (2015); [(j)] Rauer et al. (2014).

values are comparable to the expected rms of the granulation (between [3.5–15.9] ppm, with stronger fluctuations in the optical).

5. Effect of the granulation noise

5.1. Investigation on different orbital inclination angles

In this section, we investigate the effect of the granulation pattern on different orbital inclination angles ranging from *inc* = [90.85–90.25]°, with a step of 0.2°. Figure 11 (top panel) shows the orbital inclinations (decreasing *inc* in the souther stellar

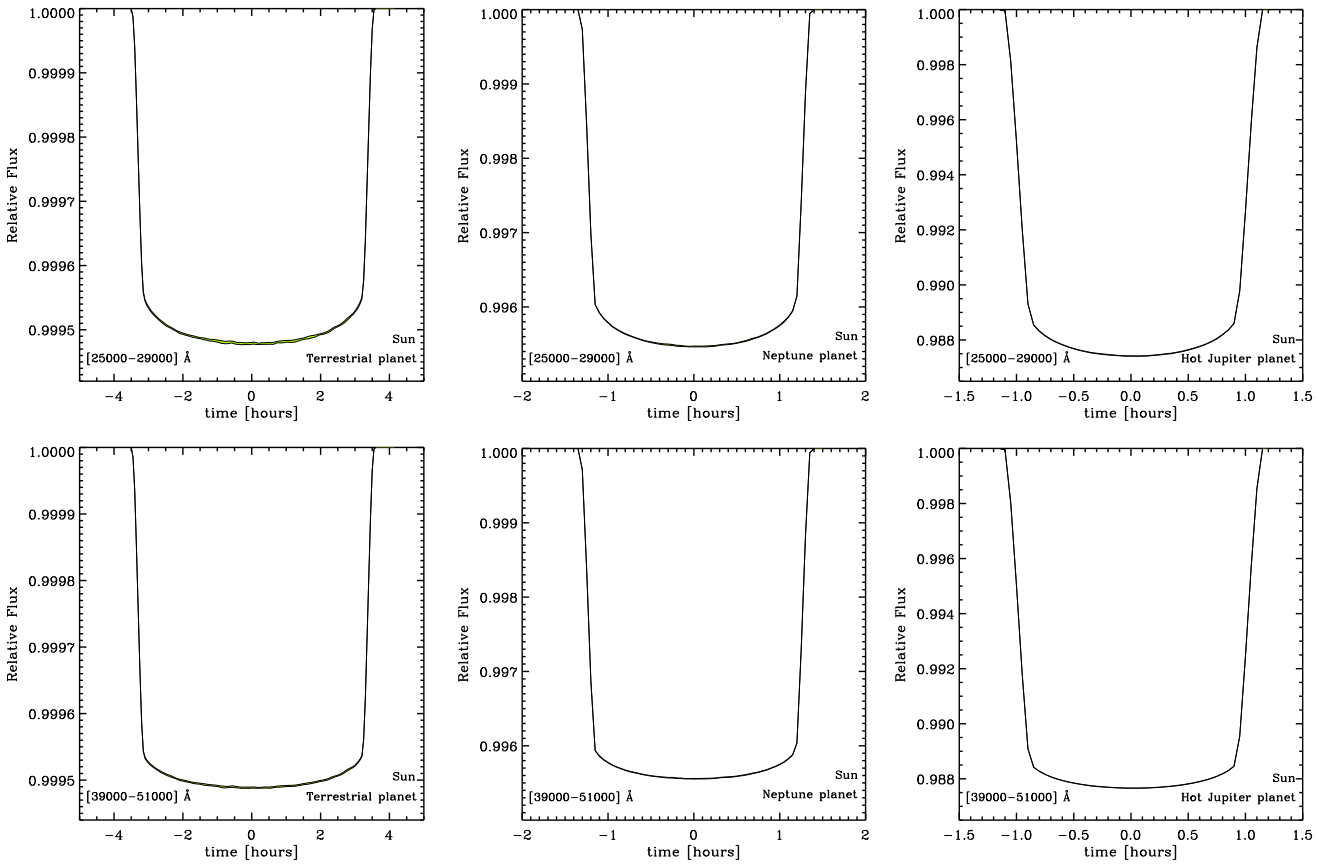

Fig. 10. Same as in Fig. 9 for the Sun and for the wavelength bands [25 000–25 250] Å (*top row*), and [39 000–51 000] Å (*bottom row*).

Table 7. Transiting curve data for the terrestrial prototype planet of Table 3 and the RHD simulations of Table 1 at different inclination orbital angles (*inc*).

Star	Wavelength [Å]	*inc* [°]	Depth	rms [ppm]
Sun	[7620–7640]	90.85	0.99951	6.3
		90.65	0.99947	4.1
		90.45	0.99945	3.1
		90.25	0.99942	3.0
K dwarf	[7620–7640]	90.85	0.99971	3.7
		90.65	0.99968	2.5
		90.45	0.99966	2.0
		90.25	0.99964	1.6

Notes. The values reported in Col. 4 are the maximum transit depth and in Col. 5 the rms of a set of values covering the central part of the transit period ([−1, 1] h). These values are representative for the wavelength bands in the optical (Table 2).

hemisphere gives similar results) represented together on the same host star. Planets transiting with inclination orbits other than 90° (Fig. 11, bottom panel; and Table 7, Col. 4) have shorter transit durations, shallower transit depths, and longer ingress and egress times than the transits at 90° (i.e., transit at the stellar center). Table 7 (Col. 4) displays the rms of the different inclined orbits for a set of values covering the central part of the transit periods. The rms value is correlated to the center-to-limb variation: increasing (or decreasing) the value of *inc* amplifies the granulation fluctuations.

5.2. Effect on the radius of the planet

Our statistical approach shows that the granulation patterns of solar and K-dwarf type stars have a non-negligible effect on the light-curve depth during the transit for small and large planets. The photosphere differs in local surface brightness because of the changes in the stellar irradiance, and as a consequence, the light-curve depth varies with time. This intrinsic error affects the determination of planetary parameters such as the planet radius. To evaluate the influence of the granulation noise, we initially fitted the averaged intensity profile of Fig. 4 (green line) with the limb-darkening law of Claret (2000; based on 1D model atmospheres of Kurucz 1979): $I_\mu/I_1 = 1 - \sum_{k=1}^{4} a_k \left(1 - \mu^{k/2}\right)$, expressed as the variation in intensity with μ-angle that is normalized to the disk-center (I_μ/I_1), and Fig. 12 displays an example. Then, we computed the light curves for a radially symmetric stellar limb-darkened disk by varying the planet radii of Table 3 to match the maximum and minimum fluctuations (green shading in the transit depth of Fig. 9) at the central time of the transit (Fig. 13). In addition to this, we we also performed the same matching process to the limits set by 1σ uncertainty on the transit distribution. In the end, the uncertainty on the radius is calculated by dividing the maximum by the minimum matching radii. Figure 13 shows that the envelope of the various computed transits for the terrestrial planet (green shade) falls between the 1σ and the 3σ uncertainties on the transit distribution.

Table 8 reports the intrinsic incertitude on the planet radius for all the prototypical planets of Table 3 and for representative wavelengths of Table 2. This uncertainty is given either for the envelope of the various computed transits (Col. 4) or for the 1σ uncertainty of the transit distribution (Col. 5). The radius

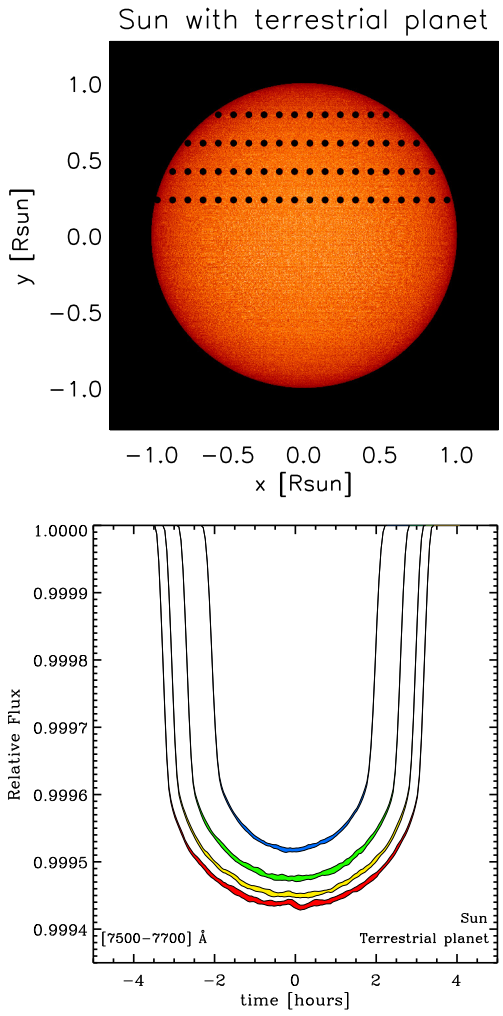

Fig. 11. *Top panel*: different transit trajectories of the prototype planet *Kepler*-11 on the Sun at the representative wavelength band of [7620–7640] Å and for four orbital inclination angles *inc* = [90.85, 90.65, 90.45, and 90.25]° (*from top to bottom* transit). An inclination angle of 90° corresponds to a planet crossing at the stellar center (Fig. 8). *Central panel*: transit light curves with colored shade denoting highest and lowest values of 42 different synthetic images to account for granulation changes during the transit. Blue corresponds to *inc* = 90.85°, green to 90.65°, yellow to 90.45°, and red to 90.25°.

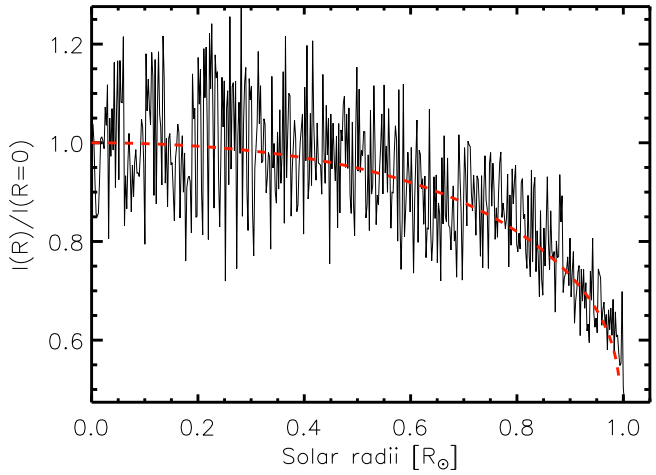

Fig. 12. Example of limb-darkening fit (red line) with the Claret law (see text) to the averaged intensity profiles of Fig. 4.

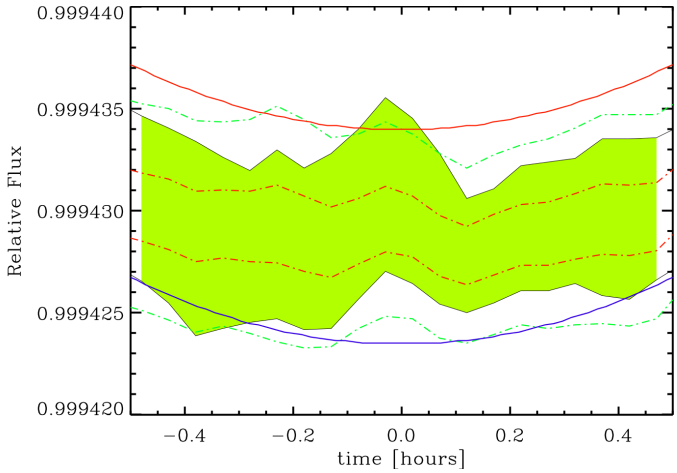

Fig. 13. Enlargement from Fig. 9 of one transit (with the green shading denoting highest and lowest values) with 42 different synthetic solar images to account for granulation changes during the transit time length for the terrestrial planet of Table 3. The dash-dotted red line is the 1σ uncertainty, while the dash-dotted light green line is the 3σ uncertainty on the transit distribution. The solid red and blue curves correspond to radially symmetric stellar limb-darkened disks with different planet radii to match the maximum (red) and minimum (blue) green shading.

uncertainty is smaller when fitting the 1σ uncertainty limits for all planets, but in particular for the terrestrial ones. It is strongly related to the rms reported in Table 5: the optical region returns larger errors as well as larger rms than those at the infrared wavelength, while the uncertainty is larger for terrestrial planets while their rms is smaller (up to 0.90% and ~0.47% for terrestrial and gaseous planets, respectively). The Sun returns higher values for the radius error than the K dwarf.

It should be noted the duration of the transits used in this work (Table 3) reach up to seven hours. In our analysis, longer transit durations may lead to lower but still significant estimates for the radius uncertainty. The effects of the granulation noise on the radius are non-negligible and should be considered for precise measurements of exoplanet transits of, in particular, planets with small diameters. The actual granulation noise is quantified in the next section. The full characterization of the granulation is essential for determining the degree of undertainty on the planet parameters. In this context, the use of 3D RHD simulations is important for estimating the amplitude of the convection-related fluctuations. This can be achieved by performing precise and continuous observations of stellar photometry and radial velocity, which are interpreted with RHD simulations, before, after, and during the transit periods.

5.3. Light curves across wavelengths and planet sizes

The aim of this section is to investigate how the granulation behaves across the different wavelength bands of Table 2. For this purpose, we used the transit light curve of three representative granulation stellar disks in the optical and near-infrared region. Following the limb-darkening procedure explained in Sect. 5.2, we fitted the temporal averaged intensity profile (green line in Fig. 4) with the limb-darkening law of Claret (2000) and used it to generate radially symmetric stellar limb-darkened disks and, the transit light curves for a terrestrial planet (Table 3). For each wavelength bin, we then subtracted the light curve generated with the granulation from the smoothed limb-darkening

Table 8. Radius and uncertainty due to the granulation fluctuations for the different prototype planets of Table 3 and 3D RHD simulations of Table 1.

Planet	Star	Wavelength [Å]	Radius max/min [%]	Radius 1σ [%]
terrestrial	Sun	[7600–7700]	0.90	0.40
Neptune			0.43	0.29
hot Jupiter			0.47	0.36
terrestrial		[25 000–29 000]	0.35	0.13
Neptune			0.22	0.11
hot Jupiter			0.08	0.05
terrestrial		[39 000–51 000]	0.20	0.11
Neptune			0.15	0.07
hot Jupiter			0.10	0.10
terrestrial	K dwarf	[7600–7700]	0.58	0.22
Neptune			0.45	0.23
hot Jupiter			0.45	0.21
terrestrial		[25 000–29 000]	0.27	0.18
Neptune			0.10	0.07
hot Jupiter			0.07	0.04
terrestrial		[39 000–51 000]	0.16	0.09
Neptune			0.10	0.05
hot Jupiter			0.07	0.04

Notes. The values reported have been computed for transit points covering the central part of the transit periods: [−1, +1] h for terrestrial planet, [−0.2, +0.2] h for the hot Neptune, and [−0.15, +0.15] h for the hot Jupiter. These values are representative for all the wavelength bands from Table 2. Column 4 shows the radius uncertainty computed for transit depth values between the maximum and minimum transit fluctuations, while Col. 5 lists this for transit depth values between 1σ uncertainty (see Fig. 13).

one. Since we did not include the atmosphere in our prototype planets, the resulting signal is the noise caused by granulation.

Figure 14 quantifies the deviations from the smoothed limb-darkening transit caused by the granulation as a function of wavelength. The amplitude of variations is $\sim 6.0 \times 10^{-6}$ for the visible and larger with respect to $\sim 2.0 \times 10^{-6}$ in the infrared. However, the fluctuations among the different wavelengths are stronger in the infrared (rms $\sim 1.3 \times 10^{-5}$) than in the visible (rms $\sim 0.5 \times 10^{-5}$), at least for the spectral resolution considered in this work. Figure 14 also displays a correlation among the different wavelength ranges in the visible and the infrared regions, at least for the spectral resolution used in this work. Higher spectral resolution in the wavelength bands is probably needed to isolate the contribution of the granulation effect on the stellar spectral lines. A more complete analysis on this aspect will be presented in a future work.

6. Conclusion

We used 3D RHD surface convection simulations with the STAGGER code to provide synthetic stellar-disk images to study the background granulation during planet transits of three prototype planets: a hot Jupiter, a hot Neptune, and a terrestrial planet.

We analyzed the effect of convection-related surface structures at different wavelengths ranging from the optical region to the far-infrared. These wavelength bands cover the range of several ground- and space-based telescopes observing planet transits and are sensitive to molecules that can give important hints on the planetary atmosphere composition. We modeled the transit light curves using the synthetic stellar-disk images obtained with the spherical-tile imaging method that was previously explained and applied in Chiavassa et al. (2010, 2012, 2014, 2015). We emulated the temporal variation of the granulation intensity, which is ∼10 min (Nesis et al. 2002) for the Sun, generating random images that cover a granulation time-series of 13.3 h. We used the data (size, flux, and duration of the transit) of three prototype planets with the purpose of studying the resulting noise caused by the granulation on the simulated transits. From the synthetic light curves, our statistical approach shows that the granulation pattern of solar and K-dwarf-type stars have a non-negligible effect on the light-curve depth during the transit for small and large planets. This intrinsic uncertainty affects the determination of the planet transit parameters such as the planet radius (up to 0.90% and ∼0.47% for terrestrial and gaseous planets, respectively), particularly for planets with small diameters. The consequences of the granulation noise on the radius are non-negligible. The full characterization of the granulation is essential to determine the degree of uncertainty on the planet parameters. In this context, the use of 3D RHD simulations is important to estimate the amplitude of the convection-related fluctuations. This can be achieved by performing precise and continuous observations of stellar photometry and radial velocity, explained with RHD simulations, before, after, and during the transit periods.

We identified two types of noise that act simultaneously during the planet transit: the intrinsic change in the granulation pattern with timescale (e.g., 10 min for solar-type stars assumed in this work) is smaller than the usual planet transit (∼hours as in our prototype cases), and the noise caused by transiting planet occulting isolated regions of the photosphere that differ in local surface brightness because of convection-related surface structures. We showed that the rms caused by the granulation pattern changes in the stellar irradiation during the transit of the terrestrial planet (between 3.5 and 2.7 ppm for the Sun and K dwarf, respectively) is close to what has been found by Jenkins (2002) and Frohlich et al. (1997): 10 to 50 ppm. This indicates that our modeling approach is reliable. We also showed that different orbital inclination angles with respect to transits at $inc = 90°$ (planet crossing at the stellar center) display a shallower transit depth, and longer ingress and egress times, as expected, but

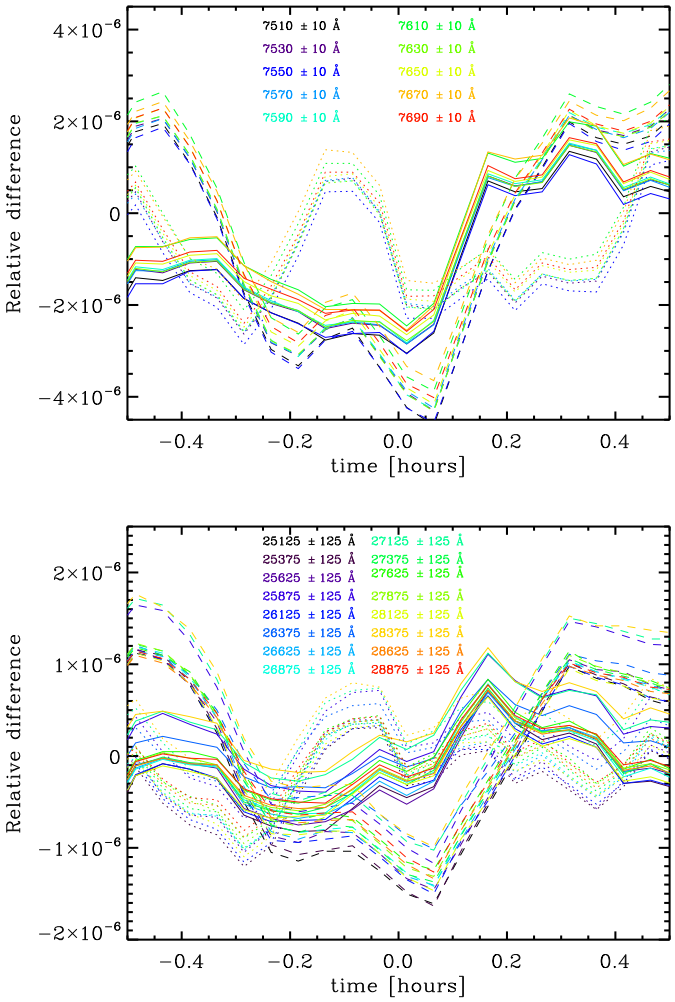

Fig. 14. Granulation noise for three representative granulation stellar disk realizations of the Sun affecting the central part of the light curve for a terrestrial planet (Table 3). The colors denotes different wavelengths ranges (Table 2) in the optical (*top panel*) and in the near infrared (*bottom panel*). The relative difference is obtained subtracting, for each wavelength range, the light curve generated with the granulation snapshot with the one computed with the appropriate radially symmetric stellar limb darkened disk (see text).

also rms values correlated to the center-to-limb variation: granulation fluctuations increase for *inc* different from 90°. Finally, the granulation noise appears to be correlated among the different wavelength ranges in the visible and the infrared regions, at least for the spectral resolution used in this work.

Three-dimensional RHD simulations are now established as realistic descriptions for the convective photospheres of various classes of stars. They have recently been employed to explain the transit of Venus in 2004 (Chiavassa et al. 2015). Chiavassa and collaborators showed that in terms of transit depth and ingress/egress slopes as well as the emerging flux, a 3D RHD simulation of the Sun is well adapted to interpret the observed data. Their light-curve fit was supported by the fact that the granulation pattern changes would affect transit depth. Modeling the transit light curve of exoplanets is crucial for current and future observations that aim to detect planets and characterize them with this method. The good and time-dependent representation of the background stellar disk is mandatory. In this context, 3D RHD simulations are useful for a detailed quantitative analysis of the transits.

Acknowledgements. R.C. is the recipient of an Australian Research Council Discovery Early Career Researcher Award (project number DE120102940). This study has received partial financial support from the French State in the frame of the "Investments for the future" Programme IdEx Bordeaux, reference ANR-10-IDEX-03-02. The authors thank the referee for helping in finding a numerical problem during the refereeing process.

References

Aigrain, S., Favata, F., & Gilmore, G. 2004, A&A, 414, 1139
Asplund, M., Nordlund, Å., Trampedach, R., Allende Prieto, C., & Stein, R. F. 2000, A&A, 359, 729
Asplund, M., Grevesse, N., Sauval, A. J., & Scott, P. 2009, ARA&A, 47, 481
Auvergne, M., Bodin, P., Boisnard, L., et al. 2009, A&A, 506, 411
Bakos, G., Noyes, R. W., Kovács, G., et al. 2004, PASP, 116, 266
Borucki, W. J., & Summers, A. L. 1984, Icarus, 58, 121
Borucki, W. J., Koch, D., Basri, G., et al. 2010, Science, 327, 977
Broeg, C., Fortier, A., Ehrenreich, D., et al. 2013, in Eur. Phys. J. Web Conf., 47, 3005
Chiavassa, A., Plez, B., Josselin, E., & Freytag, B. 2009, A&A, 506, 1351
Chiavassa, A., Collet, R., Casagrande, L., & Asplund, M. 2010, A&A, 524, A93
Chiavassa, A., Bigot, L., Kervella, P., et al. 2012, A&A, 540, A5
Chiavassa, A., Ligi, R., Magic, Z., et al. 2014, A&A, 567, A115
Chiavassa, A., Pere, C., Faurobert, M., et al. 2015, A&A, 576, A13
Claret, A. 2000, A&A, 363, 1081
Dawes, W. R. 1864, MNRAS, 24, 161
Dravins, D. 1987, A&A, 172, 211
Frohlich, C., Andersen, B. N., Appourchaux, T., et al. 1997, Sol. Phys., 170, 1
Gillon, M., Deming, D., Demory, B.-O., et al. 2010, A&A, 518, A25
Gray, D. F. 2005, The Observation and Analysis of Stellar Photospheres (Cambridge University Press)
Gustafsson, B., Edvardsson, B., Eriksson, K., et al. 2008, A&A, 486, 951
Hayek, W., Asplund, M., Carlsson, M., et al. 2010, A&A, 517, A49
Herschel, W. 1801, R. Soc. Lond. Philosoph. Trans. Ser. I, 91, 265
Jehin, E., Gillon, M., Queloz, D., et al. 2011, The Messenger, 145, 2
Jenkins, J. M. 2002, ApJ, 575, 493
Koch, D. G., Borucki, W. J., Basri, G., et al. 2010, ApJ, 713, L79
Kurucz, R. L. 1979, ApJS, 40, 1
Ludwig, H., Caffau, E., Steffen, M., et al. 2009, Mem. Soc. Astron. It., 80, 711
Magic, Z., & Asplund, M. 2014, A&A, submitted [arXiv:1405.7628]
Magic, Z., Collet, R., Asplund, M., et al. 2013, A&A, 557, A26
Mihalas, D., Dappen, W., & Hummer, D. G. 1988, ApJ, 331, 815
Mislis, D., Heller, R., Schmitt, J. H. M. M., & Hodgkin, S. 2012, A&A, 538, A4
Nesis, A., Hammer, R., Roth, M., & Schleicher, H. 2002, A&A, 396, 1003
Nordlund, A. 1982, A&A, 107, 1
Nordlund, A., & Dravins, D. 1990, A&A, 228, 155
Nordlund, Å., Stein, R. F., & Asplund, M. 2009, Liv. Rev. Sol. Phys., 6, 2
Pollacco, D. L., Skillen, I., Collier Cameron, A., et al. 2006, PASP, 118, 1407
Rauer, H., Catala, C., Aerts, C., et al. 2014, Exp. Astron., 38, 249
Ricker, G. R., Latham, D. W., Vanderspek, R. K., et al. 2010, in BAAS 42, AAS Meet. Abstr., 215, 450.06
Ricker, G. R., Winn, J. N., Vanderspek, R., et al. 2015, J. Astron. Telescopes, Instruments, and Systems, 1, 014003
Skartlien, R. 2000, ApJ, 536, 465
Stempels, H. C., Piskunov, N., & Barklem, P. S. 2001, in 11th Cambridge Workshop on Cool Stars, Stellar Systems and the Sun, eds. R. J. Garcia Lopez, R. Rebolo, & M. R. Zapaterio Osorio, ASP Conf. Ser., 223, 878
Stevenson, K. B., Harrington, J., Nymeyer, S., et al. 2010, Nature, 464, 1161
Trampedach, R., Asplund, M., Collet, R., Nordlund, Å., & Stein, R. F. 2013, ApJ, 769, 18
Wheatley, P. J., Pollacco, D. L., Queloz, D., et al. 2013, in Eur. Phys. J. Web Conf., 47, 13002
Wright, J. T., Fakhouri, O., Marcy, G. W., et al. 2011, PASP, 123, 412

A&A 515, A12 (2010)
DOI: 10.1051/0004-6361/200913907

Astronomy & Astrophysics

Radiative hydrodynamics simulations of red supergiant stars

II. Simulations of convection on Betelgeuse match interferometric observations

A. Chiavassa[1,2], X. Haubois[3], J. S. Young[4], B. Plez[2], E. Josselin[2], G. Perrin[3], and B. Freytag[5,6]

[1] Max-Planck-Institut für Astrophysik, Karl-Schwarzschild-Str. 1, Postfach 1317, 85741 Garching b. München, Germany
e-mail: chiavass@mpa-garching.mpg.de
[2] GRAAL, Université de Montpellier II – IPM, CNRS, Place Eugéne Bataillon, 34095 Montpellier Cedex 05, France
[3] Observatoire de Paris, LESIA, UMR 8109, 92190 Meudon, France
[4] Astrophysics Group, Cavendish Laboratory, JJ Thomson Avenue, Cambridge CB3 0HE, UK
[5] Centre de Recherche Astrophysique de Lyon, UMR 5574: CNRS, Université de Lyon, École Normale Supérieure de Lyon, 46 allée d'Italie, 69364 Lyon Cedex 07, France
[6] Department of Physics and Astronomy, Division of Astronomy and Space Physics, Uppsala University, Box 515, 751 20 Uppsala, Sweden

Received 18 December 2009 / Accepted 2 March 2010

ABSTRACT

Context. The red supergiant (RSG) Betelgeuse is an irregular variable star. Convection may play an important role in understanding this variability. Interferometric observations can be interpreted using sophisticated simulations of stellar convection.
Aims. We compare the visibility curves and closure phases obtained from our 3D simulation of RSG convection with CO5BOLD to various interferometric observations of Betelgeuse from the optical to the *H* band to characterize and measure the convection pattern on this star.
Methods. We use a 3D radiative-hydrodynamics (RHD) simulation to compute intensity maps in different filters and thus derive interferometric observables using the post-processing radiative transfer code OPTIM3D. The synthetic visibility curves and closure phases are compared to observations.
Results. We provide a robust detection of the granulation pattern on the surface of Betelgeuse in both the optical and the *H* band based on excellent fits to the observed visibility points and closure phases. We determine that the Betelgeuse surface in the *H* band is covered by small to medium scale (5−15 mas) convection-related surface structures and a large (≈30 mas) convective cell. In this spectral region, H_2O molecules are the main absorbers and contribute to both the small structures and the position of the first null of the visibility curve (i.e., the apparent stellar radius).

Key words. stars: individual: Betelgeuse – stars: atmospheres – hydrodynamics – radiative transfer – techniques: interferometric

1. Introduction

Betelgeuse is a red supergiant star (Betelgeuse, HD 39801, M1−2Ia−Ibe) and is one of the brightest stars in the optical and near infrared. This star exhibits variations in integrated brightness, surface features, and the depths, shapes, and Doppler shifts of its spectral lines. Visual-wavelength observations of its brightness cover almost a hundred years. The irregular fluctuations of its light curve are clearly aperiodic and resemble a series of outbursts. Kiss et al. (2006) studied the variability of different red supergiant (RSG) stars including Betelgeuse and found a strong noise component in the photometric variability, probably caused by the large convection cells. In addition to this, the spectral line variations have been analyzed by several authors, who inferred the presence of large granules and high convective velocities (Josselin & Plez 2007; Gray 2008). Gray also found line bisectors that have predominantly reversed C-shapes, and line shape variations occurring at the 1 km s^{-1} level that have no obvious connection to their shifts in wavelength.

The position of Betelgeuse on the H-R diagram is highly uncertain, because of the uncertainty in its effective temperature. Levesque et al. (2005) used one-dimensional MARCS models (Gustafsson et al. 2003, 1975) to fit the incredibly rich TiO molecular bands in the optical region of the spectrum for several RSGs. They found an effective temperature of 3650 K for Betelgeuse. Although they obtained good agreement with the evolutionary tracks, problems remain. There is a mismatch in the IR colors that could be due to atmospheric temperature inhomogeneities characteristic of convection (Levesque et al. 2006). The distance of Betelgeuse also has large uncertainties because of errors related to the positional movement of the stellar photocenter. Harper et al. (2008) derived a distance of (197 ± 45 pc) using high spatial resolution, multiwavelength, VLA radio positions combined with Hipparcos Catalogue Intermediate Astrometric Data.

Betelgeuse is one of the most well studied RSGs in term of multiwavelength imaging because of its high luminosity and large angular diameter. The existence of hot spots on its surface has been proposed to explain numerous interferometric observations with WHT and COAST (Buscher et al. 1990; Wilson et al. 1992; Tuthill et al. 1997; Wilson et al. 1997; Young et al. 2000, 2004) that detected time-variable inhomogeneities in the brightness distribution. These authors fitted the visibility and closure phase data with a circular limb-darkened disk and zero to three spots. A large spot was detected by Uitenbroek et al. (1998) with HST. The non-spherical shape of Betelgeuse was also detected by Tatebe et al. (2007) in the mid-infrared.

Haubois et al. (2009) published a reconstructed image of Betelgeuse in the H band with two spots using the same data as presented in this work. Kervella et al. (2009) resolved Betelgeuse using diffraction-limited adaptive optics in the near-infrared and found an asymmetric envelope around the star with a bright plume extending in the southwestern region. They claimed the plume was either due to the presence of a convective hot spot or caused by stellar rotation. Ohnaka et al. (2009) presented VLTI/AMBER observations of Betelgeuse at high spectral resolution and spatially resolved CO gas motions. They claimed that these motions were related to convective motions in the upper atmosphere or to intermittent mass ejections in clumps or arcs.

Radiation hydrodynamics (RHD) simulations of red supergiant stars are available (Freytag et al. 2002) to interpret past and future observations. Chiavassa et al. (2009), hereafter Paper I, used these simulations to explore the impact of the granulation pattern on observed visibility curves and closure phases and detected a granulation pattern on Betelgeuse in the K band by fitting the existing interferometric data of Perrin et al. (2004).

This paper is the second in a series aimed at exploring the convection in RSGs. The main purpose is to compare RHD simulations to high-angular resolution observations of Betelgeuse covering a wide spectral range from the optical region to the near-infrared H band, to confirm the detection of convective cells on its surface.

2. 3D radiation-hydrodynamics simulations and post-processing radiative transfer

We employed numerical simulations obtained using CO^{5}BOLD (Freytag et al. 2002; Freytag 2003; Freytag & Höfner 2008) and in particular the model st35gm03n07 that was deeply analyzed in Paper I. The model has a mass of 12 $M_\odot$, a numerical resolution of 235^3 grid points with a step of 8.6 $R_\odot$, an average luminosity over spherical shells and over time of $L = 93\,000 \pm 1300\ L_\odot$, an effective temperature of $T_{\rm eff} = 3490 \pm 13$ K, a radius of $R = 832 \pm 0.7\ R_\odot$, and surface gravity $\log(g) = -0.337 \pm 0.001$. This is our most successfull RHD simulation so far because it has stellar parameters closest to Betelgeuse ($T_{\rm eff} = 3640$ K, Levesque et al. 2005 and $\log(g) = -0.3$, Harper et al. 2008).

We used the 3D pure-LTE radiative transfer code OPTIM3D described in Paper I to compute intensity maps from all the suitable snapshots of the 3D hydrodynamical simulation. The code takes into account the Doppler shifts caused by the convective motions. The radiation transfer is calculated in detail using pre-tabulated extinction coefficients generated with the MARCS code (Gustafsson et al. 2008). These tables are functions of temperature, density and wavelength, and were computed for the solar composition of Asplund et al. (2006). The tables include the same extensive atomic and molecular data as the MARCS models. They were constructed with no micro-turbulence broadening and the temperature and density distributions are optimized to cover the values encountered in the outer layers of the RHD simulations.

3. Observations

The data presented in this work were acquired by two independent groups with different telescopes and they cover a large wavelength range from the optical to the near infrared. The log of the observations is reported in Table 1.

Table 1. Log of the observations.

Date	Telescope	Filter (central λ)
October 7, 2005	IOTA	IONIC – 16 000
October 8, 2005	IOTA	IONIC – 16 000
October 10, 2005	IOTA	IONIC – 16 000
October 11, 2005	IOTA	IONIC – 16 000
October 12, 2005	IOTA	IONIC – 16 000
October 16, 2005	IOTA	IONIC – 16 000
October 21, 1997	COAST	12 900 Å
October 24, 1997	COAST	9050 Å
October 31, 1997	COAST	9050 Å
November 11, 1997	COAST	12 900 Å
November 12, 1997	COAST	9050 Å
November 15, 1997	WHT	7000 Å
November 16, 1997	WHT	9050 Å
November 21, 1997	COAST	9050 Å
January 29, 2004	COAST	7500, 7820, 9050 Å
February 8, 2004	COAST	7500, 7820, 9050 Å
February 25, 2004	COAST	7500, 7820, 9050 Å
February 29, 2004	COAST	7500, 7820, 9050 Å
March 1, 2004	COAST	7500, 7820, 9050 Å
March 2, 2004	COAST	7500, 7820, 9050 Å

3.1. Data at 16 400 Å

The H band data were acquired with the 3 telescope interferometer IOTA (Infrared Optical Telescope Array, Traub et al. 2003) located at Mount Hopkins in Arizona. Light collected by three apertures (siderostats of 0.45 m diameter) was spatially filtered by single mode fibers to clean the wavefronts, removing high frequency atmospheric corrugations that affect the fringe contrast. The beams were then combined with IONIC (Berger et al. 2003). This integrated optics component combines 3 input beams in a pairwise manner. Fringes were encoded in the time domain using piezo-electric path modulators, and detected with a near-infrared camera utilizing a PICNIC detector (Pedretti et al. 2004).

Betelgeuse was observed in the H band (16 400 ± 1000 Å, Fig. 1) on 6 nights between Oct. 7, 2005 and Oct. 16, 2005. Five different configurations of the interferometer telescopes were used, to cover a wide range of spatial frequencies between 12 and 95 arcsec^{-1}. To calibrate the instrumental transfer function, observations of Betelgeuse were interleaved with observations of a reference (calibrator) star, HD 36167.

Data reduction was carried out using an IDL pipeline (Monnier et al. 2004; Zhao et al. 2007). To measure the closure phase, we took the phase of the complex triple product (bispectrum, Baldwin et al. 1986). The instrumental closure phase of IONIC3 drifted by less than 1 degree over many hours owing to the miniature dimensions of the integrated optics component. For both the squared visibilities and the closure phase, the random errors were calculated with the bootstrap technique, in which a statistic is repeatedly re-estimated by Monte-Carlo sampling the original data with replacement. Full details of the observations and data reduction can be found in Haubois et al. (2009).

3.2. Data from 7000 to 12 900 Å

For this wavelength range, we used data taken at two different epochs. The observations carried out in 1997 (Young et al. 2000) were acquired with the Cambridge Optical Aperture Synthesis Telescope (COAST) on baselines up to 8.9 m (with central wavelengths/bandwidths of 9050/500 and 12 900/1500 Å) and

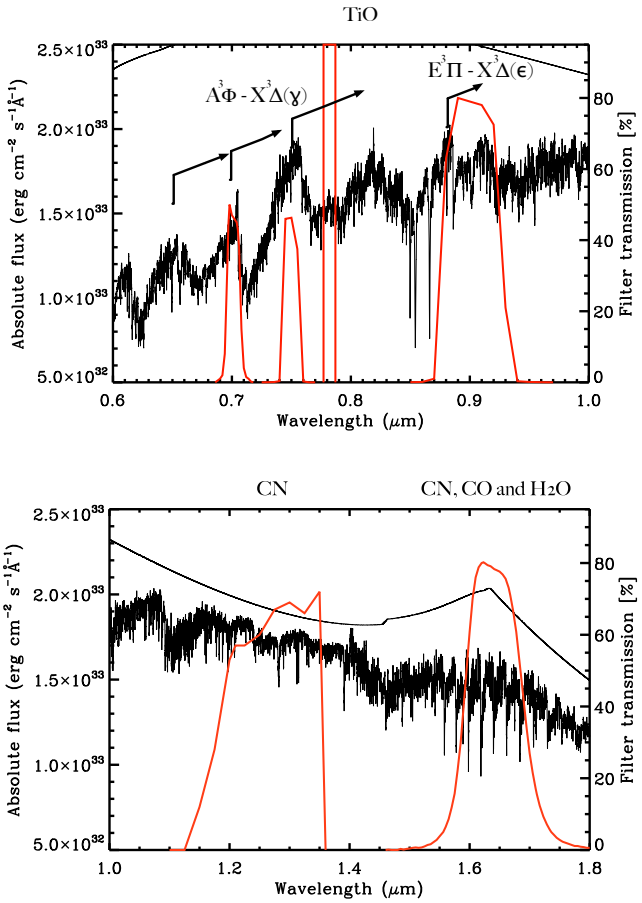

Fig. 1. Transmission curves (red) of the bandpass filters used for Betelgeuse observations at COAST and WHT: central wavelengths at 7000, 7500, 7820, and 12 900 Å and nominal bandwidths (*FWHM*) of 100, 130, 50, 500, and 1500 Å, respectively (Young et al. 2004, 2000) (the filter curve for the narrow bandpass centered on 7820 Å has been lost hence we assumed a top-hat filter); and for Betelgeuse observations at IOTA: 16 400 Å with 1000 Å bandwidth (Haubois et al. 2009). The black line is the synthetic spectrum with its continuum computed from the RHD simulation snapshot of Fig. 8; the molecules that contribute the most in every filter have been highlighted.

by non-redundant aperture masking with the William Herschel Telescope (WHT) on baselines up to 3.7 m (with central wavelengths/bandwidths of 7000/100 and 9050/500). The observations carried out in 2004 were obtained with COAST on baselines up to 6.1 m (bandpasses 7500/130, 7820/50, and 9050/500 Å). Figure 1 shows all the filters used.

3.2.1. COAST data from 1997

The COAST data were acquired during October and November 1997. Observations at 9050 Å were made using the standard beam-combiner and avalanche photodiode detectors (Baldwin et al. 1994), while 12 900 Å observations were obtained with a separate pupil-plane combiner optimized for *JHK* bands (Young et al. 1998).

Observations of Betelgeuse were interleaved with observations of calibrator stars, either unresolved or of small and known diameters. If at least three baselines were measurable and the atmospheric coherence time was sufficiently long, closure phase measurements were also collected, by recording fringes on three baselines simultaneously.

Data reduction was carried out using standard methods in which the power spectrum and bispectrum of the interference fringes were averaged over each dataset (Burns et al. 1997). The resulting visibilities had formal fractional errors in the range 2−10% of the values, and the closure phases had typical uncertainties of 5−10°. Additional uncertainties of 10−20% were added to the visibility amplitudes to accommodate potential changes in the seeing conditions between observations of the science target and calibrator stars.

3.2.2. WHT data from 1997

The observations performed with the WHT used the non-redundant aperture masking method (Baldwin et al. 1986; Haniff et al. 1987) and employed a five-hole linear aperture mask. Filters centred on both 7000 Å and 9050 Å were used to select the observing waveband; only the 7000 Å data are presented in this paper. The resulting interference fringes were imaged onto a CCD and one-dimensional fringe snapshots were recorded at 12-ms intervals. For each orientation of the mask, the fringe data were reduced using standard procedures (Haniff et al. 1987; Buscher et al. 1990) to provide estimates of the visibility amplitudes on all 10 interferometer baselines and the closure phases on the 10 (linear) triangles of baselines. As for the COAST measurements, the uncertainties in the visibility amplitudes were dominated by calibration errors, which in this instance were unusually large (fractional error ∼30%). On the other hand, the calibrated closure phase measurements had typical errors of only 1−3°. The orientation and scale of the detector were determined by observations of two close visual binaries with well-determined orbits.

3.2.3. COAST data from 2004

The observations taken in 2004 (Young et al. 2004) were acquired with COAST using the standard beam combiner and filters centered on 7500, 7820, and 9050 Å of *FWHM* 130, 50, and 500 Å, respectively. The raw interference fringe data were reduced using the same methods utilised for the 1997 COAST data to obtain a set of estimates of the visibility amplitude and closure phase for each observing waveband.

4. Comparison of simulations and observations

We compare the synthetic visibility curves and closure phases to the observations. For this purpose, we used all the snapshots from the RSG simulation to compute intensity maps with OPTIM3D. These maps were normalized to the filter transmissions of Fig. 1 as $\frac{\int I_\lambda \tau(\lambda) d\lambda}{\int \tau(\lambda) d\lambda}$, where $I(\lambda)$ is the intensity and $\tau(\lambda)$ is the optical transmission of the filter at a certain wavelength. For each intensity map, a discrete Fourier transform (*FT*) was then calculated. The visibility V is defined as the modulus $|z|$ of the complex Fourier transform $z = x + iy$ (where x is real part of the complex number z and y its imaginary part) normalized to the modulus at the origin of the frequency plane $|z_0|$, with the phase θ defined as $\tan\theta = \Im(z)/\Re(z)$. The closure phase is defined as the phase of the triple product (or bispectrum) of the complex visibilities on three baselines, which form a closed loop joining three stations A, B, and C. If the projection

of the baseline AB is (u_1, v_1), that for BC is (u_2, v_2), and thus $(u_1 + u_2, v_1 + v_2)$ for AC, the closure phase is:

$$\phi_C(u_1, v_1, u_2, v_2) = \arg(V(u_1, v_1) \times V(u_2, v_2) \times V^*(u_1 + u_2, v_1 + v_2)).$$

The projected baselines and stations are those of the observations.

Following the method explained in Paper I, we computed visibility curves and closure phases for 36 different rotation angles with a step of 5° from all the available intensity maps (≈3.5 years of stellar time), giving a total of ≈2000 synthetic visibilities and ≈2000 synthetic closure phases per filter.

4.1. Data at 16 400 Å

We begin by comparing with the 16 400 Å data because this filter is centered where the H^{-1} continuous opacity minimum occurs. Consequently, the continuum-forming region is more visible and the granulation pattern is characterized by large-scale granules of about 400−500 $R_\odot$ (≈60% of the stellar radius) evolving on a timescale of years (Fig. 4 in Paper I). On the top of these cells, there are short-lived (a few months to one year) small-scale (about 50−100 $R_\odot$) structures. The resulting granulation pattern causes significant fluctuations in the visibility curves and the signal to be expected in the second, third, and fourth lobes deviates greatly from that predicted by uniform disk (UD) and limb-darkened disk (LD) models (Fig. 11 in Paper I). The closure phases also show large departures from 0 and ±π, the values that would correspond to a point-symmetric brightness distribution.

Within the large number of computed visibilities and closure phases for this filter, we found that some match the observation data very well (Fig. 2). We selected the best-fit model snapshot by minimizing the function

$$\chi^2 = \frac{1}{N}\left[\sum_{i=1}^{N_V}\left(\frac{V_i - M_{V_i}}{\sigma_{V_i}}\right)^2 + \sum_{i=1}^{N_{\phi C}}\left(\frac{\phi_{C_i} - M_{\phi_{C_i}}}{\sigma_{\phi_{C_i}}}\right)^2\right], \quad (1)$$

where V_i is the observed visibility amplitude data with its corresponding error σ_{V_i}, M_{V_i} is the synthetic visibility amplitude at the same spatial frequency, ϕ_{C_i} is the observed closure phase with corresponding error $\sigma_{\phi_{C_i}}$, and $M_{\phi_{C_i}}$ the synthetic closure phase for the observed UV coordinates. The closest matching visibilities and closure phases correspond to a particular snapshot and rotation angle.

In Fig. 3, the simulation has been scaled to an apparent diameter of ∼45.1 mas to fit the data points in the first lobe, corresponding to a distance of 172.1 pc for the simulated star. The angular diameter is slightly larger than the limb-darkened diameter of 44.28 ± 0.15 mas found by Haubois et al. (2009). Our distance is also in agreement with Harper et al. (2008), who reported a distance of 197 ± 45 pc. Using the distance of Harper et al. and an effective temperature of 3650 K (Levesque et al. 2005), the radius is $R = 890 \pm 200\ R_\odot$, neglecting any uncertainty in $T_{\rm eff}$. On the other hand, using the distance of Harper et al. and the apparent diameter of 45 mas (Perrin et al. 2004), the radius is $R = 950 \pm 200\ R_\odot$. All these results match evolutionary tracks by Meynet & Maeder (2003) for an initial mass of between 15 and 25 $M_\odot$. The radius ($R \approx 832\ R_\odot$, see Sect. 2) and the effective temperature ($T_{\rm eff} \approx 3490$ K) of our 3D simulation are smaller because the simulations start with an initial model that has an estimated radius, a certain envelope mass, a certain potential profile, and a prescribed luminosity. However, during the run the internal structure relaxes to something not to far away from the initial guess (otherwise the numerical grid would be inappropriate). The average final radius is determined once the simulation has ended. Therefore, since the radius (and the effective temperature) cannot be tuned, the model is placed at some distance to provide the angular diameter that most closely matches the observations. Finally, within the error bars our model radius

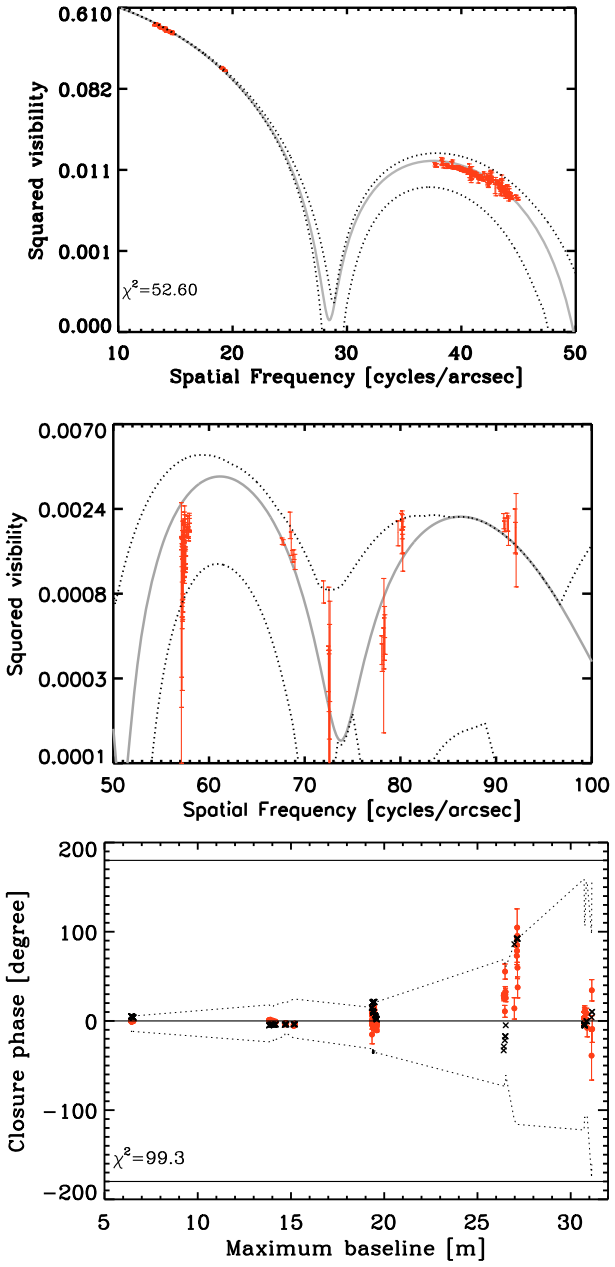

Fig. 2. *Top and central panels*: the best-matching synthetic squared visibility (grey) compared to the observations of Betelgeuse (Haubois et al. 2009, red). The reduced χ^2 is indicated. The dotted lines are the maximum and minimum amplitude of the visibility fluctuations as the snapshot is rotated. *Bottom panel*: closure phase (in degrees) versus the maximum projected baseline length for each baseline triplet. The observations (red dots with error bars) are fitted with the same intensity map and rotation angle used for the visibilities (black crosses). The axisymmetric case is represented by the solid black lines. The dotted lines are the maximum and minimum of the closure phase variation as the snapshot is rotated.

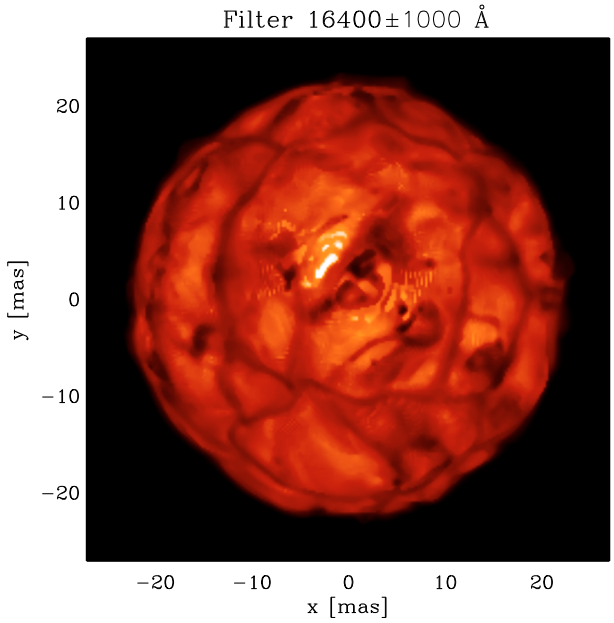

Fig. 3. Map of the linear intensity in the IONIC filter. The range is $[0;3.1 \times 10^5]$ erg cm^{-2} s^{-1} Å^{-1}. The stellar parameters of this snapshot are: $L = 92\,300\,L_\odot$, $R = 832.4\,R_\odot$, $T_{\rm eff} = 3486$ K, and $\log(g) = -0.34$. The simulation has been scaled to an apparent diameter of ∼45.1 mas, at a distance of 172.1 pc to fit the data points in the first lobe.

agrees with all other data derived using the distance determined by Harper et al. (2008).

Our RHD simulation provides a more accurate fit of the data than uniform disk and limb-darkened models used by Haubois et al. in all lobes of the visibility function. The departure from circular symmetry is more evident at high spatial frequencies (e.g., the fourth lobe) where the visibility predicted from the parametric model is lower than the observed data. The small-scale convection-related surface structures are the cause of this departure and can only be explained by RHD simulations that are permeated with irregular convection-related structures of different size. The closure phases also display a good agreement with the simulation indicating that a possible solution to the distribution of the inhomogeneities on the surface of Betelgeuse is the intensity map of Fig. 3 (though the reconstructed images found by Haubois et al. (2009) are more probable).

This is the first robust confirmation of the physical origin of surface granulation for Betelgeuse, following on from the detection in the K band (Paper I). Haubois et al. (2009) were able to reconstruct two images of Betelgeuse, using the data presented in this work, with two different image reconstruction algorithms. The image reconstructed with WISARD (Meimon et al. 2009, 2005) is displayed in Fig. 4 (left). Both images reconstructed in in Haubois et al. have two spots of unequal brightness located at roughly the same positions near the center of the stellar disk. One of these spots is half the stellar radius in size. Figure 4 compares the reconstructed image to our best-fit snapshot of Fig. 3. Fainter structures are visible in the synthetic image (right panel), while the reconstructed image (left panel) is dominated by two bright spots. Moreover, the larger spot visible in the reconstructed image is not present in our synthetic image, whereas there is good agreement in terms of location with the smaller spot located close to the center. However, it is possible that the synthetic map does not match exactly the location of the spots because it cannot perfectly reproduce the closure phase data.

4.1.1. Molecular contribution to the visibility curves

It is important to determine which molecular species contribute the most to the intensity absorption in the stellar atmosphere. For this purpose, we used the best fit snapshot of Fig. 3 and recomputed the intensity maps in the IONIC filter using only CO, CN, and H_2O molecules, because they are the largest absorbers at these wavelengths (Fig. 1 of this work and Fig. 3 of Paper I). The intensity maps displayed in Fig. 5 of this paper (top row) should be compared to the original one in Fig. 3, which accounts for all the molecular and atomic lines. The surfaces of CO and CN maps clearly show the granulation pattern and are spot-free. However, the H_2O map exhibits dark spots, which can also be identified in the original intensity map.

We calculated visibility curves from these molecular intensity maps using the same rotation angle used to generate the synthetic data in Fig. 2. Figure 5 (bottom row) shows that the H_2O visibility is the closest to the original one at both low and high spatial frequencies. We conclude that: (i) in the first lobe, the H_2O visibility is smaller than the CO and CN visibilities. Thus the radius of the star is dependent on the H_2O contribution. (ii) At higher frequencies, only the H_2O visibility can fit the observed data, whereas the CO and CN visibilities reproduce the data poorly.

4.1.2. Size distribution on the stellar surface

We also characterized the typical size distribution on the stellar surface using interferometric observables. The large range of spatial frequencies of the observation (between 12 to 95 arcsec^{-1}) is very well suited to this purpose.

Our aim was to visualize the energy within the signal as a function of spatial frequency. After the computation of the Fourier transform, FT, we obtained $\hat{I}(u,v) = FT[I(x,y)]$, where $I(u,v)$ is the most closely matching intensity map of Fig. 3. The resulting complex number $\hat{I}(u,v)$ was multiplied by low-pass and high-pass filters to extract the information from different spatial frequency ranges (corresponding to the visibility lobes). Finally, an inverse Fourier transform, $\bar{FT}$, was used to obtain the filtered image: $I_{\rm filtered}(x,y) = \bar{FT}\left[\hat{I}(u,v) \cdot \text{filter}\right]$.

Figure 6 (top left panel) shows the filtered image at spatial frequencies, ν, corresponding to the first lobe. Since we filtered the signal at high spatial frequencies, the image appears blurry and seems to contain only information about the stellar radius. However, the top right panel displays the signal related to all the frequencies higher than the first lobe: in this image, we clearly do not detect the central convective cell of ≈30 mas size (60% of the stellar radius) visible in Fig. 3. Thus, the first lobe also carries information about the presence of large convective cells.

Figure 6 (bottom row) shows the second lobe with convection-related structures of ≈10−15 mas, (30% of the stellar radius), and the third and fourth lobes with structures smaller than 10 mas. We conclude that we can detect convection-related structures of different size using visibility measurements at the appropriate spatial frequencies. However, only imaging can definitively characterize the size of granules. A first step in this direction has been carried out in Berger et al. (2010) (to be submitted soon), where the image reconstruction algorithms have been tested using intensity maps from this RHD simulation. In the case of Betelgeuse, we have fitted its interferometric observables between 12 and 95 arcsec^{-1} and thus inferred the presence of small to medium scale granules (5 to 15 mas) and a large convective cell (≈30 mas).

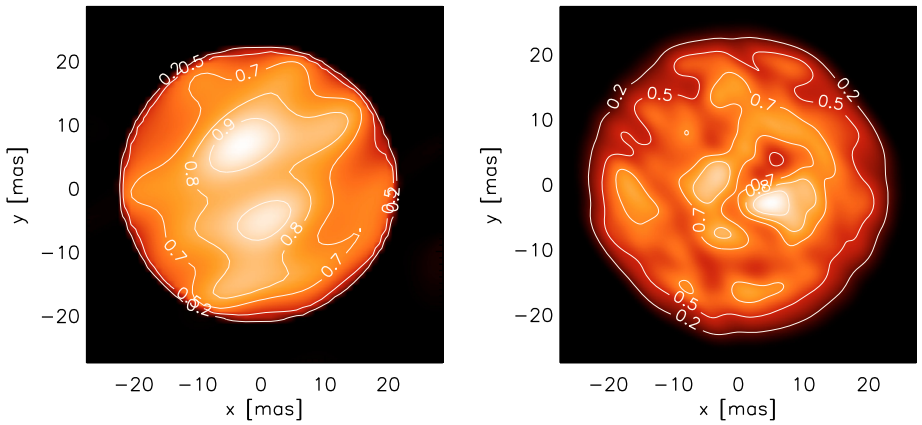

Fig. 4. *Left panel*: recontructed image from Haubois et al. (2009). *Right panel*: our best-fit 3D simulation snapshot of Fig. 3 convolved with a 6 × 6 mas PSF derived by fitting the central peak of the interferometric dirty beam. The intensities in both panels are normalized to the range [0, 1] and some contour lines are indicated (0.2, 0.5, 0.7, 0.8, 0.9 of the peak brightness).

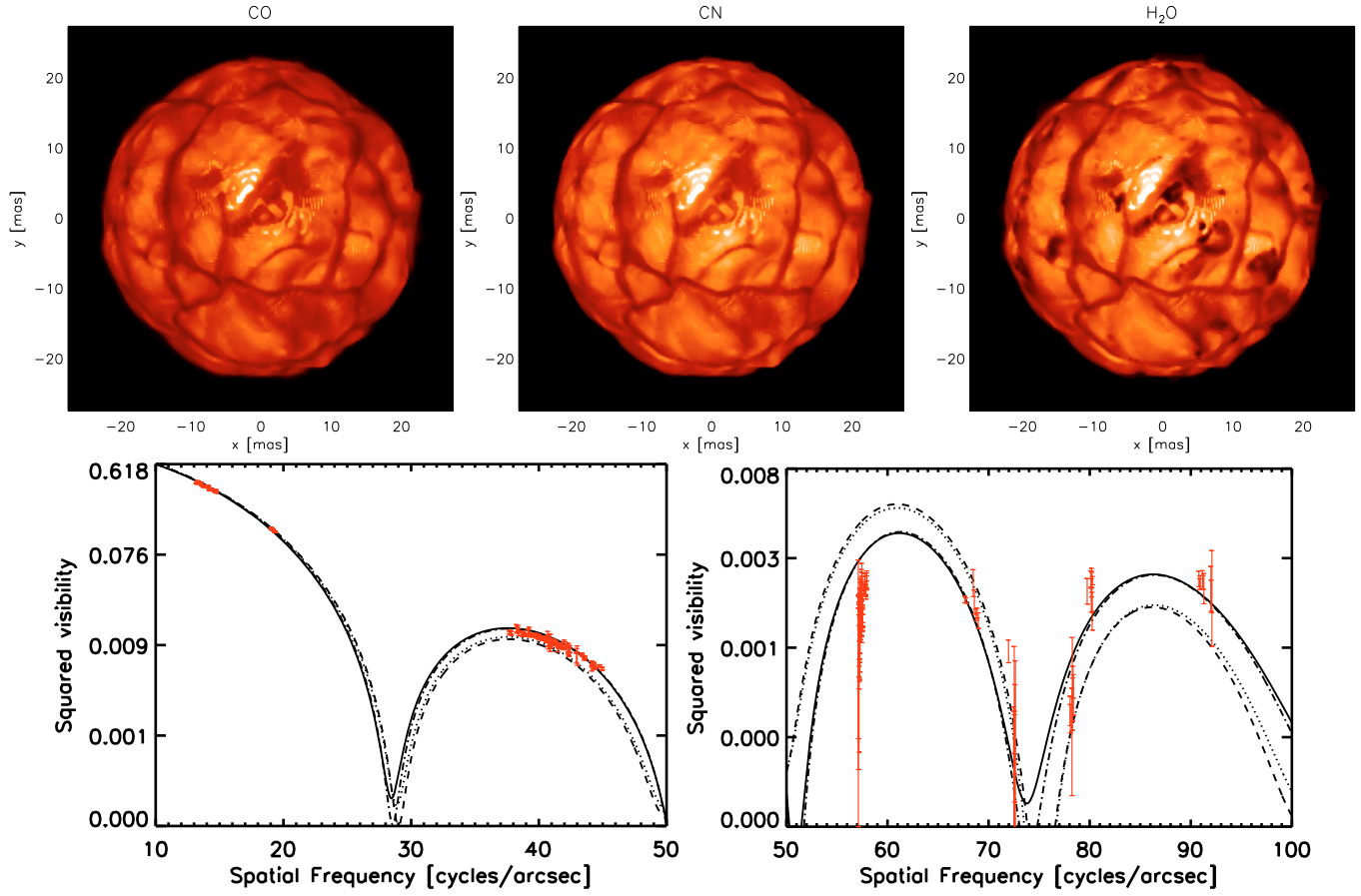

Fig. 5. *Top row*: maps of the linear intensity in the IONIC filter of the molecular species (Fig. 1). The simulation snapshot and intensity range is the same as in Fig. 3. *Bottom row*: the most closely matching visibility curve (solid line) of Fig. 2 is compared to the visibility curve obtained from the intensity maps above: CO (dotted line), CN (dashed line), and H_2O (dash dot line). Red data points are IOTA observations.

4.2. Data from 7000 to 12 900 Å

The simulated surface in the optical to near-infrared region exhibits a spectacular pattern characterized by dark spots and bright areas. The brightest areas can be up to 50 times more intense than the dark ones. In addition, this pattern changes strongly with time and has a lifetime of a few weeks. In the wavelength region below ≈1 μm, the resulting surface pattern, though related to the granulation below, is also connected to dynamical effects. The light comes from higher up in the atmosphere where the optical depth is smaller than one and where waves and shocks begin to dominate. In addition to this, the emerging intensity depends on the variation in opacity through the atmosphere and veiling by TiO molecules is very strong at these wavelengths (Fig. 1).

The filters centered on the optical part of this wavelength range are characterized by strong molecular lines, while the infrared filter probes layers closer to the continuum-forming region. Observations at wavelengths in a molecular band and in the continuum probe different atmospheric depths, and thus layers at different temperatures. They provide important information about the wavelength-dependence of limb-darkening and strong tests of our simulations.

Since the observations were performed at two different epochs, we fitted each individually, i.e., (i) the data taken in 1997

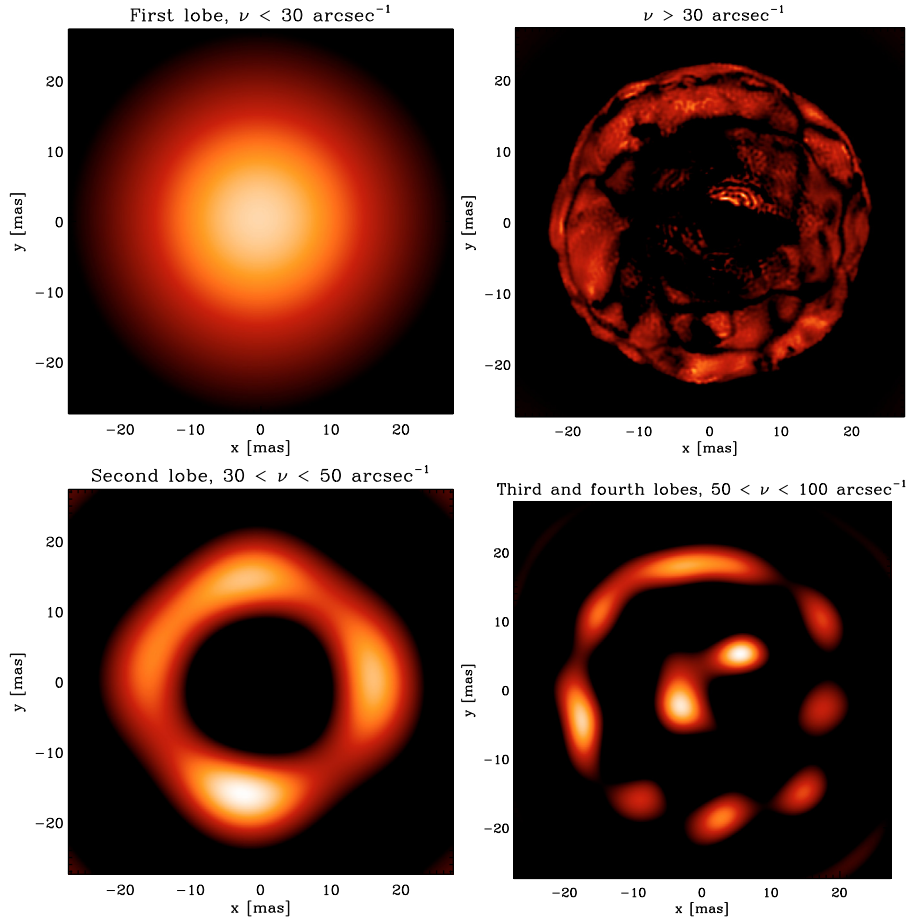

Fig. 6. Intensity maps filtered at different spatial frequencies corresponding to the lobes of the visibility curve shown in Fig. 2. The images are normalized between [0, 1].

(Young et al. 2000), and (ii) the data from 2004 (Young et al. 2004). We proceeded as described in Sect. 4.1. We note that the filter curve for the 7820 Å bandpass was lost and so a top-hat function was assumed instead; we tested the validity of this assumption by replacing the known optical-region filter curves with top-hats, which did not affect the synthetic visibility and closure phase data significantly. Among the large number of computed visibilities and closure phases for each filter, we found that there are two snapshots of the simulated star, one for each epoch, that fit the observations. At each epoch, the same rotation angle of the snapshot was found to fit all of the observed wavebands.

Figure 7 displays the comparison to the data taken in 1997. The 7000 Å synthetic image corresponds to a region with strong TiO absorption (transition $A^3\Phi - X^3\Delta(\gamma)$, see Fig. 1). This is also true for the 9050 Å image (transition $E^3\Pi - X^3\Delta(\epsilon)$) but in this case the TiO band is weaker. The relative intensity of TiO bands depend on the temperature gradient of the model and change smoothly from one snapshot to another. The map at 12 900 Å is TiO free and detects mostly CN lines: in this case, the surface intensity contrast is less strong than in the TiO bands.

Figure 8 shows the comparison with the data taken in 2004. There, the filters used span wavelength regions corresponding to TiO absorption bands of different strengths centered on 7500 Å, 7800 Å, and 9050 Å (transitions $A^3\Phi - X^3\Delta(\gamma)$ and $E^3\Pi - X^3\Delta(\epsilon)$, see Fig. 1). Again, the same snapshot fitted the whole dataset from the same epoch.

The departure from circular symmetry is more evident than in the *H* band, the first and the second lobes already showing large visibility fluctuations. The RHD simulation shows excellent agreement with the data in both the visibility curves and closure phases.

However, within the same observation epoch we had to scale the size of the simulated star to a different apparent diameter at each observed wavelength. For example, in Fig. 8 the apparent diameter varies from 47.3 to 52.6 mas. Thus, we infer that our RHD simulation fails to reproduce the TiO molecular band strengths probed by the three filters. As already pointed out in Paper I, our RHD simulations are constrained by execution time and they use a grey approximation for the radiative transfer that is well justified in the stellar interior and is a crude approximation in the optically thin layers; as a consequence, the thermal gradient is too shallow and weakens the contrast between strong and weak lines (Chiavassa et al. 2006). The intensity maps appear too sharp with respect to the observations. The implementation of non-grey opacities by employing five wavelength bins to describe the wavelength dependence of radiation fields (see Ludwig et al. 1994; Nordlund 1982, for details) should change the mean temperature structure and the temperature fluctuations. The mean thermal gradient in the outer layers, where TiO absorption has a large effect, should increase. In a subsequent step, the inclusion of the radiation pressure in the simulations should then lead to a different density/pressure structure with a less steep decline of density with radius. We expect the intensity maps probing TiO bands with different strengths to eventually

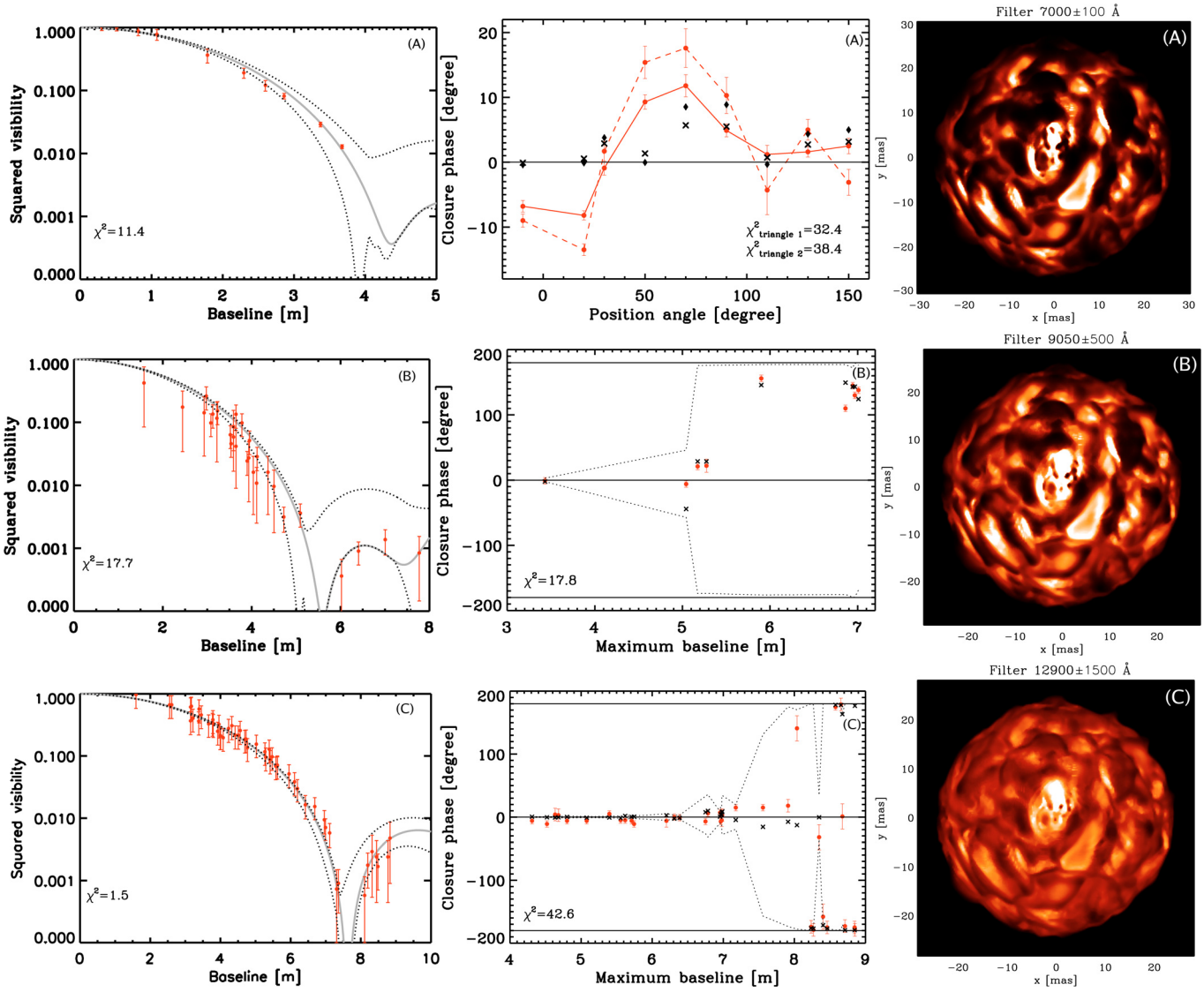

Fig. 7. Comparison to the data taken in 1997 (Young et al. 2000). The symbols in the visibility curves and closure phases plots have the same meaning as in Fig. 2. The intensity are normalized between $[0;\ 3.5 \times 10^5]$ erg cm^{-2} s^{-1} Å^{-1}. The stellar parameters of this snapshot are: L = 93 500 $L_\odot$, R = 843.3 $R_\odot$, $T_{\rm eff}$ = 3475 K and $\log(g) = -0.35$. The row marked with (A), (B) and (C) correspond to bandpass centered on 7000, 9050 and 12 900 Å, respectively. The visibility curves are plotted in left column, while the closure phases are shown in central column. The intensity maps centered on 7000 and 9050 Å have been scaled to an apparent diameter of ∼48.9 mas, at a distance of 161.1 pc fitting the data points in the first lobe; the map at 12 900 Å to an apparent diameter of ∼47.1 mas, at a distance of 167.1 pc. *Row marked with (A)*: the observed visibility amplitudes (90 visibilities) have been averaged over the position angle of the aperture mask for the sake of clarity. We performed the fitting procedure for each of the unaveraged visibilities, and then we plot the averaged value. The closure phases of two (triangle 1 in solid and triangle 2 in dashed red line) of the 10 observed triangles have been plotted as a function of the position angle of the aperture mask on the sky. The best-matching synthetic closure phases are black crosses for triangle 1 and black diamonds for triangle 2.

show larger diameter variations due to the molecular absorption as a result of these refinements.

Young et al. (2000) managed to model the data in the 7000 Å filter with two best-fit parametric models, consisting of a circular disk with superimposed bright features (Fig. 9, central panel) or dark features (left panel). We compared these parametric models to our best-fit synthetic image of Fig. 7 (top row). The convolved image, displayed in Fig. 9 (right panel), shows a closer qualitative agreement with the bright features parametric model. The 3D simulations show that the surface contrast is enhanced by the presence of significant molecular absorbers such as TiO which contribute in layers where waves and shocks start to dominate. The location of bright spots is then a consequence of the underlying activity.

5. Conclusions

We have used radiation hydrodynamical simulations of red supergiant stars to explain interferometric observations of Betelgeuse from the optical to the infrared region.

The picture of the surface of Betelgeuse portrayed by our study is the following: (i) a granulation pattern is undoubtedly present on the surface and the convection-related structures have strong signatures in the visibility curve and closure phases at high spatial frequencies in the H band and on the first and second lobes in the optical region. (ii) In the H band, Betelgeuse is characterized by a granulation pattern composed of convection-related structures of different sizes, including small to medium scale granules (5−15 mas) and a large convective cell

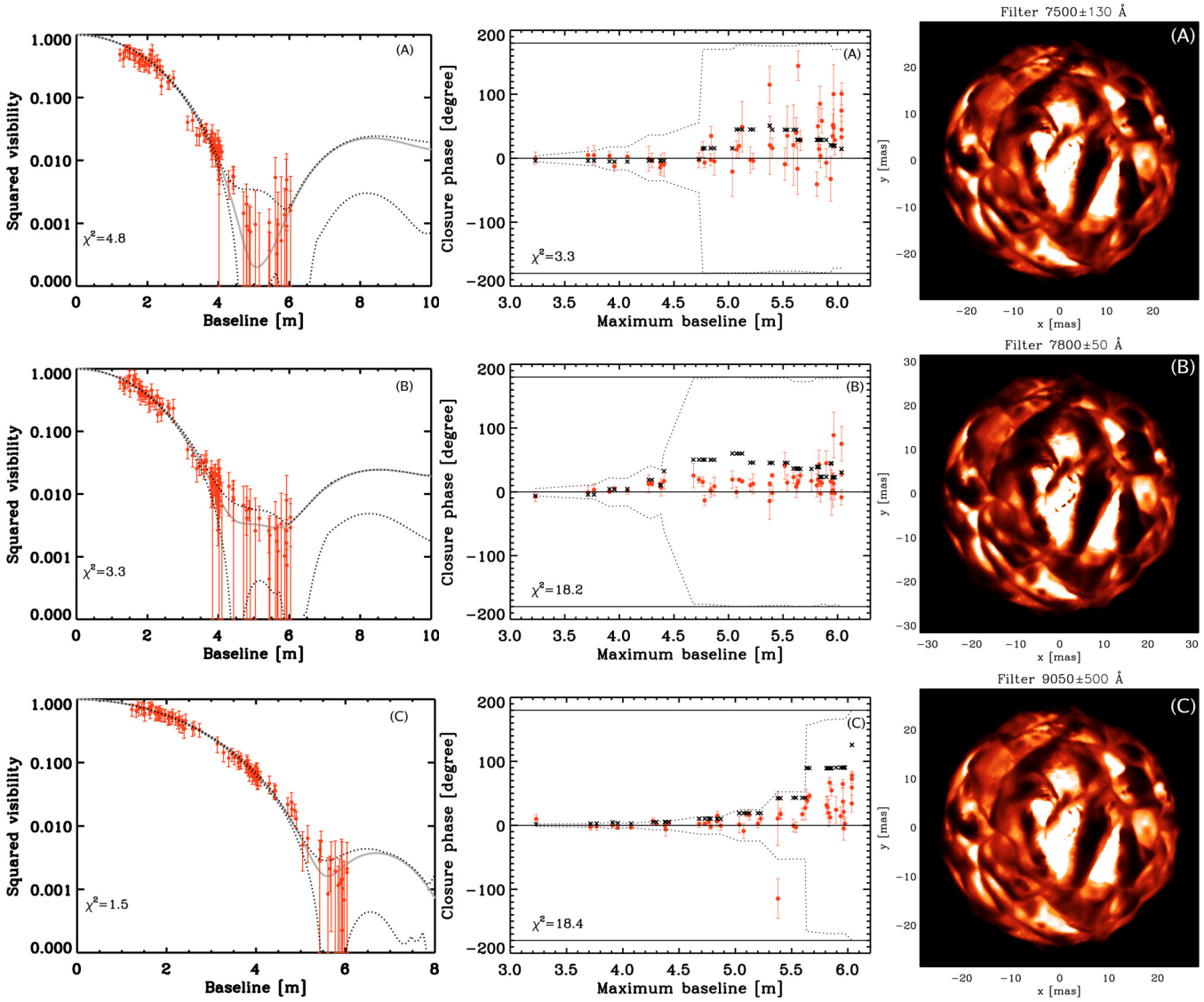

Fig. 8. Same as in Fig. 7 but for the observations of Young et al. (2004). The stellar parameters of this snapshot are: $L = 93\,800\,L_{\odot}$, $R = 840.3\,R_{\odot}$, $T_{\rm eff} = 3484$ K and $\log(g) = -0.35$. The row marked with (A), (B), and (C) correspond to bandpass centered on 7500, 7820 and 9050 Å, respectively. The intensity map centered at 7500 Å has been scaled to an apparent diameter of ∼49.7 mas, at a distance of 157.9 pc; the map at 7820 Å to an apparent diameter of ∼47.3 mas, at a distance of 165.7 pc; and the map 9050 to an apparent diameter of ∼52.6 mas, at a distance of 149.1 pc.

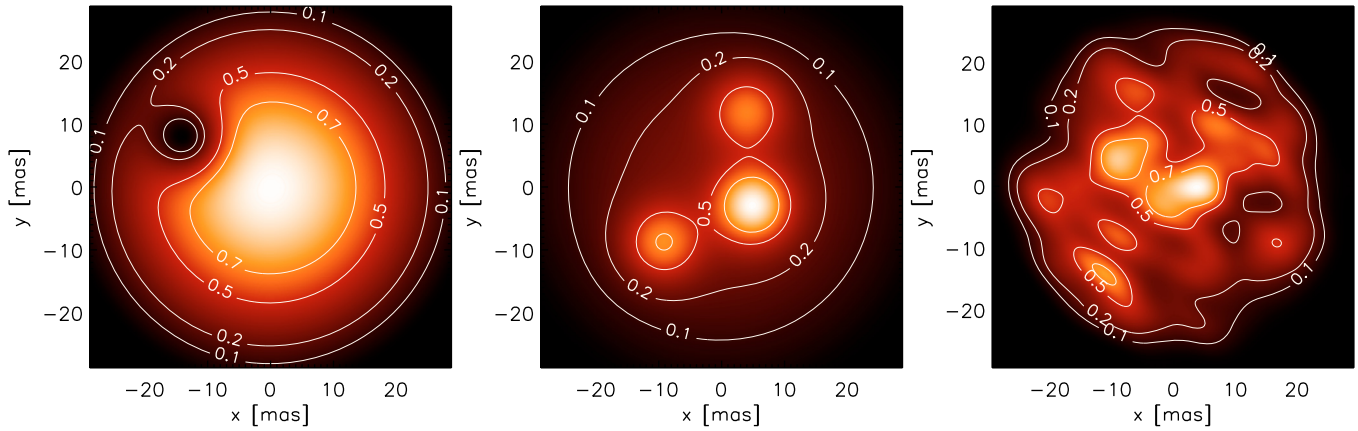

Fig. 9. *Left and central panels*: brightness distributions of the best fitting parametric models from Young et al. (2000) with dark features (*left*) and bright features (center). *Right panel*: our best fitting 3D simulation snapshot of Fig. 7 (row marked with (A)) convolved with a 10×10 mas PSF (i.e., the size of the bright features in the parametric model). The intensities in both panels are normalized to the range $[0, 1]$ and some contour lines are indicated $(0.1, 0.2, 0.5, 0.7)$.

(≈30 mas). This supports previous detections carried out using RHD simulation in the *K* band (Paper I), for parametric models and the same dataset (Haubois et al. 2009); Kervella et al. (2009) with VLT/NACO observations; and Ohnaka et al. (2009) with VLTI/AMBER observations. We have demonstrated that H_2O molecules contribute more than CO and CN to the position of the visibility curve's first null (and thus to the measured stellar radius) and to the small-scale surface structures. (iii) In the optical, Betelgeuse's surface appears more complex with areas up to 50 times brighter than dark areas. This is indicative of the underlying activity characterized by interactions between shock waves and non-radial pulsations in layers where there are strong TiO molecular bands.

These observations provide a wealth of information about both the stars and our RHD models. The comparison with the observations in the TiO bands allowed us to suggest which approximations must be replaced with more realistic treatments in the simulations. New models of higher wavelength resolution (i.e., non-grey opacities) are being developed and will be tested against these observations. From the observational point of view, additional multi-epoch observations, in both the optical and the infrared, are needed to assess the time variability of convection.

Acknowledgements. This project was supported by the French Ministry of Higher Education through an ACI (PhD fellowship of Andrea Chiavassa, post-doctoral fellowship of Bernd Freytag, and computational resources). Present support is ensured by a grant from ANR (ANR-06-BLAN-0105). We are also grateful to the PNPS and CNRS for its financial support through the years. We thank the CINES for providing some of the computational resources necessary for this work.

References

Asplund, M., Grevesse, N., & Sauval, A. J. 2006, Commun. Asteroseismol., 147, 76
Baldwin, J. E., Boysen, R. C., Cox, G. C., et al. 1994, in SPIE Conf. Ser. 2200, ed. J. B. Breckinridge, 118
Baldwin, J. E., Haniff, C. A., Mackay, C. D., & Warner, P. J. 1986, Nature, 320, 595
Berger, J.-P., Haguenauer, P., Kern, P. Y., et al. 2003, in Presented at the Society of Photo-Optical Instrumentation Engineers (SPIE) Conf., Interferometry for Optical Astronomy II, ed. W. A. Traub, Proc. SPIE, 4838, 1099
Burns, D., Baldwin, J. E., Boysen, R. C., et al. 1997, MNRAS, 290, L11
Buscher, D. F., Baldwin, J. E., Warner, P. J., & Haniff, C. A. 1990, MNRAS, 245, 7P
Chiavassa, A., Plez, B., Josselin, E., & Freytag, B. 2006, in SF2A-2006: Semaine de l'Astrophysique Francaise, ed. D. Barret, F. Casoli, G. Lagache, A. Lecavelier, & L. Pagani , 455
Chiavassa, A., Plez, B., Josselin, E., & Freytag, B. 2009, A&A, 506, 1351
Freytag, B. 2003, in Interferometry for Optical Astronomy II, ed. W. A. Traub, Proc. SPIE Conf., 4838, 348
Freytag, B., & Höfner, S. 2008, A&A, 483, 571
Freytag, B., Steffen, M., & Dorch, B. 2002, Astron. Nachr., 323, 213
Gray, D. F. 2008, AJ, 135, 1450
Gustafsson, B., Bell, R. A., Eriksson, K., & Nordlund, A. 1975, A&A, 42, 407
Gustafsson, B., Edvardsson, B., Eriksson, K., et al. 2003, in Stellar Atmosphere Modeling, ed. I. Hubeny, D. Mihalas, & K. Werner, ASP Conf. Ser., 288, 331
Gustafsson, B., Edvardsson, B., Eriksson, K., et al. 2008, A&A, 486, 951
Haniff, C. A., Mackay, C. D., Titterington, D. J., et al. 1987, Nature, 328, 694
Harper, G. M., Brown, A., & Guinan, E. F. 2008, AJ, 135, 1430
Haubois, X., Perrin, G., Lacour, S., et al. 2009, A&A, 508, 923
Josselin, E., & Plez, B. 2007, A&A, 469, 671
Kervella, P., Verhoelst, T., Ridgway, S. T., et al. 2009, A&A, 504, 115
Kiss, L. L., Szabó, G. M., & Bedding, T. R. 2006, MNRAS, 372, 1721
Levesque, E. M., Massey, P., Olsen, K. A. G., et al. 2005, ApJ, 628, 973
Levesque, E. M., Massey, P., Olsen, K. A. G., et al. 2006, ApJ, 645, 1102
Ludwig, H.-G., Jordan, S., & Steffen, M. 1994, A&A, 284, 105
Meimon, S., Mugnier, L. M., & Le Besnerais, G. 2005, J. Opt. Soc. Am. A, 22, 2348
Meimon, S., Mugnier, L. M., & Le Besnerais, G. 2009, J. Opt. Soc. Am. A, 26, 108
Meynet, G., & Maeder, A. 2003, A&A, 404, 975
Monnier, J. D., Traub, W. A., Schloerb, F. P., et al. 2004, ApJ, 602, L57
Nordlund, A. 1982, A&A, 107, 1
Ohnaka, K., Hofmann, K., Benisty, M., et al. 2009, A&A, 503, 183
Pedretti, E., Millan-Gabet, R., Monnier, J. D., et al. 2004, PASP, 116, 377
Perrin, G., Ridgway, S. T., Coudé du Foresto, V., et al. 2004, A&A, 418, 675
Tatebe, K., Chandler, A. A., Wishnow, E. H., Hale, D. D. S., & Townes, C. H. 2007, ApJ, 670, L21
Traub, W. A., Ahearn, A., Carleton, N. P., et al. 2003, in SPIE Conf. Ser. 4838, ed. W. A. Traub, 45
Tuthill, P. G., Haniff, C. A., & Baldwin, J. E. 1997, MNRAS, 285, 529
Uitenbroek, H., Dupree, A. K., & Gilliland, R. L. 1998, AJ, 116, 2501
Wilson, R. W., Baldwin, J. E., Buscher, D. F., & Warner, P. J. 1992, MNRAS, 257, 369
Wilson, R. W., Dhillon, V. S., & Haniff, C. A. 1997, MNRAS, 291, 819
Young, J. S., Badsen, A. G., Bharmal, N. A., et al. 2004
Young, J. S., Baldwin, J. E., Beckett, M. G., et al. 1998, in SPIE Conf. Ser. 3350, ed. R. D. Reasenberg, 746
Young, J. S., Baldwin, J. E., Boysen, R. C., et al. 2000, MNRAS, 315, 635
Zhao, M., Monnier, J. D., Torres, G., et al. 2007, ApJ, 659, 626

A&A 617, L1 (2018)
https://doi.org/10.1051/0004-6361/201833844

Astronomy & Astrophysics

LETTER TO THE EDITOR

Heading *Gaia* to measure atmospheric dynamics in AGB stars

A. Chiavassa[1], B. Freytag[2], and M. Schultheis[1]

[1] Université Côte d'Azur, Observatoire de la Côte d'Azur, CNRS, Lagrange, CS 34229 Nice, France
e-mail: andrea.chiavassa@oca.eu
[2] Department of Physics and Astronomy at Uppsala University, Regementsvägen 1, Box 516, 75120 Uppsala, Sweden

Received 13 July 2018 / Accepted 7 August 2018

ABSTRACT

Context. Asymptotic giant branch (AGB) stars are characterised by complex stellar surface dynamics that affect the measurements and amplify the uncertainties on stellar parameters. The uncertainties in observed absolute magnitudes have been found to originate mainly from uncertainties in the parallaxes. The resulting motion of the stellar photocentre could have adverse effects on the parallax determination with *Gaia*.
Aims. We explore the impact of the convection-related surface structure in AGBs on the photocentric variability. We quantify these effects to characterise the observed parallax errors and estimate fundamental stellar parameters and dynamical properties.
Methods. We use three-dimensional (3D) radiative hydrodynamics simulations of convection with CO5BOLD and the post-processing radiative transfer code OPTIM3D to compute intensity maps in the *Gaia G* band [325–1030 nm]. From those maps, we calculate the intensity-weighted mean of all emitting points tiling the visible stellar surface (i.e. the photocentre) and evaluate its motion as a function of time. We extract the parallax error from *Gaia* data-release 2 (DR2) for a sample of semi-regular variables in the solar neighbourhood and compare it to the synthetic predictions of photocentre displacements.
Results. AGB stars show a complex surface morphology characterised by the presence of few large-scale long-lived convective cells accompanied by short-lived and small-scale structures. As a consequence, the position of the photocentre displays temporal excursions between 0.077 and 0.198 AU (≈5 to ≈11% of the corresponding stellar radius), depending on the simulation considered. We show that the convection-related variability accounts for a substantial part of the *Gaia* DR2 parallax error of our sample of semi-regular variables. Finally, we present evidence for a correlation between the mean photocentre displacement and the stellar fundamental parameters: surface gravity and pulsation. We suggest that parallax variations could be exploited quantitatively using appropriate radiation-hydrodynamics (RHD) simulations corresponding to the observed star.

Key words. stars: atmospheres – stars: AGB and post-AGB – astrometry – parallaxes – hydrodynamics

1. Introduction

Low- to intermediate-mass stars evolve to red giant and asymptotic giant branch increasing the mass-loss during this evolution. They are characterised: (i) by large-amplitude variations in radius, brightness, and temperature of the star; and (ii) by a strong mass-loss rate driven by an interplay between pulsation, dust formation in the extended atmosphere, and radiation pressure on the dust (Höfner & Olofsson 2018). Their complex dynamics affect the measurements and amplify the uncertainties on stellar parameters.

Gaia (Gaia Collaboration 2016) is an astrometric, photometric, and spectroscopic space-borne mission. It performs a survey of a large part of the Milky Way. The second data release (*Gaia* DR2) in April 2018 (Gaia Collaboration 2018) brought high-precision astrometric parameters (i.e. positions, parallaxes, and proper motions) for over 1 billion sources brighter that $G \approx 20$. Among all the objects that have been observed, the complicated atmospheric dynamics of asymptotic giant branch (AGB) stars affect the photocentric position and, in turn, their parallaxes (Chiavassa et al. 2011). The convection-related variability, in the context of *Gaia* astrometric measurements, can be considered as "noise" that must be quantified in order to better characterise any resulting error on the parallax determination. However, important information about stellar properties, such as the fundamental stellar parameters, may be hidden behind the *Gaia* measurement uncertainty.

In this work we explore the effect of convection-related surface structures on the photocentre to estimate its impact on the *Gaia* astrometric measurements.

2. Methods

We used the radiation-hydrodynamics (RHD) simulations of AGB stars (Freytag et al. 2017) computed with CO^{5}BOLD (Freytag et al. 2012) code. The code solves the coupled non-linear equations of compressible hydrodynamics and non-local radiative energy transfer in the presence of a fixed external spherically symmetric gravitational field in a three-dimensional (3D) cartesian grid. It is assumed that solar abundances are appropriate for M-type AGB stars. The basic stellar parameters of the RHD simulations are reported in Table 1. The configuration used is the "star-in-a-box", where the evolution of the outer convective envelope and the inner atmosphere of AGB stars are taken into account in the calculation. In the simulations, convection, waves, and shocks all contribute to the dynamical pressure and, therefore, to an increase of the stellar radius and to a levitation of material into layers where dust can form. No dust is included in any of the current models. The regularity of the pulsations

Table 1. RHD simulation parameters.

Simulation	$M_\star$ $M_\odot$	$L_\star$ $L_\odot$	$R_\star$ AU	$T_{\rm eff}$ K	$\log g$ (cgs)	$t_{\rm avg}$ yr	$P_{\rm puls}$ yr	$\sigma_{\rm puls}$ yr	$\langle P\rangle$ AU	σ_P AU	$\langle P_x\rangle$ AU	$\langle P_y\rangle$ AU
st26gm07n002	1.0	6986	2.04	2524	–0.85	25.35	1.625	0.307	0.262	0.187	–0.100	0.046
st26gm07n001	1.0	6953	1.87	2635	–0.77	27.74	1.416	0.256	0.275	0.198	–0.098	0.024
st28gm06n26	1.0	6955	1.73	2737	–0.70	25.35	1.290	0.317	0.241	0.152	–0.068	–0.002
st29gm06n001	1.0	6948	1.62	2822	–0.65	25.35	1.150	0.314	0.266	0.174	–0.098	0.016
st27gm06n001	1.0	4982	1.61	2610	–0.64	28.53	1.230	0.088	0.150	0.101	–0.027	0.027
st28gm05n002	1.0	4978	1.46	2742	–0.56	25.35	1.077	0.104	0.133	0.077	–0.002	0.033
st28gm05n001	1.0	4990	1.40	2798	–0.52	25.36	1.026	0.135	0.183	0.131	–0.057	0.0174
st29gm04n001	1.0	4982	1.37	2827	–0.50	25.35	0.927	0.100	0.152	0.078	–0.002	0.023

Notes. The table shows the simulation name, the mass $M_\star$, the average emitted luminosity $L_\star$, the average approximate stellar radius $R_\star$ (we note that the radii vary by about 20% during one pulsation period), effective temperature $T_{\rm eff}$, surface gravity $\log g$, the pulsation period $P_{\rm puls}$, the half of the distribution of the pulsation frequencies $\sigma_{\rm puls}$, and the stellar time $t_{\rm avg}$ used for the averaging of the rest of the quantities. All these quantities are from Freytag et al. (2017). The last four columns are the time-averaged value of the photocentre displacement $\langle P\rangle = \langle (P_x^2 + P_y^2)^{(1/2)}\rangle$, its standard deviation (σ_P), and the time-average of P_x and P_y.

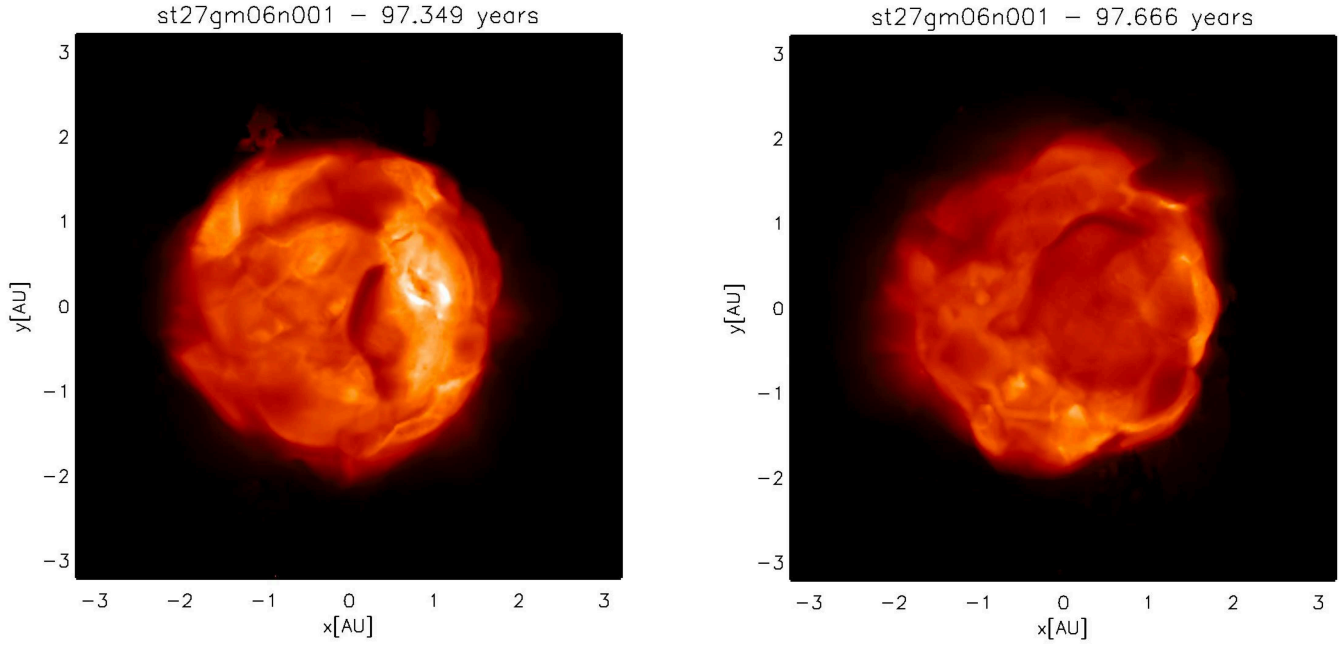

Fig. 1. Example of the squared root intensity maps (the range is $\sqrt{[0.-3000.]}$ erg s^{-1} cm^{-2} Å^{-1}) in the *Gaia G* photometric system (Evans et al. 2018) for two different snapshots of one simulation listed in Table 1. The number on the top indicates the stellar times at which the two snapshots were computed.

decreases with decreasing gravity as the relative size of convection cells increases. The pulsation period is extracted with a fit of the Gaussian distribution in the power spectra of the simulations. The period of the dominant mode increase with the radius of the simulation (Table 1 in Freytag et al. 2017).

We computed intensity maps based on snapshots from the RHD simulations integrating in the *Gaia G* photometric system (Evans et al. 2018). For this purpose, we employed the code Optim3D (Chiavassa et al. 2009), which takes into account the Doppler shifts caused by the convective motions. The radiative transfer is computed in detail using pre-tabulated extinction coefficients per unit mass, as for MARCS (Gustafsson et al. 2008) as a function of temperature, density, and wavelength for the solar composition (Asplund et al. 2009). Micro-turbulence broadening was switched off. The temperature and density distributions are optimised to cover the values encountered in the outer layers of the RHD simulations.

The surface of the deep convection zone has large and small convective cells. The visible fluffy stellar surface is made of shock waves that are produced in the interior and are shaped by the top of the convection zone as they travel outward (Freytag et al. 2017). In addition to this, on the top of the convection-related surface structures, other structures appear. They result from the opacity effect and dynamics at Rosseland optical depths smaller than 1 (i.e. further up in the atmosphere with respect to the continuum-forming region). At the wavelengths in *Gaia G*-band, TiO molecules produce strong absorption. Both of these effects affect the position of the photocentre and cause temporal fluctuations during the *Gaia* mission, as already pointed out for red supergiant stars in Chiavassa et al. (2011). In the *Gaia G* photometric system (Fig. 1), the situation is analogous with a few large convective cells with sizes of a third of the stellar radii (i.e. ≈0.6 AU) that evolve on a scale of several months to a few years, as well as a few short-lived (weeks

to month) convective cells at smaller scales ($\lesssim$10% of the stellar radius)

We calculated the position of the photocentre for each map (i.e. as a function of time) as the intensity-weighted mean of the $x-y$ positions of all emitting points tiling the visible stellar surface according to

$$P_x = \frac{\sum_{i=1}^{N}\sum_{j=1}^{N} I(i,j) * x(i,j)}{\sum_{i=1}^{N}\sum_{j=1}^{N} I(i,j)} \quad (1)$$

$$P_y = \frac{\sum_{i=1}^{N}\sum_{j=1}^{N} I(i,j) * y(i,j)}{\sum_{i=1}^{N}\sum_{j=1}^{N} I(i,j)}, \quad (2)$$

where $I(i,j)$ is the emerging intensity for the grid point (i,j) with coordinates $x(i,j)$, $y(i,j)$ of the simulation, and $N = 281$ is the total number of grid points in the simulated box. In the presence of surface brightness asymmetries, the photocentre position will not coincide with the barycentre of the star and its position will change as the surface pattern changes with time. This is displayed in the photocentre excursion plots (Figs. A.1–A.5) for each simulation in the Appendix together with the time-averaged photocentre position ($\langle P \rangle$) and its standard deviations (σ_P) in Table 1. The value of σ_P (the third column from the right in Table 1) is mostly fixed by the short time scales corresponding to the small atmospheric structures. However, the fact that $\langle P_x \rangle$ and $\langle P_y \rangle$ do not average to zero (last two columns of Table 1 and, e.g. Fig. A.6 in the Appendix), means that the photocentre tends not to be centred most of the time on the nominal centre of the star, because of the presence of a large convective cell.

Depending on the simulation, σ_P varies between 0.077 and 0.198 AU (≈5 to ≈11% of the corresponding stellar radius). This measure of the mean photocentre noise induced by the stellar dynamics in the simulations is compared in the following section to *Gaia* measurement uncertainty to extract information on stellar parameters from the astrometric measurements. It should be noted that the main information that is used to determine the astrometric characteristics of every star will be the along-scan measurement of *Gaia*. Chiavassa et al. (2011) showed that the projection of the star position along the scanning direction of the satellite with respect to a known reference point discloses similar, though slightly increased, values of σ_P. At the current state of the DR2, it is not possible to perform this on the data and we assumed the conservative value of σ_P directly extracted from the RHD simulations for the following comparisons.

3. Observations

Evolved late-type stars show convection-related variability that may be considered, in the context of *Gaia* astrometric measurement, as "noise". Chiavassa et al. (2011) demonstrated that RHD simulations can account for a substantial part of the supplementary "cosmic noise" that affects Hipparcos measurements for some prototypical red supergiant stars. As a consequence, the convection-related noise has to be quantified in order to better characterise any resulting error on the parallax.

We extracted the parallax error (σ_ϖ) from *Gaia* DR2 for a sample of semiregular variables (SRV) from Tabur et al. (2009), Glass & van Leeuwen (2007), and Jura et al. (1993) that match the theoretical luminosities of RHD simulations (Table 1). Moreover, we only considered stars with $4000 < L_\odot < 8000$ in order to compare with our simulations. It has to be noted that σ_ϖ may still vary in the following data releases because: (i) the mean number of measurements for each source amounts to 26 (Mowlavi et al. 2018) and this number will be 70–80 in total at the end of the nominal mission; (ii) and new solutions may be applied to adjust the imperfect chromaticity correction (Arenou et al. 2018). We cross-identified our sample stars with the *Gaia* DR2 as well as with the distance catalogue of Bailer-Jones et al. (2018) that uses a weak distance prior, varying as a function of Galactic longitude and latitude, to derive distances for the *Gaia* DR2[1]. The apparent K-band magnitudes were transformed to absolute K magnitudes using the *Gaia* distances of Bailer-Jones et al. (2018) and neglecting the interstellar absorption which should be very small in the local neighbourhood. The absolute K magnitudes were converted to bolometric magnitudes using the bolometric correction formula of Kerschbaum et al. (2010). The typical uncertainties in the bolometric correction (BC_K) are of the order of ±0.1 mag. Finally, the bolometric magnitudes were converted to luminosities assuming a solar $M_{bol_\odot} = 4.7$ (Torres 2010). The error bars on luminosities were calculated using the upper and lower distance limits provided by Bailer-Jones et al. (2018) for each of our sources together with the error of ±0.1 mag for BC_K. We do not correct for the variation of the K-band light curve as only amplitudes in the visual are available and the K-band amplitude of AGB stars is in general much smaller than in the visual.

4. Comparison and predictions

AGB stars are characterised by complex stellar surface dynamics that affect the measurements and the determined stellar parameters. The uncertainties in observed absolute magnitudes have been shown to originate mainly from uncertainties in the parallaxes. In this section we investigate if the parallax errors of our SRV sample can be explained by the resulting motion of the stellar photocentre seen in the RHD simulations.

Figure 2 (left panel) displays the parallax errors against the luminosity and compares these results to the standard deviations of the photocentre displacement in the simulations. The latter show good agreement with the observations. There are two luminosity families in the 3D simulations. In general the more luminous models are larger, that is, they have lower surface gravity, which causes larger convection cells and a more "fluffy" atmosphere (Freytag et al. 2017). As a consequence, for the simulation with higher luminosity (≈7000 $L_\odot$), the parallax error ratio, defined as $\langle \sigma_\varpi \rangle / \sigma_P$ (where $\langle \sigma_\varpi \rangle$ is the average error for the stars with luminosity close enough to the corresponding simulation luminosity), is [0.75–0.98]. This attests that convection-related variability accounts for a substantial part of the parallax error in *Gaia* measurements. For lower luminosities (≈5000 $L_\odot$), the ratio is [1.15–1.95], indicating that for those simulations the situation is less clear. However, the observed and simulated luminosities do not coincide exactly and the observed error bars are still very large. One limitation of the existing model grid is the restriction to 1 $M_\odot$. In the future, there will be models with other masses available. For a better comparison, we need simulations and observations with known luminosities, masses, and radii; neither is trivial.

An important piece of information is indeed hidden in the *Gaia* measurement uncertainty: using the corresponding stellar parameters of the RHD simulations of Table 1, we plotted (Fig. 2) σ_P as a function of surface gravity (central panel) and pulsation (right panel). They display a correlation between the mean photocentre displacement and the stellar fundamental parameters. While effective temperature does not show particularly correlated points, simulations with lower surface gravity (i.e. more extended atmospheres) return larger

[1] We used the TAP service at http://gaia.ari.uni-heidelberg.de/tap.html

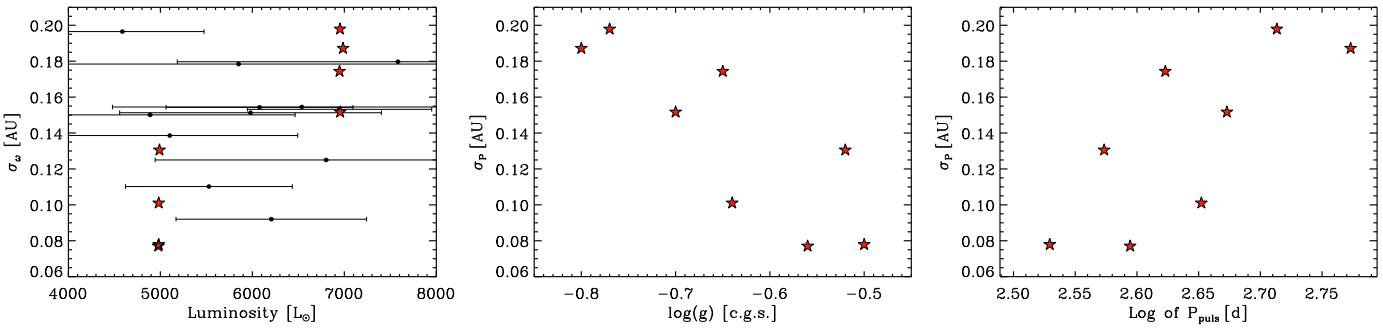

Fig. 2. *Left panel*: luminosity against the parallax error of the observations (σ_ϖ, circle symbol in black) and the standard deviation of the photocentre displacement for the RHD simulations of Table 1 (σ_P, star symbol in red). *Central panel*: σ_P against the surface gravity for the RHD simulations. *Right panel*: σ_P against the logarithm of the period.

excursions of the photocentre. This behaviour is explained by the correlation between the stellar atmospheric pressure scale height ($H_p \approx \frac{T_{eff}}{g}$) and the photocentre displacement (Freytag 2001; Ludwig 2006; Chiavassa et al. 2011).

One property of AGB stars that is well constrained by observations is the period–luminosity (P–L) relation. The uncertainties in the determination of this relation are mainly based on the calculation of the distances and on the different P–L relations used. Figure 2 (right panel) reveals the correlation between the photocentre displacement and the logarithm of the pulsation: larger values of σ_P correspond to longer pulsation periods. Global shocks induced by large-amplitude, radial, and fundamental-mode pulsations have an impact on the detailed stellar structure of the stellar atmosphere, together with small-scale shocks. Both contribute to the levitation of material and the detected photocentre displacement (Freytag et al. 2017). This result is likely associated with the P–L relation found by Freytag et al. (2017), who showed that the RHD simulations reproduce the correct period for a given luminosity compared to the observations of Whitelock et al. (2009). Given the fact that σ_P explains *Gaia* measurement uncertainties on the parallaxes (left panel), we suggest that parallax variations from *Gaia* measurements could be exploited quantitatively using appropriate RHD simulations. However, the parameter space in our simulations is still limited (Table 1). In the future we aim to extend our RHD simulations' parameters to lower and higher luminosities (i.e. shorter and longer periods) which will enable a more quantitative comparison with respect to the upcoming *Gaia* data releases.

5. Summary and conclusions

We used the snapshots from RHD simulations of AGB stars to compute intensity maps in the *Gaia G* photometric system. The visible fluffy stellar surface is made of shock waves that are produced in the interior and are shaped by the top of the convection zone as they travel outward. The surface is characterised by the presence of few large and long-lived convective cells accompanied by short-lived and small-scale structures. As a consequence, the position of the photocentre is affected by temporal fluctuations.

We calculated the standard deviation of the photocentre excursion for each simulation and found that σ_P varies between 0.077 and 0.198 AU (≈5 to ≈11% of the corresponding stellar radius) depending on the simulation. We compared the measurement of the mean photocentre noise induced by the stellar dynamics in the simulations (σ_P) to the measurement uncertainty on the parallax of a sample of AGB stars in the solar neighbourhood cross-matched with data from the *Gaia* DR2. We found good agreement with observations, suggesting that convection-related variability accounts for a substantial part of the parallax error. It should be noted that σ_ϖ may still vary in the following data releases due to the increase of *Gaia*'s measurements in number and further corrections to the parallax solution.

Here we present evidence for a correlation between the mean photocentre displacement and the stellar fundamental parameters: surface gravity and pulsation. Concerning the latter, we showed that larger values of σ_P correspond to longer pulsation periods. This result, associated with the P–L relation found by Freytag et al. (2017), and the good agreement between simulations and observations (σ_P vs. σ_ϖ), suggest that parallax variations from *Gaia* measurements could be exploited quantitatively using appropriate RHD simulations corresponding to the observed star.

Acknowledgements. This work has made use of data from the European Space Agency (ESA) mission *Gaia* (https://www.cosmos.esa.int/gaia), processed by the *Gaia* Data Processing and Analysis Consortium (DPAC, https://www.cosmos.esa.int/web/). Funding for the DPAC has been provided by national institutions, in particular the institutions participating in the *Gaia* Multilateral Agreement. AC et MS thank Patrick de Laverny for the enlightening discussions. The authors thank the referee for the helpful comments during the refereeing process.

References

Arenou, F., Luri, X., Babusiaux, C., et al. 2018, A&A, 616, A17
Asplund, M., Grevesse, N., Sauval, A. J., & Scott, P. 2009, ARA&A, 47, 481
Bailer-Jones, C. A. L., Rybizki, J., Fouesneau, M., Mantelet, G., & Andrae, R. 2018, AJ, 158, 58
Chiavassa, A., Plez, B., Josselin, E., & Freytag, B. 2009, A&A, 506, 1351
Chiavassa, A., Pasquato, E., Jorissen, A., et al. 2011, A&A, 528, A120
Evans, D. W., Riello, M., De Angeli, F., et al. 2018, A&A, 616, A4
Freytag, B. 2001, in 11th Cambridge Workshop on Cool Stars, Stellar Systems and the Sun, eds. R. J. Garcia Lopez, R. Rebolo, & M. R. Zapaterio Osorio, ASP Conf. Ser., 223, 785
Freytag, B., Steffen, M., Ludwig, H.-G., et al. 2012, J. Comput. Phys., 231, 919
Freytag, B., Liljegren, S., & Höfner, S. 2017, A&A, 600, A137
Gaia Collaboration (Prusti, T., et al.) 2016, A&A, 595, A1
Gaia Collaboration (Brown, A. G. A., et al.) 2018, A&A, 616, A1
Glass, I. S., & van Leeuwen, F. 2007, MNRAS, 378, 1543
Gustafsson, B., Edvardsson, B., Eriksson, K., et al. 2008, A&A, 486, 951
Höfner, S., & Olofsson, H. 2018, A&ARv, 26, 1
Jura, M., Yamamoto, A., & Kleinmann, S. G. 1993, ApJ, 413, 298
Kerschbaum, F., Lebzelter, T., & Mekul, L. 2010, A&A, 524, A87
Ludwig, H.-G. 2006, A&A, 445, 661
Mowlavi, N., Lecoeur-Taïbi, I., Lebzelter, T., et al. 2018, A&A, in press, DOI 10.1051/0004-6361/201833366
Tabur, V., Bedding, T. R., Kiss, L. L., et al. 2009, MNRAS, 400, 1945
Torres, G. 2010, AJ, 140, 1158
Whitelock, P. A., Menzies, J. W., Feast, M. W., et al. 2009, MNRAS, 394, 795

Appendix A: Photocentre position for the different RHD simulations

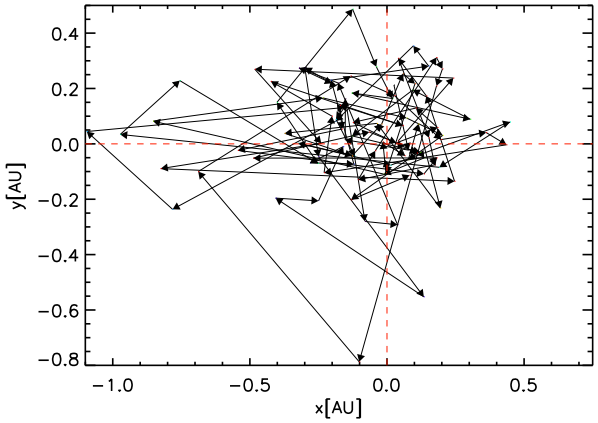

Fig. A.1. Photocentre position computed from RHD simulation st26gm07n001 in Table 1 in the *Gaia G* band filter. The different snapshots are connected by the line segments; the total time covered is reported in the Table. The dashed lines intersect at the position of the geometrical centre of the images.

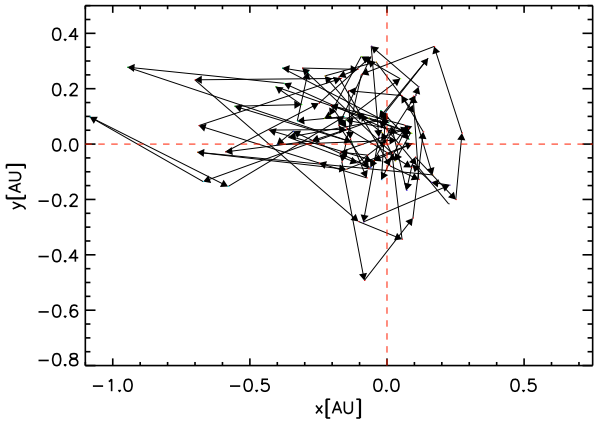

Fig. A.2. As in Fig. A.1 but for RHD simulation st26gm07n002 in Table 1.

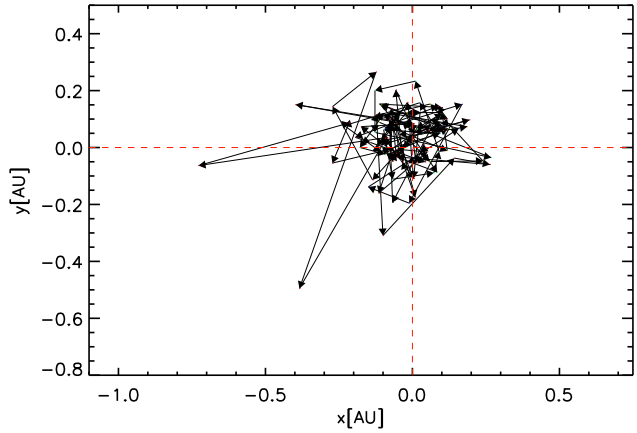

Fig. A.3. As in Fig. A.1 but for RHD simulation st27gm06n001 in Table 1.

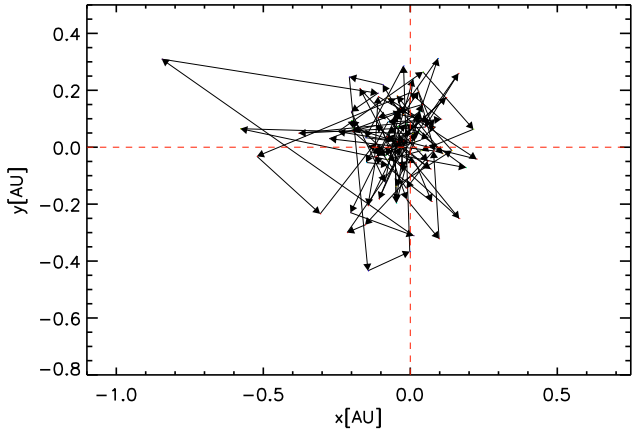

Fig. A.4. As in Fig. A.1 but for RHD simulation st28gm05n001 in Table 1.

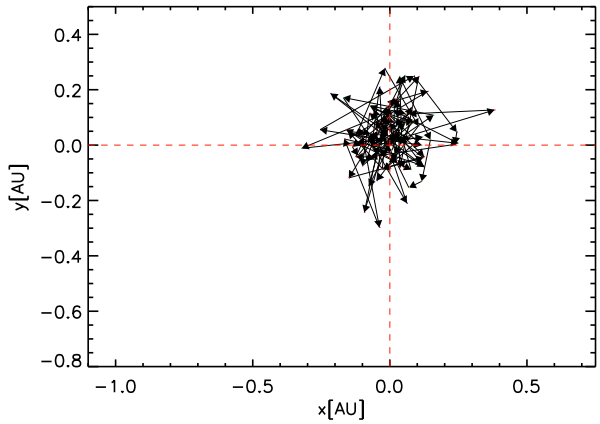

Fig. A.5. As in Fig. A.1 but for RHD simulation st28gm05n002 in Table 1.

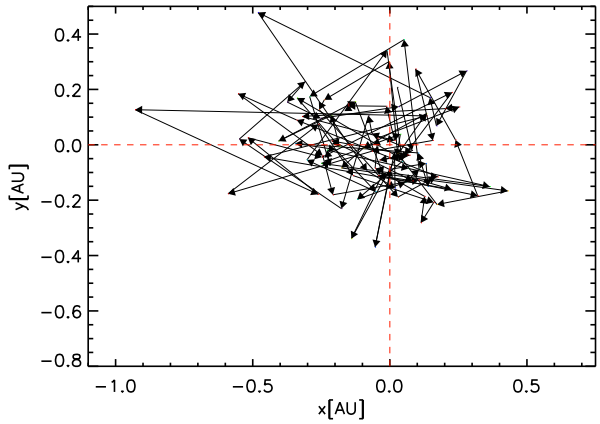

Fig. A.6. As in Fig. A.1 but for RHD simulation st28gm06n26 in Table 1.

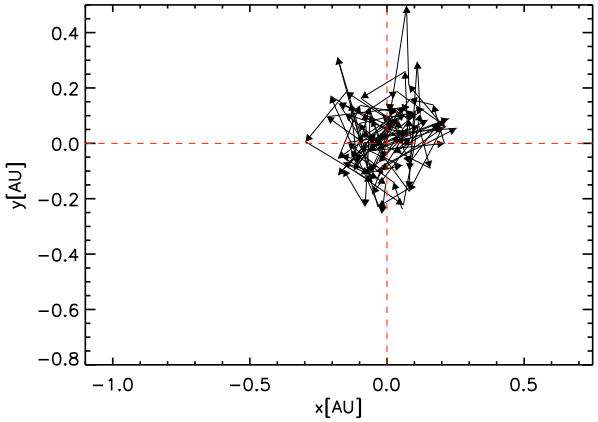

Fig. A.7. As in Fig. A.1 but for RHD simulation st29gm04n001 in Table 1.

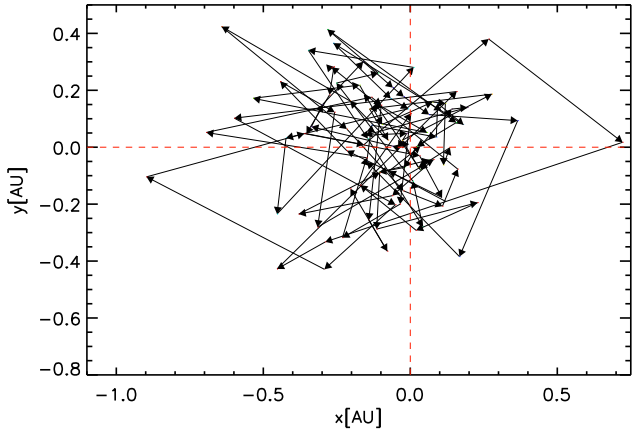

Fig. A.8. As in Fig. A.1 but for RHD simulation st29gm06n001 in Table 1.

3

Perspectives

Fig. 3.1 displays my principal works for different astrophysical problems I described in previous chapters. On purpose, I indicated only the paper where I largely contributed. In the following sections, I will present where I will drive my research in the coming years.

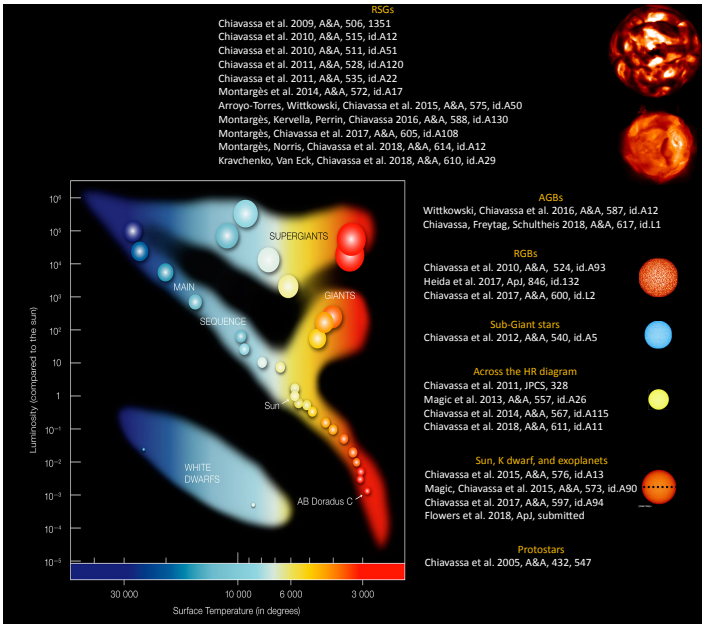

Figure 3.1: Resume of my principal publications across the H-R diagram, in which I contributed substantially.

3.1 HoRSES: High Resolution Spectroscopy for Exoplanets atmospheres and their Stars

The search for signs of life elsewhere in the Universe requires the remote detection of molecules in the atmospheres of exoplanets. Progress with high-resolution spectroscopy with ground-based instruments has led to detections of atomic and molecular species in the atmospheres of hot giant exoplanets (e.g., Wyttenbach et al. 2015; Brogi et al. 2018). From the Doppler shift of the planet spectral lines, it has been possible to constrain atmospheric winds (Brogi et al. 2016; Flowers et al. 2018), planet rotation (Snellen et al. 2014), and the orbital inclination of non-transiting planets (Brogi et al. 2012). Current detections have also the potential to constrain the universal mechanism for planet formation (Piso et al. 2016).

The advent of new high-resolution spectrographs at large and medium-size facilities (CRIRES+, GIARPS, SPIRou, IGRINS, etc...) with unprecedented throughput and spectral range will extend the sample of exoplanets that can be targeted with this technique towards cooler and smaller planets. Given the high degree of complementarity between high-resolution spectroscopy (i.e, ground base instruments) and with low-resolution spectroscopy (space-borne instruments) (Brogi et al. 2017), the synergy between the two techniques will be crucial for the next stage of comparative exo-planetology, especially on the targets found by the TESS mission. When finally implemented at the European Extremely Large Telescope, high-resolution spectroscopy will have the potential to identify biomarkers in the atmospheres of Earth analogues (Rodler & López-Morales 2014).
However, the planet-hosting stars are covered with a complex and stochastic pattern associated with convective heat transport (i.e., granulation). The convection-related structures have different sizes, depth and temporal variations compared to the stellar type concerned (Fig. 2.4). The resulting stellar activity, associated to other phenomena such as magnetic field and/or rotation, bias the characterization and detection of exoplanetary signals (Chiavassa et al. 2017a). It is of paramount importance to quantify and eliminate convective stellar noise in high spectral resolution observations of exoplanet atmospheres in order to have a solid and unequivocal detection of their chemical composition, planet rotation velocity and winds as well as their thermal structure. This can be applied now in giant planets, but, in the TESS era, it will be used for objects of comparable size to the Earth.

In this context, I started in 2017 a collaboration with M. Brogi (University of Warwick, UK), one of the worldwide know expert in high spectral resolution for ex-

oplanetary atmospheres. Together, we organized in October 2018 the first conference on this topic[1]. The event was a real (somehow unexpected) success where we managed to gather worldwide experts in the topic of exoplanet atmospheres and stellar physics meet together around the high spectral resolution spectroscopy. A follow up meeting is expected to take place in 2 years from now.
Our collaborations is concretising very recently with a first publication (Flowers et al. 2018, submitted to ApJ) where, for the first time, we used 3D RHD simulation to match CO lines of the well known hot Jupiter HD 189733b observed in transmission spectroscopy with CRIRES. A second paper (Brogi & Chiavassa) is preparation for a second non-transiting exoplanet). In planetology community, using a full consistent model for the stellar component (i.e., including granulation effect on spectral line shape, depth, and velocity) is a major improvement from previous studies, which instead relied on parameterizing an average stellar line profile through micro- and macro-turbulence(Brogi et al. 2012), and was inadequate to reproduce the complicated velocity fields in the convective envelope of the star (Fig. 3.2).

The doorway is now open and several studies are already on going or about to start. They concern the deeper analysis of several detections of atomic lines in hot Jupiters (Sodium, Potassium, Helium) as well as Molecules and their relative abundances (CO, H_2O, CH_4,...).
The ability to obtain reliable measurements of planetary properties (i.e., at high spectral resolution), including detailed characterisation of the star-host, will be the cornerstone on which the characterisation of habitable planets will be based.

[1] https://horse.sciencesconf.org and #NICEEXOPLANETS

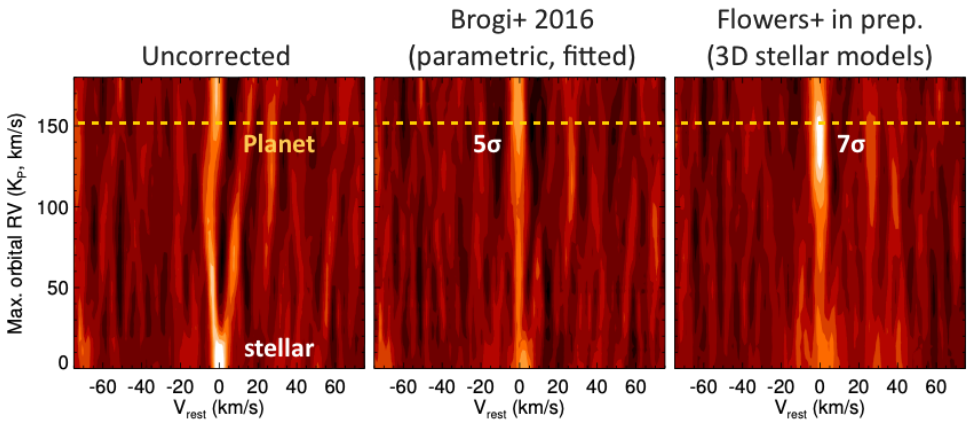

Figure 3.2: Two-dimensional significance maps of the explored planet parameter orbital radial-velocity semi-amplitude (K_P). While in left panel the expected planet value (yellow dashed line) is completely hidden by stellar signal, in central panel (paramentric approach) and right panel (3D RHD simulation correction) the planet orbital radial-velocity is recovered with an higher significatively when a proper stellar correction is applied.

3.2 Improving 3D simulations of RGSs towards the solution of the mass-loss problem

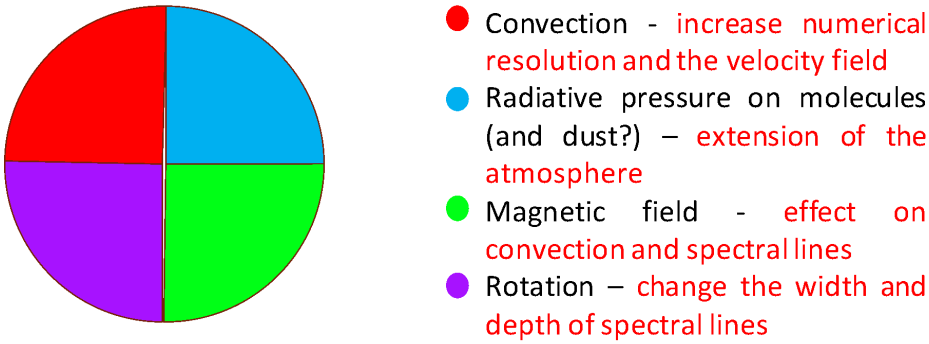

Figure 3.3: The four main limitations of 3D RHD simulations of RSG stars to be solved in order to provide a quantitative response to the problem of mass loss that affects the chemical evolution of galaxies. In red the effect on observables and/or the simulations

I PRESENTED the simulations of the red supergiants as well as the code CO^{5}BOLD. Despite the very satisfactory comparisons with observations, recent advances in instrumental techniques in interferometry (PIONIER and AMBER@VLTI), imaging (SPHERE@VLT) and spectroscopy have achieved an astonishing level of accuracy. A number of recent studies, in which I took part, have highlighted the current limitations of 3D simulations that need to be solved in order to provide a quantitative response to the problem of mass loss in red supergiants (Fig. 3.3). These four points, in which I will concentrate my research, are the cornerstone for future developments in the field, in particular the magnetic field and radiative pressure.

1. *The numerical resolution*. It affects the source function due to the lack of spatial resolution at about the optical depth of $\tau = 1$ (i.e., where the flux is formed). As a result, the emerging intensity may show, in some cases, extreme peaks of brightness with respect to the to adjacent areas. Attempts have been made to solve this problem by interpolating the source function in CO^{5}BOLD, but they have caused numerical instabilities, and in OPTIM3D. In addition to this, numerical resolution determines also the resolving power of the structures on the stellar surface. This leads to an under estimation of the simulation's velocities

that affects the gas levitation and the width of spectral lines (K. Kravchenko's thesis). The current solution is to increase the number of points at 1000^3 or more, which implies a more intensive and time consuming use of cluster computers.

2. *The radiative pressure*. Recent comparisons of simulations to interferometric observations with AMBER have shown that the extension of the observed red supergiant atmospheres is not explicable by current models (Fig. 3.4, Arroyo-Torres et al. 2015). This vision was confirmed by the observations taken with SPHERE in the optical where the extension of 3D atmospheres is too small (Kervella et al. 2016). In addition to this, the images also show a dust shell in the 3 stellar rays that could be the consequence of a photospheric ejection. The inclusion of radiative pressure in the simulations should help the gas to levitate in the outermost layers of the atmosphere, where opacity is not negligible (e.g., TiO molecules) and explain (at least in part) the mechanism of mass loss: radiative pressure on molecules.

3. *The magnetic field*. The presence of a magnetic field in stars is intimately linked to the convection across the stellar photosphere. A typically magnetic field results in the increase of atmospheric velocities and higher temperatures in the chromosphere. As a consequence, the overall structure of the stellar atmosphere is affected. In the case of evolved stars, local dynamos are expected to appear in correspondance of the large convective cells (Freytag et al. 2002). Longterm spectropolarimetric observations (e.g., those obtained with NARVAL at the Pic du Midi, Aurière et al. 2010; Mathias et al. 2018) show the detection of a signal in the spectral lines and measure an average longitudinal magnetic field of a few Gauss. The introduction of the magnetic field into 3D RHD simulations is under development and will be of paramount importance for the interpretation of observations.

4. *The stellar rotation.* Observations indicate that synthetic spectral lines are narrower and deeper than those observed (e.g., Lion et al. 2013). This may be caused by the low numerical resolution of point (1), but it may be also caused by the lack of a rotational velocity. Uitenbroek et al. (1998) found a angular rotation velocity between 2.0 and 2.5 km/s (i.e., a projected equatorial velocity of 5.0 km/s) that could (partially) contribute to the loss of mass. Recently, this result was confirmed by Kervella et al. (2018), with ALMA observations, who found a projected equatorial velocity of $\sim$ 5.47 km/s. Recently, I computed

a series of 3D RHD simulations with different projected equatorial velocities ranging from 2.0 to 6.0 km/s, which corresponds to a rotation period of 60 to 20 years, respectively. A record for this type of simulation that required an intensive use of computing resources. These simulations will be exploded soon.

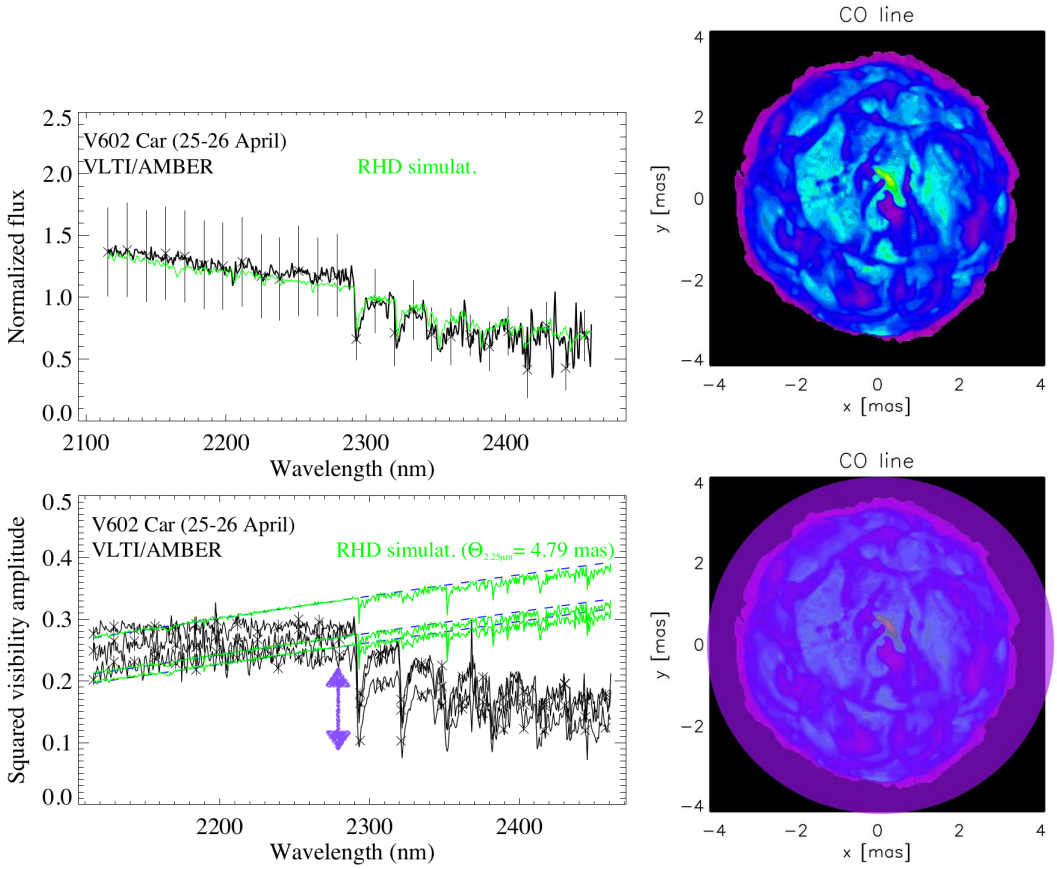

Figure 3.4: *Left column:* Interferometric observations of red supergiants with AMBER (black) compared to 3D simulation predictions (green). While the flux adjustment (top panel) is good, the visibilities show a significant disagreement (bottom panel, purple arrow). *Right column:* Synthetic image in the CO lines at about 2.3 μm. The image at the top shows the result of the 3D atmosphere calculation, while the purple shadow in the image at the bottom displays the expected atmospheric extension needed to explain the difference in visibility (Arroyo-Torres et al. 2015)

Abbreviations

1D	One-dimensional models
3D	Three-dimensional models
AGB	Asymptotic Giant Branch
box-in-a-star	local RHD simulations
CLV	Center to limb variations
CO^{5}BOLD	COnservative COde for the COmputation of COmpressible COnvection in a BOx of L Dimensions, 1=
ESO	European South Observatory
LTE	Local Thermodynamic Equilibrium
H-R	Herzsprung-Russel
HST-WFC3	photometric system
IR	InfraRed
ISM	InterStellar Medium
UBV(RI)$_C$	Johnson-Cousins, photometric system
MARCS	1D, hydrostatic, plane-parallel and spherical LTE model atmospheres
2MASS	photometric system
Optim3D	Multidimensional pure LTE radiative transfer code
RHD	Radiative HydroDynamical
RGB	Red Giant Branch stars
RSG	Red Supergiant stars
SED	Spectral Energy Distribution
SDSS	Sloan Digital Sky Survey, photometric system
SkyMapper	Photometric systems
Stagger code	multipurpose, radiative-magnetohydrodynamics code
star-in-a-box	global RHD simulations
Strömgren	Photometric system
TURBOSPECTRUM	Code for 1D spectral synthesis
UV-plane	The Fourier plane with u,v coordinates related to x, y ones in the sky
UV	UltraViolet
VALD	Vienna Atomic Line Database

Bibliography

Allard, F., Homeier, D., Freytag, B., et al. 2013, Memorie della Societa Astronomica Italiana Supplementi, 24, 128

Allende Prieto, C., Koesterke, L., Ludwig, H.-G., Freytag, B., & Caffau, E. 2013, A&A, 550, A103

Alvarez, R., Jorissen, A., Plez, B., Gillet, D., & Fokin, A. 2000, A&A, 362, 655

Alvarez, R., Jorissen, A., Plez, B., et al. 2001a, A&A, 379, 288

Alvarez, R., Jorissen, A., Plez, B., et al. 2001b, A&A, 379, 305

Alvarez, R. & Plez, B. 1998, A&A, 330, 1109

Arroyo-Torres, B., Martí-Vidal, I., Marcaide, J. M., et al. 2014, A&A, 566, A88

Arroyo-Torres, B., Wittkowski, M., Chiavassa, A., et al. 2015, A&A, 575, A50

Asplund, M., Grevesse, N., & Sauval, A. J. 2005, in Astronomical Society of the Pacific Conference Series, Vol. 336, Cosmic Abundances as Records of Stellar Evolution and Nucleosynthesis, ed. T. G. Barnes, III & F. N. Bash, 25

Asplund, M., Grevesse, N., Sauval, A. J., & Scott, P. 2009, ARA&A, 47, 481

Asplund, M., Ludwig, H., Nordlund, Å., & Stein, R. F. 2000, A&A, 359, 669

Auer, L. H. & Mihalas, D. 1972, ApJS, 24, 193

Aurière, M., Donati, J.-F., Konstantinova-Antova, R., et al. 2010, A&A, 516, L2

Beeck, B., Cameron, R. H., Reiners, A., & Schüssler, M. 2013, A&A, 558, A48

Beeck, B., Collet, R., Steffen, M., et al. 2012, A&A, 539, A121

Bigot, L., Mourard, D., Berio, P., et al. 2011, A&A, 534, L3

Bigot, L. & Thévenin, F. 2008, in SF2A-2008, ed. C. Charbonnel, F. Combes, & R. Samadi, 3

Bonifacio, P., Caffau, E., Ludwig, H.-G., et al. 2017, Mem. Soc. Astron. Italiana, 88, 90

Borucki, W. J., Koch, D., Basri, G., et al. 2010, Science, 327, 977

Borucki, W. J. & Summers, A. L. 1984, Icarus, 58, 121

Broeg, C., Fortier, A., Ehrenreich, D., et al. 2013, in European Physical Journal Web of Conferences, Vol. 47, European Physical Journal Web of Conferences, 3005

Brogi, M., de Kok, R. J., Albrecht, S., et al. 2016, ApJ, 817, 106

Brogi, M., Giacobbe, P., Guilluy, G., et al. 2018, A&A, 615, A16

Brogi, M., Line, M., Bean, J., Désert, J.-M., & Schwarz, H. 2017, ApJ, 839, L2

Brogi, M., Snellen, I. A. G., de Kok, R. J., et al. 2012, Nature, 486, 502

Caffau, E., Ludwig, H.-G., Steffen, M., Freytag, B., & Bonifacio, P. 2011, Sol. Phys., 268, 255

Chiavassa, A., Bigot, L., Kervella, P., et al. 2012, A&A, 540, A5

Chiavassa, A., Bigot, L., Thévenin, F., et al. 2011a, Journal of Physics Conference Series, 328, 012012

Chiavassa, A., Caldas, A., Selsis, F., et al. 2017a, A&A, 597, A94

Chiavassa, A., Casagrande, L., Collet, R., et al. 2018a, A&A, 611, A11

Chiavassa, A., Collet, R., Casagrande, L., & Asplund, M. 2010a, A&A, 524, A93

Chiavassa, A. & Freytag, B. 2015, in Astronomical Society of the Pacific Conference Series, Vol. 497, Why Galaxies Care about AGB Stars III: A Closer Look in Space and Time, ed. F. Kerschbaum, R. F. Wing, & J. Hron, 11

Chiavassa, A., Freytag, B., Masseron, T., & Plez, B. 2011b, A&A, 535, A22

Chiavassa, A., Freytag, B., & Schultheis, M. 2018b, ArXiv e-prints

Chiavassa, A., Haubois, X., Young, J. S., et al. 2010b, A&A, 515, A12

Chiavassa, A., Lacour, S., Millour, F., et al. 2010c, A&A, 511, A51

Chiavassa, A., Ligi, R., Magic, Z., et al. 2014, A&A, 567, A115

Chiavassa, A., Norris, R., Montargès, M., et al. 2017b, A&A, 600, L2

Chiavassa, A., Pasquato, E., Jorissen, A., et al. 2011c, A&A, 528, A120

Chiavassa, A., Pere, C., Faurobert, M., et al. 2015, A&A, 576, A13

Chiavassa, A., Plez, B., Josselin, E., & Freytag, B. 2009, A&A, 506, 1351

Collet, R., Hayek, W., Asplund, M., et al. 2011, A&A, 528, A32

Creevey, O. L., Thévenin, F., Boyajian, T. S., et al. 2012, A&A, 545, A17

Cruzalèbes, P., Jorissen, A., Rabbia, Y., et al. 2013, MNRAS, 434, 437

Davies, B., Kudritzki, R.-P., Lardo, C., et al. 2017, ApJ, 847, 112

Davies, B., Kudritzki, R.-P., Plez, B., et al. 2013, ApJ, 767, 3

De Beck, E., Decin, L., de Koter, A., et al. 2010, A&A, 523, A18

Dravins, D. 1982, ARA&A, 20, 61

Evans, D. W., Riello, M., De Angeli, F., et al. 2018, ArXiv e-prints

Flowers, E., Brogi, M., Rauscher, E., M-R Kempton, E., & Chiavassa, A. 2018, ArXiv e-prints

Freytag, B. 2001, in 11th Cambridge Workshop on Cool Stars, Stellar Systems and the Sun, ed. R. J. Garcia Lopez, R. Rebolo, & M. R. Zapaterio Osorio (Astronomical Society of the Pacific Conference Series, Volume 223), 785

Freytag, B., Liljegren, S., & Höfner, S. 2017, A&A, 600, A137

Freytag, B., Steffen, M., & Dorch, B. 2002, Astronomische Nachrichten, 323, 213

Freytag, B., Steffen, M., Ludwig, H.-G., et al. 2012, Journal of Computational Physics, 231, 919

Gaia Collaboration, Brown, A. G. A., Vallenari, A., et al. 2018, ArXiv e-prints

Gaia Collaboration, Prusti, T., de Bruijne, J. H. J., et al. 2016, A&A, 595, A1

Gray, D. F. 2008, AJ, 135, 1450

Gustafsson, B., Edvardsson, B., Eriksson, K., et al. 2008, A&A, 486, 951

Hauschildt, P. H., Baron, E., & Allard, F. 1997, ApJ, 483, 390

Hayek, W., Asplund, M., Carlsson, M., et al. 2010, A&A, 517, A49

Hertzsprung, E. 1905, Zeitschrift Fur Wissenschaftliche Photographie, Vol 3, p. 442-449, 3, 442

Höfner, S. & Olofsson, H. 2018, A&A Rev., 26, 1

Iglesias, C. A., Rogers, F. J., & Wilson, B. G. 1992, ApJ, 397, 717

Josselin, E. & Plez, B. 2007, A&A, 469, 671

Kervella, P., Decin, L., Richards, A. M. S., et al. 2018, A&A, 609, A67

Kervella, P., Lagadec, E., Montargès, M., et al. 2016, A&A, 585, A28

Kervella, P., Thévenin, F., Di Folco, E., & Ségransan, D. 2004, A&A, 426, 297

Kravchenko, K., Van Eck, S., Chiavassa, A., et al. 2018, A&A, 610, A29

Kudritzki, R. P. 1976, A&A, 52, 11

Langer, N. 2012, ARA&A, 50, 107

Lèbre, A., Aurière, M., Fabas, N., et al. 2014, A&A, 561, A85

Levesque, E. M. 2018, ArXiv e-prints

Levesque, E. M., Massey, P., Olsen, K. A. G., et al. 2005, ApJ, 628, 973

Lion, S., Van Eck, S., Chiavassa, A., Plez, B., & Jorissen, A. 2013, in EAS Publications Series, Vol. 60, EAS Publications Series, ed. P. Kervella, T. Le Bertre, & G. Perrin, 85–92

Ludwig, H., Caffau, E., Steffen, M., et al. 2009, Mem. Soc. Astron. Italiana, 80, 711

Ludwig, H., Jordan, S., & Steffen, M. 1994, A&A, 284, 105

Magic, Z., Chiavassa, A., Collet, R., & Asplund, M. 2015, A&A, 573, A90

Magic, Z., Collet, R., Asplund, M., et al. 2013a, ArXiv e-prints

Magic, Z., Collet, R., Asplund, M., et al. 2013b, A&A, 557, A26

Mathias, P., Aurière, M., Ariste, A. L., et al. 2018, A&A, 615, A116

Maxted, P. F. L. 2018, A&A, 616, A39

Michelson, A. A. & Pease, F. G. 1921, ApJ, 53

Mihalas, D., Dappen, W., & Hummer, D. G. 1988, ApJ, 331, 815

Mislis, D., Heller, R., Schmitt, J. H. M. M., & Hodgkin, S. 2012, A&A, 538, A4

Monnier, J. D. 2007, New Astronomy Review, 51, 604

Montargès, M., Chiavassa, A., Kervella, P., et al. 2017, A&A, 605, A108

Montargès, M., Kervella, P., Perrin, G., et al. 2016, A&A, 588, A130

Montargès, M., Kervella, P., Perrin, G., et al. 2014, A&A, 572, A17

Montargès, M., Norris, R., Chiavassa, A., et al. 2018, A&A, 614, A12

Nielsen, A. V. 1964, Centaurus, 9, 219

Nordlund, A. 1982, A&A, 107, 1

Nordlund, Å., Stein, R. F., & Asplund, M. 2009, Living Reviews in Solar Physics, 6, 2

Paladini, C., Baron, F., Jorissen, A., et al. 2018, Nature, 553, 310

Petit, P., Aurière, M., Konstantinova-Antova, R., et al. 2013, in Lecture Notes in Physics, Berlin Springer Verlag, Vol. 857, Lecture Notes in Physics, Berlin Springer Verlag, ed. J.-P. Rozelot & C. . Neiner, 231

Piskunov, N. E., Kupka, F., Ryabchikova, T. A., Weiss, W. W., & Jeffery, C. S. 1995, A&AS, 112, 525

Piso, A.-M. A., Pegues, J., & Öberg, K. I. 2016, ApJ, 833, 203

Plez, B. 2012, Turbospectrum: Code for spectral synthesis, Astrophysics Source Code Library

Ragland, S., Traub, W. A., Berger, J.-P., et al. 2006, ApJ, 652, 650

Rauer, H., Catala, C., Aerts, C., et al. 2014, Experimental Astronomy

Ricker, G. R., Latham, D. W., Vanderspek, R. K., et al. 2010, in Bulletin of the American Astronomical Society, Vol. 42, American Astronomical Society Meeting Abstracts #215, 450.06

Rodler, F. & López-Morales, M. 2014, ApJ, 781, 54

Russell, H. N. 1919, Proceedings of the National Academy of Science, 5, 391

Schneider, G., Pasachoff, J. M., & Willson, R. C. 2006, ApJ, 641, 565

Skartlien, R. 2000, ApJ, 536, 465

Snellen, I. A. G., Brandl, B. R., de Kok, R. J., et al. 2014, Nature, 509, 63

Stello, D., Chaplin, W. J., Basu, S., Elsworth, Y., & Bedding, T. R. 2009, MNRAS, 400, L80

Stempels, H. C., Piskunov, N., & Barklem, P. S. 2001, in Astronomical Society of the Pacific Conference Series, Vol. 223, 11th Cambridge Workshop on Cool Stars, Stellar Systems and the Sun, ed. R. J. Garcia Lopez, R. Rebolo, & M. R. Zapaterio Osorio, 878

Tessore, B., Lèbre, A., Morin, J., et al. 2017, A&A, 603, A129

Trampedach, R., Asplund, M., Collet, R., Nordlund, Å., & Stein, R. F. 2013, ApJ, 769, 18

Tremblay, P.-E., Ludwig, H.-G., Freytag, B., Steffen, M., & Caffau, E. 2013a, A&A, 557, A7

Tremblay, P.-E., Ludwig, H.-G., Steffen, M., & Freytag, B. 2013b, A&A, 559, A104

Uitenbroek, H., Dupree, A. K., & Gilliland, R. L. 1998, AJ, 116, 2501

Vasilyev, V., Ludwig, H.-G., Freytag, B., Lemasle, B., & Marconi, M. 2017, A&A, 606, A140

Vögler, A., Bruls, J. H. M. J., & Schüssler, M. 2004, A&A, 421, 741

Vögler, A., Shelyag, S., Schüssler, M., et al. 2005, A&A, 429, 335

Wedemeyer, S., Ludwig, H.-G., & Steiner, O. 2013, Astronomische Nachrichten, 334, 137

Wittkowski, M. 2004, ArXiv Astrophysics e-prints

Wittkowski, M., Abellán, F. J., Arroyo-Torres, B., et al. 2017a, A&A, 606, L1

Wittkowski, M., Arroyo-Torres, B., Marcaide, J. M., et al. 2017b, A&A, 597, A9

Wittkowski, M., Chiavassa, A., Freytag, B., et al. 2016, A&A, 587, A12

Wittkowski, M., Hauschildt, P. H., Arroyo-Torres, B., & Marcaide, J. M. 2012, A&A, 540, L12

Wood, P. R., Whiteoak, J. B., Hughes, S. M. G., et al. 1992, ApJ, 397, 552

Wright, J. T., Fakhouri, O., Marcy, G. W., et al. 2011, PASP, 123, 412

Wyttenbach, A., Ehrenreich, D., Lovis, C., Udry, S., & Pepe, F. 2015, A&A, 577, A62

Zwitter, T., Kos, J., Chiavassa, A., et al. 2018, ArXiv e-prints